THÈSE

Pour obtenir le grade de

DOCTEUR DE L'UNIVERSITÉ GRENOBLE ALPES
et de l'UNIVERSITE DE BUENOS AIRES

École doctorale : Chimie et sciences du vivant
Spécialité : Chimie Biologie
Unité de recherche : Institut Néel

Nanoparticules multifonctionnelles pour une libération contrôlée d'enzymes

Multi-Functional nanoparticles for controlled enzyme delivery

Présentée par :

Andrea Cristina MONTERO OLEAS

Direction de thèse :

Xavier CATTOEN CHARGE DE RECHERCHES, Université Grenoble Alpes	Directeur de thèse
Sara ALDABE BILMES DIRECTRICE DE RECHERCHE, Universidad de Buenos Aires	Co-directrice de thèse

Rapporteurs :

Marcelo KOGAN
FULL PROFESSOR, Universidad de Chile
Belen ALBELA
MAITRESSE DE CONFERENCES, École normale supérieure de Lyon

Thèse soutenue publiquement le **8 novembre 2024,** devant le jury composé de :

Eric PEYRIN PROFESSEUR DES UNIVERSITES, Université Grenoble Alpes	Examinateur
Fernando BATTAGLINI FULL PROFESSOR, Universidad de Buenos Aires	Président
Veronica CORTES DE ZEA BERMUDEZ FULL PROFESSOR, Universidade de Trás-os-Montes	Examinatrice
Marcelo KOGAN FULL PROFESSOR, Universidad de Chile	Rapporteur
Belen ALBELA MAITRESSE DE CONFERENCES, École normale supérieure de Lyon	Rapporteure

Acknowledgments

This thesis would not have been possible without the support and encouragement of an extraordinary team. My deepest gratitude goes to my thesis supervisors, Xavier Cattoën and Sara Bilmes, who, four years ago, gave me the invaluable opportunity to join their research groups. Working with them has allowed me to explore a fascinating and exciting field and to collaborate with brilliant individuals. I have always found you both to be attentive, encouraging, and patient. Your complementary temperaments have enabled me to perform at my best. I am truly honored to have been your student.

I would also like to extend my special thanks to Yoann Roupioz, who was my unofficial third thesis supervisor. I am grateful for his significant scientific contributions, as well as for all his support during this journey.

Thanks to Mateus Cardoso for his valuable ideas, willingness, and insightful discussions that greatly contributed to the results presented in this thesis. To Juliana Yoneda and Flavia Galdino, I am grateful for their help and kindness during the experiments at SIRIUS. To Luelc da Costa and Jefferson Bettini, thank you for their warmth and

for teaching me the patience required to obtain beautiful microscopy images.

Thanks to Alain Ibanez for his advice, teachings and discussions, and for always being so kind. To Stephanie Kodjikian and Sébastien Paris, thank you for their assistance in learning SEM and TEM. To María Luz Martínez, I am grateful for her support when I needed it, and to Diego Onna, for all his advice and for consistently being attentive to my needs. To Claudia Marchi, with whom I spent many hours in microscopy. To Tomás Mautino, for his efforts in organizing the laboratory. To Ezequiel Alba, for his help with protein purification and his friendly demeanor. To Lucy Coria, for her assistance with enzyme experiments and her valuable teachings. To Lia Pietrasanta and Silvio Luduena for their help with the AFM measurements.

Thanks to Phillipe Trens for the nitrogen adsorption measurements and for his invaluable help in interpreting them.

Thanks to my academic advisor, Ernesto Marceca, for his support in managing the complex procedures of the cotutelle at UBA.

A heartfelt thank you to everyone involved in the bureaucratic process: Andre, Ale, Mariana, and Cintia from INQUIMAE, and Magali and Camille from UGA.

I am grateful to the DQIAQF–INQUIMAE, the Institute Néel, SyMMES, and CNPEM for providing a workspace for this doctoral thesis and to all the individuals I had the opportunity to meet and collaborate with.

Thanks to the Nanoandes network, through which my passion for nanoscience grew and which introduced me to remarkable scientists who made this thesis possible.

I also extend my gratitude to all the institutions that have contributed to this work: CONICET, CNRS, UBA, UGA, and USFQ.

I would like to thank my thesis committee for agreeing to evaluate and discuss my work.

Throughout these four years, having friends to rely on, both personally and professionally, has been crucial. Thanks to my dear friends from Grenoble, Italia, Ricardo, Valentina, Bruno, Kylia, Julius, Emre, Vartika, Javier, and Tibaldo, who made my arrival in Grenoble during the pandemic more manageable. I am grateful for all the ideas, discussions, cherished lunches, coffee breaks, funny moments and hikes that made my time in Grenoble one of the most special periods of my life. I am blessed to have worked with you all in such a great atmosphere.

To my dear friends Anita, Carlita, Andrea, Silvy, Dennisse, and Nina, for their encouragement and regular video calls, even while we are spread across the world.

To Gerardo, for being the best teammate and for always supporting me in life. Your love and patience mean the world to me.

Finally, and most importantly, I dedicate this thesis to my parents and siblings. Thank you for everything! You have been a fundamental pillar in my life. Your love and unconditional support have given me the strength and motivation to complete this journey.

This work was supported by the French National Research Agency in the framework of the "Investissements d'avenir" program (ANR-15-IDEX-02), by Universidad de Buenos Aires, Argentina (UBACyT 20020190100299BA & 20020220200115BA), by CONICET (PIP 112202101 00205), and by ANPCyT PICT 2021 I-A-0045.

Abstract

Nanomaterials hold great potential for directing molecules through fluids to specific sites. A diversity of nano-objects, such as liposomes, polymers or nanoparticles have indeed been explored as nanovehicles (NVs). Among these, inorganic-based NVs are particularly advantageous due to their low cost, good biocompatibility, and versatility to be surface-modified for targeted delivery. Transported within a nano-vehicle, a molecule is protected from degradation and can be released at the target site by external stimuli such as chemical, magnetic, light, or ultrasound triggers. Light, in particular, is promising due to its non-invasive nature and capability for remote control.

Mesoporous silica nanoparticles (*m*SiO_2) stand out due to their tunable size, porous structure, and surface functionality, making them suitable for applications in nanomedicine. Gold nanoparticles (AuNPs) add unique properties to *m*SiO_2-based systems with their localized surface plasmon resonance bands, enabling efficient light-to-heat conversion through the photothermal effect. This combination of high loading capacity and photothermal properties is harnessed in core-shell Au@*m*SiO_2 particles. Designing these particles requires careful consideration of factors such as the diameter of the core-shell particles, the size and functionalization of the pores, and the shape of the gold core to optimize photothermal efficiency and targeted delivery.

This thesis introduces a novel synthesis of large-pore Au@*m*SiO_2 particles aimed at effectively encapsulating proteins, with potential applications in protein therapy. The synthesis mechanism was systematically explored through a *one-pot* method, resulting in a rational and reproducible design of Au@*m*SiO_2 particles with precise size control. To achieve large-pore Au@*m*SiO_2 particles, seed-growth synthesis methods were employed, wherein a silica shell with larger pores was grown on a pre-synthesized seed. Two strategies were investigated for creating large-pore structures: (1) using pore-expanding agents to produce silica shells with pores up to 7 nm in diameter, and (2) employing stratified growth in a biphasic medium, where large hemimicelles acted as templates to create pores up to 20 nm in diameter.

The stability of the synthesized particles was assessed under conditions simulating physiological environments (100 mM PBS) to evaluate their reliability for biomedical applications. The stability of the nanoparticles was found to depend on both the synthesis method and particle concentration. Notably, the biphasic growth method produced the most stable nanoparticles, which maintained their morphology for up to 3 days post-incubation in high-salinity medium, even at concentrations below the silica solubility limit.

The protein retention and protection capabilities of the synthesized nanoparticles were demonstrated using three model

proteins—bovine serum albumin, horseradish peroxidase, and red fluorescent protein—each possessing distinct structures and molecular weights. The results indicated that protein absorption capacity was directly correlated with pore size and protein structure. Moreover, the stability of the adsorbed proteins was examined, revealing that proteins encapsulated within large-pore nanoparticles exhibited greater stability compared to free proteins in solution.

In conclusion, this thesis presents an optimized synthesis method combining one-pot and biphasic growth approaches to produce nanoparticles with adjustable pore sizes (ranging from 3 to 20 nm), controlled final diameters (~100 nm), high stability under near physiological conditions, and optimal protein retention. These large-pore Au@*m*SiO_2 nanoparticles represent a significant advancement in the field of nanomedicine, offering a promising platform for controlled protein delivery.

Résumé

Les nanomatériaux ont un potentiel important pour transporter des molécules vers des sites spécifiques. Divers nano-objets, comme les liposomes, polymères et nanoparticules, ont été explorés comme nanovecteurs (NVs). Les NVs inorganiques sont particulièrement avantageux en raison de leur faible coût, leur biocompatibilité et leur flexibilité pour une modification de surface en vue d'une délivrance ciblée. Transportées dans un nanovecteur, les molécules sont protégées de la dégradation et peuvent être libérées au site ciblé par des stimuli externes tels que chimiques, magnétiques, lumineux ou ultrasonores. La lumière est intéressante grâce à son caractère non invasif et son contrôle à distance.

Les nanoparticules de silice mésoporeuse (*m*SiO_2) se distinguent par leur taille modulable, leur structure poreuse et leur fonctionnalité de surface, les rendant appropriées pour des applications en nanomédecine. Les nanoparticules d'or (AuNPs) apportent des propriétés uniques aux systèmes basés sur les *m*SiO_2 grâce à leurs bandes de résonance plasmonique de surface , permettant une conversion efficace de la lumière en chaleur par effet photothermique. Cette combinaison de grande capacité de chargement et de propriétés photothermiques est exploitée dans les particules Au@*m*SiO_2 à géométrie cœur-coquille cœur-shell. La conception de ces particules

nécessite un contrôle minutieux de facteurs comme le diamètre des particules et la taille des pores, ainsi que la forme du cœur en or pour optimiser l'efficacité photothermique et la délivrance ciblée.

Cette thèse présente une méthode de synthèse innovante de particules Au@*m*SiO_2 à pores larges, destinées à l'encapsulation efficace de protéines, avec des applications potentielles en thérapie protéique. Le mécanisme de synthèse via une méthode *one-pot* a été exploré de manière systématique, aboutissant à une conception rationnelle et reproductible de particules Au@*m*SiO_2 avec un contrôle précis de la taille. Pour obtenir des particules à pores larges, des méthodes de préparation de type *seed-growth* ont été employées, par croissance d'une coquille de silice à pores larges autour d'un noyau préformé. Deux stratégies ont été explorées : (1) l'utilisation d'agents d'expansion des pores pour produire des coques de silice avec des pores jusqu'à 7 nm de diamètre, et (2) la croissance stratifiée dans un milieu biphasique, où de grandes hémimicelles ont servi de gabarits pour créer des pores jusqu'à 20 nm de diamètre.

La stabilité des particules synthétisées a été évaluée dans des conditions simulant les environnements physiologiques (PBS 100 mM) pour évaluer leur fiabilité pour des applications biomédicales. La méthode de croissance biphasique a produit les nanoparticules les plus stables, qui ont maintenu leur morphologie jusqu'à 3 jours d' incubation dans un milieu à haute salinité.

Les capacités de rétention et de protection des protéines ont été démontrées en utilisant trois protéines modèles—albumine sérique bovine, peroxydase du raifort et protéine fluorescente rouge—avec des structures et poids moléculaires distincts. Les résultats ont montré que la capacité d'adsorption des protéines était directement corrélée à la taille des pores et à la structure des protéines. De plus, la stabilité des protéines encapsulées dans des nanoparticules à pores larges s'est révélée supérieure à celle des protéines libres en solution.

En conclusion, cette thèse présente une méthode de synthèse optimisée combinant les méthodes *one-pot* et de croissance biphasique pour produire des nanoparticules avec des tailles de pores ajustables (de 3 à 20 nm), des diamètres finaux contrôlés (~100 nm), grande stabilité dans des conditions physiologiques, et qui sont optimales pour la rétention des protéines. Ces nanoparticules Au@*m*SiO_2 à pores larges représentent une avancée significative dans le domaine de la nanomédecine, offrant une plateforme prometteuse pour la délivrance contrôlée de protéines.

Resumen

Los nanomateriales ofrecen un gran potencial para dirigir moléculas hacia lugares específicos dentro de fluidos. Se han explorado diversos tipos de nanoobjetos, como liposomas, polímeros y nanopartículas, como nanovehículos (NVs). Entre ellos, los NVs inorgánicos son especialmente ventajosos debido a su bajo costo, buena biocompatibilidad y la capacidad de modificar su superficie para una liberación dirigida. Dentro de un nanovehículo, una molécula está protegida de la degradación y puede liberarse en el sitio deseado mediante estímulos externos como químicos, magnetismo, luz o ultrasonido. La luz es especialmente prometedora por ser no invasiva y permitir el control remoto.

Las nanopartículas de sílice mesoporosa (*m*SiO_2) destacan por su tamaño ajustable, su estructura porosa y la posibilidad de funcionalizar la superficie, lo que las hace ideales para aplicaciones en nanomedicina. Las nanopartículas de oro (AuNPs) aportan propiedades únicas a los sistemas basados en *m*SiO_2 gracias a sus bandas de resonancia plasmónica superficial localizada. Esto permite una conversión eficiente de luz en calor mediante el efecto fototérmico. Esta combinación de alta capacidad de carga y propiedades fototérmicas se utiliza en las partículas *core-shell* Au@*m*SiO_2. Para

diseñar estas partículas, es crucial considerar factores como el diámetro de las partículas, el tamaño y la funcionalización de los poros, y la forma del *core* de oro para optimizar la eficiencia fototérmica y la liberación dirigida.

Esta tesis presenta una nueva síntesis de partículas de Au@*m*SiO_2 con poros grandes, con el objetivo de encapsular proteínas de manera efectiva para aplicaciones en terapia proteica. Se exploró el mecanismo de síntesis mediante un método *one-pot*, logrando un diseño reproducible de partículas Au@*m*SiO_2 con un control preciso del tamaño. Para obtener partículas con poros grandes, se utilizaron métodos de síntesis por crecimiento de semillas, donde se creció una capa de sílice con poros más grandes sobre una semilla pre-sintetizada. Se investigaron dos estrategias para crear estas estructuras: (1) usar agentes expansores de poros para producir capas de sílice con poros de hasta 7 nm de diámetro, y (2) emplear crecimiento estratificado en un medio bifásico, donde grandes hemimicelas actuaron como plantillas para crear poros de hasta 20 nm de diámetro.

La estabilidad de las partículas sintetizadas se evaluó en condiciones que simulan ambientes fisiológicos (100 mM PBS) para determinar su fiabilidad en aplicaciones biomédicas. La estabilidad de las nanopartículas dependió del método de síntesis y de la concentración de partículas. El método de crecimiento bifásico resultó en nanopartículas más estables, que mantuvieron su forma durante

hasta 3 días en un medio de alta salinidad, incluso a concentraciones por debajo del límite de solubilidad de la sílice.

Se demostraron las capacidades de retención y protección de proteínas de las nanopartículas sintetizadas utilizando tres proteínas modelo: albúmina de suero bovino, peroxidasa de rábano y proteína fluorescente roja, cada una con estructuras y pesos moleculares diferentes. Los resultados mostraron que la capacidad de absorción de proteínas estaba directamente relacionada con el tamaño de los poros y la estructura de las proteínas. Además, las proteínas encapsuladas en nanopartículas de poro grande demostraron una mayor estabilidad en comparación con las proteínas libres en solución, indicando que las paredes de los poros protegen eficazmente las proteínas de factores de estrés ambientales.

En conclusión, esta tesis presenta un método de síntesis optimizado que combina métodos *one-pot* y crecimiento bifásico para producir nanopartículas con tamaños de poro ajustables (de 3 a 20 nm), diámetros finales controlados (~100 nm), alta estabilidad en condiciones cercanas a la fisiológicas, y que son óptimas para retener proteínas. Estas nanopartículas de Au@*m*SiO_2 con poros grandes representan un avance significativo en el campo de la nanomedicina, ofreciendo una plataforma prometedora para la liberación controlada de proteínas.

List of Abbreviations

ABTS	2,2′-azino-bis(3-ethylbenzothiazoline-6-sulfonic acid)
AFM	Atomic Force Microscopy
Au@*m*SiO_2	Gold-silica core-shell nanoparticle
AuNP(s)	Gold nanoparticle(s)
AuNRa	Gold nanorods
b-Au@*m*SiO_2	Au@*m*SiO_2 synthesized with biphasic stratification
BSA	Bovine Serum Albumin
CD	Circular Dichroism
CMC	Critical Micelle Concentration
cryo-EFTEM	Energy-filtered transmission electron microscopy under criogenic conditions
CTAB	Cetyl trimethylammonium bromide
CTAC	Cetyl trimethylammonium chloride
DLS	Dynamic Light Scattering
e-Au@*m*SiO_2	Au@*m*SiO_2 synthesized with pore-expanding agents
FTIR	Fourier-transform Infrared Spectroscopy
$HAuCl_4$	Chloroauric Acid
HRP	Horseradish Peroxidase
LMCT	Ligand-to-Metal Charge Transfer
lp-Au@*m*SiO_2	Large-pores Au@*m*SiO_2
LSRP	Localized Surface Plasmon Resonance
mSiO_2	Mesoporous Silica
MSN(s)	Mesoporous Silica Nanoparticle(s)
NIR	Near-Infrared
NP(s)	Nanoparticle(s)
PBS	Phosphate Buffer Saline
PDT	Photodinamic Therapy
PTT	Photothermal Therapy
SEM	Scanning Electron Microscope
SNP	Non-porous Silica Nanoparticles
sp-Au@*m*SiO_2	Small-pores Au@*m*SiO_2
SSL	Silica Solubility Limit
TEM	Transmission Electron Microscopy
TEOA	Triethanolamine
TEOS	Tetraethyl orthosilicate
TIPB	1,3,5-triisopropylbenzene
TPOS	Tetrapropoxysilane

Contents

Chapter 1 Introduction..... 1
1.1. Motivation..... 1
1.2. Objectives..... 2
1.3. State of the Art..... 3
1.3.1. Nano-carriers for Protein Delivery..... 3
1.3.2. Mesoporous Silica Nanoparticles..... 5
1.3.3. Gold Nanoparticles..... 9
1.3.4. Core-shell Gold Silica Au@*m*SiO_2 Nanoparticles..... 16
1.3.5. Synthesis Routes..... 20
1.4. Summary and Outline of this Thesis..... 36
1.5. References..... 39
Chapter 2 Methods and Materials..... 57
2.1. Nanoparticles Synthesis..... 58
2.1.1. *One-pot* Synthesis of Au@*m*SiO_2 59
2.1.2. Synthesis of Large-pores Au@*m*SiO_2 62
2.1.3. Synthesis of Non-porous Silica Nanoparticles..... 70
2.1.4. Sample Nomenclature..... 71
2.2. Particles Characterization..... 72
2.2.1. Electron Microscopy for Imaging..... 72
2.2.2. Dynamic Light Scattering..... 73
2.2.3. ζ-potential..... 74
2.2.4. Atomic Force Microscopy..... 74
2.2.5. UV-vis spectroscopy..... 75
2.2.6. Infrared Spectroscopy..... 76
2.2.7. Nitrogen Sorption..... 76
2.2.8. Photothermal Conversion..... 77
2.3. Methods Used to Study Synthesis Mechanisms..... 77
2.3.1. CMC Determination..... 77
2.3.2. TEOS Hydrolysis Kinetics Analysis..... 78
2.3.3.Monitoring the Au@*m*SiO_2 Precursor State Formation by UV-vis Spectroscopy..... 80
2.3.4. Monitoring Au@*m*SiO_2 Formation by SEM..... 81
2.3.5. pH Monitoring of the Synthesis of Au@*m*SiO_2 82
2.4. Protein Loading Protocols..... 82
2.4.1. *m*Cherry Expression and Purification..... 83
2.4.2. Protein Loading on Nanoparticles..... 85
2.4.3. HRP Enzymatic Activity..... 86

2.4.4. Energy Filtering Transmission Electron Microscopy for Protein Visualization 87
2.4.5. Circular Dichroism of Adsorbed Proteins 88
2.5. Nanoparticles Stability 89
2.5.1. Stability of Au@*m*SiO_2 Nanoparticles 89
2.5.2. Stability of Nanoparticles in the Presence of Proteins 90
2.6. References 91
Chapter 3 One-pot Synthesis of Au@*m*SiO_2 93
3.1. Introduction 93
3.2. Simplest *One-pot* Synthesis of Au@*m*SiO_2 95
3.3. Au@*m*SiO_2 Synthesis Mechanism 98
3.3.1. The Precursor State 100
3.3.2. From the Precursor to the Au@*m*SiO_2 103
3.3.3. Summary of Mechanism 109
3.4. Tuning the Particles Through Synthesis Parameters 111
3.4.1. Surfactant Mixtures 111
3.4.2. Alcohols 117
3.4.3. Base Source 120
3.4.4. Temperature and Gold Salt Concentration 125
3.5. Conceptualization 126
3.6. Conclusions 128
3.7. References 130
Chapter 4 Two-steps Synthesis of Large-pores Au@*m*SiO_2 135
4.1. Introduction 135
4.2. Growth with Pore-expanding Agents 138
4.3. Growth by Biphasic Stratification 144
4.4. Au@*m*SiO_2 Particles Stability 153
4.4.1. Morphological Evolution Upon Incubation in Phosphate Buffer 154
4.4.1.1. *e*-Au@*m*SiO_2 154
4.4.1.2. *b*-Au@*m*SiO_2 158
4.4.1.3. *sp*-Au@*m*SiO_2 162
4.5. Summary of Au@*m*SiO_2 Particle Stability 164
4.6. Conclusions 166
4.7. References 168
Chapter 5 Protein Loading on Au@*m*SiO_2 Nano-vehicles 173
5.1. Introduction 173
5.2. The Particles Explored 176
5.3. The Proteins Explored 179
5.4. Protein Loading on Nanoparticles 182
5.4.1. Bovine Serum Albumin 182

5.4.2. *m*Cherry…… 193
5.4.3. Horseradish Peroxidase…….. 202
5.4.4. Summary of Protein Loading……. 211
5.5. Particle Stability…….. 211
5.5.1. Stability of Nanoparticles Loaded with BSA……... 212
5.5.2. Stability of Nanoparticles Loaded with *m*Cherry and HRP…..……...…… 217
5.6. Summary and Conclusions…….. 218
5.7. References…….. 221
Chapter 6 Au@*m*SiO$_2$ Light-induced Heating…… 227
6.1. Introduction……..…….. 227
6.3.Characterization of the Au@*m*SiO$_2$ Heating at the Macroscale…….……... 232
6.4.Theoretical Modelling of the Plasmonic Heating at the Nanoscale……...…… 237
6.5. Conclusions……..…… 244
6.6. References…… 247
Chapter 7 Conclusions and Outlooks…… 249
7.1. References…… 254
Appendix…… 255
Appendix 1. Stepwise Methods for the Synthesis of Au@*m*SiO$_2$... 255
Appendix 2. Methods for the One-pot Synthesis of Au@*m*SiO$_2$.... 257
Appendix 3. First Derivatives of the Sorption Isotherms of *b*-Au@*m*SiO$_2$ ……..…….…….... 259
Appendix 4. Linearized forms of isotherms of BSA, *m*Cherry, and HRP adsorbed on *lp*-Au@*m*SiO$_2$..... 260
Appendix 5. Review of Maximum Protein Adsorption Capacity on MSN…….…… 264
Appendix 6. Pairwise Structure Alignment of GFP and *m*Cherry… 267
Appendix 7. Emission and Excitation Spectra of Free *m*Cherry in Solution and Adsorbed on *lp*- Au@*m*SiO$_2$ Particles 271
References……. 272

Chapter 1

Introduction

1.1. Motivation

Proteins are at the forefront of therapeutic research due to their ability to perform highly specific biological functions, making them invaluable in treating a wide range of diseases. However, for protein therapies to be fully effective, efficient delivery systems are needed to ensure that these proteins reach their target sites intact. Developing systems to deliver proteins while preserving their stability is a key challenge, as proteins are often prone to degradation, loss of function, or aggregation during delivery. This highlights the need for advanced nanovehicles that can not only protect proteins but also provide controlled release and targeted delivery, overcoming the limitations of conventional methods.

Au@*m*SiO_2 nanoparticles, with a gold core and a mesoporous silica shell, offer a promising solution to these challenges. The mesoporous silica shell serves as an effective platform for protein retention, while the gold core can convert visible light into heat. This light-induced heating may trigger the controlled, on-demand release of proteins, addressing the need for precise delivery systems.

The primary motivation of this thesis is to tackle the inherent challenges in designing these nanoparticles, aiming to fine-tune their properties for optimal performance in protein delivery. This involves optimizing particle size and pore dimensions to ensure they are suitable for efficient protein encapsulation and controlled release.

A crucial aspect of this work is adherence to the principles of pharmaceutical quality by design, which emphasize integrating quality throughout the entire product lifecycle—from synthesis to application. Therefore, understanding the synthesis mechanism at a fundamental level is essential for developing reliable and effective nanovehicles.

In summary, this thesis is motivated by the need of advance protein delivery systems through the development of Au@*m*SiO_2 nanoparticles. The goal is to design nanoparticles that are optimized for efficient protein retention, stability during transport, and controlled, on-demand release.

1.2. Objectives

The primary objective of this thesis is to develop a robust synthetic route for a novel type of large-pore Au@*m*SiO_2 nanoparticles, specifically designed for on-demand protein delivery. The synthesized nanoparticles must demonstrate high hydrolytic stability and protein loading capacity, ensuring they protect and preserve the structural integrity and functionality of the cargo proteins. Moreover, these nanoparticles should efficiently convert light into heat when irradiated at the localized surface plasmon resonance (LSPR) of the gold core, providing enough energy to trigger controlled protein release.

The specific objectives are as follows:

i. **Synthesize Au@*m*SiO_2 Nanoparticles:** Develop a reliable, reproducible, and effective synthesis method for Au@*m*SiO_2 nanoparticles with a diameter of 100 nm or smaller to enable cellular entry. The mesopores must be optimized to be large enough to accommodate proteins, and the particles should demonstrate adequate hydrolytic stability to maintain protein integrity during transport. Additionally, the nanoparticles should feature a gold core with a diameter of 15-30 nm to facilitate protein release through light-induced heating.

ii. **Characterize Protein Loading:** Assess the loading of proteins onto Au@*m*SiO_2 with varying pore sizes using model proteins such as bovine serum albumin (BSA), horseradish peroxidase (HRP), and the fluorescent protein *m*Cherry. This involves evaluating the efficiency of the nanoparticles in retaining proteins, determining the protein localization on the nanoparticles, and identifying key factors influencing protein loading. Additionally, assess the stability of both the encapsulated proteins and the nanoparticles to understand how well the system preserves protein functionality and nanoparticle integrity.

iii. **Evaluate Plasmonic Heating Efficiency:** Assess the effectiveness of plasmonic heating induced by light irradiation of Au@*m*SiO_2 at their LSPR wavelength. Determine whether this heating can serve as an effective stimulus for controlled protein release.

1.3. State of the art

1.3.1. Nano-carriers for protein delivery

Proteins are complex macromolecules essential for a myriad of biological processes, functioning as enzymes, signaling molecules, structural components, and more. They are composed of one or more chains of amino acids that folds into specific three-dimensional structures that determine the protein's function. The correlation between protein structure and function highlights the significance of studying proteins at multiple levels, from their primary amino acid sequence to their intricate three-dimensional conformations [1]. Aberrations in protein structure or function are often implicated in various diseases, making them key targets for therapeutic intervention [2]. Advances in protein delivery methods, including the use of nanocarriers, have opened new avenues for targeting and treating diseases at the molecular level. Nanoparticles, in

particular, offer a promising platform for enhancing the stability, bioavailability, and targeted delivery of therapeutic proteins, thereby improving the efficacy of protein-based treatments [3].

Compared to other therapeutic drugs, delivering proteins poses unique challenges due to their intrinsic properties, such as large sizes, varying surface charges, and fragile tertiary structures [2]. These macromolecules often suffer from instability during delivery [4], making the selection of appropriate delivery vehicles crucial. Over the past decade, nanocarrier-based protein delivery approaches have garnered significant interest as promising therapeutic strategies. These approaches include lipid-containing colloidal systems like liposomes and solid lipid nanoparticles, polymeric nanocarriers, inorganic nanoparticles or nanotubes, and protein-based carriers [4–6]. A primary function of these nanocarriers is to shield proteins from premature degradation and denaturing interactions within the biological environment [7]. Additionally, nanocarriers can prevent proteolysis of proteins and increase the size of the delivered cargo thereby reducing renal filtration [8]. The high surface area to volume ratio of nanocarriers enhances pharmacokinetics and biodistribution of the payload [9]. Furthermore, the chemical and physical properties of nanocarriers can be tailored through controlled synthesis, assembly, and biocompatible chemical modifications, optimizing them for specific therapeutic applications [4].

Proteins can be loaded into nanocarriers using different strategies. This methods include direct conjugation through chemical or genetic modifications, which can attach the protein to the carrier via covalent bonds, ensuring a stable and controlled release. Alternatively, proteins can be adsorbed onto the surface of nanocarriers, taking advantage of electrostatic and hydrophobic interactions to achieve a non-covalent attachment. Another common approach is encapsulation, where proteins are either covalently or non-covalently attached within the nanocarrier matrix. This encapsulation can protect the protein from environmental degradation and improve its pharmacokinetic profile by

facilitating sustained and targeted release. These diverse loading strategies enable the fine-tuning of nanocarrier systems to meet specific therapeutic needs, enhancing the overall efficacy of protein-based treatments [4, 5].

1.3.2. Mesoporous silica nanoparticles

Mesoporous silica have garnered significant interest in the scientific community due to their unique structural properties and versatile applications. Introduced in the early 1990s, ordered mesoporous silicas were first synthesized using surfactant templates to create an ordered porous structure [10, 11]. This breakthrough allowed for the development of materials with uniform pore sizes and large surface areas, which are highly advantageous for various applications, including drug delivery, catalysis, and adsorption.

The field of mesoporous silica evolved with the development of various mesostructured architectures, each offering distinct advantages. The M41-series [10], particularly MCM-41, MCM-48, and MCM-50, represent some of the most well-known structures. MCM-41 features a 2D hexagonal structure, MCM-48 exhibits a 3D cubic structure, and MCM-50 possesses a lamellar structure. Additionally, anionic surfactant-templated mesoporous silicas (AMS-series) [12], Institute of Bioengineering and Nanotechnology (IBN)-series [13], and the Santa Barbara Amorphous (SBA-series) [14] further expand the repertoire of mesoporous materials, offering varied pore geometries and surface characteristics.

1.3.2.1. Physicochemical properties

One of the key advantages of mesoporous silica nanoparticles (MSNs) is their customizable morphology, size, pore structure and surface properties

(Figure 1.1). By varying synthesis conditions such as the type and concentration of surfactants, the choice of silica precursor, and specific reaction parameters, it is possible to produce MSNs with precise control over their shape and size. This tunability extends to the pore size and volume, enabling the efficient encapsulation of molecules of various sizes and the achievement of desired release profiles [6, 15].

The surface properties of MSNs can be tailored using functionalization reactions, enhancing their functionality for specific applications. MSNs possess a hydrophilic surface rich in hydroxyl groups, making them versatile for functionalization by introducing groups on both the exterior and interior porous surfaces [15]. Surface coatings can improve the biocompatibility, stability, and dispersibility of MSNs in aqueous environments. Functional groups, polymers, proteins, and other molecules can be grafted onto the MSN surface to facilitate targeted delivery, controlled release, and improved interaction with biological systems [16–24].

MSNs are renowned for their high loading capacity, attributable to their large surface area and porous structure. The uniform and well-defined pores of MSNs can encapsulate a significant amount of therapeutic agents, making them ideal for drug delivery applications [25–27]. This high loading capacity, combined with the ability to control the release kinetics through surface modifications and pore size tunning, positions MSNs as a powerful tool in the field of nanomedicine.

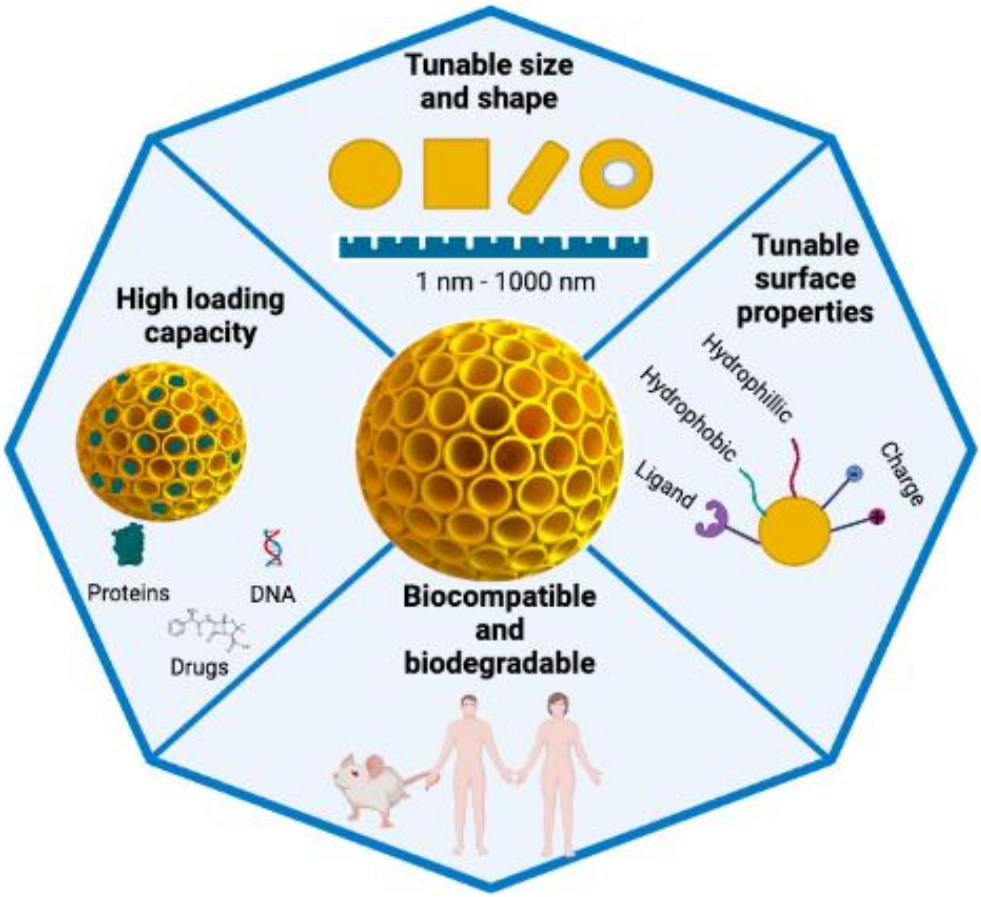

Figure 1.1. The design of mesoporous silica nanoparticles involves several key aspects: tunable size and shape, tunable surface properties, high loading capacity, and biocompatibility and biodegradability. These properties influence the physical characteristics, biodistribution, and overall performance of the nanoparticles.

1.3.2.2. Toxicity

A critical factor in the use of MSNs in biomedical applications is their toxicity. The toxicity of silica nanoparticles has been extensively investigated and found to be generally low compared with other nanomaterials [21, 28–30]. However, it must be assessed on a case-by-case basis due to the wide range of configurations resulting from variations in surface chemistry, porosity, size, and distribution of siloxane groups. MSN toxicity is primarily associated with surface silanol (≡SiOH) groups, which can hydrogen bond to membrane components or,

when dissociated to form SiO^-, interact electrostatically with the positively charged tetraalkylammonium-containing phospholipids. Both processes can lead to strong interactions and potentially cause membranolysis and leakage of cellular components [27].

One major concern is that the high surface-to-volume ratio of nanoparticles could enhance cellular interactions and trigger toxicity. However, mesoporous silica exhibits lower toxicity compared to non-porous silica due to the mesoporosity reducing the effective MSN/membrane contact area [21]. Additionally, the low extents of condensation of the MSN siloxane framework facilitate rapid dissolution into non-toxic soluble silicic acid species [31] that can be excreted via urine or faeces [32]. The potential for toxicity can be further minimized due to the high drug-loading capacity of MSN, which significantly lowers the required dosage compared to other nanocarriers [27].

1.3.2.3. Applications in protein delivery

MSNs exhibit exceptional multifunctional capabilities and have been employed to deliver various proteins for disease treatment, modification of cellular functions, or bioimaging [33]. Some notable examples include the delivery of therapeutic human proteasomes to prevent tau protein aggregates in Alzheimer's disease [34] gene editing facilitated by *Cre* protein delivery [35], delivery of superoxide dismutase to reduce oxidative stress that leads to apoptosis [36], and the development of novel adjuvant delivery systems and vaccines [37, 38]

One of the most significant advantages of MSN-based delivery applications is their ability to respond on-demand to specific stimuli. For instance, MSNs with disulfide bonds in their structure can selectively deliver proteins to cancer cells due to the degradation of disulfide bonds upon exposure to glutathione. This release mechanism is based on the fact that cancer cells have glutathione concentrations several times higher than normal cells, resulting in GSH-

responsive degradation and a higher degradation rate in cancer cells compared to normal cells [39]. Another example includes dual-responsive nanoparticles designed for RNase A delivery and targeted release in cancer cells. These nanoparticles degrade upon exposure to both oxidative and redox conditions [40].

MSN have shown promising advancements in various delivery strategies capable of transporting proteins into cells, and achieving efficient loading and targeted delivery. However, further research is needed to optimize these systems to ensure higher efficiency and specific on-demand protein delivery, ultimately enhancing their therapeutic potential.

1.3.3. Gold nanoparticles

The field of metal nanoparticles science was fundamentally shaped by Michael Faraday's groundbreaking experiments on gold sols in the 19th century. Faraday observed that the red color of a solution was due to the presence of colloidal gold, formed by reducing chloroaurate with white phosphorus [41]. Following Faraday's landmark research in 1857, various methods for synthesizing metal nanoparticles have emerged. Among these, the classical method involving the reduction of chloroauric acid in aqueous solution using trisodium citrate became particularly notable after John Turkevich's work in the 1950s [42]. The methods to synthesize gold nanoparticles with controlled sizes, shapes, and properties has stimulated extensive research into optimizing synthesis conditions and techniques.

Gold nanoparticles (AuNPs) are at the forefront of different applications ranging from biomedical fields to imaging and catalysis due to their exceptional optical and physicochemical properties [43–46]. Their unique surface plasmon resonance (SPR) characteristics enable applications in various domains. In biomedicine, AuNPs are employed for diagnostic imaging, drug delivery, and photothermal therapy. Their biocompatibility and ability to be functionalized

with a wide range of biomolecules make them ideal candidates for targeted drug delivery systems, where they can deliver therapeutic agents directly to specific cells or tissues.

1.3.3.1. Physicochemical Properties

AuNPs exhibit surface plasmon resonance (SPR), a phenomenon arising from the interaction of electromagnetic radiation with the free electrons at their surface (Figure 1.2 a). This interaction induces collective oscillations known as localized plasmon oscillations within the visible spectrum, primarily due to *d*–*d* transitions. The oscillation of these surface electrons leads to a separation of charges, resulting in dipole oscillations aligned with the electric field of incident electromagnetic waves. The frequency at which these oscillations reach maximum amplitude is termed the SPR frequency [47–49].

Exciting plasmons not only leads to significant enhancement of the electric field near the structure's surface but also results in extremely large absorption and scattering cross-sections at the resonance frequency. Spherical AuNPs with particle diameter between ~10–30 nm display a SPR band centered at approximately 520 nm in the visible spectrum [47, 48]. When the symmetry of a AuNP is altered, such as by elongating a sphere into a nanorod, multiple SPR modes emerge due to the various axes and vertices on the AuNP surface [47, 48]. Gold nanorods (AuNR) exhibit two distinct SPR modes: a transverse SPR aligned with the short axis of the rod and a longitudinal SPR (LSPR) aligned with the long axis [47, 50–53]. By adjusting the aspect ratio of the AuNR, the energy of the LSPR can be tuned across a wide range of the electromagnetic spectrum, from the middle of the visible region (~600 nm) to the infrared region (~1800 nm) (Figure 1.2 b) [50, 53–55]. A linear relationship exists between the aspect ratio and the wavelength of the LSPR (λ_{max}) [50, 53]. The intensity of the SPR band can also be modified by other factors that modify the surface electron charge density, such as surface morphology, composition, and dielectric environment [49].

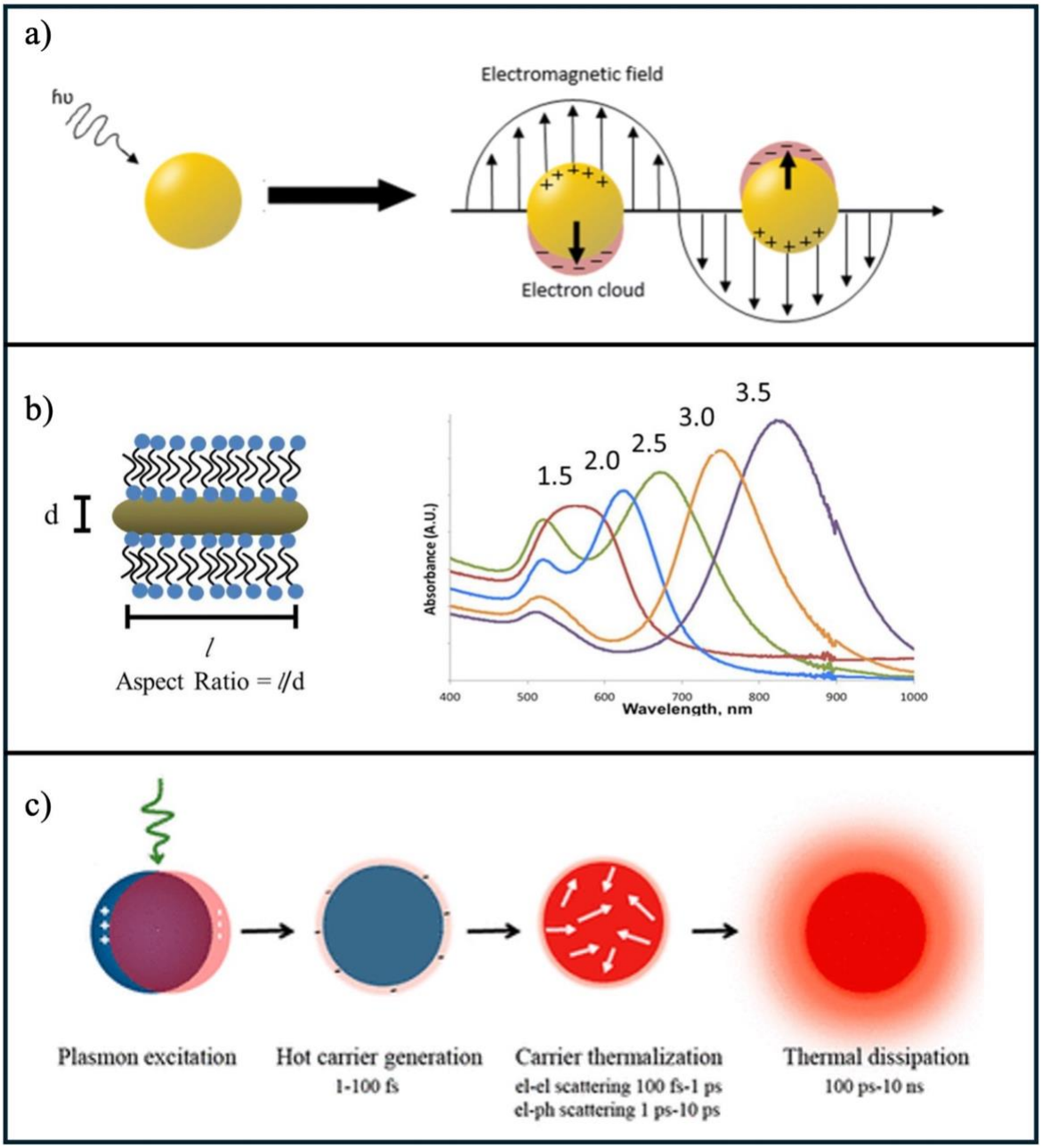

Figure 1.2. Optical properties of AuNPs. (a) Scheme of surface plasmon resonance (SPR) of gold nanoparticles. Representation of the conduction electrons oscillating across the gold nanoparticles in the electromagnetic field of incident light. (b) AuNRs possess two separate plasmon absorbances, one corresponding to the short (transverse) axis and the other corresponding to the longitudinal axis. l/d is the aspect ratio. By adjusting the aspect ratio of the AuNR, the UV-vis-NIR extinction spectra can be tuned. (c) Scheme of the photothermal effect, including photoexcitation and subsequent relaxation processes of the SPR. Figure adapted from [49, 56, 57]

When excited, SPR generates an intense electromagnetic field near the surface of the AuNP, which can extend over a distance comparable to the nanoparticle's diameter. This electromagnetic field interacts with molecules or solids in close proximity to the AuNP surface [47, 48], thereby enhancing the scattering spectra of molecules adsorbed on gold nanorods, such as in surface-enhanced Raman spectroscopy (SERS), or facilitating the detection of changes in the local chemical environment of specific analytes [58–60].

1.3.3.1.1. Photothermal effect

AuNPs efficiently convert absorbed light into heat through the photothermal effect. This effect is characterized by an increase in the temperature of a material due to light absorption. Upon plasmon excitation, photon interactions with a metal nanoparticle are described by its extinction cross section, which is the sum of the absorption and scattering cross sections. The absorbed energy can be dissipated either through photon re-emission (luminescence) or phonon generation (heat). Given that the luminescence quantum yield of plasmonic nanoparticles is below 1%, it is assumed that nearly all absorbed energy is converted into heat [61, 62].

The photothermal conversion process begins with the illumination of a metal nanoparticle. The nanoparticle absorbs light within a specific wavelength range, inducing surface plasmon resonance through electron oscillations. These electrons are excited to a higher energy state and undergo electron-electron scattering within femtosecond timescales [63], redistributing the hot electrons. Subsequently, heat is transferred to the metal lattice via electron-phonon coupling and then dissipates to the surrounding medium through phonon-phonon coupling within 100–380 ps [64, 65] (Figure 1.2 c). Heat dissipation to the surrounding medium depends on the particle size, laser sources, and medium [66–68]. At the SPR wavelength, the absorption cross section significantly exceeds the nanoparticle's physical cross section [52], resulting in a substantially elevated temperature in and around a single AuNP [69, 70].

The photothermal conversion of AuNPs has garnered considerable attention in recent research, with numerous studies quantitatively measuring the heat generated by irradiated AuNPs to calculate photothermal conversion efficiency [61, 71–73]. The prevailing method involves irradiating nanoparticles with lasers at their SPR and monitoring the resulting heating process through bulk or surface temperature measurements. However, this approach primarily measures macroscopic temperatures resulting from the collective effect of nanomaterials rather than the temperature generated by individual particles.

Theoretical calculations, such as those based on the Green's dyadic mathematical method, provide a means to quantify heat generation by mapping the heating power density within AuNPs [74]. Additionally, electromagnetic and thermodynamic simulations indicate that photothermal conversion heat is highly concentrated near the surface (<20 nm) of the irradiated AuNPs and strongly depends on the size and shape of the nanoparticles [75].

Given that photothermal conversion happens on the picosecond timescale and operates at nanoscale dimensions beyond the reach of traditional thermometry, precise temperature measurements under these conditions are essential. Such measurements are crucial for understanding photothermal properties, heat generation mechanisms, and their applications across physical, chemical, and biological fields.

1.3.3.2. Toxicity

AuNPs are among the most widely utilized nanomaterials for FDA-approved biomedical applications [76–78]. This preference is attributed to their unique optical properties and comparatively low toxicity relative to other metal-based nanomaterials [79]

Numerous studies have investigated the toxicity of AuNPs using various models, including animal models [80–85]. These studies indicate that factors such as surface chemistry, shape, and size significantly influence AuNP toxicity.

Spherical AuNPs have been shown to be less toxic and more biocompatible than gold nanorods [86, 87]. The toxicity of AuNRs is associated with the presence of cetyltrimethylammonium bromide (CTAB), which is used during synthesis to direct the rod shape [86]. Consequently, alternative synthesis methods for AuNRs synthesis that avoid CTAB, such as those using polyethylene glycol (PEG), phosphatidylcholine, and poly(acrylic acid), can reduce their toxicity [86–89].

There is no clear consensus regarding the relationship between AuNP size and toxicity. Some studies report that smaller AuNPs are more toxic than larger ones [90, 91] likely due to their higher surface area, which increases interactions with biomolecules [92]. However, this finding is not universal, as there are contradictory reports assessing the toxicity of small-sized AuNPs [93].

While there are numerous toxicity studies on various shapes and sizes of AuNPs, comparing their toxicities is challenging due to differences in surface chemistry associated with different synthesis methods and capping agents used to direct specific shapes [93]. Therefore, as with all nanomaterials, the toxicity evaluation of AuNPs intended for different biomedical applications must be conducted on a case-by-case basis.

1.3.3.3. Applications in drug delivery

AuNPs have demonstrated effectiveness in developing drug nanocarriers for the delivery of various molecules, including peptides, plasmid deoxynucleic acids, proteins, small interfering ribonucleic acids, and small drugs [94]. Different molecules can be easily attached to the surface of AuNPs during or post-synthesis, ranging from large molecules like nucleic acids, antibodies, and polymers to peptides, drugs, fluorescence markers, or functional groups [95]. The molecules attached to AuNPs change their surface properties, facilitating the capture of the desired drug. The drug can either be immobilized on the AuNP surface or encapsulated within AuNP-based complexes. In either scenario, cell-

specific targeting molecules are also affixed to AuNPs to ensure targeted delivery of the drug to the intended site [96].

Noteworthy examples of AuNP-based drug delivery systems include pH-sensitive systems designed for delivering antitumor drugs, leveraging the lower pH characteristic of specific tumors [97]. Systems that conjugate antimicrobial drugs with AuNPs effectively enhance drug solubility and cellular membrane permeability, thereby minimizing side effects and enabling efficient delivery of numerous molecules to the target site [98].

In recent years, considerable attention has been focused on designing on-demand AuNP-based drug delivery systems. Specifically, the heat generated by AuNPs via photothermal conversion has garnered significant interest. Photothermal therapy (PTT) using AuNPs represents a promising strategy for targeted treatment of tumor cells [99]. Gold nanorods with plasmon absorbances in the near-infrared (NIR) region bind to tumor cells and, upon NIR laser excitation, release heat into the tumor environment, inducing tumor cell death [100, 101]. Studies have demonstrated that AuNPs facilitate the identification and photothermal ablation of tumor cells *in vitro*, underscoring their potential as theranostic anticancer agents [102]. Various shapes of AuNPs have been evaluated for photothermal therapy, with AuNRs proving most effective due to their strong absorbance in the NIR and scattering properties, as well as their small size compared to nanoshells and nanocages, facilitating distribution throughout biological systems [99].

The use of spherical AuNPs as photothermal therapeutics has been less explored, primarily because their LSPR is in the visible range (500-550 nm), limiting light penetration into internal tissues. However, exploiting their ability to undergo photothermal conversion upon visible spectrum irradiation could be advantageous for delivering therapeutic drugs to superficial tissues such as the epidermis, targeting damaged cells for localized therapy.

1.3.4. Core-shell gold silica Au@*m*SiO_2 nanoparticles

Au@*m*SiO_2 particles, consisting of a gold core and a mesoporous silica shell (Figure 1.3a), represent a promising platform that combines the unique optical properties of gold nanoparticles with the high loading capacity and controlled release properties of mesoporous silica. These nanoparticles are of particular interest for biomedical applications [103]. Beyond biomedical applications, these particles are of particular interest in the field of catalysis because the silica shell enhances the durability and tolerance of AuNPs in harsh environments [104, 105].

Liz-Marzán et al. (1996) first reported a method for synthesizing MSN with a spherical gold core using a stepwise strategy. This process begins with the synthesis of AuNPs via the Turkevich-Frens method, followed by stabilization using aminopropyltrimethoxysilane, as the amine groups bind to the gold surface and stabilize it. Finally, the silica shell is grown through multiple additions of the silica precursor in an alkaline medium [106]. Subsequent modifications to this method introduced the use of CTAB as AuNPs stabilizer and template for forming the mesoporous silica shell [107]. Building on this principle, a method for synthesizing AuNRs coated with a mesoporous silica shell was later described, requiring additional steps due to the seed-mediated growth method for AuNRs synthesis [107–109]. Further advancements led to the development of *one-pot* methodologies, significantly simplifying the process by allowing the formation of both the gold core and the silica shell in the same reaction vessel [104, 110, 111]. In recent years, variations of these methodologies have been developed to synthesize Au@*m*SiO_2 particles with different shell and core sizes.

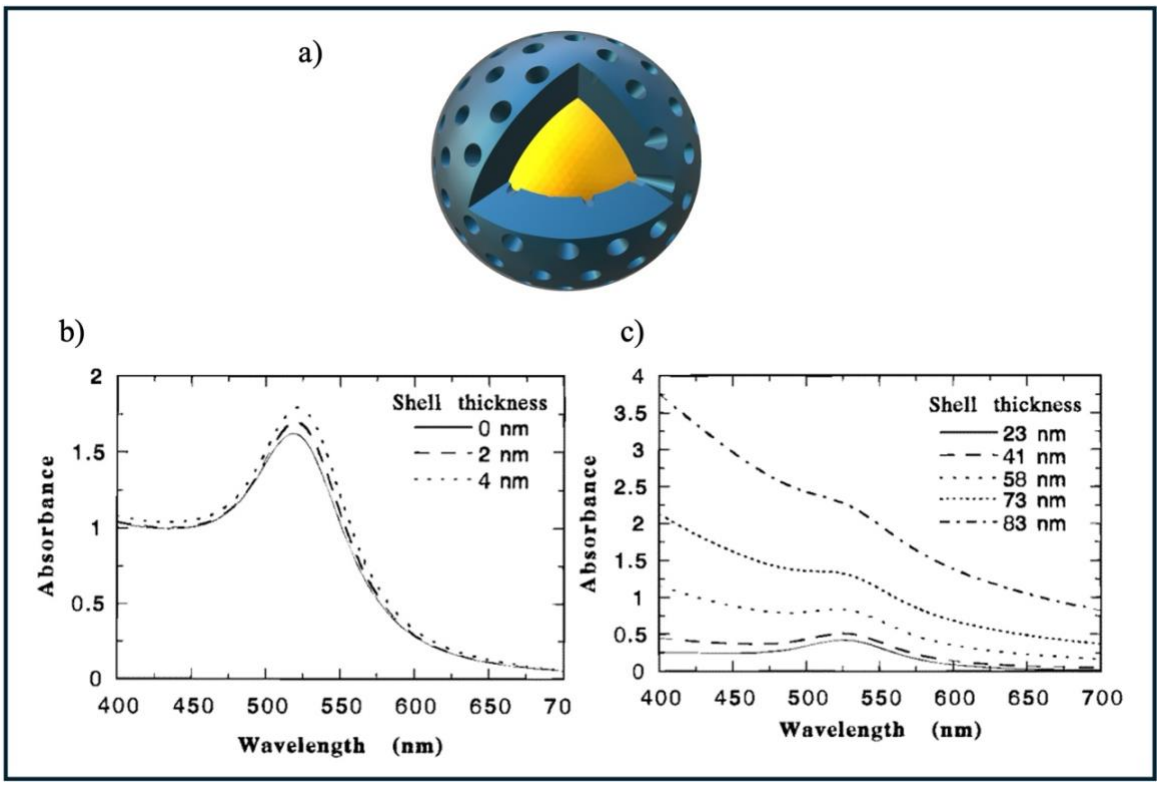

Figure 1.3. (a) Schematic representation of a Au@*m*SiO_2 nanoparticle. Influence of (b) thin and (c) thick silica shells on the UV-visible spectra of aqueous Au@*m*SiO_2 nanoparticle. Adapted from [106].

1.3.4.1. Physicochemical Properties

Au@*m*SiO_2 particles retain the physicochemical properties of both MSN and AuNPs. However the position of the surface plasmon resonance of AuNPs is sensitive to particle size, shape, and the electronic properties of the surrounding medium [112]. The introduction of a silica shell alters the local refractive index around the particles, leading to slight variations in the SPR of silica-coated AuNPs compared to bare AuNPs [106].

For thin silica shells (less than 4 nm) in water or ethanol media, as the shell thickness increases, there is an increase in the intensity and a red shift in the position of the SPR band (Figure 1.3 b). For silica shells thicknesses between 20 and 70 nm, the spectra show a strong increase in extinction at shorter

wavelengths due to particle scattering (Figure 1.3 c). This also results in the weakening of the gold SPR and a blue shift in its position. With silica shells thicker than 80 nm, particle scattering masks the SPR band [106].

The introduction of the silica shell produces variation on the absorption and refractive index and induce variations in the properties of AuNPs, such as the photothermal or photoacoustic effect, as observed through mathematical modeling [69, 113, 114].

1.3.4.2. Applications in drug delivery

Au@*m*SiO_2 particles have demonstrated diverse applications across imaging, catalysis, biosensing, and drug delivery [103]. In the field of drug delivery, significant examples include the use of Au@*m*SiO_2 particles with a total diameter of 109 nm and a spherical core of 20 nm for the delivery of doxorubicin to cancer cells, resulting in reduced cancer cell viability [115]. Another notable application involves Au@*m*SiO_2 particles coated with the antimicrobial agent cinnamaldehyde, with a total diameter of 326 nm, which effectively inhibit biofilm formation by various bacterial species [116].

One of the most promising applications of Au@*m*SiO_2 particles involves those with anisotropic gold cores (rod or star-shaped), which exhibit surface plasmon resonance (SPR) in the near-infrared (NIR) region. Since silica is optically transparent to NIR radiation, these particles are highly suitable for photothermal therapy (PTT) and photodynamic therapy (PDT) [103].

Au@*m*SiO_2 particles with rod-like cores have shown particular efficacy in cancer PTT therapy. For example, Au@*m*SiO_2 particles were synthesized with a rod core having an aspect ratio of 2.4 (180 nm length and 75 nm width), a 14 nm silica shell, and functionalized with peptides to mimic the *in vivo* behavior of the rabies virus to recognize brain cells. Once in the target cells, the particles were

irradiated for 5 minutes with an 808 nm laser, increasing the local temperature to 50 ˚C and effectively suppressing brain tumors in mice [117].

Despite the promising results of PTT in various diseases treatment, its effectiveness is limited by the inability of NIR light to penetrate deeply into tissues, making it suboptimal for treating all types of tumors. To address this limitation, PTT has been combined with the delivery of chemotherapeutic drugs, enhancing treatment efficiency through PDT. For instance, Au@*m*SiO_2 particles with nanorods having 52 nm length and 13 nm width, a 25 nm silica shell, and loaded with doxorubicin were shown to inhibit tumor growth rate in mice by 66.5% [118]. Also, Au@*m*SiO_2 particles with rods of 40 nm length and 10 nm width, a 24 nm silica shell, loaded with cisplatin, and functionalized with β-cyclodextrins, adamantine, and lactobionic acid successfully prevented tumor progression in mice. This complex of Au@*m*SiO_2 particles demonstrated efficiency in providing a triple therapy combining PTT, PDT, and chemotherapy [119].

1.3.4.3. Toxicity

The toxicity of Au@*m*SiO_2 particles has been evaluated *in vitro* using cell cultures and has been shown to be dependent mainly on shape, and dosage. When cancer cell cultures were exposed to spherical and rod-shaped AuNPs and their respective Au@*m*SiO_2 homologs with silica shells, it was observed that cell viability was higher for cells exposed to Au@*m*SiO_2, suggesting that the silica shell has a cytotoxicity-inhibiting effect [120]. Furthermore, when cancer cell cultures were exposed to Au@*m*SiO_2 with spherical cores and silica shells of 50, 100, and 200 nm, no signs of cytotoxicity were observed at concentrations below 200 pmol/L. However, at a concentration of 400 pmol/L of Au@*m*SiO_2 with a 200 nm silica shell, cell viability decreased by 10% [120]. In another study, both spherical and rod-shaped Au@*m*SiO_2 particles were tested on cancer cell cultures and human fibroblasts. No signs of toxicity were observed at doses up to 100 μg/mL of nanoparticles [115].

This reduced Au@*m*SiO_2 toxicity, combined with their therapeutic efficacy, underscores the potential of Au@*m*SiO_2 particles as a safe and effective option for medical treatments. However, more studies must be conducted using animal models and under conditions similar to those required for their specific applications.

1.3.5. Synthesis routes

1.3.5.1. Gold nanoparticles synthesis

The most commonly used synthesis routes for AuNPs is the Turkevich–Frens method that was devised by John Turkevich in the 1950s [42] and further refined by Frens in the 1970s [121]. The Turkevich-Frens method involves the reduction of gold salts, typically chloroauric acid, in near-boiling water using sodium citrate as the reducing agent. Sodium citrate reduces the gold ions to form gold atoms, which aggregate to create small clusters. Additionally, sodium citrate acts as a stabilizing agent, controlling the growth of the nanoparticles and preventing excessive aggregation. Initially, small stable gold seeds (>1.5 nm) form, with unreduced gold ions remaining in the electronic double layer (EDL) of these seeds. Subsequent reduction within the EDL facilitates seed growth, ultimately forming the final AuNPs [122] (Figure 1.4).

In addition to the Turkevich–Frens method, the Brust–Schiffrin method, developed by Mathias Brust and David J. Schiffrin in the mid-1990s, represents another significant approach for obtaing gold nanoclusters (AuNC) having size range of 1.5–5.2 nm [123] . This method involves the synthesis of AuNC in an organic solvent at room temperature using sodium borohydride ($NaBH_4$) as the reducing agent and thiol-based compounds as stabilizing agents. The use of organic solvents and specific stabilizers results in highly monodisperse and stable AuNCs.

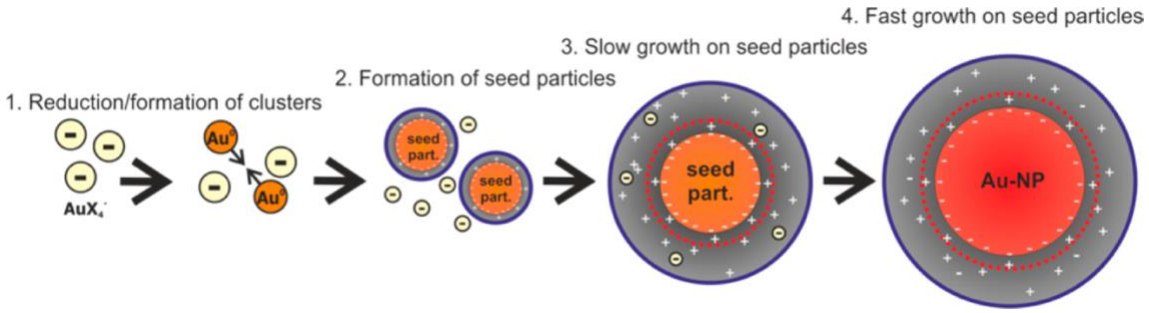

Figure 1.4. General mechanism of the Turkevich synthesis as deduced by Polte [131]. Reproduced from [122]

Morevover, non-spherical gold nanoparticles can also be obtained by fine-tuning the synthesis parameters. Anisotropic growth of gold nanoparticles can be promoted by employing different surfactants, halides, or reducing agents that block certain growth directions [124–129]. Gold nanorods are among the most commonly studied anisotropic shapes due to their unique optical properties. AuNRs are synthesized using a seed-mediated growth method, where small spherical gold particles that act as seeds are first created through nucleation. These seeds are then added to a growth solution containing a gold salt, silver nitrate, and high concentrations of cetyltrimethylammonium bromide, which directs the growth into a rod shape [49, 130].

The synthesis of AuNPs with desired sizes, shapes, and properties has spurred extensive research into varying synthesis conditions and methodologies. Despite the advancements provided by techniques like the Turkevich–Frens and Brust–Schiffrin methods, the precise influence of synthesis parameters on the final characteristics of nanoparticles remains an area of active investigation and is not yet fully understood [122, 132]. Further exploration and refinement of synthesis protocols are essential for comprehensively elucidating the roles played by different experimental conditions in nanoparticle synthesis and tailoring AuNPs for diverse applications.

1.3.5.2. Mesoporous silica nanoparticles synthesis

The synthesis of mesoporous silica typically begins with a sol-gel process in which a tetraalkoxysilane, such as tetraethoxysilane (TEOS), is hydrolyzed in a suitable solvent. This reaction generates silanol and siloxane species, which, in the presence of a templating agent, condense to form oligomers and small clusters [133, 134]. As these clusters condense further, siloxane bridges are formed, eventually leading to the creation of nanoparticles. These sol-gel reactions are nucleophilic substitutions, beginning with nucleophilic addition and followed by the removal of an alcohol or water molecule.

The mechanism of the nucleophilic attack on the silicon atom varies depending on the type of catalyst employed, which can be acidic, basic, or nucleophilic (Figure 1.5). In acidic catalysis, the protonation of the alkoxy group facilitates the attack of water or silanol on the silicon atom, generating a pentacoordinate intermediate that subsequently eliminates an alcohol molecule. Under basic catalysis, hydroxide anions initiate the nucleophilic attack, forming an anionic pentacoordinate intermediate, which leads to the removal of an alkoxide group. For nucleophilic catalysis, a nucleophile coordinates with the silicon center, creating a reactive intermediate that drives nucleophilic substitution, producing an alcohol, a silanol, and regenerating the catalyst in the process [135].

The condensation process includes oxolation and alcoxolation reactions, leading to the formation of soluble oligomers that condense in particles. The reaction kinetics are influenced by the strength of the nucleophilic agent, the charge of the electrophilic center, and the readiness of the leaving group to be substituted or eliminated. In a base-catalyzed process, hydroxyde anions drive the hydrolysis reaction, influencing the proton transfer step and the equilibrium between silanol and silanolate species, which is determined by pH and p*Ka* values [133, 134].

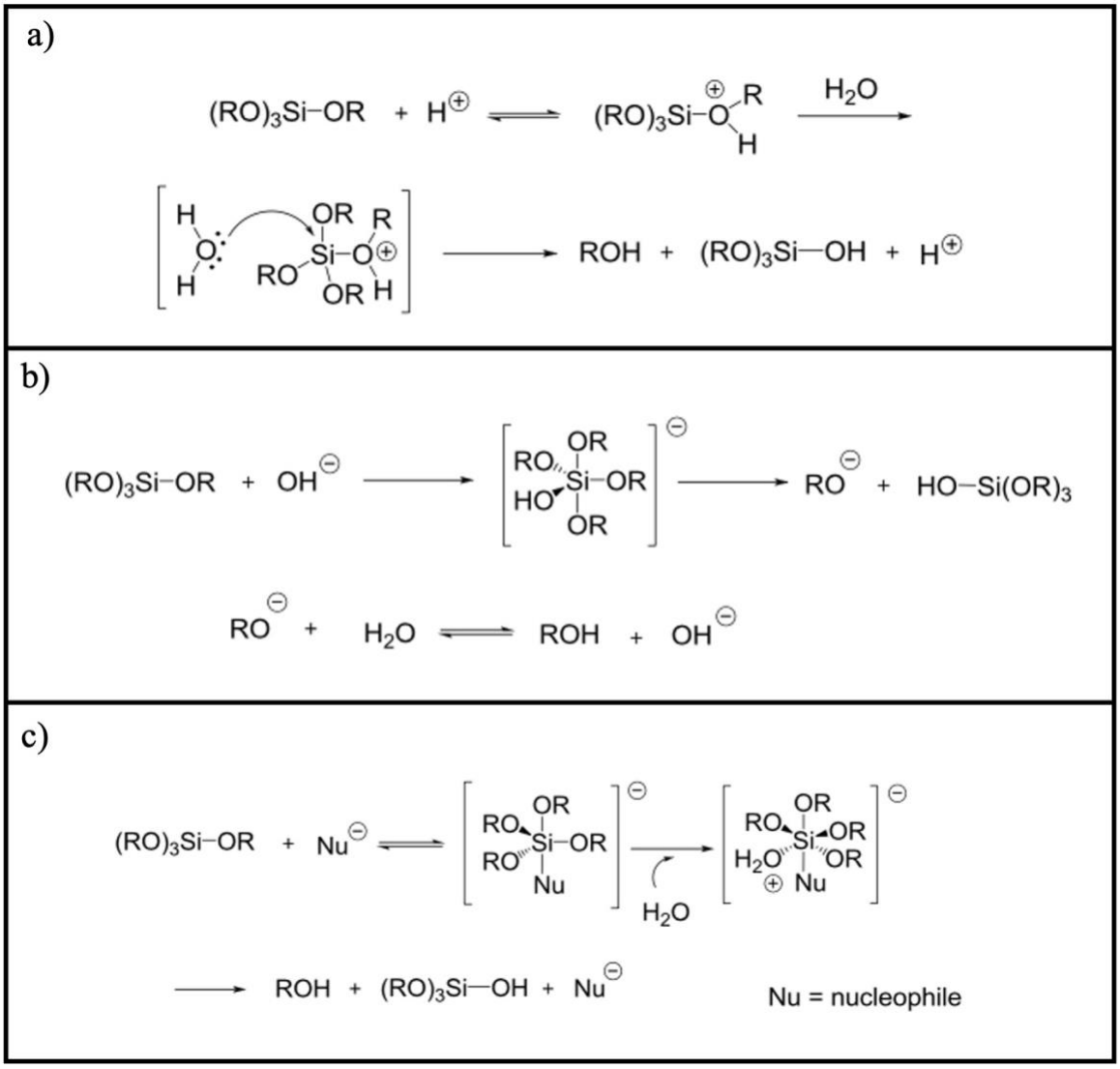

Figure 1.5. Hydrolysis of tetraalkoxysilane promoted by a) acid, b) basic, and c) nucleophilic catalysis. Reproducted from [135].

The classic synthesis of MSN typically involves hydrolyzing and condensing silicon alkoxides in a basic aqueous medium with a structuring agent, usually CTAB. The process begins with the solubilization of CTAB, forming spherical micelles. TEOS, the silica precursor, is then dispersed in water and encapsulated in the micelles. Hydrolysis occurs and the hydrolyzed silanolates are adsorbed onto the micelles surfaces via electrostatic forces, triggering a shift in micelle shape from spheres to rods. As the TEOS concentration increases,

micelles aggregate, leading to condensation between silanes and the formation of the MSN structure (Figure 1.6) [136].

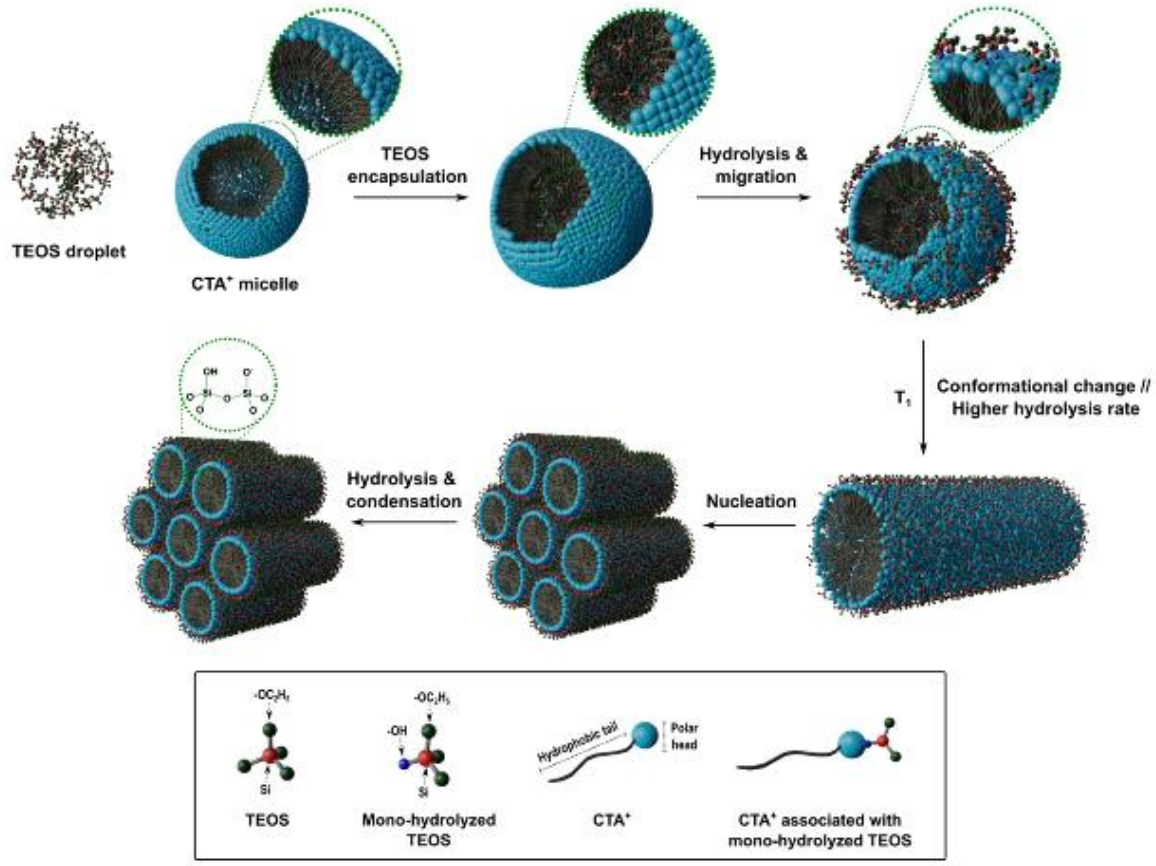

Figure 1.6. Mechanism of Formation of CTAB-Templated MSN in water using CTAB as structuring agent, TEOS as silica source and NaOH as base source. Reproduced from [136].

Many variations of this classic method can alter particle formation mechanisms, depending on surfactants, bases, solvents, or additives used. These variations are often best explained by an aggregative growth model, where silica clusters aggregate, with final particle size mainly defined by the moment when the particles reach electrostatic or steric stabilization [137].

After synthesis, the template is removed using various methods, with the most common being calcination [138], ion exchange [139], microwave [140] or ultrasound [141] assisted extraction, amog others. For ion exchnge template

molecules are extracted from the mesopores by treating as-made compounds with an ethanolic solution of ammonium nitrate at 60 ˚C [139]. Calcination involves subjecting the nanoparticles to 500 ˚C within a furnace for at least 2 hours.

The particle size, pore size, and morphology of MSNs can be successfully modulated by appropriately combining the synthesis components and their concentrations, as well as by varying the reaction conditions such as temperature and stirring speed. Additional additives like co-solvents, co-surfactants, or swelling agents can be incorporated to fine-tune the nanoparticles according to specific requirements.

1.3.5.2.1. Particle Size control

Strategies for tuning nanoparticle size typically focus on controlling reaction kinetics and colloidal stabilization, which are sensitive to various factors including the type and concentration of precursors, ionic strength, surfactant type, base source, pH, and temperature.

The hydrolysis rate can be controlled by properly choosing the reaction conditions. The precursor type and concentration, the base source and pH, the temperature, and stirring velocity are some of the factors described in the literature that directly influence the kinetics of the silicon preursor hydrolysis and consequently the size of the particles [32, 142, 143]. However, hydrolysis rate control is not trivial, because factors that increase hydrolysis rate also alter the rate of condensation, which is why each system must be studied on a case-by-case basis.

The alkoxide chain length on the precursor (*e.g.* Si-OMe, Si-OEt, Si-OPr, and Si-OBu) directly affects the particle size, with longer alkyl chain leading to larger particles probably due to its slower hydrolysis rate [144]. In MSN synthesized with TEOS-ammonia combination, smaller nanoparticles can be obtained by decreasing the concentration of both reagents and increasing the reaction

temperature [145]. Also by varying TEOS concentration it is possible to control monodispersity [146, 147]. When TEOS is present in excess or is added too slowly, nucleation occurs on an extended period of time, leading to polydisperse particles [148].

Binary surfactant systems composed of a cationic surfactant, usually CTAB, and a non-ionic copolymer such as Pluronic F127 have been used to control particle growth [149–152]. Co-surfactants change the structure of the CTA^+ micelles therefore affecting the micelle packing behavior and particle size. Similarly, the use of a poly(ethylene glycol) (PEG)-modified silane, as a strong growth inhibitor, allows to obtain nanoparticles beetween 5 to 13 nm when added immediatly after addition of the silicon precursor [153]. Other additives, such as tertiary amines and amino acids, have also been used as growth inhibitors. These additives complex with the particles and stabilize them as colloids. Also, when triethanolamine (TEOA) is used, particles can be tuned beetwen 100 to 50 nm by varying the TEOA:TEOS ratio [154]. Additionally, the use of other amines, such as diethanolamine or NH_3, also results in the production of small particles [155]. Furthermore, employing L-lysine as a base source yields ultrasmall particles with sizes below 10 nm [153].

Temperature increments from 30 to 70 ˚C can change the particle size from 29 to 113 nm [147]. For MSN paricles synthesized in neutral conditions particle size increases with a slight increase in the pH in the range of 6 to 7.5 [155].

1.3.5.2.2. Pore size and morphology control

Traditional synthesis methods with CTAB typically produce pore sizes ranging from 2-3 nm, which has prompted the development of techniques to enlarge these pores and broaden the applications of these nanomaterials. In this section, the principal methods aimed at enlarging MSN pore sizes are categorized into one-step methods and seed-growth methods.

I. *One-step* methods

One-step methods are the most common strategies employed to enlarge the pores of MSNs. These methods involve the simultaneous formation of small nuclei and their growth into the final particle. They can be classified into three main categories: template enlargement, organosilane-assisted co-condensation, and biphasic stratification methods.

a) Template enlargement

These methods are the simplest in terms of methodology and involve enlarging micelles size by using several strategies (Figure 1.7 a). The most common strategy is using surfactants with longer chain lengths, which leads to the assembly of larger micelles and results in enlarged pore particles. Combinations of multiple surfactants leads to larger binary micelles and have been used to vary pore size and morphology. For instance, CTAB combined with F127, and *N*,*N*-dimethylhexadecylamine (DMHA) can produce MSNs with pore diameters ranging from 2.6 to 4.6 nm [156, 157].

The template can also be modified by slight alterations in the surfactant's molecular composition, such as changing the counterions associated with cetyltrimethylammonium or modifying the carbon chain length. For example, MSNs synthesized under basic conditions using cetyltrimethylammonium chloride (CTAC) have worm-like pores, while those synthesized with tosylate ion (CTATOS) have slightly larger stellate pores. Using octylammonium bromide (OTAB) results in larger pore sizes and smaller particle diameters [160].

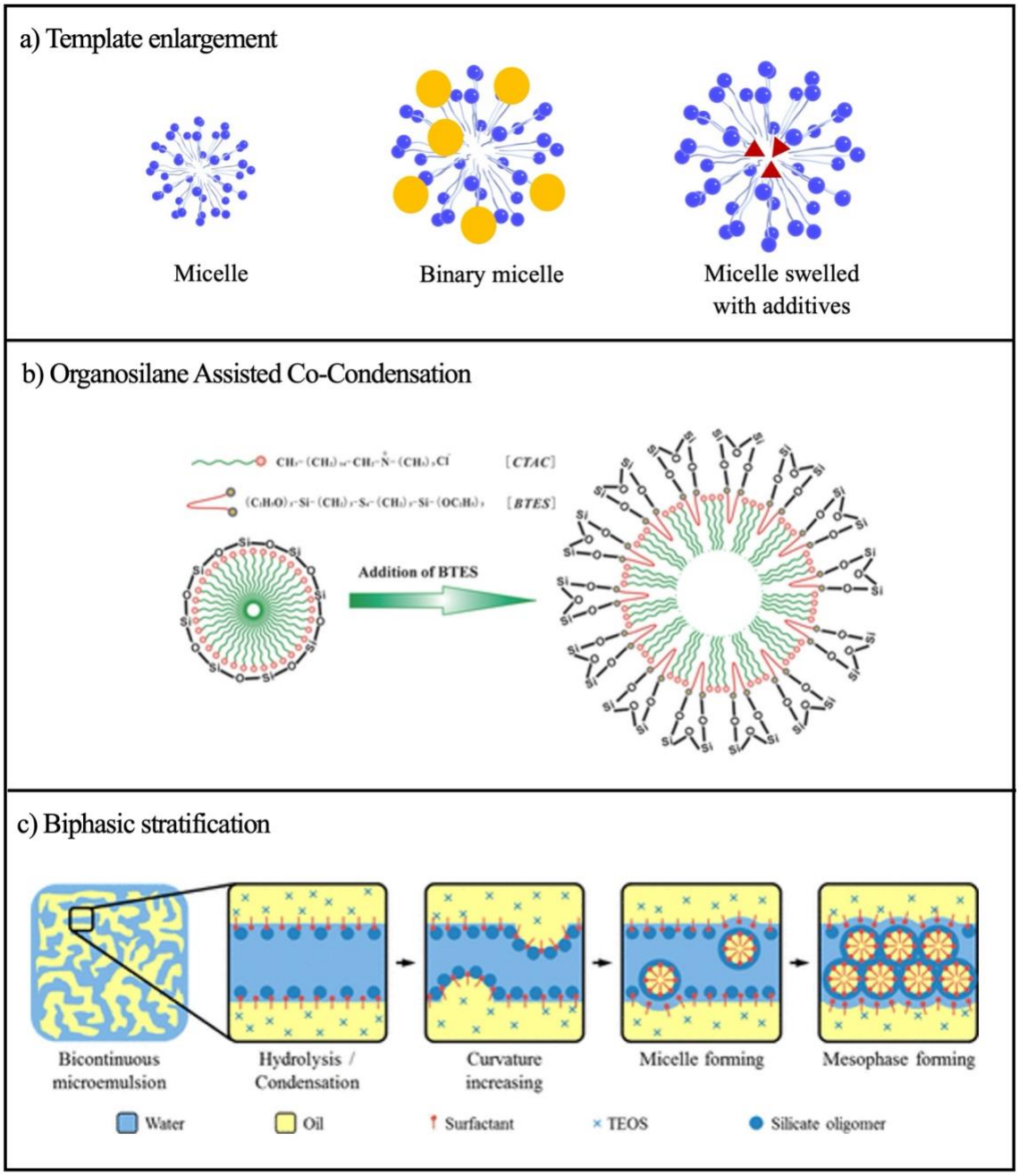

Figure 1.7. Strategies for enlarging pores through methods involving Particle Nucleation and Growth in *One-Step*. (a) Template enlargement: Some strategies to enlarge the template include the formation of binary micelles through the use of surfactant mixtures or the use of additives that modify the micelles. (b) Example of Organosilane Assisted Co-Condensation methods. The CTAC micelle is enlarged by incorporating the hydrophobic long organic chains of the as-hydrolyzed bis[3-(triethoxysilyl)propyl] tetrasulfide (BTES) into the hydrophobic part of the initially formed CTAC micelles. Adapted from [158]. (c) Proposed mechanism for the biphasic stratification method. Adapted from [159].

Other additives like, trialkylbenzenes, alcohols or alkanes can also be added to enlarge the micelles. These additives act as swelling agents and enter

the core of the micelles thus expanding it. That is the case of particles synthesized using 1,3,5-triisopropylbenzene (TIPB) as expanding agent and tetrapropoxysilane (TPOS) as precursor leading to a tuneable pore size from 4 to 8 nm depending of the TIPB amount. However, the particle size is polidisperse and vary from 50 to 380 nm [161].

Larger pores up to 16 nm can be generated by using tosylate ion (CTATOS), combined with small organic amines such as triethanolamine (TEOA) and 2-amino-2-(hydroxymethyl)propane-1,3-diol (AHMPD) and triethyleneamine (TEA) at low concentration (pH ~ 7) and the pore morphology can vary from stellate, raspberry, or worm-like by an apropiate choice of the small organic amines and it concentration [162]. Dendritic particles with a wide pore distribution with openings up to 40 nm can be obtained by mixing CTAB with TEOA and partially fluorinated short-chain anionic fluorocarbon surfactant (Capstone FS-66) [163]

b) Organosilane Assisted Co-Condensation

This method is similar to the template enlargement method but includes an organosilane in addition to the silica precursor. The organosilanes hydrolyze and condense simultaneously in the presence of a surfactant [164, 165]. The hydrophobic fragments of the organosilane assist in directing the self-assembly process, influencing the morphology and mesostructure of the resulting particles, which can have large pores up to 10 nm [164]. Commonly used organosilanes include monopodal and dipodal types. Monopodal organosilanes have one organic substituent and three hydrolysable substituents, following the formula $R–(CH_2)_n–Si–X_3$, where X is a hydrolysable group and R is a non-hydrolyzable organic radical [164]. Dipodal organosilanes consist of bridged silsesquioxanes with the formula $X_3Si–R–SiX_3$, commonly including disulfides, diamines, and benzene groups [164].

One of the earliest reports of the con-condesation method involved the co-condensation of the organosilane tridecafluorooctyltriethoxysilane (F13) with TEOS [166]. The use of multiple organosilanes has also been reported. For

example, the co-condensation of phenyltriethoxysilane (PTES) and 3-(trihydroxysilyl)propylmethyl-phosphonate (THSPMP) with TEOS led to the formation of monodisperse ultra-large pore particles [167]. Even larger pores were obtained using more hydrophobic organosilanes such as 1,2-bis(triethoxysilyl)ethane (BTSE) and 1,4-bis(triethoxysilyl)-benzene (BTSB) [168]. Another approach involved bis[3-(triethoxysilyl)propyl] tetrasulfide (BTES), assembled at the interface of CTAC micelles and co-condensed with TEOS, leading to the expansion of CTAC micelles and the formation of dendritic particles with pores ranging from 8 to 13 nm [158] (Figure 1.7 b).

c) Biphasic stratification

In the biphasic stratification method, it is possible to obtain dendritic MSNs with pore sizes ranging from 4 to 15 nm [145, 164, 169–175]. This method involves the condensation of the silica precursor at the interface between the bottom aqueous phase, which contains a base and surfactant, and the upper organic phase, where the silica precursor is dissolved in a hydrophobic solvent [145, 164].

Several mechanisms have been proposed for the formation of these particles [159, 170, 176], the most widely accepted mechanism suggests that the particles form due to the creation of a bicontinuous microemulsion phase in the biphasic system. The silica precursor forms monomers and oligomers that interact with the hydrophilic heads of the surfactant (CTAC or CTAB). As condensation progresses, the area occupied by the surfactant-silicate heads increases, causing a curvature at the water-oil interface. These curvatures lead to the formation of closed micellar structures, either spherical or cylindrical, which aggregate to form a micellar mesophase that acts as nucleation sites for the particles. The nuclei grow using the mesophase as a template, resulting in a hierarchical structure [159] (Figure 1.7 c). As a result, particles with a bimodal pore size distribution are obtained, featuring large pores ranging from 15-50 nm and small pores between 2-4 nm, which are localized within the nanoparticle walls [159, 164].

II. Seed-growth methods

While *one-step* methodologies offer a straightforward approach to obtaining MSNs with large pores, achieving high monodispersity with these methods remains challenging. The use of additives typically causes significant changes in the hydrolysis and condensation rates of the silica precursor, which greatly affect the final particle size distribution [161, 177]. To address this, strategies based on the synthesis of silica seed particles and their subsequent growth into larger mesoporous structures have proven efficient for independently controlling pore size and particle size [178]. These methods, known as seed-growth methods, involve synthesizing seeds in the first stage — which can occur in the same pot or a different one— and then adding more silica precursor in a second stage to promote growth on these seeds [177, 179–181].

To achieve large pores using the seed-growth method, pore-expanding agents can be added during the growth stage. By adapting the approach described previously, with TIPB as a micelle expander and TPOS as the silica precursor added only during the growth stage, it is possible to obtain pores up to 10 nm (Figure 1.8). These pores can be easily tuned between 4 and 10 nm by adjusting the amount of TIPB added. Importantly, these particles have been shown to be highly monodisperse, with their size tunable between 60 and 100 nm by varying the concentration of the silica source [177]. Notably, TPOS is chosen as the precursor due to its slow hydrolysis kinetics, which helps limit the steady-state concentration of hydrolyzed silicate species. This strategy prevents the formation of new nanoparticles and favors the growth on pre-existing ones. Consequently, the resulting pores exhibit a conical morphology, and the diameter of their openings can be adjusted by varying the amount of pore-expanding agent used [182].

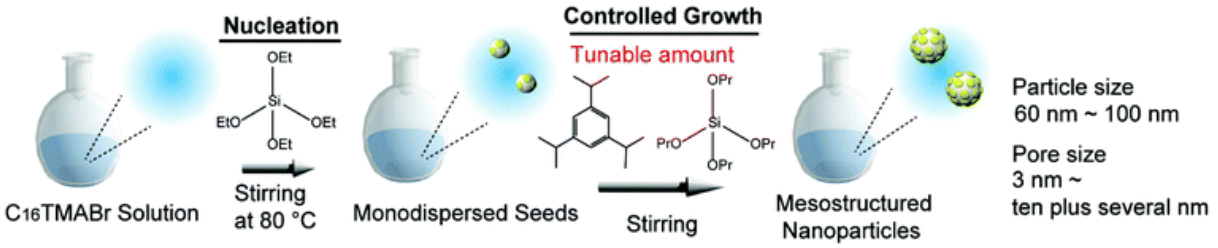

Figure 1.8. Scheme of separate nucleation and growth method for obtaining MSN with large pores using TIPB as a micelle expander during growth. Adapted from [177].

1.3.5.3. Core-shell gold-silica Au@*m*SiO_2 synthesis

Significant efforts have been made to develop core-shell Au@*m*SiO_2 particles, however, as common in materials science, the development of scalable, controlled, and reproducible methods remains a challenge. One of the most promising approaches was introduced by Croissant et al. [111], whose method produces high yields of Au@*m*SiO_2 in a small solvent volume, serving as a starting point for our work. Au@*m*SiO_2 nanoparticles can be synthesized via stepwise or *one-pot* methods. The stepwise method, where the gold core is first synthesized and then coated with a silica shell, offers greater control over the size and uniformity of both components, making it ideal for tailoring particle properties. However, Croissant's *one-pot* method simplifies the process by combining the formation of the gold core and silica shell in a single reaction vessel, offering advantages in simplicity, cost-effectiveness, and scalability.

Currently, the stepwise method remains the most widely used due to the precise control it provides over nanoparticle characteristics. However, the *one-pot* method holds great potential for large-scale production. Despite the widespread interest in Au@*m*SiO_2 particles for various applications, there is still limited understanding of their synthesis mechanisms. Further research is needed to develop more rational, robust, and reproducible designs.

1.3.5.3.1. Stepwise methods

In the stepwise methods [105, 183–187], gold is generally synthesised by the Turkevich-Frens method or its derivatives to obtain spherical AuNPs. When other gold shapes are required, the process may require seed growth methods using halide surfactants or weak/mild reducting agents that block some of the growing directions. Then, the recovered nanoparticles are introduced in a second batch where a silicon precursor is incorporated under appropriate conditions (surfactants, pH) to grow the mesoporous silica layer using the classic Stöber method or its variants. During the synthesis process, the partially hydrolyzed silica precursor condenses around the core, forming the silica shell. The thickness of this silica shell can be tailored by adjusting the reaction time and reagent concentrations. These methods give very good results in terms of morphological control, but usually yield particles on the mg scale, which limits the possibilities of scaling up. Table A1 (Appendix 1) shows a compilation of reported Au@*m*SiO_2 stepwise synthesis.

1.3.5.3.2. *One-pot* methods

The *one-pot* methods consist in the formation of gold nanoparticles and almost simultaneously the sol-gel synthesis of the mesoporous silica shell [104, 110, 111, 188–191]. A key requirement for the formation of the core-shell structure is that the silica nucleation must be heterogeneous using AuNPs as anchor sites, which is possible provided strong interactions exist between the forming silicates and the surfactant-covered AuNPs.

The gold cores are synthesized *in situ* within the same batch where the silicon precursor is subsequently added. This process involves reducing a gold (III) precursor ($HAuCl_4$ or $KAuCl_4$) to generate AuNPs, which are typically stabilized with the CTAB surfactant. CTAB prevents aggregation and acts as anchor for the forming silicate species. Following gold core formation, the hydrolysis and condensation of the silica precursor occur, promoting the formation of the silica shell using the CTAB attached to the gold cores as a

template. Finally, the CTAB template is removed by calcination or acidic extraction. Table A2 (Appendix 2) details the *one-pot* methods for Au@*m*SiO_2 synthesis reported so far.

One-pot syntheses of core-shell particles offer several advantages: larger scales than stepwise methods, reduced time and reagent consumption, and scalability. However, *one-pot* methods have been scarcely explored for the synthesis of Au@*m*SiO_2 particles. In the few reported studies, Au@*m*SiO_2 particles ranging from 50 to 350 nm with spherical gold cores between 5 and 40 nm are obtained in two steps. In the first step, a reductant is added to a solution of $HAuCl_4$ and a surfactant (CTAB, DTAB, CTAC) to grow AuNPs. Then, TEOS or TMOS is incorporated to grow the mesoporous shell. Critical aspects of this synthesis include avoiding agglomeration of core particles in the reaction medium, controlling the uniformity, thickness, and mesostructure of the shell, and avoiding the formation of pure silica particles.

1.3.5.3.3. Au@*m*SiO_2 *one-pot* synthesis limitations

Despite the interest in exploiting the promising applications of Au@*m*SiO_2 particles, developing robust, reproducible, and scalable synthesis methods remains a challenge. The *one-pot* synthesis method, while generally not requiring complicated setups or advanced synthetic skills, faces notable limitations as reported in the literature.

One primary issue is reproducibility; methodologies often lead to Au@*m*SiO_2 particles of varying sizes and morphologies when replicated across different laboratories and research groups, in particular when the nucleation occurs under non-stabilized conditions [191–193]. Another significant challenge is morphology control; alongside core-shell nanoparticles, synthesis can inadvertently produce gold-free MSN byproducts .

Moreover, literature frequently omits essential details such as yield and critical synthesis parameters *eg*, stirring speed, pH, vessel characteristics, stir

bar size and shape, speed of reagent addition, which are crucial for reproducibility. This lack of detail complicates scaling up synthesis efforts, typically restricting these methods to small-scale applications.

Information on the stability of synthesized Au@*m*SiO_2 particles is also sparse, contrasting with extensive research on the stability of AuNPs and MSN. Only limited studies, notably by the Liz-Marzán group, have studied the hydrolytic stability of Au@*m*SiO_2 in water and ethanol media synthesized using a stepwise methodology [185].

Furthermore, comprehensive analyses of the porosity of Au@*m*SiO_2 silica shells are lacking, leaving ambiguity regarding pore size and morphology generated by different *one-pot* methodologies. Current reports allows maximum pore sizes around 4 nm, with minimal exploration into how synthesis variables influence pore formation. Methods to effectively enlarge these pores remain undocumented, thus limiting the material's versatility for various applications.

A critical gap in the current literature is the absence of explanations for the formation mechanism of Au@*m*SiO_2. Understanding these mechanisms is essential for rational design and successful application of this nanomaterial, particularly in biomedical fields.

1.4. Summary and outline of this thesis

In the last few decades, there has been significant progress in the development of multifunctional nanoparticles for biomedical applications, with AuNPs and MSNs being the most studied nanomaterials. The synthesis routes, morphology control, stability, toxicity, and biocompatibility of these nanoparticles have been the subjects of extensive research. Au@*m*SiO_2 nanoparticles emerge as a highly potent combination of both materials, enabling

to merge the unique optical response of AuNPs with the high cargo loading capacity of MSNs.

Despite the promising applications of Au@*m*SiO_2, synthesis methods that allow fine-tuning of size, texture, and morphology are still underdeveloped. *One-pot* methods offer several advantages over stepwise methods, particularly in terms of simplicity, time efficiency, and yield. However, these methods offer little flexibility, and their synthesis mechanisms are not yet fully understood. Understanding these mechanisms is crucial for achieving rational design of Au@*m*SiO_2 and their successful use as nanocarriers.

Although synthesis strategies for Au@*m*SiO_2 are not well explored, several research groups have used them as nanocarriers for drug delivery, showing promising results as PPT and PDT agents. The most commonly used Au@*m*SiO_2 in this field have rod-shaped gold cores, which exhibit photothermal conversion when irradiated in the NIR, allowing tissue penetration by light. However, exploiting the ability of spherical Au@*m*SiO_2 cores to undergo photothermal conversion upon visible spectrum irradiation could be advantageous for delivering therapeutic drugs to superficial tissues such as the epidermis, or for tissues reachable by optical fibers. This thesis focuses on the design of Au@*m*SiO_2 with large-pores to encapsulate and transport large molecules like proteins, aiming to develop a functional nanovehicle for protein delivery in superficial tissues.

This thesis is divided into five main chapters, in addition to this introductory chapter and the conclusions and future work.

Chapter 2 provides a detailed description of the methods and techniques utilized in this research. This methodology chapter lays the groundwork by explaining the experimental setups, materials used, and the specific procedures followed to synthesize and characterize the nanoparticles, assessing protein loading, and evaluating the photothermal effects of the designed Au@*m*SiO_2 nanoparticles.

Chapter 3 begins by proposing a mechanism for the *one-pot* synthesis of Au@*m*SiO_2 nanoparticles, detailing how the particles form and evolve during the synthesis process. It then explores the optimization of various synthesis parameters—including surfactant type, alcohol type, base source, and temperature—to achieve precise control over the size and morphology of the nanoparticles. Through this approach, the chapter provides insights into both the fundamental mechanisms of particle formation and practical strategies for refining the synthesis method.

Chapter 4 presents two effective strategies for enlarging the pores of Au@*m*SiO_2. Both strategies allow to obtain good control over the final particle diameter and monodispersity, which are crucial for practical applications. This chapter also disscusses how the stability of these particles is influenced by the synthesis method used and the nanoparticle concentration. Stability studies are conducted to evaluate whether these large-pore Au@*m*SiO_2 particles can be reliably used in biomedical applications.

Chapter 5 assesses the capacity of Au@*m*SiO_2 to encapsulate proteins, an critical factor for their use as protein delivery nanovehicles. This chapter explores how protein loading is influenced by the pore size of the silica shell and the inherent characteristics of the proteins. The localization of the loaded proteins is determined using several innovative techniques, including circular dichroism, atomic force microscopy, and energy-filtered transmission electron microscopy under cryogenic conditions, which are employed for the first time in this context. Additionally, the stability of encapsulated proteins is compared to that of free (non-adsorbed) proteins to evaluate whether encapsulation within Au@mSiO_2 nanoparticles confers any stability advantages.

Chapter 6 evaluates the efficiency of light-induced heating in Au@*m*SiO_2 nanoparticles when irradiated at their LSPR This chapter employs two approaches to characterize plasmonic heating: monitoring the temperature changes under laser irradiation and calculating the temperature increase of individual nanoparticles through computational modeling.

Finally, Chapter 7 summarizes the overall findings and conclusions of the thesis. It reviews the success of the synthetic strategies developed, the effectiveness of the large-pore Au@*m*SiO_2 particles in encapsulating and stabilizing proteins, and the potential implications for biomedical applications. This chapter also presents potential future research directions and applications for Au@*m*SiO_2, suggesting how the findings of this thesis could be built upon to further advance the field.

1.5. References

1. Pal S (2020) Chapter 7 - Protein folding. In: Pal S (ed) Fundamentals of Molecular Structural Biology. Academic Press, pp 149–169

2. Leader B, Baca QJ, Golan DE (2008) Protein therapeutics: a summary and pharmacological classification. Nat Rev Drug Discov 7:21–39. https://doi.org/10.1038/nrd2399

3. Peer D, Karp JM, Hong S, et al (2007) Nanocarriers as an emerging platform for cancer therapy. Nat Nanotechnol 2:751–760. https://doi.org/10.1038/nnano.2007.387

4. Gu Z, Biswas A, Zhao M, Tang Y (2011) Tailoring nanocarriers for intracellular protein delivery. Chem Soc Rev 40:3638–3655. https://doi.org/10.1039/C0CS00227E

5. Du J, Jin J, Yan M, Lu Y (2012) Synthetic Nanocarriers for Intracellular Protein Delivery. Current Drug Metabolism 13:82–92. https://doi.org/10.2174/138920012798356862

6. Qin X, Yu C, Wei J, et al (2019) Rational Design of Nanocarriers for Intracellular Protein Delivery. Advanced Materials 31:1902791. https://doi.org/10.1002/adma.201902791

7. Faraji AH, Wipf P (2009) Nanoparticles in cellular drug delivery. Bioorg Med Chem 17:2950–2962. https://doi.org/10.1016/j.bmc.2009.02.043

8. Lee KY, Yuk SH (2007) Polymeric protein delivery systems. Progress in Polymer Science 32:669–697. https://doi.org/10.1016/j.progpolymsci.2007.04.001

9. Chou LYT, Ming K, Chan WCW (2010) Strategies for the intracellular delivery of nanoparticles. Chem Soc Rev 40:233–245. https://doi.org/10.1039/C0CS00003E

10. Kresge CT, Leonowicz ME, Roth WJ, et al (1992) Ordered mesoporous molecular sieves synthesized by a liquid-crystal template mechanism. Nature 359:710–712. https://doi.org/10.1038/359710a0

11. Yanagisawa T, Shimizu T, Kuroda K, Kato C (1990) The Preparation of Alkyltrimethylammonium–Kanemite Complexes and Their Conversion to Microporous Materials. Bulletin of the Chemical Society of Japan 63:988–992. https://doi.org/10.1246/bcsj.63.988

12. Han L, Che S (2013) Anionic surfactant templated mesoporous silicas (AMSs). Chem Soc Rev 42:3740–3752. https://doi.org/10.1039/C2CS35297D

13. Han Y, Ying JY (2005) Generalized Fluorocarbon-Surfactant-Mediated Synthesis of Nanoparticles with Various Mesoporous Structures. Angewandte Chemie International Edition 44:288–292. https://doi.org/10.1002/anie.200460892

14. Zhao D, Huo Q, Feng J, et al (1998) Nonionic Triblock and Star Diblock Copolymer and Oligomeric Surfactant Syntheses of Highly Ordered, Hydrothermally Stable, Mesoporous Silica Structures. J Am Chem Soc 120:6024–6036. https://doi.org/10.1021/ja974025i

15. Kankala RK, Han YH, Na J, et al (2020) Nanoarchitectured Structure and Surface Biofunctionality of Mesoporous Silica Nanoparticles. Advanced Materials 32:. https://doi.org/10.1002/adma.201907035

16. Chen M, He X, Wang K, et al (2013) A pH-responsive polymer/mesoporous silica nano-container linked through an acid cleavable linker for intracellular controlled release and tumor therapy in vivo. J Mater Chem B 2:428–436. https://doi.org/10.1039/C3TB21268H

17. Croissant JG, Zhang D, Alsaiari S, et al (2016) Protein-gold clusters-capped mesoporous silica nanoparticles for high drug loading, autonomous gemcitabine/doxorubicin co-delivery, and in-vivo tumor imaging. Journal of Controlled Release 229:183–191. https://doi.org/10.1016/j.jconrel.2016.03.030

18. Hu Y, Ke L, Chen H, et al (2017) Natural material-decorated mesoporous silica nanoparticle container for multifunctional membrane-controlled targeted drug delivery. International Journal of Nanomedicine 12:8411–8426. https://doi.org/10.2147/IJN.S148438

19. Palanikumar L, Choi ES, Cheon JY, et al (2015) Noncovalent Polymer-Gatekeeper in Mesoporous Silica Nanoparticles as a Targeted Drug Delivery Platform. Advanced Functional Materials 25:957–965. https://doi.org/10.1002/adfm.201402755

20. Prabhakar N, Zhang J, Desai D, et al (2016) Stimuli-responsive hybrid nanocarriers developed by controllable integration of hyperbranched PEI with mesoporous silica nanoparticles for sustained intracellular siRNA delivery. International Journal of Nanomedicine 11:6591–6608. https://doi.org/10.2147/IJN.S120611

21. Slowing II, Trewyn BG, Lin VS-Y (2007) Mesoporous Silica Nanoparticles for Intracellular Delivery of Membrane-Impermeable Proteins. J Am Chem Soc 129:8845–8849. https://doi.org/10.1021/ja0719780

22. Tu J, Boyle AL, Friedrich H, et al (2016) Mesoporous Silica Nanoparticles with Large Pores for the Encapsulation and Release of Proteins. In: ACS Publications. https://pubs.acs.org/doi/pdf/10.1021/acsami.6b11324.

23. Yildirim A, Demirel GB, Erdem R, et al (2013) Pluronic polymer capped biocompatible mesoporous silica nanocarriers. Chem Commun 49:9782–9784. https://doi.org/10.1039/C3CC45967E

24. Zhang X, Li F, Guo S, et al (2014) Biofunctionalized polymer-lipid supported mesoporous silica nanoparticles for release of chemotherapeutics in multidrug resistant cancer cells. Biomaterials 35:3650–3665. https://doi.org/10.1016/j.biomaterials.2014.01.013

25. Ashley CE, Carnes EC, Phillips GK, et al (2011) The targeted delivery of multicomponent cargos to cancer cells by nanoporous particle-supported lipid bilayers. Nature Mater 10:389–397. https://doi.org/10.1038/nmat2992

26. Li Z, Nyalosaso JL, Hwang AA, et al (2011) Measurement of Uptake and Release Capacities of Mesoporous Silica Nanoparticles Enabled by Nanovalve Gates. J Phys Chem C 115:19496–19506. https://doi.org/10.1021/jp2047147

27. Tarn D, Ashley CE, Xue M, et al (2013) Mesoporous Silica Nanoparticle Nanocarriers: Biofunctionality and Biocompatibility. Acc Chem Res 46:792–801. https://doi.org/10.1021/ar3000986

28. Fubini B, Fenoglio I, Elias Z, Poirot O (2001) Variability of Biological Responses to Silicas: Effect of Origin, Crystallinity, and State of Surface on Generation of Reactive Oxygen Species and Morphological Transformation of Mammalian Cells. JEP(T) 20:. https://doi.org/10.1615/JEnvironPatholToxicolOncol.v20.iSuppl.1.90

29. Hudson SP, Padera RF, Langer R, Kohane DS (2008) The biocompatibility of mesoporous silicates. Biomaterials 29:4045–4055. https://doi.org/10.1016/j.biomaterials.2008.07.007

30. Yu T, Malugin A, Ghandehari H (2011) Impact of Silica Nanoparticle Design on Cellular Toxicity and Hemolytic Activity. ACS Nano 5:5717–5728. https://doi.org/10.1021/nn2013904

31. He Q, Zhang Z, Gao Y, et al (2009) Intracellular Localization and Cytotoxicity of Spherical Mesoporous Silica Nano- and Microparticles. Small 5:2722–2729. https://doi.org/10.1002/smll.200900923

32. Narayan R, Nayak UY, Raichur AM, Garg S (2018) Mesoporous silica nanoparticles: A comprehensive review on synthesis and recent advances. Pharmaceutics 10:. https://doi.org/10.3390/pharmaceutics10030118

33. Xu C, Lei C, Yu C (2019) Mesoporous Silica Nanoparticles for Protein Protection and Delivery. Front Chem 7:. https://doi.org/10.3389/fchem.2019.00290

34. Han DH, Na H-K, Choi WH, et al (2014) Direct cellular delivery of human proteasomes to delay tau aggregation. Nat Commun 5:5633. https://doi.org/10.1038/ncomms6633

35. Martin-Ortigosa S, Peterson DJ, Valenstein JS, et al (2014) Mesoporous silica nanoparticle-mediated intracellular cre protein delivery for maize genome editing via loxP site excision. Plant Physiol 164:537–547. https://doi.org/10.1104/pp.113.233650

36. Chen Y-P, Chen C-T, Hung Y, et al (2013) A New Strategy for Intracellular Delivery of Enzyme Using Mesoporous Silica Nanoparticles: Superoxide Dismutase. J Am Chem Soc 135:1516–1523. https://doi.org/10.1021/ja3105208

37. Wang T, Jiang H, Zhao Q, et al (2012) Enhanced mucosal and systemic immune responses obtained by porous silica nanoparticles used as an oral vaccine adjuvant: Effect of silica

architecture on immunological properties. International Journal of Pharmaceutics 436:351–358. https://doi.org/10.1016/j.ijpharm.2012.06.028

38. Yang P, Gai S, Lin J (2012) Functionalized mesoporous silica materials for controlled drug delivery. Chem Soc Rev 41:3679–3698. https://doi.org/10.1039/C2CS15308D

39. Yang Y, Wan J, Niu Y, et al (2016) Structure-Dependent and Glutathione-Responsive Biodegradable Dendritic Mesoporous Organosilica Nanoparticles for Safe Protein Delivery. Chem Mater 28:9008–9016. https://doi.org/10.1021/acs.chemmater.6b03896

40. Shao D, Li M, Wang Z, et al (2018) Bioinspired Diselenide-Bridged Mesoporous Silica Nanoparticles for Dual-Responsive Protein Delivery. Advanced Materials 30:1801198. https://doi.org/10.1002/adma.201801198

41. Faraday M (1857) X. The Bakerian Lecture. —Experimental relations of gold (and other metals) to light. Philosophical Transactions of the Royal Society of London 147:145–181. https://doi.org/10.1098/rstl.1857.0011

42. Turkevich J, Stevenson PC, Hillier J (1951) A study of the nucleation and growth processes in the synthesis of colloidal gold. Discuss Faraday Soc 11:55–75. https://doi.org/10.1039/DF9511100055

43. Ishida T, Murayama T, Taketoshi A, Haruta M (2020) Importance of Size and Contact Structure of Gold Nanoparticles for the Genesis of Unique Catalytic Processes. Chem Rev 120:464–525. https://doi.org/10.1021/acs.chemrev.9b00551

44. Kumari Y, Kaur G, Kumar R, et al (2019) Gold nanoparticles: New routes across old boundaries. Advances in Colloid and Interface Science 274:102037. https://doi.org/10.1016/j.cis.2019.102037

45. Li C, Chai OJH, Yao Q, et al (2021) Electrocatalysis of gold-based nanoparticles and nanoclusters. Mater Horiz 8:1657–1682. https://doi.org/10.1039/D0MH01947J

46. Bolaños K, Kogan MJ, Araya E (2019) Capping gold nanoparticles with albumin to improve their biomedical properties. Int J Nanomedicine 14:6387–6406. https://doi.org/10.2147/IJN.S210992

47. Eustis S, El-Sayed MA (2006) Why gold nanoparticles are more precious than pretty gold: Noble metal surface plasmon resonance and its enhancement of the radiative and nonradiative properties of nanocrystals of different shapes. Chem Soc Rev 35:209–217. https://doi.org/10.1039/B514191E

48. Jain PK, Huang X, El-Sayed IH, El-Sayed MA (2008) Noble Metals on the Nanoscale: Optical and Photothermal Properties and Some Applications in Imaging, Sensing, Biology, and Medicine. Acc Chem Res 41:1578–1586. https://doi.org/10.1021/ar7002804

49. Lohse SE, Murphy CJ (2013) The Quest for Shape Control: A History of Gold Nanorod Synthesis. Chem Mater 25:1250–1261. https://doi.org/10.1021/cm303708p

50. Ali MRK, Snyder B, El-Sayed MA (2012) Synthesis and Optical Properties of Small Au Nanorods Using a Seedless Growth Technique. Langmuir 28:9807–9815. https://doi.org/10.1021/la301387p

51. Hulteen JC, R. Martin C (1997) A general template-based method for the preparation of nanomaterials. Journal of Materials Chemistry 7:1075–1087. https://doi.org/10.1039/A700027H

52. Jain PK, Lee KS, El-Sayed IH, El-Sayed MA (2006) Calculated Absorption and Scattering Properties of Gold Nanoparticles of Different Size, Shape, and Composition: Applications in Biological Imaging and Biomedicine. J Phys Chem B 110:7238–7248. https://doi.org/10.1021/jp057170o

53. Orendorff CJ, Murphy CJ (2006) Quantitation of Metal Content in the Silver-Assisted Growth of Gold Nanorods. J Phys Chem B 110:3990–3994. https://doi.org/10.1021/jp0570972

54. Link S, El-Sayed MA (1999) Spectral Properties and Relaxation Dynamics of Surface Plasmon Electronic Oscillations in Gold and Silver Nanodots and Nanorods. J Phys Chem B 103:8410–8426. https://doi.org/10.1021/jp9917648

55. Prescott SW, Mulvaney P (2006) Gold nanorod extinction spectra. Journal of Applied Physics 99:123504. https://doi.org/10.1063/1.2203212

56. Fuller MA, Köper I (2019) Biomedical applications of polyelectrolyte coated spherical gold nanoparticles. Nano Convergence 6:11. https://doi.org/10.1186/s40580-019-0183-4

57. Zhang Z, Zhang C, Zheng H, Xu H (2019) Plasmon-Driven Catalysis on Molecules and Nanomaterials. Acc Chem Res 52:2506–2515. https://doi.org/10.1021/acs.accounts.9b00224

58. Gabudean AM, Focsan M, Astilean S (2012) Gold Nanorods Performing as Dual-Modal Nanoprobes via Metal-Enhanced Fluorescence (MEF) and Surface-Enhanced Raman Scattering (SERS). J Phys Chem C 116:12240–12249. https://doi.org/10.1021/jp211954m

59. Lee CH, Hankus ME, Tian L, et al (2011) Highly Sensitive Surface Enhanced Raman Scattering Substrates Based on Filter Paper Loaded with Plasmonic Nanostructures. Anal Chem 83:8953–8958. https://doi.org/10.1021/ac2016882

60. Zhao T, Wu H, Yao SQ, et al (2010) Nanocomposites Containing Gold Nanorods and Porphyrin-Doped Mesoporous Silica with Dual Capability of Two-Photon Imaging and Photosensitization. Langmuir 26:14937–14942. https://doi.org/10.1021/la102556u

61. Chen J, Ye Z, Yang F, Yin Y (2021) Plasmonic Nanostructures for Photothermal Conversion. Small Science 1:2000055. https://doi.org/10.1002/smsc.202000055

62. Fang Y, Chang W-S, Willingham B, et al (2012) Plasmon Emission Quantum Yield of Single Gold Nanorods as a Function of Aspect Ratio. ACS Nano 6:7177–7184. https://doi.org/10.1021/nn3022469

63. Link S, El-Sayed MA (2000) Shape and size dependence of radiative, non-radiative and photothermal properties of gold nanocrystals. International Reviews in Physical Chemistry 19:409–453. https://doi.org/10.1080/01442350050034180

64. Rashidi-Huyeh M, Palpant B (2004) Thermal response of nanocomposite materials under pulsed laser excitation. Journal of Applied Physics 96:4475–4482. https://doi.org/10.1063/1.1794894

65. Roper DK, Ahn W, Hoepfner M (2007) Microscale Heat Transfer Transduced by Surface Plasmon Resonant Gold Nanoparticles. J Phys Chem C Nanomater Interfaces 111:3636–3641. https://doi.org/10.1021/jp064341w

66. Hu M, Hartland GV (2002) Heat Dissipation for Au Particles in Aqueous Solution: Relaxation Time versus Size. J Phys Chem B 106:7029–7033. https://doi.org/10.1021/jp020581+

67. Plech A, Kotaidis V, Grésillon S, et al (2004) Laser-induced heating and melting of gold nanoparticles studied by time-resolved x-ray scattering. Phys Rev B 70:195423. https://doi.org/10.1103/PhysRevB.70.195423

68. Wilson OM, Hu X, Cahill DG, Braun PV (2002) Colloidal metal particles as probes of nanoscale thermal transport in fluids. Phys Rev B 66:224301. https://doi.org/10.1103/PhysRevB.66.224301

69. Pustovalov VK (2005) Theoretical study of heating of spherical nanoparticle in media by short laser pulses. Chemical Physics 308:103–108. https://doi.org/10.1016/j.chemphys.2004.08.005

70. Zeng N, Murphy AB (2009) Heat generation by optically and thermally interacting aggregates of gold nanoparticles under illumination. Nanotechnology 20:375702. https://doi.org/10.1088/0957-4484/20/37/375702

71. Jauffred L, Samadi A, Klingberg H, et al (2019) Plasmonic Heating of Nanostructures. Chem Rev 119:8087–8130. https://doi.org/10.1021/acs.chemrev.8b00738

72. Ma H, Xue M (2021) Recent advances in the photothermal applications of two-dimensional nanomaterials: photothermal therapy and beyond. J Mater Chem A 9:17569–17591. https://doi.org/10.1039/D1TA04134G

73. Zhao L, Liu Y, Xing R, Yan X (2020) Supramolecular Photothermal Effects: A Promising Mechanism for Efficient Thermal Conversion. Angewandte Chemie International Edition 59:3793–3801. https://doi.org/10.1002/anie.201909825

74. Baffou G, Quidant R, Girard C (2009) Heat generation in plasmonic nanostructures: Influence of morphology. Applied Physics Letters 94:153109. https://doi.org/10.1063/1.3116645

75. Baffou G, Quidant R, García de Abajo FJ (2010) Nanoscale Control of Optical Heating in Complex Plasmonic Systems. ACS Nano 4:709–716. https://doi.org/10.1021/nn901144d

76. Cooper DR, Bekah D, Nadeau JL (2014) Gold nanoparticles and their alternatives for radiation therapy enhancement. Front Chem 2:86. https://doi.org/10.3389/fchem.2014.00086

77. De Jong WH, Hagens WI, Krystek P, et al (2008) Particle size-dependent organ distribution of gold nanoparticles after intravenous administration. Biomaterials 29:1912–1919. https://doi.org/10.1016/j.biomaterials.2007.12.037

78. Patra CR, Bhattacharya R, Mukhopadhyay D, Mukherjee P (2010) Fabrication of gold nanoparticles for targeted therapy in pancreatic cancer. Advanced Drug Delivery Reviews 62:346–361. https://doi.org/10.1016/j.addr.2009.11.007

79. Sani A, Cao C, Cui D (2021) Toxicity of gold nanoparticles (AuNPs): A review. Biochem Biophys Rep 26:100991. https://doi.org/10.1016/j.bbrep.2021.100991

80. Chen H, Dorrigan A, Saad S, et al (2013) In Vivo Study of Spherical Gold Nanoparticles: Inflammatory Effects and Distribution in Mice. PLOS ONE 8:e58208. https://doi.org/10.1371/journal.pone.0058208

81. Fraga S, Faria H, Soares ME, et al (2013) Influence of the surface coating on the cytotoxicity, genotoxicity and uptake of gold nanoparticles in human HepG2 cells. Journal of Applied Toxicology 33:1111–1119. https://doi.org/10.1002/jat.2865

82. Jo M-R, Bae S-H, Go M-R, et al (2015) Toxicity and Biokinetics of Colloidal Gold Nanoparticles. Nanomaterials 5:835–850. https://doi.org/10.3390/nano5020835

83. Schulz M, Ma-Hock L, Brill S, et al (2012) Investigation on the genotoxicity of different sizes of gold nanoparticles administered to the lungs of rats. Mutation Research/Genetic Toxicology and Environmental Mutagenesis 745:51–57. https://doi.org/10.1016/j.mrgentox.2011.11.016

84. Uchiyama MK, Deda DK, Rodrigues SF de P, et al (2014) In vivo and In vitro Toxicity and Anti-Inflammatory Properties of Gold Nanoparticle Bioconjugates to the Vascular System. Toxicological Sciences 142:497–507. https://doi.org/10.1093/toxsci/kfu202

85. Zhang X-D, Wu H-Y, Wu D, et al (2010) Toxicologic effects of gold nanoparticles in vivo by different administration routes. International Journal of Nanomedicine 5:771–781. https://doi.org/10.2147/IJN.S8428

86. Alkilany AM, Nagaria PK, Hexel CR, et al (2009) Cellular Uptake and Cytotoxicity of Gold Nanorods: Molecular Origin of Cytotoxicity and Surface Effects. Small 5:701–708. https://doi.org/10.1002/smll.200801546

87. Murphy CJ, Gole AM, Stone JW, et al (2008) Gold Nanoparticles in Biology: Beyond Toxicity to Cellular Imaging. Acc Chem Res 41:1721–1730. https://doi.org/10.1021/ar800035u

88. Niidome T, Yamagata M, Okamoto Y, et al (2006) PEG-modified gold nanorods with a stealth character for *in vivo* applications. Journal of Controlled Release 114:343–347. https://doi.org/10.1016/j.jconrel.2006.06.017

89. Takahashi H, Niidome Y, Niidome T, et al (2006) Modification of Gold Nanorods Using Phosphatidylcholine to Reduce Cytotoxicity. Langmuir 22:2–5. https://doi.org/10.1021/la0520029

90. Coradeghini R, Gioria S, García CP, et al (2013) Size-dependent toxicity and cell interaction mechanisms of gold nanoparticles on mouse fibroblasts. Toxicology Letters 217:205–216. https://doi.org/10.1016/j.toxlet.2012.11.022

91. Pan Y, Leifert A, Ruau D, et al (2009) Gold Nanoparticles of Diameter 1.4 nm Trigger Necrosis by Oxidative Stress and Mitochondrial Damage. Small 5:2067–2076. https://doi.org/10.1002/smll.200900466

92. Shang L, Nienhaus K, Nienhaus GU (2014) Engineered nanoparticles interacting with cells: size matters. J Nanobiotechnol 12:5. https://doi.org/10.1186/1477-3155-12-5

93. Adewale OB, Davids H, Cairncross L, Roux S (2019) Toxicological Behavior of Gold Nanoparticles on Various Models: Influence of Physicochemical Properties and Other Factors. Int J Toxicol 38:357–384. https://doi.org/10.1177/1091581819863130

94. Siddique S, Chow JCL (2020) Gold Nanoparticles for Drug Delivery and Cancer Therapy. Applied Sciences 10:3824. https://doi.org/10.3390/app10113824

95. Vinhas R, Cordeiro M, Carlos FF, et al (2015) Gold nanoparticle-based theranostics: disease diagnostics and treatment using a single nanomaterial. Nanobiosensors in Disease Diagnosis 4:11–23. https://doi.org/10.2147/NDD.S60285

96. Jeong EH, Jung G, Hong CA, Lee H (2014) Gold nanoparticle (AuNP)-based drug delivery and molecular imaging for biomedical applications. Arch Pharm Res 37:53–59. https://doi.org/10.1007/s12272-013-0273-5

97. Ding X, Yin C, Zhang W, et al (2020) Designing Aptamer-Gold Nanoparticle-Loaded pH-Sensitive Liposomes Encapsulate Morin for Treating Cancer. Nanoscale Res Lett 15:68. https://doi.org/10.1186/s11671-020-03297-x

98. Ahangari A, Salouti M, Heidari Z, et al (2013) Development of gentamicin-gold nanospheres for antimicrobial drug delivery to Staphylococcal infected foci. Drug Delivery 20:34–39. https://doi.org/10.3109/10717544.2012.746402

99. Kennedy LC, Bickford LR, Lewinski NA, et al (2011) A New Era for Cancer Treatment: Gold-Nanoparticle-Mediated Thermal Therapies. Small 7:169–183. https://doi.org/10.1002/smll.201000134

100. Loo C, Lowery A, Halas N, et al (2005) Immunotargeted Nanoshells for Integrated Cancer Imaging and Therapy. Nano Lett 5:709–711. https://doi.org/10.1021/nl050127s

101. O'Neal DP, Hirsch LR, Halas NJ, et al (2004) Photo-thermal tumor ablation in mice using near infrared-absorbing nanoparticles. Cancer Letters 209:171–176. https://doi.org/10.1016/j.canlet.2004.02.004

102. Huang X, El-Sayed IH, Qian W, El-Sayed MA (2006) Cancer Cell Imaging and Photothermal Therapy in the Near-Infrared Region by Using Gold Nanorods. J Am Chem Soc 128:2115–2120. https://doi.org/10.1021/ja057254a

103. Moreira AF, Rodrigues CF, Reis CA, et al (2018) Gold-core silica shell nanoparticles application in imaging and therapy: A review. Microporous and Mesoporous Materials 270:168–179. https://doi.org/10.1016/j.micromeso.2018.05.022

104. Chen J, Zhang R, Han L, et al (2013) One-pot synthesis of thermally stable gold@mesoporous silica core-shell nanospheres with catalytic activity. Nano Research 6:871–879. https://doi.org/10.1007/s12274-013-0363-1

105. Sekhar ACS, Meera CJ, Ziyad KV, et al (2013) Synthesis and catalytic activity of monodisperse gold–mesoporous silica core–shell nanocatalysts. Catal Sci Technol 3:1190–1193. https://doi.org/10.1039/C3CY20772B

106. Liz-Marzán LM, Giersig M, Mulvaney P (1996) Synthesis of Nanosized Gold−Silica Core−Shell Particles. Langmuir 12:4329–4335. https://doi.org/10.1021/la9601871

107. Nooney RI, Thirunavukkarasu D, Chen Y, et al (2003) Self-Assembly of Mesoporous Nanoscale Silica/Gold Composites. Langmuir 19:7628–7637. https://doi.org/10.1021/la034522e

108. Gorelikov I, Matsuura N (2008) Single-Step Coating of Mesoporous Silica on Cetyltrimethyl Ammonium Bromide-Capped Nanoparticles. Nano Lett 8:369–373. https://doi.org/10.1021/nl0727415

109. Pellas V, Hu D, Mazouzi Y, et al (2020) Gold Nanorods for LSPR Biosensing: Synthesis, Coating by Silica, and Bioanalytical Applications. Biosensors (Basel) 10:146. https://doi.org/10.3390/bios10100146

110. Song JT, Zhang XS, Qin MY, Zhao YD (2015) One-pot two-step synthesis of core-shell mesoporous silica-coated gold nanoparticles. Dalton Transactions 44:7752–7756. https://doi.org/10.1039/c5dt00912j

111. Croissant J, Zink JI (2012) Nanovalve-Controlled Cargo Release Activated by Plasmonic Heating. J Am Chem Soc 134:7628–7631. https://doi.org/10.1021/ja301880x

112. Underwood S, Mulvaney P (1994) Effect of the Solution Refractive Index on the Color of Gold Colloids. Langmuir 10:3427–3430. https://doi.org/10.1021/la00022a011

113. Chen M, He Y, Zhu J (2019) Quantifying and Comparing the Near-Field Enhancement, Photothermal Conversion, and Local Heating Performance of Plasmonic SiO2@Au Core-Shell Nanoparticles. Plasmonics 14:1019–1027. https://doi.org/10.1007/s11468-018-0889-x

114. Kumar D, Ghai DP, Soni RK (2018) Simulation Studies of Photoacoustic Response from Gold-Silica Core-Shell Nanoparticles. Plasmonics 13:1833–1841. https://doi.org/10.1007/s11468-018-0697-3

115. Dias DR, Moreira AF, Correia IJ (2016) The effect of the shape of gold core–mesoporous silica shell nanoparticles on the cellular behavior and tumor spheroid penetration. J Mater Chem B 4:7630–7640. https://doi.org/10.1039/C6TB02668K

116. Ramasamy M, Lee J-H, Lee J (2017) Development of gold nanoparticles coated with silica containing the antibiofilm drug cinnamaldehyde and their effects on pathogenic bacteria. International Journal of Nanomedicine 12:2813–2828. https://doi.org/10.2147/IJN.S132784

117. Lee C, Hwang HS, Lee S, et al (2017) Rabies Virus-Inspired Silica-Coated Gold Nanorods as a Photothermal Therapeutic Platform for Treating Brain Tumors. Adv Mater 29:. https://doi.org/10.1002/adma.201605563

118. Shen S, Tang H, Zhang X, et al (2013) Targeting mesoporous silica-encapsulated gold nanorods for chemo-photothermal therapy with near-infrared radiation. Biomaterials 34:3150–3158. https://doi.org/10.1016/j.biomaterials.2013.01.051

119. Luo G-F, Chen W-H, Lei Q, et al (2016) A Triple-Collaborative Strategy for High-Performance Tumor Therapy by Multifunctional Mesoporous Silica-Coated Gold Nanorods. Advanced Functional Materials 26:4339–4350. https://doi.org/10.1002/adfm.201505175

120. Zeng Q, Zhang Y, Ji W, et al (2014) Inhibitation of Cellular Toxicity of Gold Nanoparticles by Surface Encapsulation of Silica Shell for Hepatocarcinoma Cell Application. ACS Appl Mater Interfaces 6:19327–19335. https://doi.org/10.1021/am505417v

121. Frens G (1973) Controlled Nucleation for the Regulation of the Particle Size in Monodisperse Gold Suspensions. Nature Physical Science 241:20–22. https://doi.org/10.1038/physci241020a0

122. Wuithschick M, Birnbaum A, Witte S, et al (2015) Turkevich in New Robes: Key Questions Answered for the Most Common Gold Nanoparticle Synthesis. ACS Nano 9:7052–7071. https://doi.org/10.1021/acsnano.5b01579

123. Brust M, Walker M, Bethell D, et al (1994) Synthesis of thiol-derivatised gold nanoparticles in a two-phase Liquid–Liquid system. J Chem Soc, Chem Commun 801–802. https://doi.org/10.1039/C39940000801

124. DuChene JS, Niu W, Abendroth JM, et al (2013) Halide Anions as Shape-Directing Agents for Obtaining High-Quality Anisotropic Gold Nanostructures. Chem Mater 25:1392–1399. https://doi.org/10.1021/cm3020397

125. Ferrier RCJ, Gines G, Gasparutto D, et al (2015) Tuning Optical Properties of Functionalized Gold Nanorods through Controlled Interactions with Organic Semiconductors. Journal of Physical Chemistry C 119:17899. https://doi.org/10.1021/acs.jpcc.5b04785

126. Pelaz B, Grazu V, Ibarra A, et al (2012) Tailoring the Synthesis and Heating Ability of Gold Nanoprisms for Bioapplications. Langmuir 28:8965–8970. https://doi.org/10.1021/la204712u

127. Scarabelli L, Coronado-Puchau M, Giner-Casares JJ, et al (2014) Monodisperse Gold Nanotriangles: Size Control, Large-Scale Self-Assembly, and Performance in Surface-Enhanced Raman Scattering. ACS Nano 8:5833–5842. https://doi.org/10.1021/nn500727w

128. Tian F, Bonnier F, Casey A, et al (2014) Surface enhanced Raman scattering with gold nanoparticles: effect of particle shape. Anal Methods 6:9116–9123. https://doi.org/10.1039/C4AY02112F

129. Yasun E, Li C, Barut I, et al (2015) BSA modification to reduce CTAB induced nonspecificity and cytotoxicity of aptamer-conjugated gold nanorods. Nanoscale 7:10240–10248. https://doi.org/10.1039/C5NR01704A

130. Pastoriza-Santos I, Pérez-Juste J, Liz-Marzán LM (2006) Silica-coating and hydrophobation of CTAB-stabilized gold nanorods. Chemistry of Materials 18:2465–2467. https://doi.org/10.1021/cm060293g

131. Polte J (2015) Fundamental growth principles of colloidal metal nanoparticles – a new perspective. CrystEngComm 17:6809–6830. https://doi.org/10.1039/C5CE01014D

132. Scarabelli L, Sánchez-Iglesias A, Pérez-Juste J, Liz-Marzán LM (2015) A “Tips and Tricks” Practical Guide to the Synthesis of Gold Nanorods. Journal of Physical Chemistry Letters 6:4270–4279. https://doi.org/10.1021/acs.jpclett.5b02123

133. Brinker CJ, Scherer GW (1990) CHAPTER 2 - Hydrolysis and Condensation I: Nonsilicates. In: Brinker CJ, Scherer GW (eds) Sol-Gel Science. Academic Press, San Diego, pp 20–95

134. Pierre AC (2020) Introduction to Sol-Gel Processing. Springer International Publishing, Cham

135. Monge Marcet A (2011) Organic-inorganic hybrid silica materials derived from imidazolium salts and prolinamides. Applications in catalysis. Https://theses.fr/2011ENCM0007, Universitat Autònoma de Barcelona

136. Alvarado Meza R, Santori T, Cattoën X (2023) A kinetic approach to the mechanism of formation of mesoporous silica nanoparticles. Journal of Sol-Gel Science and Technology. https://doi.org/10.1007/s10971-023-06130-w

137. Semeykina V, Zharov I (2022) Medium controlled aggregative growth as a key step in mesoporous silica nanoparticle formation. Journal of Colloid and Interface Science 615:236–247. https://doi.org/10.1016/j.jcis.2022.01.166

138. García-Uriostegui L, Meléndez-Ortiz HI, Mata-Padilla JM, Toriz G (2023) Fast fabrication of mesostructured MCM-41-type nanoparticles by microwave-induced synthesis. Ceramics International 49:28693–28701. https://doi.org/10.1016/j.ceramint.2023.06.126

139. Lang N, Tuel A (2004) A Fast and Efficient Ion-Exchange Procedure To Remove Surfactant Molecules from MCM-41 Materials. Chem Mater 16:1961–1966. https://doi.org/10.1021/cm030633n

140. Oliveira MR, Barboza YT, Silva TSL, et al (2024) One-Pot Synthesis and Surfactant Removal from MCM-41 Using Microwave Irradiation. Molecules 29:460. https://doi.org/10.3390/molecules29020460

141. Pirez C, Wilson K, F. Lee A (2014) An energy-efficient route to the rapid synthesis of organically-modified SBA-15 via ultrasonic template removal. Green Chemistry 16:197–202. https://doi.org/10.1039/C3GC40474A

142. Frickenstein AN, Hagood JM, Britten CN, et al (2021) Mesoporous Silica Nanoparticles: Properties and Strategies for Enhancing Clinical Effect. Pharmaceutics 13:570. https://doi.org/10.3390/pharmaceutics13040570

143. Pal N, Lee J-H, Cho E-B (2020) Recent Trends in Morphology-Controlled Synthesis and Application of Mesoporous Silica Nanoparticles. Nanomaterials 10:2122. https://doi.org/10.3390/nano10112122

144. Yamada H, Urata C, Ujiie H, et al (2013) Preparation of aqueous colloidal mesostructured and mesoporous silica nanoparticles with controlled particle size in a very wide range from 20 nm to 700 nm. Nanoscale 5:6145–6153. https://doi.org/10.1039/C3NR00334E

145. Noureddine A, Maestas-Olguin A, Tang L, et al (2023) Future of Mesoporous Silica Nanoparticles in Nanomedicine: Protocol for Reproducible Synthesis, Characterization, Lipid Coating, and Loading of Therapeutics (Chemotherapeutic, Proteins, siRNA and mRNA). ACS Nano 17:16308–16325. https://doi.org/10.1021/acsnano.3c07621

146. Kim JW, Kim LU, Kim CK (2007) Size Control of Silica Nanoparticles and Their Surface Treatment for Fabrication of Dental Nanocomposites. Biomacromolecules 8:215–222. https://doi.org/10.1021/bm060560b

147. Zainala NA, Shukor S, Wabb HAA, Razakb K (2013) Study on the effect of synthesis parameters of silica nanoparticles entrapped with rifampicin. Chem Eng 32:432–434

148. Candela-Noguera V, Amorós P, Aznar E, et al (2024) Systematic study of the implications of calcination and solvent extraction of the surfactant in MCM-41-type mesoporous silica nanoparticles. Microporous and Mesoporous Materials 373:113119. https://doi.org/10.1016/j.micromeso.2024.113119

149. Febvay S, Marini DM, Belcher AM, Clapham DE (2010) Targeted cytosolic delivery of cell-impermeable compounds by nanoparticle-mediated, light-triggered endosome disruption. Nano Lett 10:2211–2219. https://doi.org/10.1021/nl101157z

150. Kim TW, Chung PW, Lin VSY (2010) Facile synthesis of monodisperse spherical MCM-48 mesoporous silica nanoparticles with controlled particle size. Chemistry of Materials 22:5093–5104. https://doi.org/10.1021/cm1017344

151. Meng H, Xue M, Xia T, et al (2011) Use of size and a copolymer design feature to improve the biodistribution and the enhanced permeability and retention effect of doxorubicin-loaded mesoporous silica nanoparticles in a murine xenograft tumor model. ACS Nano 5:4131–4144. https://doi.org/10.1021/nn200809t

152. Nguyen NH, Truong-Thi N-H, Nguyen DTD, et al (2022) Non-ionic surfactants As co-templates to control the mesopore diameter of hollow mesoporous silica nanoparticles for drug delivery applications. Colloids and Surfaces A: Physicochemical and Engineering Aspects 655:130218. https://doi.org/10.1016/j.colsurfa.2022.130218

153. Ma K, Werner-Zwanziger U, Zwanziger J, Wiesner U (2013) Controlling Growth of Ultrasmall Sub-10 nm Fluorescent Mesoporous Silica Nanoparticles. Chem Mater 25:677–691. https://doi.org/10.1021/cm303242h

154. Möller K, Kobler J, Bein T (2007) Colloidal suspensions of nanometer-sized mesoporous silica. Advanced Functional Materials 17:605–612. https://doi.org/10.1002/adfm.200600578

155. Qiao ZA, Zhang L, Guo M, et al (2009) Synthesis of mesoporous silica nanoparticles via controlled hydrolysis and condensation of silicon alkoxide. Chemistry of Materials 21:3823–3829. https://doi.org/10.1021/cm901335k

156. Gu J, Huang K, Zhu X, et al (2013) Sub-150 nm mesoporous silica nanoparticles with tunable pore sizes and well-ordered mesostructure for protein encapsulation. Journal of Colloid and Interface Science 407:236–242. https://doi.org/10.1016/j.jcis.2013.06.028

157. He Q, Cui X, Cui F, et al (2009) Size-controlled synthesis of monodispersed mesoporous silica nano-spheres under a neutral condition. Microporous and Mesoporous Materials 117:609–616. https://doi.org/10.1016/j.micromeso.2008.08.004

158. Wu M, Meng Q, Chen Y, et al (2015) Large-Pore Ultrasmall Mesoporous Organosilica Nanoparticles: Micelle/Precursor Co-templating Assembly and Nuclear-Targeted Gene Delivery. Advanced Materials 27:215–222. https://doi.org/10.1002/adma.201404256

159. Moon D-S, Lee J-K (2012) Tunable synthesis of hierarchical mesoporous silica nanoparticles with radial wrinkle structure. Langmuir 28:12341–12347. https://doi.org/10.1021/la302145j

160. Möller K, Bein T (2017) Talented Mesoporous Silica Nanoparticles. Chem Mater 29:371–388. https://doi.org/10.1021/acs.chemmater.6b03629

161. Yamada H, Ujiie H, Urata C, et al (2015) A multifunctional role of trialkylbenzenes for the preparation of aqueous colloidal mesostructured/mesoporous silica nanoparticles with controlled pore size, particle diameter, and morphology. Nanoscale 7:19557–19567. https://doi.org/10.1039/C5NR04465K

162. Zhang K, Xu L-L, Jiang J-G, et al (2013) Facile Large-Scale Synthesis of Monodisperse Mesoporous Silica Nanospheres with Tunable Pore Structure. J Am Chem Soc 135:2427–2430. https://doi.org/10.1021/ja3116873

163. Huang M, Liu L, Wang S, et al (2017) Dendritic Mesoporous Silica Nanospheres Synthesized by a Novel Dual-Templating Micelle System for the Preparation of Functional Nanomaterials. Langmuir 33:519–526. https://doi.org/10.1021/acs.langmuir.6b03282

164. Hao P, Peng B, Shan B-Q, et al (2020) Comprehensive understanding of the synthesis and formation mechanism of dendritic mesoporous silica nanospheres. Nanoscale Advances 2:1792–1810. https://doi.org/10.1039/D0NA00219D

165. Wang Y, Zhang B, Ding X, Du X (2021) Dendritic mesoporous organosilica nanoparticles (DMONs): Chemical composition, structural architecture, and promising applications. Nano Today 39:101231. https://doi.org/10.1016/j.nantod.2021.101231

166. Pereira C, Alves C, Monteiro A, et al (2011) Designing Novel Hybrid Materials by One-Pot Co-condensation: From Hydrophobic Mesoporous Silica Nanoparticles to Superamphiphobic Cotton Textiles. ACS Appl Mater Interfaces 3:2289–2299. https://doi.org/10.1021/am200220x

167. Paula AJ, Montoro LA, Filho AGS, Alves OL (2011) Towards long-term colloidal stability of silica-based nanocarriers for hydrophobic molecules: beyond the Stöber method. Chem Commun 48:591–593. https://doi.org/10.1039/C1CC16535F

168. Shan B-Q, Xing J-L, Yang T-Q, et al (2019) One-pot co-condensation strategy for dendritic mesoporous organosilica nanospheres with fine size and morphology control. CrystEngComm 21:4030–4035. https://doi.org/10.1039/C9CE00593E

169. Ernawati L, Balgis R, Ogi T, Okuyama K (2017) Tunable Synthesis of Mesoporous Silica Particles with Unique Radially Oriented Pore Structures from Tetramethyl Orthosilicate via Oil-Water Emulsion Process. Langmuir 33:783–790. https://doi.org/10.1021/acs.langmuir.6b04023

170. Febriyanti E, Suendo V, Mukti RR, et al (2016) Further Insight into the Definite Morphology and Formation Mechanism of Mesoporous Silica KCC-1. Langmuir 32:5802–5811. https://doi.org/10.1021/acs.langmuir.6b00675

171. Gustafsson H, Isaksson S, Altskär A, Holmberg K (2016) Mesoporous silica nanoparticles with controllable morphology prepared from oil-in-water emulsions. Journal of Colloid and Interface Science 467:253–260. https://doi.org/10.1016/j.jcis.2016.01.026

172. Nandiyanto ABD, Kim S-G, Iskandar F, Okuyama K (2009) Synthesis of spherical mesoporous silica nanoparticles with nanometer-size controllable pores and outer diameters. Microporous and Mesoporous Materials 120:447–453. https://doi.org/10.1016/j.micromeso.2008.12.019

173. Noureddine A, Hjelvik EA, Croissant JG, et al (2019) Engineering of large-pore lipid-coated mesoporous silica nanoparticles for dual cargo delivery to cancer cells. J Sol-Gel Sci Technol 89:78–90. https://doi.org/10.1007/s10971-018-4772-1

174. Polshettiwar V, Cha D, Zhang X, Basset JM (2010) High-Surface-Area Silica Nanospheres (KCC-1) with a Fibrous Morphology. Angewandte Chemie International Edition 49:9652–9656. https://doi.org/10.1002/anie.201003451

175. Shen D, Yang J, Li X, et al (2014) Biphase stratification approach to three-dimensional dendritic biodegradable mesoporous silica nanospheres. Nano Lett 14:923–932. https://doi.org/10.1021/nl404316v

176. Maity A, Das A, Sen D, et al (2017) Unraveling the Formation Mechanism of Dendritic Fibrous Nanosilica. Langmuir 33:13774–13782. https://doi.org/10.1021/acs.langmuir.7b02996

177. Yamamoto E, Mori S, Shimojima A, et al (2017) Fabrication of colloidal crystals composed of pore-expanded mesoporous silica nanoparticles prepared by a controlled growth method. Nanoscale 9:2464–2470. https://doi.org/10.1039/C6NR07416B

178. Yamamoto E, Kuroda K (2018) Chapter One - Preparation and Controllability of Mesoporous Silica Nanoparticles. In: Tamanoi F (ed) The Enzymes. Academic Press, pp 1–10

179. Cauda V, Schlossbauer A, Kecht J, et al (2009) Multiple Core−Shell Functionalized Colloidal Mesoporous Silica Nanoparticles. J Am Chem Soc 131:11361–11370. https://doi.org/10.1021/ja809346n

180. Lin Y-S, Lu C-YD, Hung Y, Mou C-Y (2009) Uniform Mesoporous Silica Hexagon and Its Two-Dimensional Colloidal Crystal. ChemPhysChem 10:2628–2632. https://doi.org/10.1002/cphc.200900251

181. Nakamura T, Mizutani M, Nozaki H, et al (2007) Formation Mechanism for Monodispersed Mesoporous Silica Spheres and Its Application to the Synthesis of Core/Shell Particles. J Phys Chem C 111:1093–1100. https://doi.org/10.1021/jp0648240

182. Guerrero-Florez V, Barbara A, Kodjikian S, et al (2024) Dynamic Light Scattering Unveils Stochastic Degradation in Large-pore Mesoporous Silica Nanoparticles. J Colloid Interface Sci 676:1098–1108. https://doi.org/10.1016/j.jcis.2024.07.151

183. Li H, Li Z, Liu L, et al (2015) An efficient gold nanocarrier for combined chemo-photodynamic therapy on tumour cells. RSC Adv 5:34831–34838. https://doi.org/10.1039/C4RA17249C

184. Wu C, Lim Z-Y, Zhou C, et al (2013) A soft-templated method to synthesize sintering-resistant Au–mesoporous-silica core–shell nanocatalysts with sub-5 nm single-cores. Chem Commun 49:3215–3217. https://doi.org/10.1039/C3CC39202C

185. Sanz-Ortiz MN, Sentosun K, Bals S, Liz-Marzán LM (2015) Templated Growth of Surface Enhanced Raman Scattering-Active Branched Gold Nanoparticles within Radial Mesoporous Silica Shells. ACS Nano 9:10489–10497. https://doi.org/10.1021/acsnano.5b04744

186. An J, Yang X-Q, Cheng K, et al (2017) In Vivo Computed Tomography/Photoacoustic Imaging and NIR-Triggered Chemo-Photothermal Combined Therapy Based on a Gold Nanostar-, Mesoporous Silica-, and Thermosensitive Liposome-Composited Nanoprobe. ACS Appl Mater Interfaces 9:41748–41759. https://doi.org/10.1021/acsami.7b15296

187. Santana Vega M, Guerrero Martínez A, Cucinotta F (2019) Facile Strategy for the Synthesis of Gold@Silica Hybrid Nanoparticles with Controlled Porosity and Janus Morphology. Nanomaterials (Basel) 9:348. https://doi.org/10.3390/nano9030348

188. Li X, Shao Y, Lv S, et al (2021) Au@mSiO2 core–shell nanoparticles loaded with fluorescent dyes: synthesis and application for imaging performance. Dalton Trans 50:5624–5631. https://doi.org/10.1039/D1DT00253H

189. Veneziano R, Derrien G, Tan S, et al (2012) One step synthesis of gold-loaded radial mesoporous silica nanospheres and supported lipid bilayer functionalization: Towards bio-multifunctional sensors. Small 8:3674–3682. https://doi.org/10.1002/smll.201200758

190. Hammond-Pereira E, Bryant K, Graham TR, et al (2020) Mesoporous silica-encapsulated gold core-shell nanoparticles for active solvent-free benzyl alcohol oxidation. Reaction Chemistry and Engineering 5:1939–1949. https://doi.org/10.1039/d0re00198h

191. Zhang S, Xu X, Zhang G, et al (2019) One-pot one-step synthesis of Au@SiO2 core-shell nanoparticles and their shell-thickness-dependent fluorescent properties. RSC Advances 9:17674–17678. https://doi.org/10.1039/c9ra02543j

192. Gundanna SK, Mitra A, Bhatta LKG, Bhatta UM (2021) Effect of thermal treatment on the surface/interfacial behaviour of Au@SiO2 nanoparticles in the presence of CTAB surfactant molecules. Powder Technology 381:503–508. https://doi.org/10.1016/j.powtec.2020.12.010

193. Zhang G, Dong L, Zhang S, et al (2021) One-pot synthesis of Au@mSiO2 yolk-shell nanoparticles with enhanced catalytic and surface-enhanced Raman scattering (SERS) properties. Journal of Alloys and Compounds 871:. https://doi.org/10.1016/j.jallcom.2021.159631

Chapter 2

Methods and Materials

This chapter provides a comprehensive overview of the synthesis methods utilized for the nanoparticles studied in this thesis, as well as the primary characterization techniques and methodologies applied. A brief theoretical background of these techniques is included, emphasizing the type of information they provide, their advantages, and the necessary instrumentation, as relevant to this work.

The first section describes the protocols for synthesizing Au@*m*SiO_2 particles, as well as other particles used in this thesis. The second section provides details on the characterization techniques utilized to analyze the synthesized materials. The third section focuses on the methodologies employed to elucidate the synthesis mechanism of Au@*m*SiO_2 nanoparticles. The fourth section explains the procedures for loading proteins onto the nanoparticles, including the molecular biology techniques used for protein production and characterization. Finally, the fifth section discusses the methods used to evaluate the stability of the particles.

2.1. Nanoparticles synthesis

Table 2.1 lists the primary reagents used in this thesis, along with their abbreviations and the corresponding product brands.

Table 2.1. Primary Reagents Employed

Reagent	Abbreviation	Brand
Gradient HPLC grade water	Water	Fisher
Cetyl trimethylammonium bromide	CTAB	Sigma Aldrich (H5882) Alfa Aesar (A15235)
Tetrachloroauric(III) acid trihydrate	HAuCl4	Sigma Aldrich
Tetraethyl orthosilicate	TEOS	Sigma Aldrich
Sodium hydroxide	NaOH	Sigma Aldrich
Brij C10	Brij C10	Sigma Aldrich
Pluronic® F127	F127	Sigma Aldrich
Cetyl trimethylammonium chloride	CTAC	Sigma Aldrich
Triethanolamine	TEOA	Sigma Aldrich
Sodium tetraborate	Borax	Sigma Aldrich
Isopropanol	IPA	Sigma Aldrich
Butanol	-	Sigma Aldrich
Ethanol	EtOH	Sigma Aldrich
1,3,5-Triisopropylbenzene	TIPB	Sigma Aldrich
Tetrapropyl orthosilicate	TPOS	Alfa Aesar
Bovine serum albumin	BSA	Sigma Aldrich
Horseradish peroxidase	HRP	Sigma Aldrich
2,2′-azino-bis (3-ethylbenzothiazoline-6-sulfonic acid)	ABTS	Sigma Aldrich

2.1.1. *One-pot* synthesis of Au@*m*SiO_2

The *one-pot* methodology was adapted from reference [1]. In a 250 mL round bottom flask, a mixture composed of CTAB (0.64 g, 1.8 mmol), water (100 mL) and ethanol (40 mL) was heated to 70 °C and stirred at 400 rpm using an olive stir bar (12 × 25 mm). A tetrachloroauric acid solution (100 mM, 1.5 mL, 0.15 mmol) was added and the mixture was stirred for 5 minutes at 600 rpm. A freshly prepared sodium hydroxide solution (2.0 M, 0.20 mL, 0.40 mmol) was then added and the solution was stirred for 30 min. Then TEOS (1.0 mL, 4.5 mmol) was added dropwise over 2 minutes. Subsequently, a sodium hydroxide solution (2.0 M, 0.40 mL, 0.80 mmol) was added, which led to the discoloration, immediately followed by the appearance of blue to purple colored species. The reaction mixture was stirred at 70 °C, 600 rpm for 2 h. The resulting Au@*m*SiO_2 particles were centrifuged at 7000 rpm (6092 RCF) for 20 minutes and washed with ethanol three times. Finally, the template was removed by calcination at 500 °C for 2 h after a heating ramp of 10 °C/min. The detailed scheme of the protocol is presented in Figure 2.1.

To tune the characteristics of the Au@*m*SiO_2 particles, modifications were made to the previously described process. First, CTAB was combined with a co-surfactant The co-surfactant solution was added to the reaction mixture 20 minutes after the first NaOH addition, and TEOS was added 15 minutes after the co-surfactant addition. Second, the synthesis with Brij C10:CTAB (1:5) was further studied by changing some parameters: change of alcohol, base source and use of complexing agents. For all syntheses, the reaction mixture was kept for 2 h under stirring at 600 rpm.

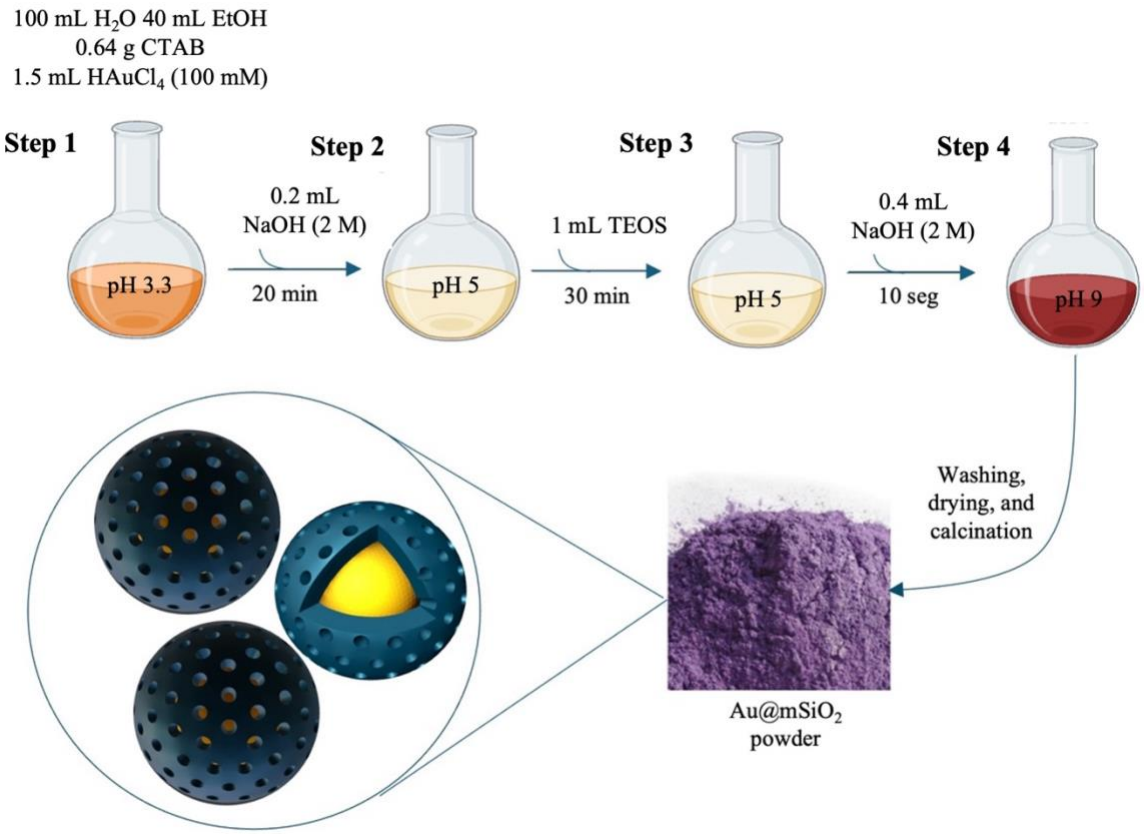

Figure 2.1. Scheme of the protocol for the synthesis of Au@*m*SiO_2 particles by the *one-pot* method.

2.1.1.1. Surfactants

The structuring agents used were: cetyl trimethylammonium bromide (CTAB), the triblock copolymer Pluronic® F127 (F127), cetyl trimethylammonium chloride 25 wt. % in H_2O (CTAC), and Brij C10 whose structures and molecular weights are shown in Table 2.2. The synthesis using the Brij C10:CTAB (1:5) combination was the most robust and the particles exhibited the best colloidal stability (see chapter 3). Therefore the tunning of parameters hereafter was performed using C10:CTAB (1:5) as the structuring agent.

Table 2.2. Structures and molar masses of the surfactant used.

Surfactant	Structure	MW/ g.mol^{-1}
CTAB	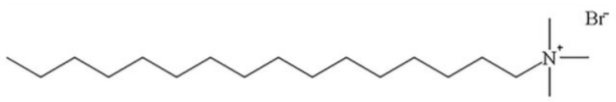	364
CTAC	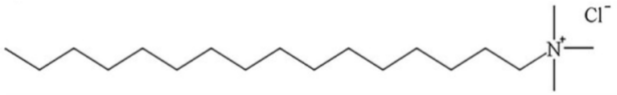	320
F127	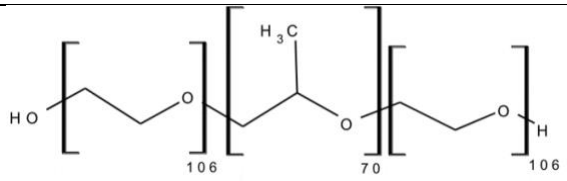	12800
Brij C10	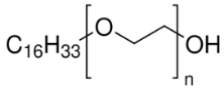 n=10	683

2.1.1.2. Alcohol

The alcohols used were ethanol, isopropanol and butanol. To study the effect of the alcohol in the synthesis, the method described in section 1.1 was followed using Brij C10: CTAB (1:5) as the structuring agent and replacing the 40 mL of ethanol by isopropanol or butanol.

2.1.1.3. Base source and additives

The bases used were sodium hydroxide (NaOH), sodium tetraborate (borax), and triethanolamine (TEOA). All the reactions were performed as described in section 2.1.1 using Brij C10:CTAB (1:5) as structuring agent. Reactions with borax were performed by replacing the second amount of NaOH by 10 mL of a 0.1 M borax solution (14 mmol). The reactions with TEOA were performed in two ways. In the first, the second addition of NaOH was replaced by 0.20 mL of TEOA (1.5 mmol), in this case, TEOA was the trigger of the reaction.

In the second, the procedure was carried out as described in section 1.1 using NaOH as the trigger, but in addition, TEOA (0.20 mL, 1.5 mmol) was added 1 or 10 minutes after NaOH.

2.1.1.4. Other parameters

The reaction temperature, stirring speed and gold precursor concentration were also studied on the Au@*m*SiO_2 synthesis reaction with Brij C10:CTAB (1:5). The temperatures studied were 50, 60, 70, and 80 ˚C. The stirring speeds were 400 and 600 rpm using always a 12 × 25 mm olive stir bar. $HAuCl_4$ gold precursor amounts were either1.05 and 0.5 mmol.

2.1.2. Synthesis of large-pores Au@*m*SiO_2

The synthesis of large-pore Au@*m*SiO_2 (*lp*-Au@*m*SiO_2), was accomplished using a two-step method: (1) the synthesis of small Au@*m*SiO_2 particles, approximately 50 nm in size, which serve as seeds, and (2) the growth of a large-pore silica shell (pore size >3 nm) on these seeds. This approach involved adapting two previously reported methods for synthesizing large-pore MSN to facilitate the growth of the Au@*m*SiO_2 seeds: using pore-expanding agents [2] and employing biphasic stratification [3].

2.1.2.1. Au@*m*SiO_2 seed synthesis

In a 250 mL round bottom flask, a mixture composed of CTAB (0.64 g, 1.8 mmol), water (100 mL), and ethanol (35 mL) was heated to 70 ˚C and stirred at 400 rpm using an olive stir bar (12 × 25 mm). $HAuCl_4$ (100 mM, 1.5 mL, 0.15 mmol) was added and the mixture was stirred for 5 minutes at 600 rpm. Afterwards NaOH (2.0 M, 0.20 mL) was added, and the solution was stirred for 15 min. Then, a solution of 0.25 mg Brij C10 in 3.4 mL water was added. After 10 minutes, TEOS (0.16 mL, 0.20 mL, 0.40 mL or 0.80 mL for x = 0.2, 0.25, 0.5, or 1 respectively) was added dropwise over 2 minutes immediately followed by NaOH

(2.0 M, 0.40 mL). 10 minutes later, a solution composed of 200 μL TEOA in 4.8 mL ethanol was added, and the reaction mixture was stirred for 16 h at 70 ˚C, 600 rpm. The detailed scheme of the protocol is presented in Figure 2.2.



Figure 2.2. Scheme of the protocol for the synthesis of Au@*m*SiO_2 seed particles. The modifications, denoted within the red box, reflect modifications to the process, specifically the amount of TEOS introduced. The variable *x* denotes the TEOS volume, where *x* values of 0.2, 0.25, 0.5, and 1 correspond to TEOS volumes of 0.16 mL, 0.2 mL, 0.4 mL, and 0.8 mL, respectively.

2.1.2.2. Growing using pore-expanding agents

A pore-expanding agent, 1,3,5-Triisopropylbenzene (TIPB), was utilized in varying amounts of 0 mL, 0.15 mL, 0.30 mL, 0.46 mL, 0.76 mL, or 1.5 mL (corresponding to y = 0, 0.2, 0.4, 0.6, 1, or 2, respectively), and added to a seed colloidal solution (140 mL) prepared using TEOS (x = 1). Subsequently, 0.8 mL of tetrapropyl orthosilicate (TPOS) (2.8 mmol) was added, and the reaction mixture was stirred at 400 rpm for 48 hours at 30 ˚C. These particles are denoted as *e*-Au@*m*SiO_2-*y* (*y* indicates the amount of TIPB: 0, 0.2, 0.4, 1.0 or 2).

Additionally, variations of this protocol were implemented using Au@*m*SiO_2 seeds synthesized with different amounts of TEOS (0.16 mL, 0.4 mL, or 0.8 mL, corresponding to x = 0.2, 0.5, or 1, respectively) while keeping TIPB constant (y = 2). These particles are denoted as *e*-*x*-Au@*m*SiO_2 (*x* indicates the amount of TEOS: 0.2, 0.5, or 1).

After 48 h of reaction, the *e*-Au@*m*SiO_2 particles were collected by centrifugation at 21 000 rpm (41 000 rcf) for 20 minutes. The resulting particles were washed with ethanol and centrifuged three times. Finally, the template was removed by calcination at 500 ˚C for 2 hours with a heating ramp of 10 ˚C/min. A detailed scheme of the protocol is presented in Figure 2.3.

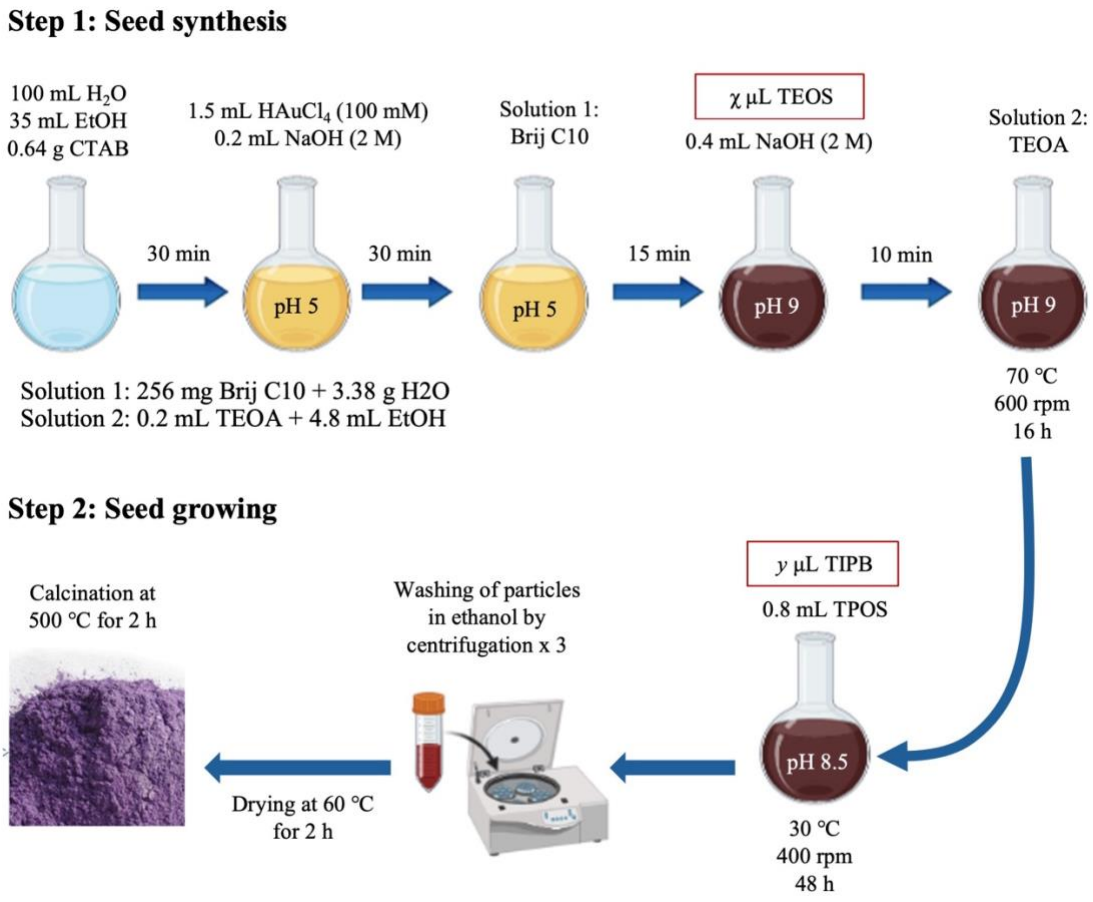

Figure 2.3. Scheme of the protocol for the synthesis of large-pore Au@*m*SiO_2 particles via growing using pore-expanding agents (*e*-Au@*m*SiO_2). The variations highlighted in the red box indicate the changes made to the process, which involve varying the amount of TEOS added in the seed synthesis (x = 0.2, 0.5, or 1 corresponding to 0.16 mL, 0.4 mL, or 0.8 mL respectively) and varying the amount of TIPB in the shell growth (y = 0, 0.2, 0.4, 0.6, 1 or 2 corresponding to 0 mL, 0.15 mL, 0.30 mL, 0.46 mL, 0.76 mL or 1.5 mL, respectively).

2.1.2.3. Growth using biphasic stratification

For the growth of the silica shell via biphasic stratification, four distinct methods were employed:

Method A

Sodium hydroxide (2.0 M, 0.70 mL) and CTAC (25wt. % solution, 45 mL, 34 mmol) were added to the seed solution. The mixture was stirred at 50 °C and 400 rpm for one hour. After adjusting the stirring speed to 250 rpm, a TEOS solution in cyclohexane (625 μL in 25 mL, 2.8 mmol) was added slowly (25 mL in 2 minutes) using a syringe to form a biphasic system. A condenser was adapted, then the reaction mixture was maintained at 50 °C with continuous stirring for 16 hours.

This method was applied to synthesize particles with varying amounts of TEOS during seed synthesis (0.16 mL, 0.2 mL, 0.4 mL, or 0.8 mL), corresponding to x = 0.2, 0.25, 0.5, or 1, respectively. A detailed scheme of the protocol is presented in Figure 2.4. These particles are denoted as *b*-Au@*m*SiO_2-*A* (*x* indicates the amount of TEOS: 0.2, 0.25, 0.5, or 1 and *A* denotes the method).

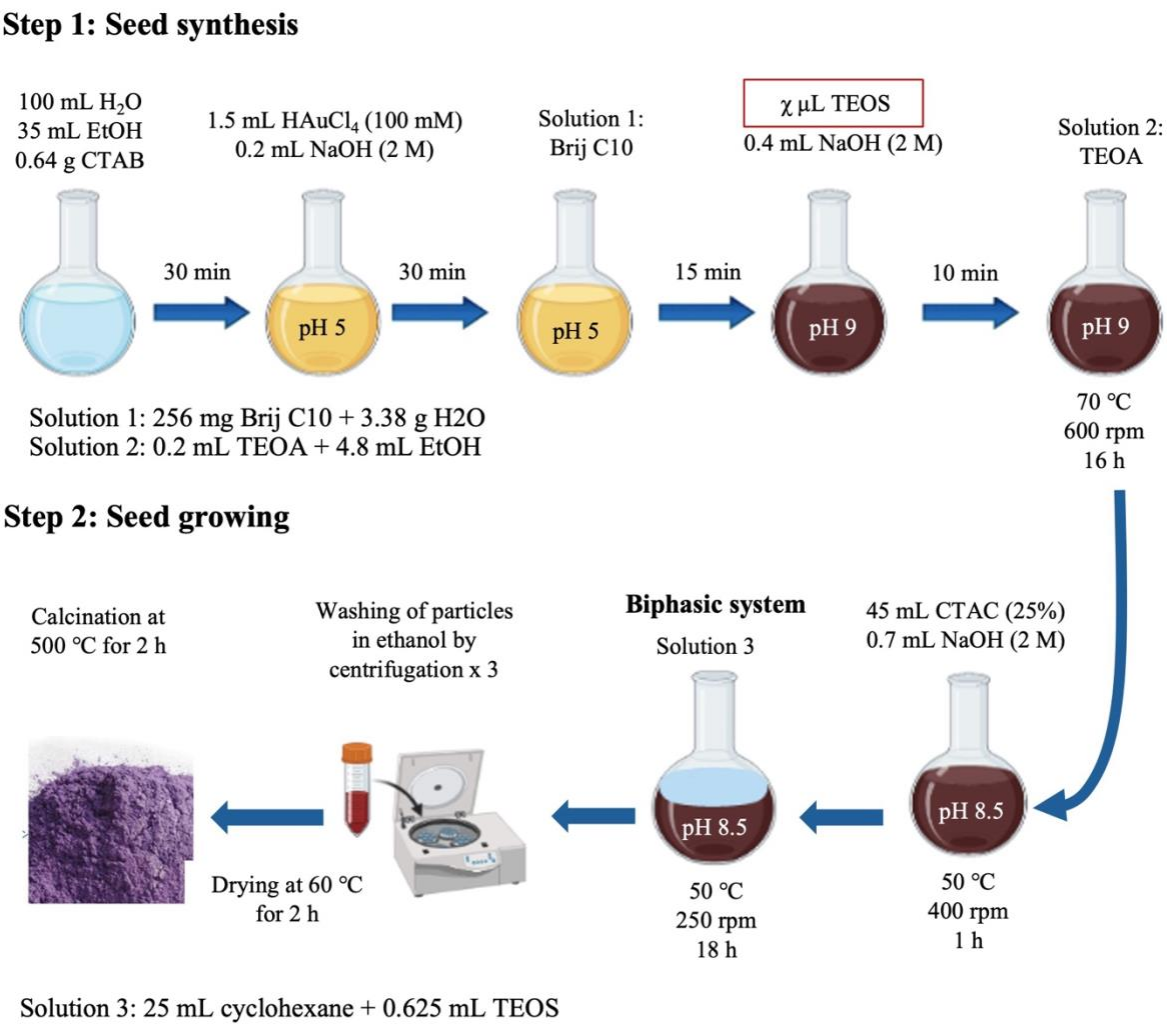

Figure 2.4. Scheme of the protocol for the synthesis of large-pores Au@mSiO$_2$ particles via biphasic stratification using Method A (*b*-Au@mSiO$_2$-*A*). The figure illustrates the variation in the amount of TEOS used during seed synthesis, with x = 0.2, 0.25, 0.5, or 1 corresponding to 0.16 mL, 0.2 mL, 0.4 mL, or 0.8 mL respectively.

Method B

Variations of Method A were conducted while utilizing the seeds synthesized with 0.16 mL TEOS (x = 0.2). The primary modification involved a reduction in the amount of TEOS used during the shell growth phase. Specifically, the volume of TEOS solution in cyclohexane was decreased by half to 312 µL in 25 mL (1.4 mmol).

A detailed schematic of this modified protocol is illustrated in Figure 2.5. The resulting particles were designated as *b*-Au@*m*SiO_2-*B* (*B* indicates the method used).

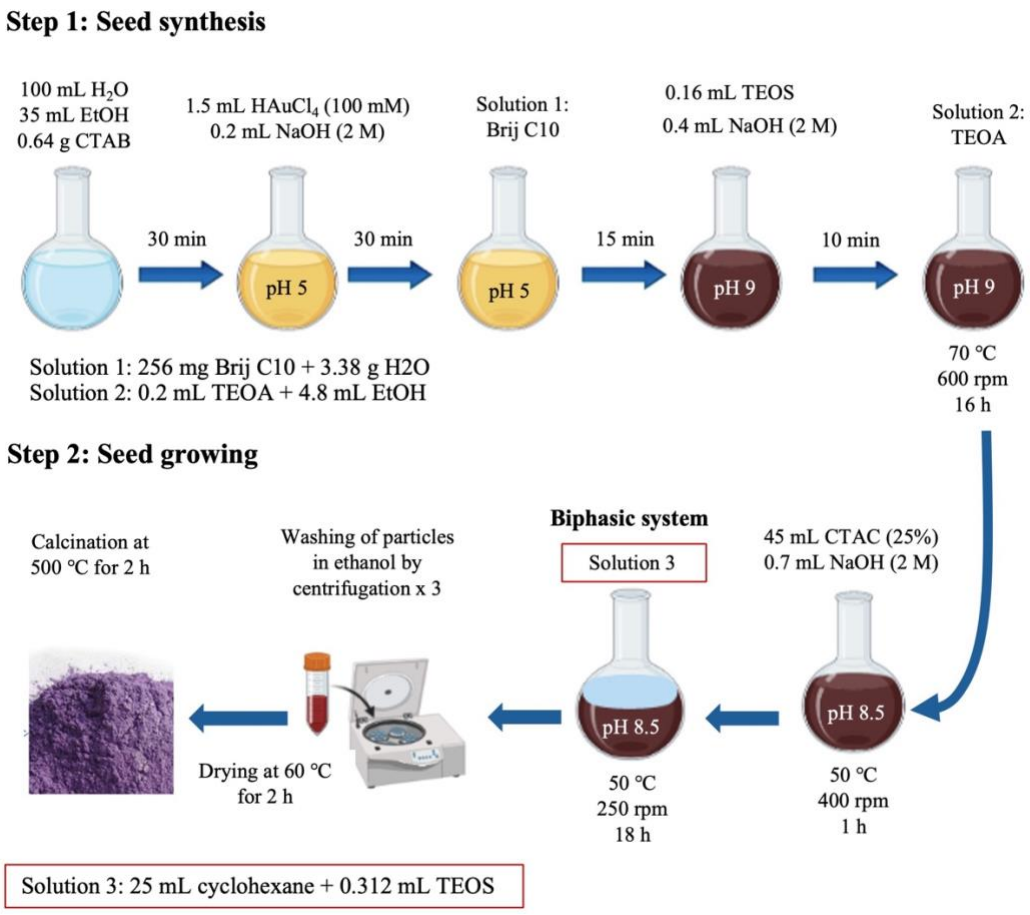

Figure 2.5. Scheme of the protocol for the synthesis of large-pores Au@*m*SiO_2 particles via biphasic stratification, using Method B (*b*-Au@*m*SiO_2-*B*). The figure highlights the modification in the amount of TEOS added during the shell growth phase, with 0.312 mL of TEOS solution in cyclohexane used instead of 0.625 mL.

Method C

This method involves two consecutive shell growth steps. The first shell growth was conducted as described previously, by adding a solution of TEOS in cyclohexane (625 µL in 25 mL, 2.8 mmol) to the seed solution synthesized with 0.16 mL of TEOS. The reaction was maintained at 50 °C with stirring at 250 rpm

for 16 hours. After this time, the upper cyclohexane phase was cautiously removed and replaced with a new TEOS in cyclohexane solution (625 µL in 25 mL, 2.8 mmol). The reaction mixture was then stirred at 250 rpm for an additional 12 hours to facilitate the growth of a second shell of mesoporous silica.

A detailed schematic of this protocol is provided in Figure 2.6. The resulting particles were designated as *b*-Au@*m*SiO_2-*C* (*C* indicates the method used).

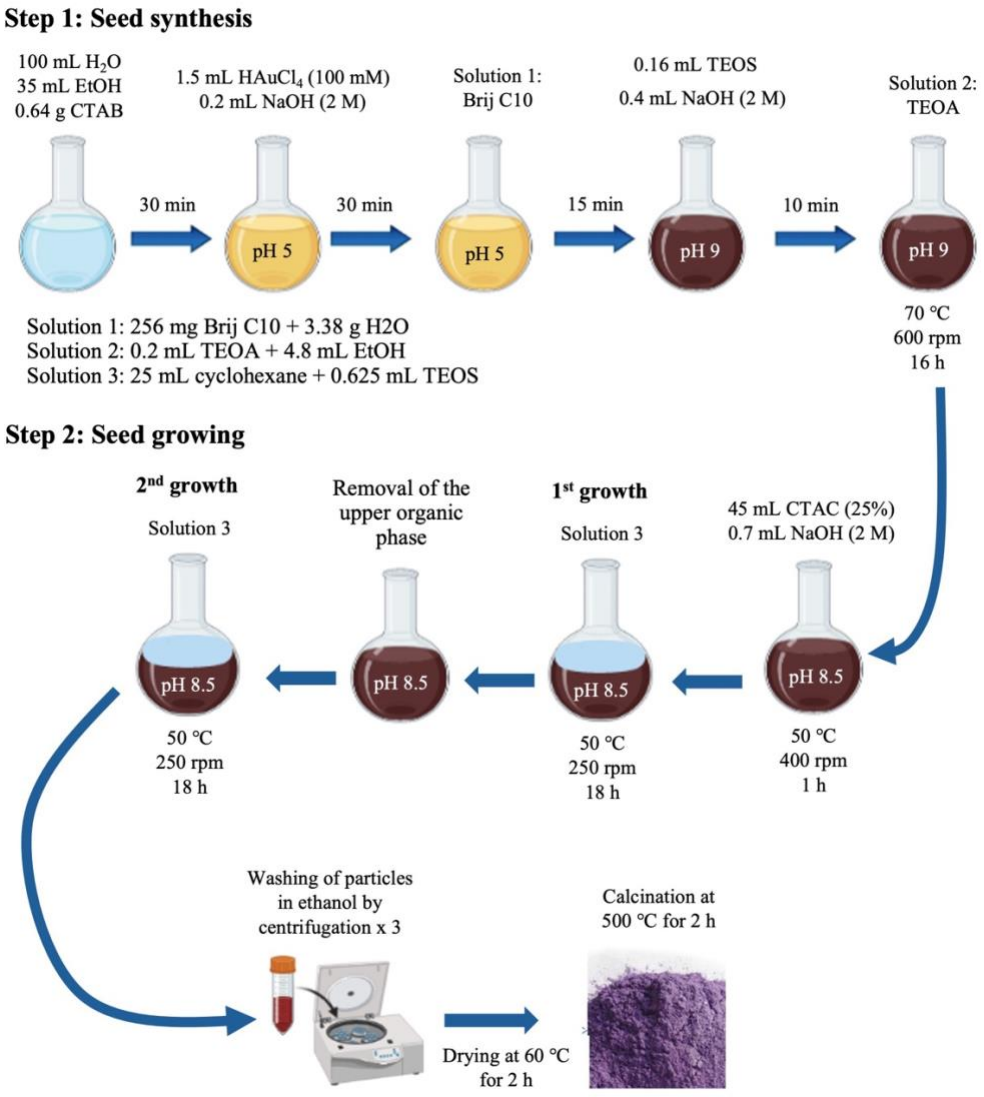

Figure 2.6. Scheme of the protocol for the synthesis of large-pores Au@*m*SiO_2 particles via biphasic stratification, using Method C (*b*-Au@*m*SiO_2-*C*). The figure illustrates the two consecutive shell growth steps involved in the process.

Method D

In this variation, the seed nanoparticles were isolated and washed prior to the silica shell growth. Seed nanoparticles synthesized with 0.16 mL TEOS (x = 0.2) were collected by centrifugation at 21 000 rpm (41 000 rcf) for 20 minutes and subsequently washed twice with ethanol. The seeds were then resuspended in 36 mL of water under sonication for 30 minutes.

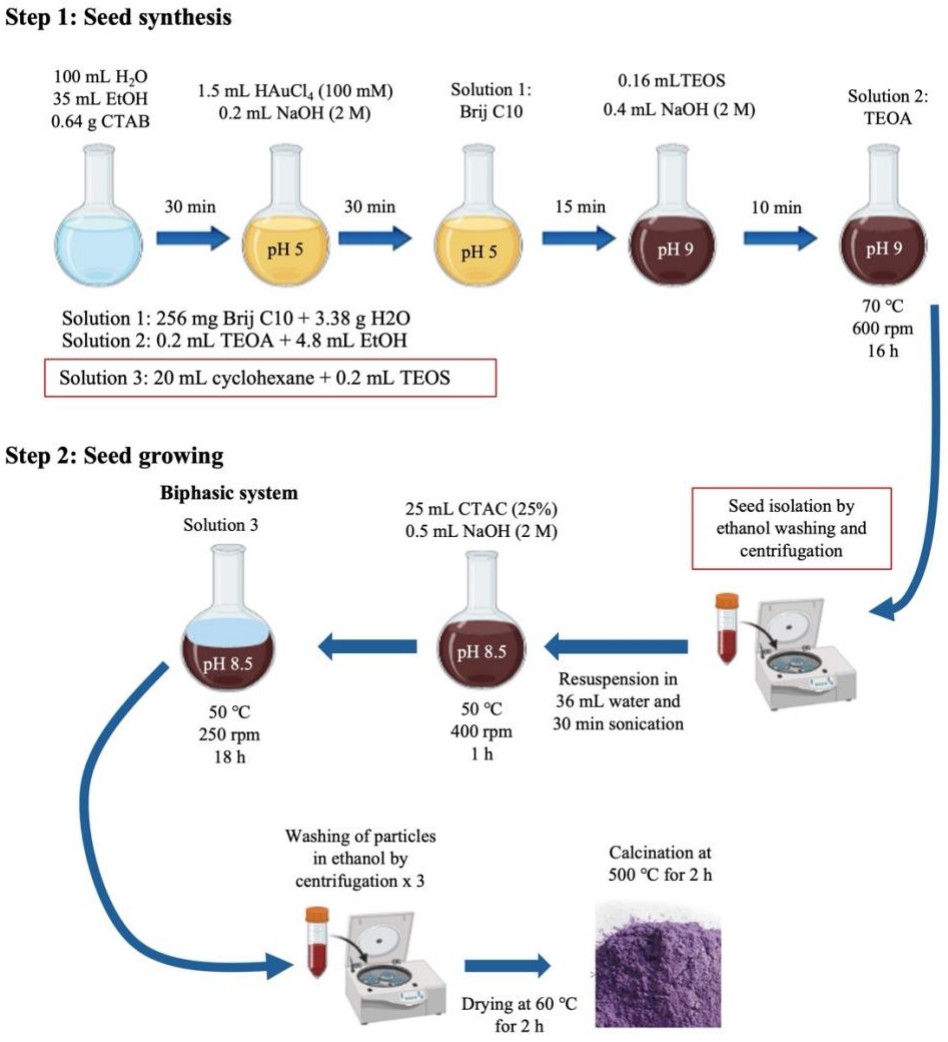

Figure 2.7. Scheme of the protocol for the synthesis of large-pores Au@mSiO$_2$ particles via biphasic stratification, using Method D (*b*-Au@mSiO$_2$-*D*). The figure illustrates the process of seed isolation and washing prior to the shell growth.

To this seed suspension, sodium hydroxide (2.0 M, 0.5 mL, 1.0 mmol) and CTAC (25% wt solution, 24 mL, 18 mmol) were added. The mixture was stirred at 400 rpm at 50 °C for one hour. The stirring speed was then reduced to 250 rpm, and a TEOS solution in cyclohexane (200 µL in 20 mL, 0.9 mmol) was added slowly to create a biphasic system. The reaction was maintained at 50 °C with stirring at 250 rpm for 16 hours.

A detailed scheme of the protocol is presented in Figure 2.7. These particles are denoted as *b*-Au@*m*SiO_2-*D* (*D* indicates the method used).

To collect the *b*-Au@*m*SiO_2 particles, the reaction solution was kept without stirring for 1 h, and the particles present in the underlying aqueous phase were collected by centrifugation at 21 000 rpm (41 000 rcf) for 20 minutes. The resulting *b*-Au@*m*SiO_2 particles were washed with ethanol and centrifuged three times. Finally, the template was removed by calcination at 500°C for 2 h with a heating ramp of 10 °C/min.

2.1.3. Synthesis of non-porous silica nanoparticles

Non-porous silica nanoparticles (SNP) were synthesized following a Stöber protocol [4] In a 250 mL round bottom flask, a mixture composed of absolute ethanol (70 mL), water (6 mL), ammonia solution (32%, 5.4 mL, 91 mmol), and TEOS (2.15 mL, 9.6 mmol) was stirred at 400 rpm using an olive stir bar (12 × 25 mm) at 30 °C for 2 h. The resulting silica particles were centrifuged at 7 000 rpm (7500 rcf) for 20 minutes, washed with ethanol three times and dried at 60 °C for 2 h to obtain nanoparticles powder.

2.1.4. Sample nomenclature

To facilitate the identification of particles synthesized using various methods, distinct codes were established. For particles synthesized with pore-expanding agents, the code ***e*-Au@*m*SiO$_2$** is used, while for particles synthesized via biphasic stratification, the code ***b*-Au@*m*SiO$_2$** is employed. The prefixes ***e*** and ***b*** denote the method used to obtain the large pores, ***e*** for pore-expanding and ***b*** for biphasic stratification. Table 2.3 provides a detailed overview of the nomenclature used.

Table 2.3. Codes of the synthesized Au@*m*SiO$_2$ particles

Code	**Growing method**	**Amount of TEOS in the seed synthesis (*x*)**	**Amount of TIPB in the growing (*y*)**	**Biphasic growing method (*A,B,C, or D*)**
sp-Au@*m*SiO$_2$	*One-pot* method	NA	NA	NA
e-Au@*m*SiO$_2$	Pore-expanding agents	ND	ND	NA
e-Au@*m*SiO$_2$-*y*	Pore-expanding agents	1	0, 0.2, 0.4, 1.0 or 2	NA
e-*x*Au@*m*SiO$_2$	Pore-expanding agents	0.2, 0.5, or 1	2	NA
b-Au@*m*SiO$_2$	Biphasic stratification	ND	NA	ND
b-*x*Au@*m*SiO$_2$-*A*	Biphasic stratification	0.2, 0.25, 0.5, or 1	NA	*A*
b-Au@*m*SiO$_2$-*B*	Biphasic stratification	0.2	NA	*B*
b-Au@*m*SiO$_2$-C	Biphasic stratification	0.2	NA	*C*
**b*-Au@*m*SiO$_2$-*D*	Biphasic stratification	0.2	NA	*D*

ND= not defined

NA= not applicable

*Denoted as *lp*-Au@*m*SiO$_2$ in Chapters 4 and 5

For *e*-*x*Au@*m*SiO$_2$, the variable ***x*** indicates the amount of TEOS used in the seed synthesis. For *e*-Au@*m*SiO$_2$-*y*, ***y*** represents the amount of TIPB utilized during the growth phase.

Similarly, for *b*-*x*Au@*m*SiO_2, ***x*** denotes the variation in the amount of TEOS used during seed synthesis, and the suffixes ***A***, ***B***, ***C***, or ***D*** specify the biphasic stratification method employed.

2.2. Particles characterization

2.2.1. Electron Microscopy for imaging

Electron microscopy uses an accelerated electron beam which, upon impact with the sample, generates a series of signals directly related to the structure of the object under investigation. The transmitted or scattered electrons are detected, and the signal is processed to form images, through which the structure of the material, size and distribution of particles, interfaces, etc. can be resolved [5].

In this thesis, two variants of electron microscopes were used: Scanning Electron Microscope (SEM) and Transmission Electron Microscope (TEM).

2.2.1.1. Scanning electron microscopy

A Field Emission Scanning Electron Microscope (FE-SEM) Zeiss Gemini ULTRA plus was used (Institute Néel, France and CMA, UBA). For the analysis of Au@*m*SiO_2 particles, the microscope was operated at 10.0 kV at a working distance of 7 mm. For the analysis of non-porous particles, the microscope was operated at 3 kV at a working distance of 3 mm. A dilute particle suspension (3 µL) was dried on a doped silicon wafer for observation. The micrographs obtained were analyzed with the ImageJ software. The mean particle size and standard deviation were determined on approximately 100 particles.

2.2.1.2. Transmission Electron Microscope

TEM micrographs were recorded using a Philips CM300 electron microscope operating at 300 kV (Institute Néel, France). One drop of a dilute nanoparticle suspension in ethanol was deposited on a carbon coated copper grid then dried for observation. The estimated size of the particles as well as the dimensions of the silica shells and gold nanoparticles were calculated using the Image J software.

2.2.2. Dynamic Light Scattering

Dynamic light scattering (DLS) is a technique that analyzes temporal fluctuations in the intensity of light scattered by a laser impinging on a particle suspension. These fluctuations contain information about the dynamics of the particles in the medium at a given temperature and viscosity, so that by using appropriate mathematical models and settings, the diffusion coefficient of the particles in the medium can be obtained, from which the hydrodynamic diameter of the particles can be calculated [6].

DLS measurements were conducted on a VASCO Kin™ (Institute Néel, France) or a Zetasizer Malver (LNLS, Brazil) instrument at 25 °C. Samples were prepared by suspending the calcined particles in water at an approximate concentration of 1% (m/v). The hydrodynamic diameter of the particles was calculated using the Stokes-Einstein equation, based on the cumulant fit using the integrated software package.

2.2.3. ζ-potential

The ζ-potential of a particle suspension is the potential difference between the medium and the stationary fluid layer attached to the dispersed particle. This potential is not measured directly but is calculated based on theoretical models and experimentally determined electrophoretic mobility. The ζ-potential provides insight into the magnitude of the charge within the double layer surrounding the particles, which affects the stability of the colloidal system. A high ζ-potential indicates significant electrostatic repulsion between particles, thereby reducing aggregation and contributing to system stability. Generally, a ζ-potential of ±25 mV is used as an empirical threshold to distinguish between stable and unstable colloidal systems [6].

ζ-potential measurements were conducted on a Cordouan VASCO Kin™ instrument (Institute Néel, France) at 25 °C. Samples were prepared by suspending the calcined particles in a 10 mM phosphate buffer solution at an approximate particle concentration of 1% (m/v). To assess the ζ-potential as a function of pH, particles were suspended in 10 mM acetate buffer for pH values ranging from 2.2 to 5, and in 1.0 mM phosphate buffer for pH values between 6 and 7.4.

2.2.4. Atomic Force Microscopy

Atomic Force Microscopy (AFM) is a high-resolution imaging technique widely used to characterize the surface topography of particles at the nanoscale. By utilizing a sharp probe that scans across the sample's surface, AFM provides detailed information on particle size, shape, and surface structure.

AFM measurements were performed in collaboration with Lia Pietrasanta and Silvio Ludueña (CMA, UBA) on a Bruker Dimension AFM-STM DI-VEECO

MMAFM NANOSCOPE IIIA (Bruker Nanosurface Division, USA) operating in a tapping mode in air. Particles were dispersed in water (1 mg/mL). After sonication for 60 min, the suspension was allowed to sediment to separate the aggregated particles. The particles suspension was used for drop-casting on a silicon wafer (10 × 10 mm) to form a particle monolayer. For drop-casting, a humidity control chamber (70%) was used. 7 μL of particle suspension were deposited on a silicon wafer held in a vertical position then left to dry overnight. The samples were imaged at room temperature using NANOWORLD silicon probes (type SSS-NCH) with a tip radius of curvature of 2 nm. Particle features, including diameter, pore size, and heights, were analyzed from the micrographs using the Gwyddion software [7].

2.2.5. UV-visible spectroscopy

When a beam of UV-Vis light is incident on gold nanoparticles, the light interacts with the conduction electrons on the nanoparticle surface, causing them to oscillate collectively, a phenomenon known as surface plasmon resonance (SPR). This interaction leads to both absorption and scattering of light, with the absorbed energy manifesting as a characteristic SPR peak in the UV-Vis spectrum, typically around 520-550 nm. The extent of absorption and scattering depends on the nanoparticle size, shape, and environment, such as the presence or not of asilica shell.

For most experiments a spectrophotometer with double monochromator and photomultiplier detection (UV3101PC Shimadzu) was used. For measurements with lower spectral resolution, an Ocean Optics fibre-optic equipment with diode array detection was used. Measurements were performed at room temperature in the spectral range λ = 200- 800 nm.

2.2.6. Infrared spectroscopy

Infrared spectroscopy provides information on the presence of organic and inorganic functional groups. In this work it was used to check the removal of the surfactant (template) after calcination of the particles. FTIR spectra were measured using a Thermo Fisher Nicolet™ iN™10 spectrometer in transmission mode on KBr pellets obtained with 0.5 mg of nanoparticles pressed within 140 mg of potassium bromide. The spectra were recorded at a resolution of 4 cm^{-1}.

2.2.7. Nitrogen sorption

Nitrogen (N_2) sorption is a technique used to characterize porous materials by measuring the amount of nitrogen gas adsorbed and desorbed at low temperatures and varying pressures. The sample is first degassed to remove impurities, then exposed to nitrogen gas at liquid nitrogen temperatures (77 K). Adsorption and desorption isotherms are generated by tracking the volume of gas absorbed at different pressures. These isotherms are analyzed using the BET method to determine surface area, the BJH method for pore size distribution, and to calculate the total pore volume, providing a detailed understanding of the material's porosity without altering the sample.

N_2 sorption measurements were performed on a Micromeritics Tristar 3000 apparatus at 77 K at the Institut Charles Gerhardt, Montpellier in collaboration with Prof Philippe Trens. Prior to the measurement, the calcined particles were degassed for 12 h at 80 °C under vacuum, 10^{-5} Torr. Langmuir-specific surface area calculations were carried out using the BET model within the range of $0.05 < p/p^{\circ} < 0.25$. The pore size from the adsorption branch was calculated using the BJH method.

The geometry of the mesopores was assessed using the Gurwich method, which is sensitive in the case of rigid cylindrical pores. In this case, the pore

diameter is estimated as D = 4V/S where V is the mesopores volume and S the specific surface area of the material.

2.2.8. Photothermal conversion

The ability of the Au@*m*SiO_2 particles to dissipate heat was analyzed by irradiating a stirred colloid suspension by a collimated laser beam (2.3 mm in diameter) at a wavelength of 532 nm. A Au@*m*SiO_2 particle suspension (1.0 mg/mL) was formed by suspending 18.0 mg of calcined *sp*-Au@*m*SiO_2 synthesized with Brij C10:CTAB (1:5) in 18.0 g of water by sonication. A quartz cuvette was filled with 2.0 mL of colloid, and a small magnetic stir bar was added. The mixture was kept under stirring while light (Spectra Physics Millenia 532 nm CW, 0-800 mW) was shined from the top of the cuvette for 8 minutes, then the laser was turned off. The temperature was monitored using a digital thermometer with a type K probe.

2.3. Methods used to study synthesis mechanisms

2.3.1. CMC Determination

The CMC of CTAB was determined by conductimetry under the conditions used in the synthesis of *sp*-Au@*m*SiO_2. A solution of 5 mM CTAB solution was prepared by dissolving CTAB (36 mg, 0.10 mmol) in 20 mL of a solution of NaOH (8.6 mM) in 28% ethanol-water (made of 178 mL H_2O, 72 mL Ethanol and 86 mg NaOH). The solution temperature was set to 70 °C, and the conductivity was measured using a Mettler Toledo FiveEasy Plus conductimeter. Increasing

amounts of the water-ethanol-NaOH solution were added and the conductivity was measured at different concentrations of CTAB. The CMC is determined by plotting the measured conductivity values in function of the corresponding CTAB concentrations and corresponds to the concentration at which the conductivity plot shows a distinct change in slope, indicating the onset of micelle formation.

2.3.2. TEOS hydrolysis kinetics analysis

The TEOS hydrolysys kinetics was analized by monitoring the pH of the reaction over the first minute after triggering the reaction with NaOH. This is base on the premise that under basic conditions, the hydrolysis rate increases linearly with the hydroxide concentration [8]. To study the effect of surfactants, co-surfactants, and additives on the kinetics of TEOS hydrolysis, the pH of the reaction for the *one-pot* synthesis of *sp*-Au@*m*SiO_2 was monitored over the first minute after triggering the reaction with NaOH.

The conditions for studying each system are detailed below.

2.3.2.1. Effect of CTAB on TEOS hydrolysis kinetics

Two separate reaction vessels were prepared with the following components: H_2O (100 mL), EtOH (40 mL) and NaOH (2.0 M, 600 µL). CTAB (0.64 g) was added to one of the reaction vessels. Both solutions were stirred at 600 rpm and heated to 70 ˚C. A pH electrode was introduced into each solution to reach stabilization of the initial pH. Subsequently, TEOS (1.0 mL) was added at t = 0 s. The pH of each solution was recorded over the initial minutes following the addition of NaOH, and the hydrolysis kinetic curve was obtained by graphing pH as a function of time.

2.3.2.2. Effect of Brij C10 in TEOS hydrolysis kinetics

Two separate reaction vessels were prepared with the following components: H_2O (100 mL), EtOH 40 mL), NaOH (2.0 M, 600 µL) and CTAB (0.64 g). Brij C10 (0.25 g) was added to one of the reaction vessels to achieve a Brij C10:CTAB ratio of 1:5. Both solutions were stirred at 600 rpm and heated to 70 °C. A pH electrode was introduced into each solution to reach stabilization of the initial pH. Subsequently, TEOS (1.0 mL) was added to each reaction vessel. The pH of each solution was recorded over the initial minutes following the addition of NaOH, and the hydrolysis kinetic curve was obtained by graphing pH as a function of time.

2.3.2.3. Effect of isopropanol in TEOS hydrolysis kinetics

Two separate reaction vessels were prepared with the following components: H_2O (100 mL), NaOH (2.0 M, 600 µL), CTAB (0.64 g) and Brij C10 (0.25 g). Ethanol (40 mL) was added to one vessel, while isopropanol (IPA, 40 mL) was added to the other. Both solutions were stirred at 600 rpm and heated to 70° C. A pH electrode was introduced into each solution to reach stabilization of the initial pH. Subsequently, TEOS (1.0 mL) was added to each reaction vessel. The pH of each solution was recorded over the first minutes following the addition of NaOH, and the hydrolysis kinetic curve was obtained by graphing pH as a function of time.

2.3.2.4. Effect of triethanolamine in TEOS hydrolysis kinetics

Two separate reaction vessels were prepared with the following components: H_2O (100 mL), ethanol (40 mL), NaOH (2.0 M, 600 µL), CTAB (0.64 g)

and Brij C10 (0.25 g). Triethanolamine (TEOA) (200 µL) was added to one of the reaction vessels to achieve a Brij C10:CTAB:TEOA ratio of 1:5:4. Both solutions were stirred at 600 rpm and heated to 70 ˚C. A pH electrode was introduced into each solution to reach stabilization of the initial pH. Subsequently, TEOS (1.0 mL) was added to each reaction vessel. The pH of each solution was recorded over the initial minutes following the addition of NaOH, and the hydrolysis kinetic curve was obtained by graphing pH as a function of time.

2.3.3. Monitoring the Au@*m*SiO_2 precursor state formation by UV-vis spectroscopy

To study the precursor state formation in the *sp*-Au@*m*SiO_2 synthesis, UV-vis spectra were measured at different steps of the reaction (See Figure II-1). All reactions were conducted in a final volume of 3 mL, at 70 ˚C with stirring at 400 rpm. Aliquots of 200 µL were measured in a 1 mm path length quartz cuvette using a Shimadzu UV3101 spectrophotometer.

2.3.3.1. Reaction mixture at Step 0

The spectrum of $HAuCl_4$ in the synthesis conditions but without CTAB was measured. A solution composed of H_2O (2.14 mL), ethanol (0.86 mL), and $HAuCl_4$ (100 mM, 32 µL) was prepared, heated to 70 ˚C, and stirred at 400 rpm. The pH of the reaction was monitored with pH strips and was 3.

2.3.3.2. Reaction mixture at Step 1

A stock solution containing: H_2O (35 mL), ethanol (15 mL), and CTAB (0.22 g) was prepared. In a 5 mL glass vial, 2.9 mL of the stock solution was added, along with $HAuCl_4$ (100 mM, 32 µL). The pH at this point was 3.3.

2.3.3.3. Reaction mixture at Step 2

A stock solution containing: 35 mL of H_2O, 15 mL of ethanol, and 0.224 g of CTAB was prepared. In a 5 mL glass vial, 2.9 mL of the stock solution was added, along with 32 μL of $HAuCl_4$ (100 mM) and 4.2 μL NaOH (2 M). The pH at this point was 5.

2.3.3.4. Reaction mixture at Step 3

A stock solution containing: H_2O (35 mL), ethanol (15 mL), and CTAB (0.22 g) was prepared. In a 5 mL glass vial, 2.9 mL of the stock solution was added, along with $HAuCl_4$ (100 mM, 32 μL), NaOH (2.0 M, 4.2 μL) and TEOS (21 μL). The pH at this point was 5.

2.3.3.5. Reaction mixture containing Brij C10 at Step 3

To analyze the effect of Brij C10 on the AuNP formation, two stock solutions were prepared: one containing H_2O (35 mL), ethanol (15 mL), and CTAB (0.22 g), and Brij C10 (0.089 g), and another identical solution without Brij C10. In two separate 5 mL glass vials, 2.9 mL of the stock solution without Brij C10 was added to one vial, and 2.9 mL of the stock solution with Brij C10 was added to the second vial. Then, $HAuCl_4$ (100 mM, 32 μL), NaOH (2.0 M, 4.2 μL), and TEOS (21 μL) were added to each vial. The pH in both reaction mixtures was 5.

2.3.4. Monitoring Au@*m*SiO_2 formation by SEM

To track the formation of *sp*-Au@*m*SiO_2 throughout the reaction, samples were periodically collected at various time points after initiating the reaction with a base. At each time point, a 200 μL aliquot of the reaction mixture was transferred to an *Eppendorf* tube containing a silicon wafer. The aliquots were

then rapidly frozen in liquid nitrogen to halt the reaction and subsequently freeze-dried.

The silicon wafer containing the freeze-dried sample was used for SEM analysis. The micrographs obtained were analyzed with the ImageJ software. The particle size analysis was performed on approximately 50 particles.

2.3.5. pH monitoring of the synthesis of Au@*m*SiO_2

The pH was monitored throughout the reaction duration by conducting the synthesis in a three-necked balloon. Before adding the NaOH trigger, the electrode of the pH meter (Adwa, AD11) was inserted into one of the necks of the balloon, and the pH was recorded. Approximately every 5 minutes, the electrode was immersed in 150 mM PBS buffer, pH 7.0, to check correct calibration. The pH values were transferred every second to a computer for further processing.

2.4. Protein loading protocols

The loading capacity of particles was evaluated using three model proteins: Bovine serum albumin (BSA), Horseradish peroxidase (HRP), and the fluorescent protein mCherry. BSA and HRP were purchased from Sigma Aldrich (product numbers B2518, and P8375 respectively) and were suspended in phosphate buffer, 10 mM, pH 7, to achieve a concentration of 10 mg/mL. The *m*Cherry recombinant protein was obtained and purified at the Instituto de Biociencias, Biotecnología y Biología Traslacional (IB3, UBA).

2.4.1. *m*Cherry expression and purification

*m*Cherry, a recombinant protein also known as *Discosoma coral* red fluorescent protein (DsRed), is a mutant version of a Green Fluorescent Protein (GFP)-like protein originally cloned from the reef coral *Discosoma*. This protein is characterized by a prominent emission maximum at 616 nm, making it useful for various fluorescent applications [9, 10].

Recombinant proteins, such as *m*Cherry, are produced from recombinant DNA sequences that have been engineered or isolated from an organism and subsequently expressed in a different host organism. The process of producing recombinant proteins generally involves several critical steps: cloning the gene of interest into an expression vector, transforming the vector into a suitable host organism, inducing the expression of the recombinant protein, and finally, purifying the protein to obtain it in a usable form.

In this study, the *m*Cherry protein was produced starting from an expression vector that had already been cloned with the *m*Cherry coding DNA. *Escherichia coli* DH5α bacteria were transformed by heat shock with the ampicillin-resistant vector pBAD_mCherry that was a gift from Robert Campbell & Michael Davidson & Roger Tsien (Addgene plasmid # 54667) [11, 12]. The protein gene was under an arabinose-induced promoter and included an *N*-terminal histidine tag for purification. Transformed colonies were stored in 30% glycerol at -80 ˚C (UltraFreezer Righi, Argentina). Plasmid incorporation was confirmed by MiniPrep, followed by agarose gel electrophoresis.

For protein purification, transformed DH5α bacteria were inoculated in pre-cultures of 10 mL LB medium with 50 μg/mL ampicillin and were grown overnight at 37 ˚C with agitation (220 RPM, Thermo Scientific MaxQ6000, Massachusetts, USA). The next day the preculture was added to a 2 L Erlenmayer flask containing 500 mL LB medium with 50 μg/mL ampicillin and was grown at 37 ˚C with agitation (220 RPM) until OD600 of 0.6 was reached. Protein expression was induced with 2 g of solid arabinose (final concentration 0.4%) and the mixture

was incubated overnight at 18 ˚C with agitation (220 RPM). Bacteria were harvested the following morning by centrifugation at 5,000 RPM and 4 ˚C in 200 mL flasks (Beckman J-14 rotor, Indiana, USA). The obtained pellet -of characteristic bright magenta color- was resuspended in 25 mL of 100 mM sodium phosphate buffer pH 7.6, with 1% Triton X-100, 10 mM imidazole, and 0.5 mM PMSF protease inhibitor, and kept on ice. The suspension was sonicated on ice for 10 minutes in 10''/30'' ON/OFF cycles at 35% amplitude (Sonics Vibra-cell, Connecticut, USA). The lysate was centrifuged twice at 20,000 RPM (Beckman J-20 rotor, Indiana, USA). The obtained pellet lost the magenta color indicating the absence of folded *m*Cherry protein therein. The resulting supernatant, containing soluble *m*Cherry, was eluted through a 3 mL NTA-nickel His-trap resin column previously equilibrated with sodium phosphate buffer pH 7.6, 20 mM imidazole. The resin turned intense magenta, indicating *m*Cherry binding, while the eluted supernatant remained transparent. The column was eluted using an imidazole gradient, with fractions collected at 20 mM, 50 mM, 100 mM, 250 mM, 400 mM, and 600 mM imidazole. The fractions were kept on ice and analyzed by UV absorption at 280 nm (protein absorption) and 585 nm (*m*Cherry absorption maximum). Protein purity was assessed with a 16% SDS-PAGE (90 V stacking, 160 V running) stained by Coomassie blue. Pictures of the gels were obtained with a gel documentation system (InGenius 3, Syngene, UK). Fractions containing *m*Cherry were dialyzed overnight in sodium phosphate buffer pH 7.6. The next day, the purified protein was centrifuged at 15,000 RPM (220.87 rotor, Hermle, Germany), and an absorption profile was measured using a UV-Vis spectrophotometer (Jasco, Japan). Quantified protein and a dialyzed buffer aliquot were stored in 2 mL Eppendorf tubes at -20˚C. For lyophilization, the protein was frozen inside Eppendorf tubes and placed inside the freeze dryer (Biobase, China). Prior to use in particle loading, 2 mg/mL stock solutions were prepared by suspending the lyophilized powder in 10 mM phosphate buffer.

2.4.2. Protein loading on nanoparticles

Protein loading was performed on three types of particles: *sp*-Au@*m*SiO_2, *lp*-Au@*m*SiO_2, and non-porous particles. The *sp*-Au@*m*SiO_2 particles were synthesized according to the protocol detailed in Section 2.1.1, utilizing a BrijC10:CTAB:TEOS:$HAuCl_4$ molar ratio of 1:5:12.8:0.42:3.4. The *lp*-Au@*m*SiO_2 particles were prepared via biphasic stratification with seed isolation and washing, as described in Section 2.1.3.3.4 (Method D). SNPs were synthesized as outlined in Section 2.1.4. Calcined particles were suspended in water at a concentration of 10 mg/mL, sonicated for 30 minutes, and subsequently filtered through 0.8 μm syringe filters (Minisart® NML, Sartorius) to eliminate aggregates.

For BSA and HRP, 0.2 mL of protein stock solution (10 mg/mL) was combined with 0.4 mL of *sp*-Au@*m*SiO_2, *lp*-Au@*m*SiO_2, or SNP suspensions, 0.15 mL of 100 mM phosphate buffer (PB), and 0.75 mL of MilliQ water in Eppendorf tubes. For *m*Cherry loading, 50 μL of protein stock solution (2 mg/mL) was mixed with 0.2 mL of the particle suspensions, 50 μL of 100 mM PB, and 0.2 mL of MilliQ water. The mixtures were incubated at 25 °C with agitation (400 rpm, Eppendorf shaker) for 2 hours.

Following incubation, protein-loaded particles were collected by centrifugation (12 000 rpm (20130 rcf), 10 min, 4 °C). The supernatants were reserved for protein quantification. The particle pellets were resuspended in 0.2 mL of water and subjected to three washing cycles, each involving centrifugation under the same conditions. Supernatants from each wash were collected for subsequent protein quantification.

2.4.2.1. Protein quantification

The concentration of adsorbed BSA and HRP on the particles was determined via absorbance measurements. Calibration curves were established for BSA by preparing a series of standard solutions, followed by absorbance

readings at 280 nm using a Nanodrop spectrophotometer (ThermoFisher). The protein concentration in the supernatant was calculated using the BSA calibration curve. For HRP quantification, the protein concentration in the supernatant was determined at 403 nm, utilizing an extinction coefficient of 102 mM^{-1} cm^{-1} for the native enzyme state [13].

For *m*Cherry, protein concentration was quantified via fluorescence spectroscopy. Calibration curves for *m*Cherry were generated, and fluorescence measurements were taken at an emission wavelength of 600 nm, with excitation at 574 nm, using a TECAN Spark fluorimeter. The concentration of *m*Cherry in the supernatant was derived from the calibration curve.

The amount of protein adsorbed onto the particles was calculated by subtracting the protein concentration in the supernatant from the initial total protein concentration added to the suspension. This value was then normalized to the number of particles in the suspension, yielding the amount of protein adsorbed per particle.

2.4.3. HRP enzymatic activity

Enzymatic activity is defined as the rate at which a substrate is converted into a product under specific pH and temperature conditions. The activity is assay-dependent, and the kinetics of the enzyme can be studied by monitoring product formation over time, allowing for the determination of substrate affinity and other kinetic parameters. Typically, enzyme-catalyzed reactions initially exhibit a linear relationship between substrate conversion and time, from which the reaction rate is derived. However, as the substrate is depleted, the reaction rate decreases and eventually stops. Therefore, kinetic constants should be derived from the linear portion of the reaction progress curve.

In this study, HRP enzymatic activity was quantified by measuring the oxidation of 2,2′-azino-bis(3-ethylbenzothiazoline-6-sulfonic acid) (ABTS), which produces a colored product with a maximum absorbance at 420 nm. The activity

of both free and adsorbed HRP on *lp*-Au@*m*SiO_2 particles was determined using UV-Vis spectroscopy by monitoring the absorbance of oxidized ABTS (0.5 mM) at 420 nm ($\varepsilon = 36 \times 10^3\ M^{-1}\ cm^{-1}$) at 25 °C. Citrate-phosphate buffers (McIlvaine's buffer) were used, prepared with citric acid and potassium phosphate monobasic (Merck) across a pH range of 2 to 8.

For the activity assays of adsorbed HRP, HRP-loaded particle pellets were resuspended in 0.5 mL water. A 10-fold diluted solution was prepared for measuring the activity of free HRP at a concentration of 0.1 mg/mL. The enzymatic reactions were conducted in 96-well microplates, where each well contained 5 µL of HRP sample, 190 µL of buffer, and 5 µL of 3% hydrogen peroxide. Absorbance measurements were taken immediately over time using an Epoch microplate spectrophotometer (BioTek, Agilent). One unit of enzymatic activity was defined as the amount of enzyme required to transform 1 µmol of ABTS per minute under the specified pH and temperature conditions [14].

2.4.4. Energy filtering transmission electron microscopy for protein visualization

Energy-filtered transmission electron microscopy (EFTEM) is a powerful technique for mapping the spatial distribution of elements, such as carbon and silicon, within a sample at high resolution. By applying an energy filter to the transmitted electrons, EFTEM selectively images electrons that have lost specific amounts of energy due to inelastic scattering by particular elements. This allows for the generation of element-specific images, here the nanoscale distribution of carbon or silicon within the sample [15].

For EFTEM analysis, pellets of *lp*-Au@*m*SiO_2 and *sp*-Au@*m*SiO_2 particles (1 mg) loaded with proteins were used. The pellets were resuspended in 0.5 mL of water, and a 10-fold diluted solution was prepared for imaging. Additionally,

particle samples without protein contact were analyzed as controls. A 3 µL aliquot of each sample was applied to copper grids (Lacey-carbon #01895), with excess liquid removed before vitrification by immersion in liquid ethane. Approximately 10 micrographs were acquired using a JEOL1400 microscope, and carbon and silicon maps were generated by processing the micrographs with the DigitalMicrograph software.

2.4.5. Circular dichroism of adsorbed proteins

Circular dichroism (CD) spectroscopy is a valuable technique for evaluating the stability of proteins by monitoring changes in their secondary structure under various conditions, such as temperature variations or exposure to chemical denaturants. CD measures the differential absorption of left- and right-handed circularly polarized light by the chiral amino acids within a protein. This results in a spectrum that reflects the protein's secondary structure, including alpha-helices and beta-sheets. By analyzing how the CD spectrum changes with temperature, the melting temperature (*Tm*) of the protein can be determined. *Tm* represents the temperature at which the protein begins to unfold, providing a quantitative measure of its stability [16].

For the CD measurements, pellets of *lp*-Au@*m*SiO_2 and *sp*-Au@*m*SiO_2 particles (1 mg) with and without adsorbed proteins, were resuspended in 0.2 mL of 10 mM phosphate buffer. The CD spectra of these particle suspensions, along with the phosphate buffer and protein solutions, were measured under the same conditions using a quartz cuvette (path length of 0.5 mm, Hellma Analytics) on a circular dichroism spectrophotometer (Olis DSM20 with xenon arc lamp) at the Cedro beamline of the Brazilian Synchrotron Light Laboratory (LNLS - Sirius). Spectra were obtained across the wavelength range of 185–280 nm. Six continuous scans were performed for each sample, and the measurements were conducted in triplicate, with the mean values used for analysis.

The CD spectra were corrected for solvent and particle contributions and expressed in units of mean residue ellipticity (deg cm^2 $dmol^{-1}$), based on the protein concentration and the number of amino acid residues in each protein. For thermal stability tests, the temperature was varied from 20 °C to 90 °C in 5 °C increments. Quantitative analysis of secondary structure was performed using the BeStSel™ software (2014-2024, ELTE Eötvös Loránd University, Budapest, Hungary). This software decomposes the CD spectrum into eight secondary structural elements: regular and distorted α-helix, left-twisted, relaxed, and right-twisted anti β-strand, parallel β-strand, turns, and other structures [17]. For clarity, the percentage values of regular and distorted α-helix were combined to provide the total α-helix content, while left-twisted, relaxed, right-twisted anti β-strands, and parallel β-strands were summed to yield the total β-strand content.

2.5. Nanoparticles stability

2.5.1. Stability of Au@*m*SiO_2 nanoparticles

The stability of Au@*m*SiO_2 particles under conditions that simulate physiological environments was assessed by monitoring their morphology over time. A 5 mg/mL suspension of was prepared by sonicating a mixture of calcined Au@*m*SiO_2 particles in water for 30 minutes. This suspension was then diluted to achieve final concentrations of 1 mg/mL and 0.1 mg/mL in 137 mM phosphate buffer saline (PBS 1×). The particle suspensions were incubated at 37 °C. At various time points, aliquots of 5 μL were taken, diluted with 100 μL of ethanol, and subsequently dried on silicon wafers for SEM analysis. The particle size analysis was performed on approximately 50 particles.

2.5.2. Stability of nanoparticles in the presence of proteins

The stability of the particles in the presence of proteins in a simulated physiological medium was evaluated by observing changes in particle morphology over time. Pellets of Au@*m*SiO_2 (1 mg), with and without adsorbed proteins were resuspended in 0.2 mL of 100 mM PBS 1×. The suspensions were maintained at 37 °C, and aliquots of 5 μL were periodically collected. These aliquots were diluted with 100 μL of ethanol and then dried on silicon wafers for SEM analysis. The particle size was determined on approximately 50 particles.

2.6. References

1. Croissant J, Zink JI (2012) Nanovalve-Controlled Cargo Release Activated by Plasmonic Heating. J Am Chem Soc 134:7628–7631. https://doi.org/10.1021/ja301880x

2. Yamamoto E, Mori S, Shimojima A, et al (2017) Fabrication of colloidal crystals composed of pore-expanded mesoporous silica nanoparticles prepared by a controlled growth method. Nanoscale 9:2464–2470. https://doi.org/10.1039/C6NR07416B

3. Shen D, Yang J, Li X, et al (2014) Biphase stratification approach to three-dimensional dendritic biodegradable mesoporous silica nanospheres. Nano Lett 14:923–932. https://doi.org/10.1021/nl404316v

4. Stöber W, Fink A, Bohn E (1968) Controlled growth of monodisperse silica spheres in the micron size range. Journal of Colloid and Interface Science 26:62–69. https://doi.org/10.1016/0021-9797(68)90272-5

5. Cosgrove T (2010) Electron Microscopy. Colloid Science: Principles, Methods and Applications. Chichester

6. Bhattacharjee S (2016) DLS and zeta potential - What they are and what they are not? J Control Release 235:337–351. https://doi.org/10.1016/j.jconrel.2016.06.017

7. Nečas D, Klapetek P (2012) Gwyddion: an open-source software for SPM data analysis. centr.eur.j.phys 10:181–188. https://doi.org/10.2478/s11534-011-0096-2

8. Alvarado Meza R, Santori T, Cattoën X (2023) A kinetic approach to the mechanism of formation of mesoporous silica nanoparticles. Journal of Sol-Gel Science and Technology. https://doi.org/10.1007/s10971-023-06130-w

9. Fradkov AF, Chen Y, Ding L, et al (2000) Novel fluorescent protein from Discosoma coral and its mutants possesses a unique far-red fluorescence. FEBS Letters 479:127–130. https://doi.org/10.1016/S0014-5793(00)01895-0

10. Wall MA, Socolich M, Ranganathan R (2000) The structural basis for red fluorescence in the tetrameric GFP homolog DsRed. Nat Struct Mol Biol 7:1133–1138. https://doi.org/10.1038/81992

11. Campbell RE, Tour O, Palmer AE, et al (2002) A monomeric red fluorescent protein. Proc Natl Acad Sci USA 99:7877–7882. https://doi.org/10.1073/pnas.082243699

12. Shaner NC, Campbell RE, Steinbach PA, et al (2004) Improved monomeric red, orange and yellow fluorescent proteins derived from Discosoma sp. red fluorescent protein. Nat Biotechnol 22:1567–1572. https://doi.org/10.1038/nbt1037

13. Veitch NC, Williams RJP (1990) Two-dimensional 1H-NMR studies of horseradish peroxidase C and its interaction with indole-3-propionic acid. European Journal of Biochemistry 189:351–362. https://doi.org/10.1111/j.1432-1033.1990.tb15496.x

14. Kadnikova EN, Kostić NM (2002) Oxidation of ABTS by hydrogen peroxide catalyzed by horseradish peroxidase encapsulated into sol–gel glass.: Effects of glass matrix on reactivity. Journal of Molecular Catalysis B: Enzymatic 18:39–48. https://doi.org/10.1016/S1381-1177(02)00057-7

15. Aronova MA, Kim YC, Zhang G, Leapman RD (2007) Quantification and Thickness Correction of EFTEM Phosphorus Maps. Ultramicroscopy 107:232–244. https://doi.org/10.1016/j.ultramic.2006.07.009

16. Greenfield NJ (2006) Using circular dichroism spectra to estimate protein secondary structure. Nat Protoc 1:2876–2890. https://doi.org/10.1038/nprot.2006.202

17. Micsonai A, Wien F, Kernya L, et al (2015) Accurate secondary structure prediction and fold recognition for circular dichroism spectroscopy. Proceedings of the National Academy of Sciences 112:E3095–E3103. https://doi.org/10.1073/pnas.1500851112

Chapter 3

One-pot synthesis of Au@*m*SiO_2

3.1 Introduction

The design of Au@*m*SiO_2-based nanovehicles for on-demand protein delivery requires mastery of synthesis techniques and a thorough understanding of the underlying synthesis mechanisms to enable the rational design of these particles. This chapter focuses on studying a *one-pot* method with the goal of prioritizing green, simple, economical, and reproducible synthesis strategies. By optimizing this method, the objective is to produce tailored Au@*m*SiO_2 that subsequently can be evaluated for use as nanovehicles in protein delivery systems.

The *one-pot* method for synthesizing Au@*m*SiO_2 nanoparticles offers several advantages, as discussed in Chapter 1, Section 1.3.5.3. This approach enables the formation of gold cores and subsequently the synthesis of a mesoporous silica shell through the heterogeneous nucleation of silica on surfactant-stabilized gold nanoparticles, with cetyltrimethylammonium bromide (CTAB) commonly serving as both a stabilizer and template. The method is particularly advantageous due to its higher yields, potential scalability, and reduced time and reagent consumption, approaching the principles of green synthesis. However, despite these advantages, the synthesis mechanism remains not fully understood, and the method faces significant challenges, including ensuring replicability, achieving uniform shell formation, and preventing the creation of empty silica particles during synthesis.

The aim of this chapter is to develop a robust *one-pot* synthesis protocol for Au@*m*SiO_2 particles suitable for photothermal conversion, using minimal reagents to promote sustainable chemistry practices [1]. The optimized Au@*m*SiO_2 nanoparticles should be smaller than 100 nm, with pore sizes larger than 3 nm, making them capable of encapsulating proteins within their pores. To address this goal, the chapter begins with an in-depth analysis of the synthesis with minimal components detailing the chemical steps involved. In order to reduce the particle diameter and enlarge pores, several synthesis parameters were modified following the criteria usually employed for mesoporous silica. Characterization of the synthesized nanoparticles with transmission and scanning electron microscopy (TEM/SEM), UV-Vis spectroscopy, dynamic light scattering (DLS), and nitrogen sorption allow to draw a mechanism and the role of each component, as well as to assess the efficiency, reproducibility, and uniformity of the particles produced by the *one-pot* method.

Subsequently, a systematic analysis examines the impact of varying synthesis components and conditions—including the type and concentration of surfactants, alcohols, base sources, precursor concentrations, and reaction temperature—on the morphology and size of the nanoparticles. This section details how each parameter influences the final nanoparticle structure, offering strategies for fine-tuning size and morphology based on experimental data. The analysis highlights that while certain physical properties, such as size and morphology, can be effectively controlled through careful adjustment of synthesis parameters, others, like the enlargement of pores, cannot be precisely regulated.

Finally, the chapter concludes by emphasizing the key factors that influence the synthesis of Au@*m*SiO_2, enabling precise control over particle shape and silica shell thickness. This control is essential for designing nanoparticles tailored for specific applications, particularly for their use as protein delivery vehicles.

3.2 Simplest *one-pot* synthesis of Au@*m*SiO_2

The reactants for the simplest way to prepare Au@*m*SiO_2 are CTAB, $HAuCl_4$, TEOS and NaOH in 28% v/v ethanol:water. This protocol, based on that reported in reference [2] is presented in Figure 3.1. It approaches the principles of green synthesis [1] provided that excess surfactant can be recovered and recycled.

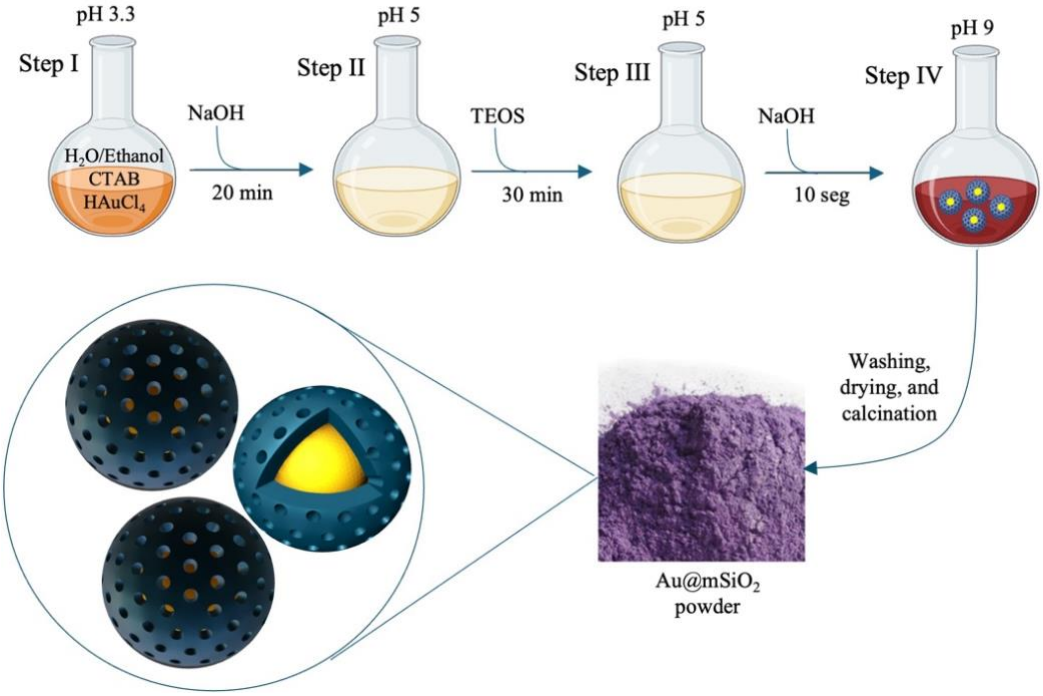

Figure 3.1. The reaction starts with a bright orange solution of $HAuCl_4$ at 1.05 mM in a 28% ethanol-water (a). A first addition of NaOH (2.8 mM), leads to a pale-yellow solution with pH=5 (b). TEOS is added dropwise, with no apparent change (c). NaOH is added a second time (total amount 8.2 mM), the solution become colorless then red.

Each component of the system has a specific role in providing the conditions for the AuNP formation to be fast enough to serve as a growth site for the *m*SiO_2 shell. The solvent (ethanol-water mixture) has the role of providing the reductant (EtO^-) and guarantees the dissolution of TEOS [3]. The surfactant —CTAB— is known to stabilize the formed AuNPs [4–6] and acts as a template for the growth of mesoporous silica [2, 7–9]. NaOH has a double role: it provides

(i) the formation of EtO^- necessary for Au(III) reduction and (ii) the best conditions for TEOS hydrolysis and condensation.

This *one-pot* method yielded 208 mg of Au@*m*SiO_2 with one or more 15±5 nm gold cores at their center representing a 71% yield, for 140 mL of solvent. The recovered particles after drying and calcination at 500 °C had an average diameter of 194±15 nm (Figure 3.2a). The UV-vis spectra show that Au@*m*SiO_2 exhibits a typical SPR absorption peak at 530 nm (Figure 3.2b). The textural properties were investigated by nitrogen adsorption at 77.4 K (Figure 3.2c) The complete characterization data is presented in Table 3.1.

The sorption isotherm obtained belong to the type IV IUPAC classification, characteristic of the mesoporous materials. Its shape is typical of CTAB-templated materials, such as MCM-41, with an inflexion located at p/p° 0.25 characteristic of small mesopores, after which a plateau is reached evidencing the absence of both larger mesopores and significant extent of external surface. The nitrogen uptake at $p/p^\circ>0.9$ is characteristic of the nitrogen condensation between nanoparticles in the dry state [10]. Additionally, the *t*-plot reveals no microporosity. The specific surface area of the material derived using the BET transform of the sorption isotherm was found to be 770 m^2g^{-1}. The pore size distribution estimated by the Barrett–Joyner–Halanda (BJH) model is shown in Figure 3.2d. It shows a narrow mesoporosity centered around 2.4 nm, which is consistent with other CTAB templated mesoporous silica. Additionally, capillary condensation occurs in a very limited relative pressure range, which confirms that the mesopores are very similar in diameter. The pore diameters calculated by the Gurwich method (D_{pore} = 4V/A) are very close to those observed using the BJH transform (See Table 3.1). The Gurwich calculation being valid only for cylindrical pores, suggests that the mesopores are homogeneous and cylindrical.

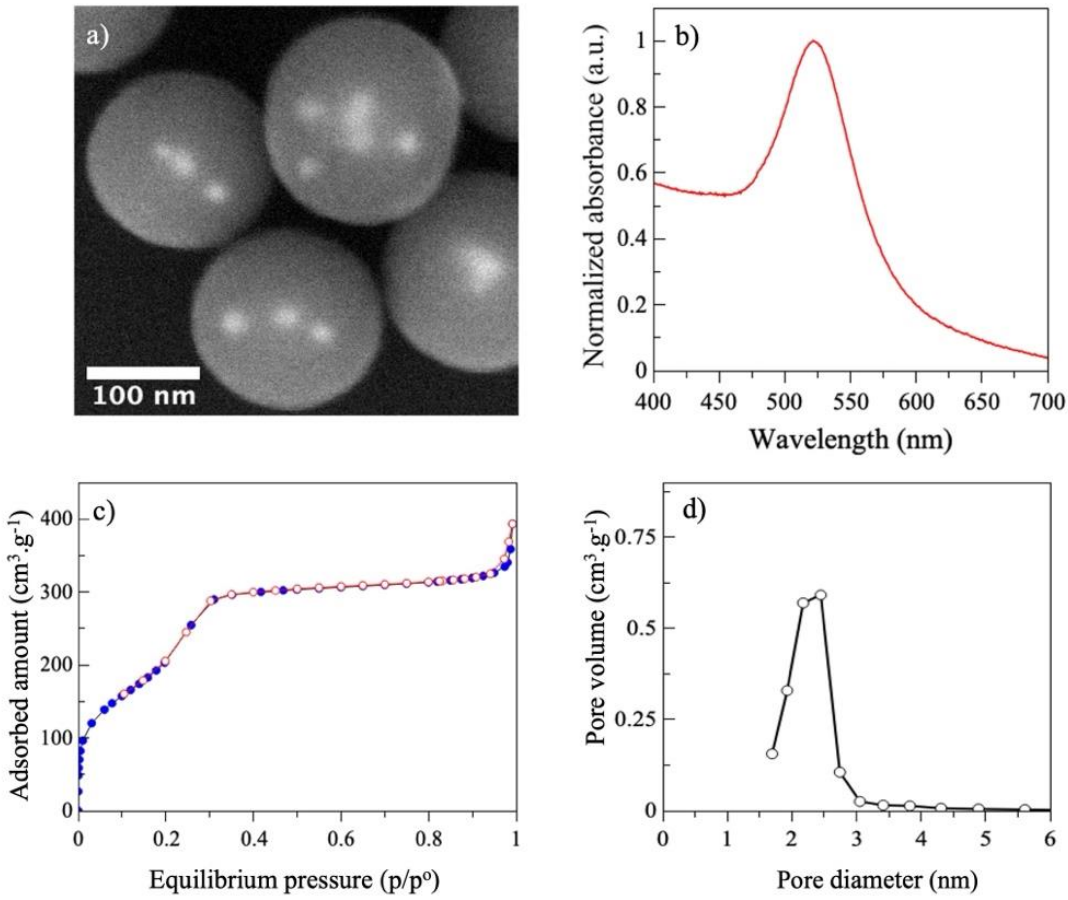

Figure 3.2. Characterization of Au@*m*SiO_2 obtained by the *one-pot* method. a) SEM image, b) UV-vis spectra, c) N_2 adsorption (blue line) /desorption (red line) isotherms, and c) pore size distribution.

Table 3.1. Characterization data and textural parameters of Au@*m*SiO_2 synthesized by the *one-pot* method described above.

[a]D_{part} (nm)	[a]D_{Au} (nm)	[b]DLS (nm)	[c]ξ (mV)	[d]S_{BET} (m^2/g)	[d]Mesopore volume (cm^3/g)	[d]BJH Pore diameter (nm)	[d]Gurwich pore diameter (nm)
194 ± 15	15±5	240	-16	757	0.47	2.3 -2.5	2.5

[a]Diamenter obtained from SEM microscopies
[b]Hydrodynamic diameter
[c]ξ-potential measured in 1 mM NaCl
[d]Textural parameters derived from the N_2-sorption isotherm

3.3 Au@*m*SiO_2 synthesis mechanism.

For solving the mechanism, it is necessary to understand the processes leading to the formation of the mesoporous silica layer and those influencing the reduction of Au(III) to AuNPs in the reaction medium. In principle, it is assumed that these two processes can occur independently, meaning that the presence of Au species does not interfere with the growth of the mesoporous silica layer. To investigate this, the reaction was analyzed using UV-vis spectroscopy and electron micrographs of aliquots freeze-dried at different stages of the reaction. The critical micelle concentration (CMC) of CTAB and the hydrolysis of TEOS were also evaluated in a medium simulating the synthesis conditions, but without gold.

The growth of a silica shell depends on the surfactant because micelles are required as template. The first CMC of CTAB in a basic 28% ethanol-water medium was determined at 2.7 mM by conductivity (Figure 3.3), well below the concentration of CTAB in the reaction medium (12.5 mM). Therefore, this suggests that the synthesis medium contains CTAB micelles, TEOS, and gold precursor in the ethanol-water mixture.

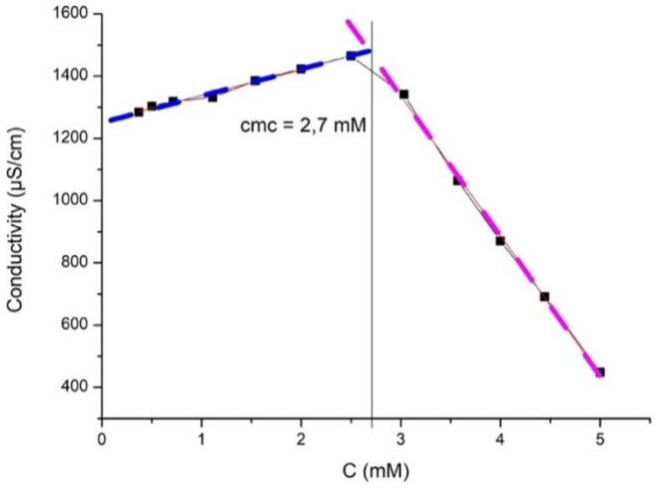

Figure 3.3. Determination of the CMC of CTAB by conductivity measurement at 28% vol EtOH, 72% vol H_2O, 8.6 mM NaOH, 70 ˚C.

After triggering the reaction with NaOH, the following reactions take place, leading to the nucleation and growth of both Au and *m*SiO_2:

Gold reduction:

$$2\ Au(III)X_4^- + 3\ RCH_2\text{-}OH + 6OH^- \rightarrow 3RCH{=}O + 6H_2O + 2Au(0) + 8X^- \quad (1)$$

with X = Cl, Br, or OH

Hydrolysis: $\equiv Si\text{-}OEt + OH^- \rightarrow \equiv Si\text{-}OH + EtO^- \rightarrow \equiv Si\text{-}O^- + EtOH$ (2)

Condensation: $\equiv Si\text{-}O^- + Si\text{-}OEt + H_2O \rightarrow \equiv Si\text{-}O\text{-}Si\equiv + EtOH + OH^-$ (3)

$$\equiv Si\text{-}O^- + \equiv Si\text{-}OH \rightarrow \equiv Si\text{-}O\text{-}Si\equiv + OH^-$$

The success of core-shell particle formation depends on the mismatch between the reduction of the gold salts with nucleation-growth of AuNPs and the hydrolysis-condensation of TEOS. Thus, the AuNPs formed at the beginning of the reaction act as a nucleation center for the hydrolyzed TEOS. The molar fraction of ethanol in the solvent is 0.11 which, as pointed out by Quinson *et al* [12], is the optimal for providing an adequate amount of reducing agent to facilitate reaction (1) while preventing excessive AuNP growth. Additionally, in the ethanol-water medium, the development of the mesoporous shell follows the path of the modified Stöber method, which has been previously described for synthesizing spherical MCM-41 particles [13, 14].

The kinetics of TEOS hydrolysis was monitored by following the pH evolution [11] under similar synthesis conditions with and without CTAB in the absence of gold salts (See Chapter 2, section 2.3.2 for details). Figure 3.4 shows that the reaction without CTAB exhibits identical hydrolysis kinetics compared to the reaction with CTAB. This indicates that TEOS is homogeneously distributed in the reaction medium and not encapsulated in the CTAB micelles, as described for MCM-41 synthesis in water [11]. The only notable difference in reaction kinetics is the turbidity (cloud point) of the medium after 40 seconds in the case

of CTAB, whereas the same without CTAB shows no turbidity at 5 minutes. This result implies that the presence of CTAB favors the formation of particles.

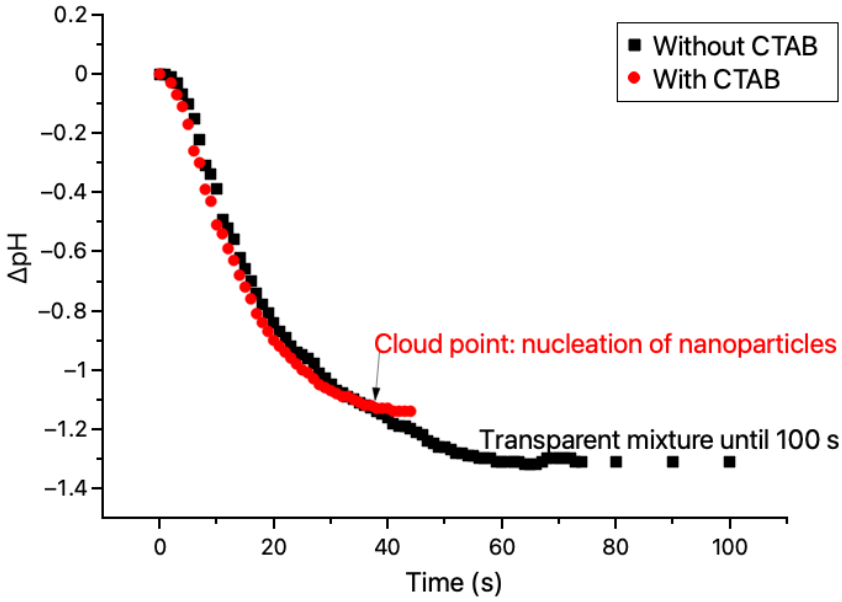

Figure 3.4. Reaction kinetics monitored by pH evolution in solution containing TEOS, ethanol, and water. Reaction performed (black) in the absence of CTAB and (red) in the presence of CTAB 12.5 mM.

3.3.1 The precursor state

The precursor state is defined as the molecular configuration of the assembled reagents before triggering the reaction, *ie* just before Step 4 (Figure 3.1). To analyze the precursor state, the spectrum of a solution of 0.1 mM $HAuCl_4$ in 28% ethanol-water at 70 ˚C was measured. The spectrum exhibits the well-known LMCT band at 226 nm and a 315 nm weak band assigned to low probability *d-d* transitions in symmetrical complexes (Figure 3.5a) [15]. In the CTAB-containing solution, $HAuCl_4$ undergoes a fast partial ligand substitution of Cl by Br that shifts the LMCT from 226 nm to 260 nm and the 315 nm band to 396 nm with enhanced absorbance (Figure 3.5b) [15–17]. This enhancement of the absorption coefficient, resulting in an intense orange color, is attributed to the strong interaction between AuX_4^- with CTA^+ — $[X_4Au^-—CTA^+]$ — which induces

a geometric distortion favoring vibronic coupling of the Au-Br bond, assisted by the localization of CTA^+ in the Stern layer of the micelle [18–22].

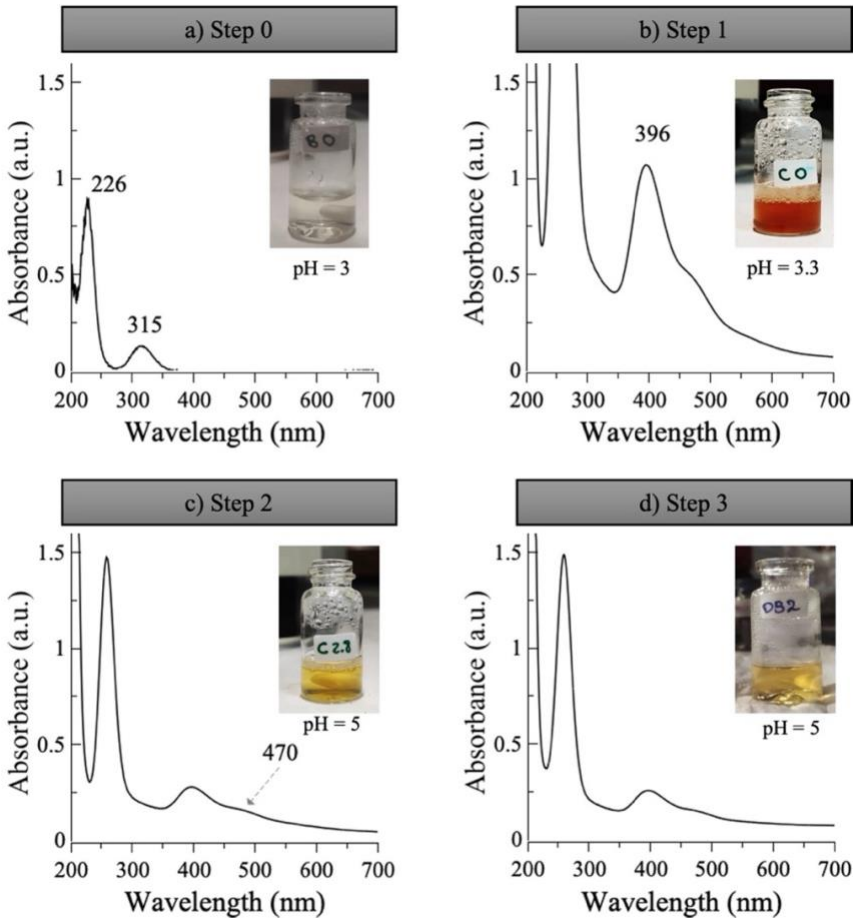

Figure 3.5. Analysis of the Au@*m*SiO_2 precursor evolution by UV-vis spectrophotometry (a) Step 0: spectrum of $HAuCl_4$ in solvent 28% ethanol:water at pH=3 (b) spectrum of $HAuCl_4$ in solvent 28% ethanol:water and CTAB at pH = 3.3 (c) spectrum of $HAuCl_4$ in solvent 28% ethanol:water, CTAB, and NaOH 2.8 mM at pH=5 (d) spectrum of $HAuCl_4$ in solvent 28% ethanol:water, CTAB, TEOS and NaOH 2.8 mM at pH=5. The inset in each spectrum shows the color of the solution at each stage of precursor evolution.

As the pH is increased to 5 after NaOH addition in step 2, the absorbance of the complex band at 396 nm decreases (Figure 3.5c), likely due to the substitution of Cl or Br ligands in $[X_4Au^-\text{-}CTA^+]$ by OH, resulting in a more rigid structure that relaxes the vibronic coupling. Additionally, the reduction of Au(III) to Au (I) or Au(0), may induce the formation of Au clusters attached to the micelles. In step 3, the addition of TEOS does not alter the UV-vis spectrum

denoting negligible TEOS - [X_4Au^-—CTA^+] interactions (Figure 3.5c). At pH 5, the hydrolysis of TEOS would occur at a very low rate [23, 24] thus partially hydrolyzed TEOS available to interact with micelles can be disregarded. It should be noted that TEOS is fully soluble in the 28% ethanol-water mixture [11].

In summary, the precursor state can be described as mostly [X_4Au^-—CTA^+] complexes, non-hydrolyzed TEOS, few gold clusters surrounded by micelles, and the remaining AuX_4^- distributed in solution. Figure 3.6 schematizes the distribution of species prior to triggering the reaction that was determined by UV-vis spectroscopy. This precursor state establishes the initial condition for the reaction pathway.

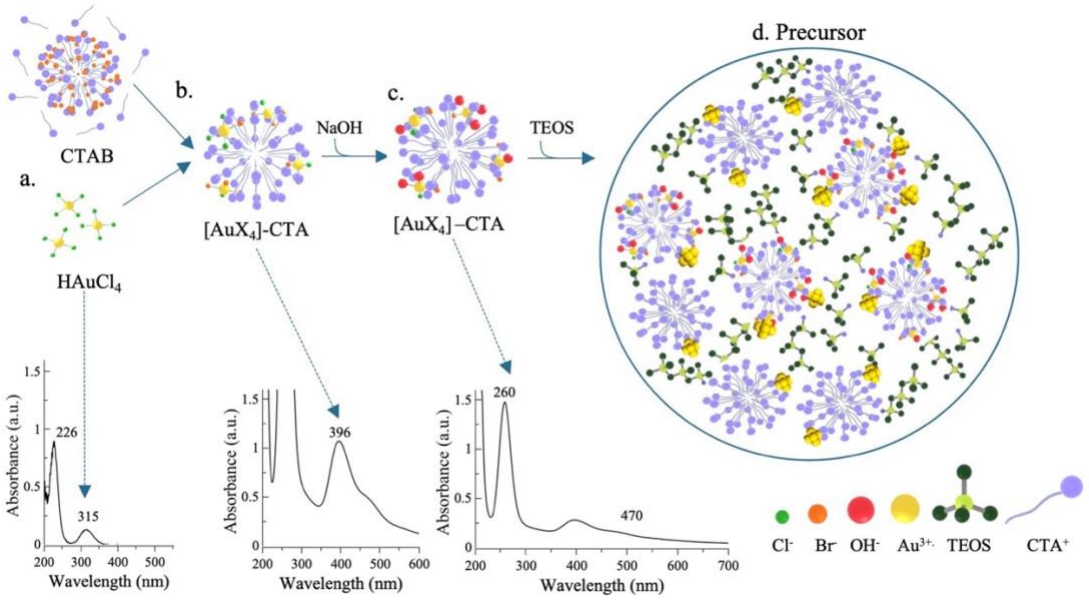

Figure 3.6. Scheme and UV-vis spectra at each step before the precursor state formation. (a) The formation of the precursor state starts with a solution of $HAuCl_4$ whose spectra show bands at 226 and 315 nm (b). When this solution is added to the CTAB solution in ethanol-water, the system turns intense orange and there is a shift of the LMCT band to 260 nm due to the substitution of Cl by Br and from 315 to 396 nm due to the formation of a complex [X_4Au^-—CTA^+] (X = Cl or Br) (c). Upon first NaOH addition, the system reaches pH = 5 and the system turns pale yellow. The 260 nm band decreases in intensity and the 396 nm band shifts towards 470 nm due to the replacement of the Cl or Br halide by OH in the [X_4Au^-—CTA+] complex (X=Cl, Br or OH) and the formation of gold clusters (e). When TEOS is added, there is no detectable change in the spectrum. TEOS is homogeneously dispersed in the solvent and gold clusters surrounded by micelles, the [X_4Au^-—CTA^+] complex, and the remaining AuX_4^- species are distributed in the solution.

3.3.2 From the precursor to the Au@*m*SiO_2

Once the precursor state was established, the progression of the reaction after triggering (step 4 of Figure 3.1) was studied by following the reaction with electron microscopy and pH monitoring as shown in Figure 3.7 and Figure 3.8 respectively. The process can be divided into three stages based on Au@*m*SiO_2 particle diameter (D_{part}) and pH evolution. During *Stage I*, AuNPs start to form and there is a rapid pH decrease from 10.2 to 9.6; in *Stage II*, the *m*SiO_2 shell develops, with D_{part} increasing, while AuNPs become quasi-spherical, and there is a less pronounced pH decrease from 9.6 to 8.4; in *Stage III*, D_{part} stabilizes, AuNPs become monodisperse, and pH reaches 8. These findings are schematized in Figure 3.9.

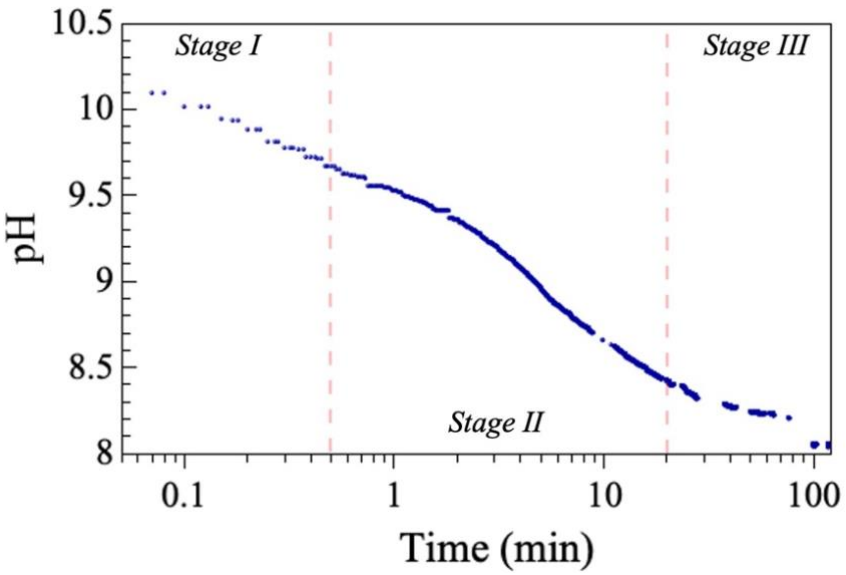

Figure 3.7. Evolution of the pH during the Au@*m*SiO_2 synthesis. Full view over the two hours of synthesis with time axis in logarithmic scale to visualize the three stages of the synthesis. The dotted red lines delimit each stage.

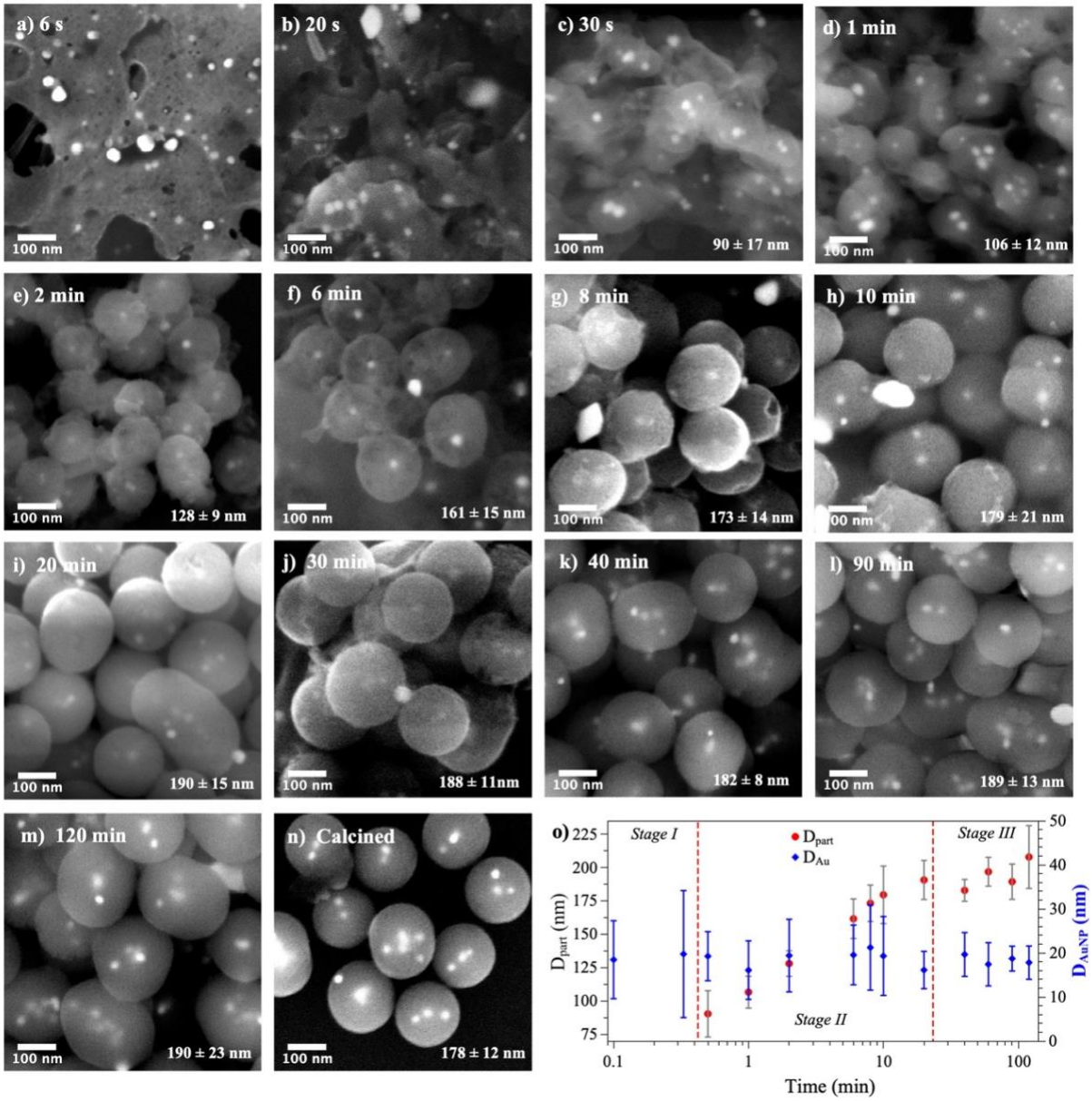

Figure 3.8. SEM follow-up of the *one-pot* synthesis of Au@*m*SiO_2. a-m) SEM images at different times of the reaction. n) Au@*m*SiO_2 after washing, drying and calcination at 500 ˚C, o) Diameter of Au@*m*SiO_2 (red) and Au cores (blue) over the reaction. The dotted red lines delimit each phase of the synthesis.

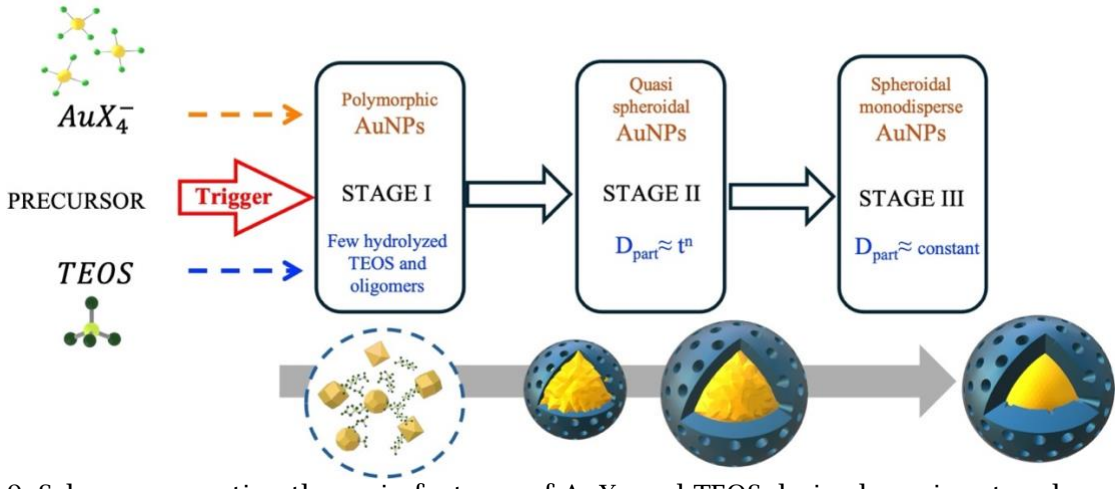

Figure 3.9. Scheme presenting the main features of AuX_4^- and TEOS derived species at each stage of Au@*m*SiO_2 formation.

3.3.2.1 Stage I:

Nucleation and growth of AuNPs are the dominant features in this stage while there is incipient hydrolysis and condensation of TEOS. The sudden change of pH (Figure 3.8) produces a sufficient concentration of reductant, EtO^-, enabling the reduction of Au(III) species. Several processes occur in less than 10 sec as revealed by the reaction color changes from yellow to colorless, then violet, culminating in the final red-wine characteristic of spheroidal AuNPs. Considering that AuNPs are formed following a mechanism close to the Turkevich-Frens synthesis [25–27] the ephemeral colorless batch is assigned to the presence of Au(I), and to a less extent, to the substitution of Cl or Br by OH in AuX_4^-, which occurs at a slower rate than an electron transfer reaction [17]. As seen in Figure 3.8a the AuNPs formed in this stage are polymorph and polydisperse, consistent with the initial steps of the Turkevich-Frens synthesis [25–27].

The AuNP growth is controlled by the low reactivity of OH rich AuX_4^- at pH = 9.5 (X = Cl, Br or OH); these species are attracted to the Au seeds, leading to reduction at their surface. This transformation of a reactive gold species into a

less reactive species happens just in appropriate time to produce a small but enough quantity of gold primary particles [25]. As the particle grows, it remains attached to CTA^+ molecules, which in turn are mostly forming a micelle [25].

The fraction of reduced Au(0) at *Stage I* can be estimated from the absorption at 400 nm, as proposed by several authors [12, 28]. In this case, this is a rough estimation as we considered that 100% of initial Au(III) is reduced at $t \to \infty$, and the absorption coefficient of 5*d* to 6*sp* interband transition of Au(0) is independent on the changes in the particle size and shape, as well as on the surroundings. Absorption at 400 nm was taken from UV-vis spectra at 5 min, 120 min and 24 hours (Figure 3.10a) with the same synthesis protocol of Scheme 1 done in 3 mL flasks. This qualitative analysis is validated by the linear relationship absorption at LSPR – absorption at 400 nm (Figure 3.10c). Assuming that 24 hours is $t \to \infty$, and all initial Au(III) has been reduced to Au(0) as the NaOH:$HAuCl_4$ mole ratio is 8:1, we estimate the Au(III) reduced at the end of *Stage I*. It was calculated that *ca* 5% of initial Au(III) was reduced to Au(0), leaving unreacted AuX_4^- species dispersed in the solution or trapped either in micelles and/or *m*SiO_2 units. These species may participate in the growth of primary particles, the dissolution of Au(0), or the formation of new Au(0) primary particles. The AuNPs, embedded within a hydrolyzed TEOS and silica oligomers, are suitable seeds for the nucleation of *m*SiO_2 units.

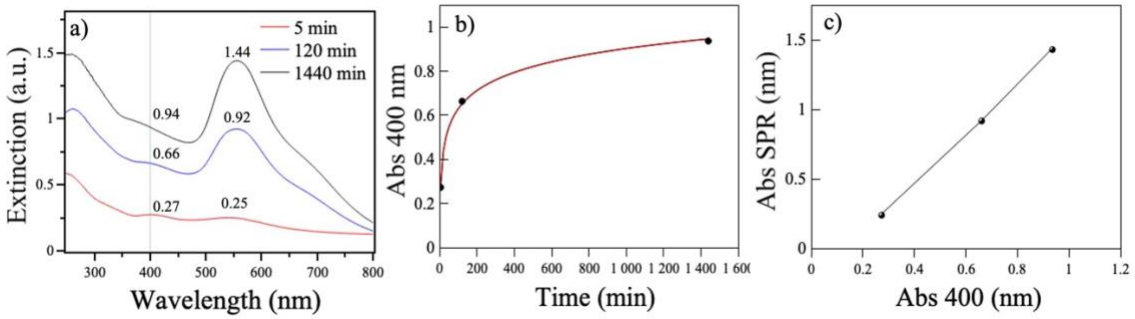

Figure 3.10. (a) UV-vis spectra of Au@*m*SiO_2 synthesis reaction after 5 min (red), 120 min (blue), and 2 hours (black). Extinction at 400 nm and in the SPR band are marked. (b) Extinction at 400 nm as a function of synthesis time. (c) Linear relationship of extinction at 400 nm and SPR extinction

3.3.2.2 Stage II

This stage is dominated by the growth of the mesoporous shell up to a steady-state diameter with concomitant transformations on the AuNPs (Figure 3.8c-d and g). *m*SiO_2 nucleates on AuNPs formed in *Stage I*, forming spherical particles. The time at which the particles start to be detected —*ca* 30 s after triggering (Figure 3.8c)— is close to the time at which the cloud point is observed in pH monitoring experiments under similar conditions without gold (Figure 3.4). pH drops from 9.6 to 8.4 over the course of the reaction at this stage (Figure 3.7). This pH variation is consistent with a silicate concentration at the end of stage *Stage II* of 7.7 mM, *ie* 24% of the initial TEOS amount at nucleation under the hypothesis that only singly hydrolyzed species are present at *Stage II*.

In parallel, AuNPs evolves to spheroidal and more monodisperse NPs with 15 nm average diameter. This process is also reported for the Turkevich-Frens synthesis [21, 25–27, 29]. Also, the increase of fraction of Au^0 formed in this stage goes from 5% to 50% as estimated from the absorbance at 400 nm (Figure 3.10) Thus, as the NP diameter remains nearly constant, Au nucleation and growth also proceed in *Stage II* either in solution, at the surface of the growing mesoporous shell or even inside the *m*SiO_2 shell (Figure 3.8c-i). As proposed for the Turkevich Frens synthesis, the formation of Au(I) by the comproportionation reaction [21] should contribute to AuNP smoothing:

$$Au^{3+} + 2Au^{0} \rightleftharpoons 3Au^{+} \qquad (4)$$

Reaction (4) provides Au(I) that may be further reduced on the AuNP. The participation of reaction (4) in the whole process allows to explain the slow pH decay in *Stages I* and *II*. As AuX_4^- is a square planar complex with dimension lower than 0.5 nm [30] unreacted AuX_4^- may diffuse through the silica shell —even when pores are clogged by CTAB— either from the outside solution or when trapped in the freshly formed silica shell.

The growth rate of the mesoporous layer indicates a nucleation-growth process involving monomer addition, aggregation, coalescence and Ostwald

ripening that occur simultaneously [31, 32]. Thus, it should be possible to restrict growth by modification of the surface with hydrophilic moieties or by surface complexation with appropriate ligands.

3.3.2.3 Stage III

Stage III is characterized by nearly constant D_{part}, indicating a steady state between aggregation-condensation and dissolution processes (Figure 3.8 j-m). A relevant feature of this stage is the higher fraction of ovoidal particles with more than one AuNP which should be a consequence of the aggregation and dissolution of the core-shell particles. In the same time, AuNPs embedded in *m*SiO_2 become more spheroidal and with less size dispersion indicating that dissolution of Au(0) by unreacted AuX_4^- takes place even at this stage. The ovoidal shape of the composite core-shell particles is also a difference with *m*SiO_2 synthetized in Au-free systems that are mainly spherical.

At this stage, the Au@*m*SiO_2 particles reach a size, surface charge, and structure for which colloidal stabilization can be achieved.

3.3.2.4 Final processing

Final processing involves washing, drying and calcination for full removal of CTAB. The colloidal and hydrolytic stability of the final particles will allow their application to specific problems. After calcination, in addition to CTAB removal, the de-hydroxylation of the silica surface is clearly detected in the FTIR spectra (Figure 3.11) by the decrease of the 963 cm^{-1} band. Importantly, no significant changes can be detected in D_{part} that means that the pore structure does not collapse under the applied thermal treatment.

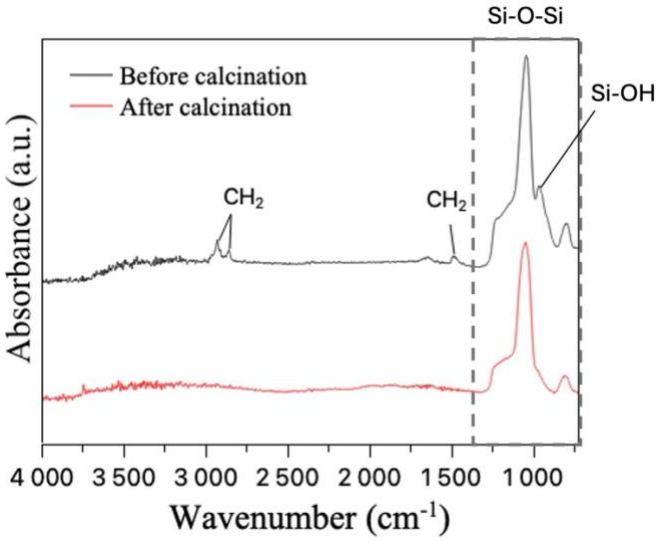

Figure 3.11. FT-IR spectra (black) of Au@*m*SiO_2 before calcination (blue) Au@*m*SiO_2 after calcination. After calcination, the spectrum exhibit bands centered at around 2925, 2853, and 1481 cm^{-1} corresponding to C−H stretching of the CH_2 and CH_3 groups of CTAB surfactant. These bands disappear after calcination, indicating successful surfactant removal. Additionally, the reduction of the band at 963 cm^{-1} (Si−OH) after calcination suggests dihydroxylation. The prominent peaks at around 1070, 800, and 460 cm^{-1}, characteristic of Si−O−Si bond vibrational modes, dominate the spectrum after calcination.

3.3.3 Summary of mechanism

Based on our experimental observations and the published literature, the mechanism shown in Figure 3.12 is proposed. A CTA^+-AuX_4^- complex is assembled in a water-ethanol medium due to the strong electrostatic interactions between the positive head of CTA^+ and the ionized Au(III) species. When the first amount of NaOH is added to reach pH 5, the halogen ligands (Br or Cl) are partially replaced by OH and the some of the resulting Au(III) complexes are reduced to Au(I) by ethanol oxidation. When TEOS is added it is dispersed homogeneously in the reaction medium. At this point a mixture of mostly [X_4Au^-—CTA^+] complexes, non-hydrolyzed TEOS, few gold clusters surrounded by micelles, and the remaining AuX_4^- distributed in solution set as the precursor state of the reaction.

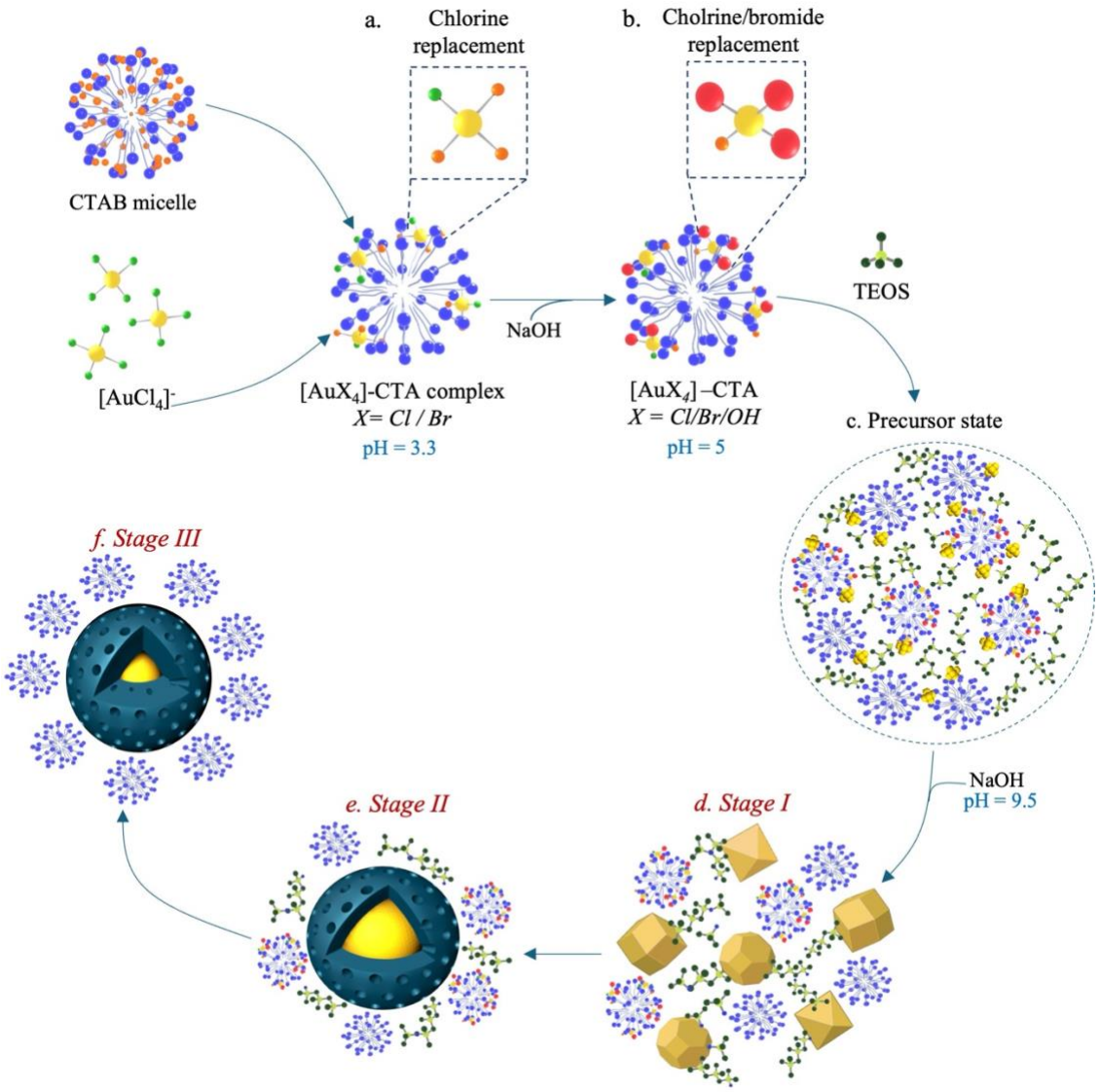

Figure 3.12. Mechanism of the *one-pot* synthesis of Au@*m*SiO_2 (a)The CTA^+—AuX_4^- complex is assembled due to electrostatic interactions between the positive head of CTA^+ and the ionized Au(III) species. (b) NaOH is added (pH= 5) the halogen ligands Br or Cl of the complex are partially replaced by OH, and some Au(III) complexes are reduced to Au(I) by ethanol oxidation. (c) TEOS is added and is homogeneously dispersed in the reaction medium. (d) *Stage I*: A second NaOH addition triggers the Au(III) and Au(I) reduction to form AuNPs, and TEOS hydrolyze and condense around AuNP using the CTAB micelles as a template. (e) *Stage II:* AuNPs become more spheroidal and the mesoporous shell grows. (f) *Stage III:* Au@*m*SiO_2 consolidate their structure.

The NaOH added immediately after TEOS promotes two reactions that take place with a slight time lag. First, within the initial seconds, *Stage I* take place; Au(III) and Au(I) species are reduced and allow the nucleation and growth of

AuNPs. Simultaneously TEOS is partially hydrolyzed (Figure 3.4). During *Stage II* the silica shell is formed by condensation of hydrolyzed TEOS on the previously formed AuNPs and using the CTAB micelles as a template (Figure 3.7). Also the gold cores dissolve and re-form into a more stable spheroidal shape. Finally, the Au@*m*SiO_2 consolidate their structure during *Stage III* with the mesoporous shell reaching a up a steady-state diameter where size, surface charge, and structure for which colloidal stabilization can be achieved.

3.4 Tuning the particles through synthesis parameters

To fine-tune the particle diameter (D_{part}) and pore diameter, the role of several synthesis parameters was analyzed, including surfactants, alcohol chain length, and the base source.

3.4.1 Surfactant mixtures.

The incorporation of nonionic surfactants that form hybrid micelles may either modify the micelle diameter thus modifying the shell template or act as complexant preventing interaction between silica species and limiting the shell growth [33]. On this basis, we explore the Au@*m*SiO_2 obtained when a low molar fraction of triblock copolymers (Pluronics) or nonionic ethoxylated fatty alcohols (Brij) are incorporated to the system before shell synthesis. Figure 3.13 and Table 3.2 presents the complete characterization data and textural properties of the obtained calcined particles for F127:CTAB (1:175) (b), Brij C10: CTAB (1:5) (c), and Brij C10: CTAB (1:2.5).

The incorporation of Pluronic F127 or Brij C10 in the step 2 at pH = 5 results in a decrease in the final shell thickness, as seen in the SEM micrographs in Figure 3.13c for F127:CTAB (1:175), Brij C10: CTAB (1:10), and Brij C10: CTAB (1:5). The Brij C10:CTAB molar ratio also has influence on D_{part}, with size increasing from 86±6 nm to 140 ±14 nm, when the amount of Brij C10 is halved.

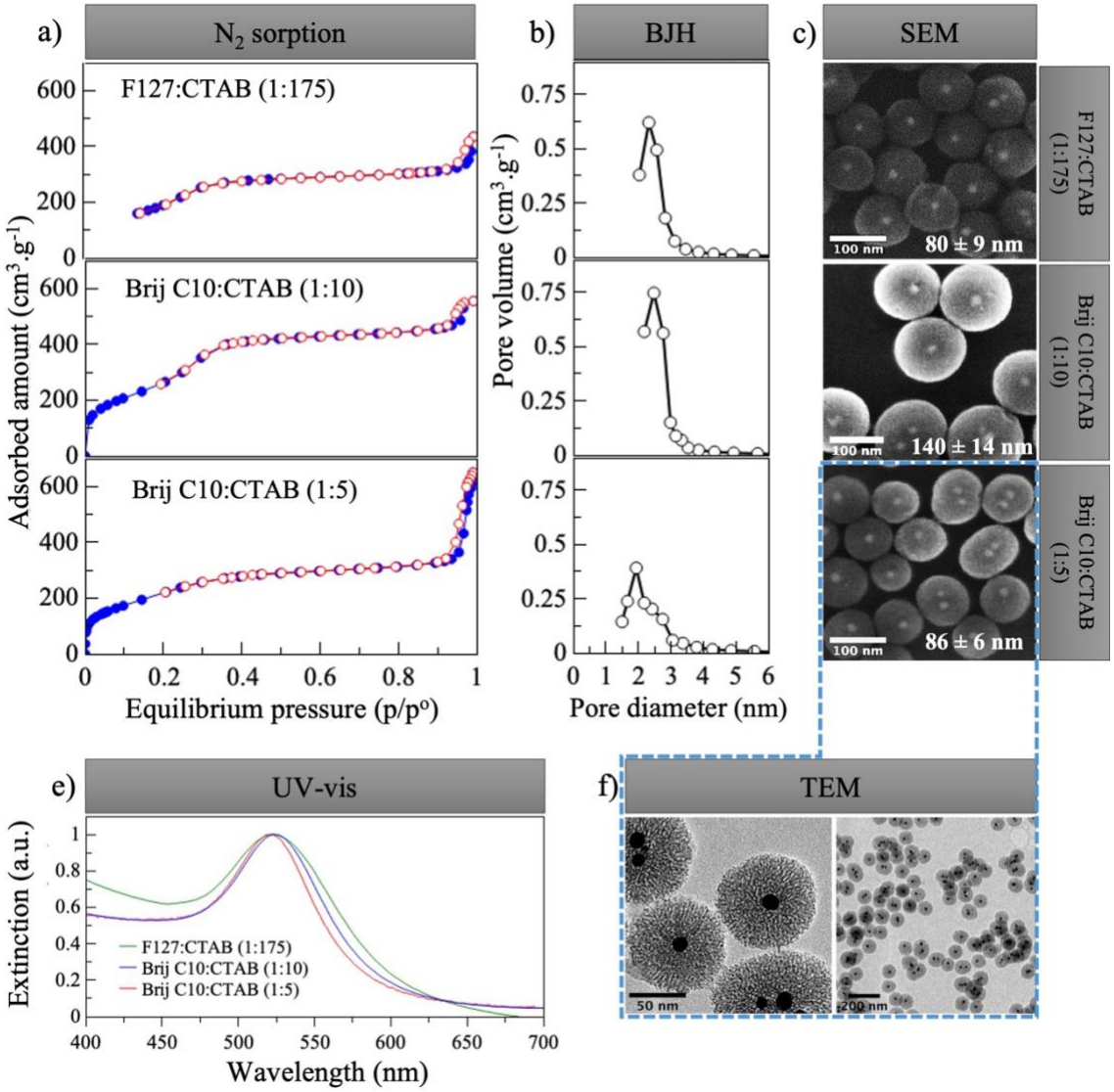

Figure 3.13. Characterization of Au@*m*SiO_2 obtained by *one-pot* method using CTAB and co-surfactants. From top to bottom: F127:CTAB (1:175), Brij C10:CTAB (1:10), Brij C10:CTAB (1:5). a) N_2 adsorption (blue line) /desorption (red line) isotherms. b) pore size distributions. c) SEM micrographs, where the white dots correspond to the gold cores and the grey zones to the silica shells. e) Normalized UV-vis spectra of Au@*m*SiO_2 obtained using CTAB and surfactant-CTAB mixtures. f) TEM micrographs of Au@*m*SiO_2 synthesized with BrijC10:CTAB (1:5) at different magnification. The black dots correspond to the gold core and the grey area to the silica shell.

Figure 3.13a-b present N_2 sorption isotherm and pore size distribution derived from BJH analysis. The textural properties of the Au@*m*SiO_2 particles synthesized with different co-surfactants are compiled in Table 3.2. Gurwich pore diameters are very close to those observed using the BJH approach, which

suggests that the mesopores are homogeneous and locally cylindrical regardless of the surfactant used. The extinction spectra of the core-shell particles obtained with the different surfactant-CTAB mixtures exhibit a maximum extinction at 525 nm, as expected for 15 nm diameter spherical AuNPs (Figure 3.13e).

Table 3.2. Characterization data of Au@*m*SiO_2 obtained with CTAB and different surfactant mixtures.

Surfactant mixture	**[a]D_{part} (nm)**	**[a]D_{Au} (nm)**	**[b]DLS (nm)**	**SBET (m2/g)**	**[c]Mesopore volume (cm3/g)**	**[c]BJH Pore diameter (nm)**	**[c]Gurwich pore diameter (nm)**
F127:CTAB (1:175)	80 ± 9	15±5	148	778	0.45	2.3	2.3
Brij C10:CTAB (1:10)	140±10	15±5	202	988	0.66	2.5	2.7
Brij C10:CTAB (1:5)	86 ± 6	15±5	159	790	0.46	2.0	2.3

[a]Diamenter obtained from SEM

[b]Hydrodynamic diameter

[c]Textural parameters derived from the N_2-sorption isotherm

Surfactant mixtures in the molar ratios used in this study do not impact *Stage I*, as they do not alter significantly the precursor state, and the reduction of Au(III) to Au(0) in the presence of F127 or BrijC10 is negligible [34]. The kinetics of TEOS hydrolysis in Au-free system also remain unchanged; similar behaviors are indeed observed in the presence and absence of BrijC10 (Figure 3.14), indicating that the hybrid micelles did not affect the initial steps of hydrolysis and condensation of TEOS. Furthermore, the cloud point observed during the monitoring of pH evolution remains consistent within the order of detection of the first particles observed when tracking the reaction progress by SEM (Figure 3.14).

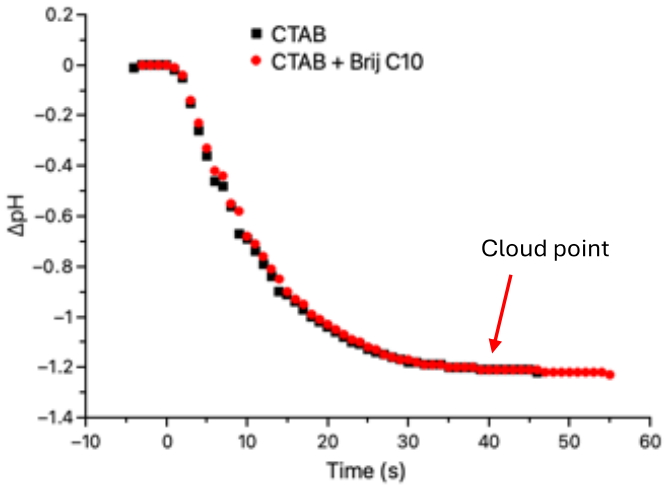

Figure 3.14. Reaction kinetics monitored by pH evolution in solution containing TEOS, ethanol, and water, and CTAB. Reaction performed (black) in the absence of Brij C10 and (red) in the presence of Brij C10 (Brij C10:CTAB 1:5).

Additionally, the UV-vis spectrum of the precursor state with and without Brij C10 is nearly identical in both cases (Figure 3.15), confirming that Brij C10 does not alter the precursor state of the reaction, and therefore, *Stage I* remains unchanged.

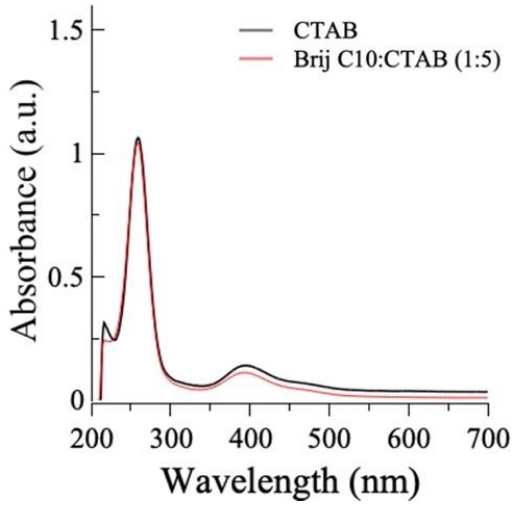

Figure 3.15. UV-vis spectra of Au@*m*SiO_2 prior to NaOH trigger (black) in the absence of Brij C10 (red) in the presence of Brij C10.

However, the addition surfactant mixtures introduce significant modifications to *Stage II*. Considering the additive rule for hybrid micelles in

water [35], hybrid micelles of CTAB:BrijC10 (1:5) are expected to form. The fact that the pore diameter does not change with surfactant mixtures may be due to similar micelle size or because micelle-silica interactions lead to co-surfactant migration to the surface of the particle when building blocks are assembled. This modification of the particle surface allows to reach colloidal stability in a shorter time [36, 37] which inhibits aggregation and smaller particles are obtained (Figure 3.16).

Despite minimal differences between Au@*m*SiO_2 particles synthesized with F127:CTAB (1:175) and Brij C10:CTAB (1:5) (see Table 3.2), those obtained with Brij C10 exhibit better dispersibility and colloidal stability in water and aqueous solutions. Considering this, the study of the synthesis mechanism with Brij C10: CTAB (1:5) was conducted using SEM monitoring and UV-vis analyses.

Figure 3.16 shows the SEM follow-up of the synthesis using Brij C10:CTAB (1:5). Similar to the reaction without Brij C10 (Figure 3.7), AuNPs are formed within the initial seconds, and their size remains constant as the reaction progresses. The addition of Brij C10 results in a reduction in the final particle size. The silica shell begins to appear 30 seconds into the reaction, reaching its final size within the first 10 minutes. This leads to smaller final particle sizes compared to the synthesis without Brij C10.

Based on the results we consider that the synthesis with Brij C10:CTAB (1:5) whose TEM images are shown in Figure 3.13f , is the optimal one in this series. This synthesis meets the set requirements: it is statistically reproducible, provides calcined Au@*m*SiO_2 particles with D_{part} < 100 nm, and ensures good colloidal stability in aqueous solutions. In the following sections, we analyze the role of synthesis variables for this surfactant mixture.

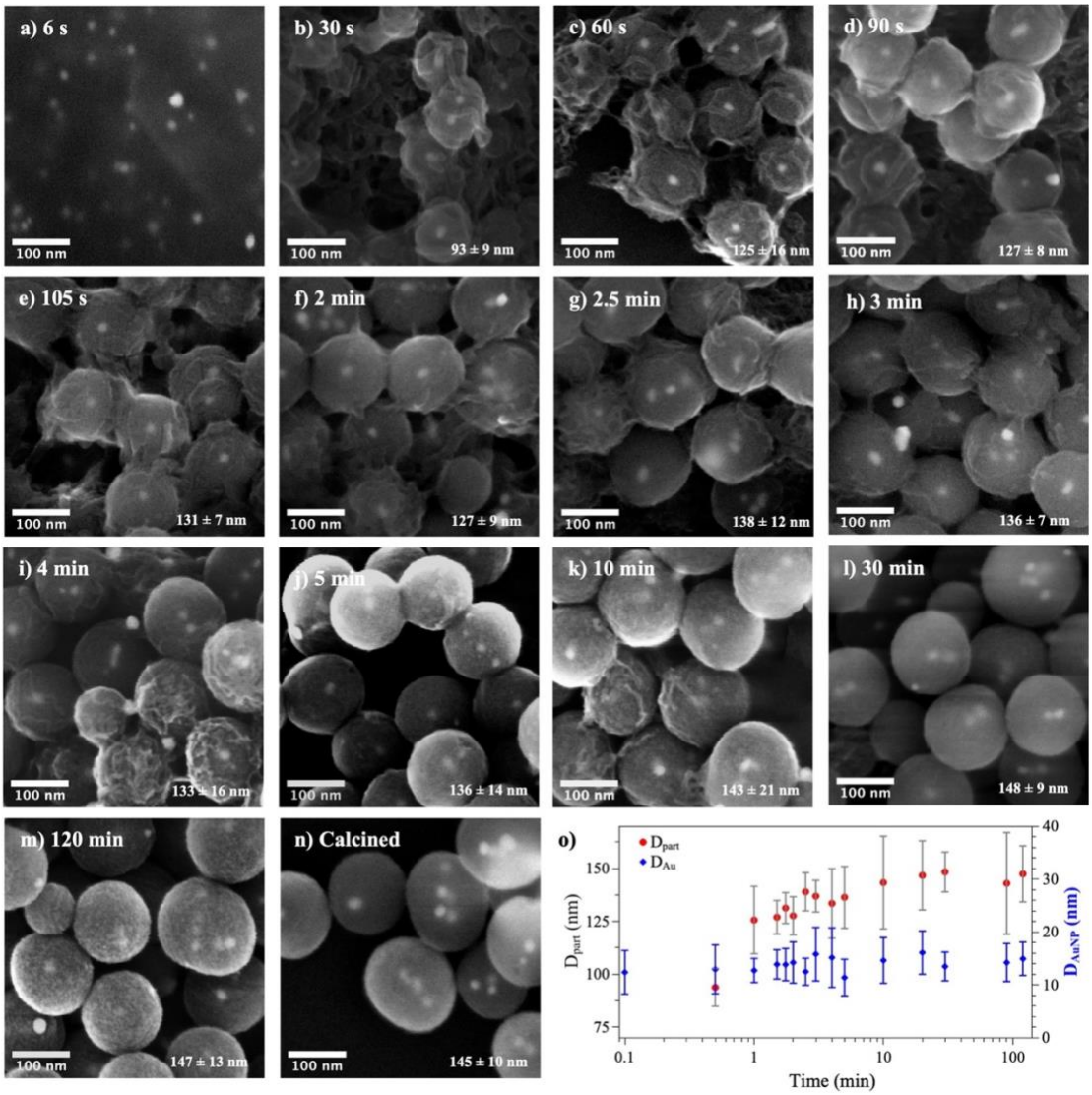

Figure 3.16. SEM follow-up of the synthesis *one-pot* of Au@*m*SiO_2 using Brij C10 as co-surfactant. a-m) SEM images at different times of the reaction. n) Au@*m*SiO_2 after washing, drying and calcination at 500 °C o) Diameter of Au@*m*SiO_2 (red) and Au cores (blue) over the reaction.

Replacing CTAB by CTAC in the 1:5 molar ratio mixture with Brij C10 results in two types of particles: those without an Au core (D_{part} ~ 87 nm) and those with an Au core (D_{part} ~ 150 nm), as seen in Figure 3.17. Although CTAC and CTAB share the same molecular structure, they differ in the counterion, with Cl being more electronegative than Br. This change in the counterion significantly alters the formation of AuNPs. In the absence of Br^-, the initially formed complex

consists of $AuCl_4^-$—CTA^+ and $AuCl_2^-$—CTA^+. These species are more reactive than their brominated analogues, resulting in faster AuNP growth [38]. Therefore, using CTAC instead of CTAB modifies the precursor state and *Stage I*. During the precursor state formation, the [X_4Au^-—CTA^+] complex is not substituted by Br. Consequently, larger AuNPs are produced due to the higher reactivity of $AuCl_4^-$, leading to less inhibition of AuNP growth.

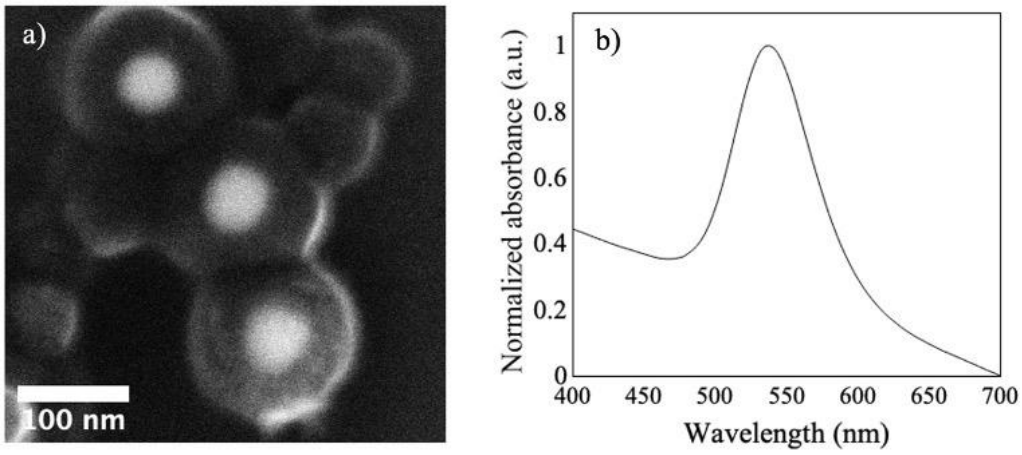

Figure 3.17. Au@*m*SiO_2 obtained by *one-pot* method using Brij C10:CTAC (1:5) as surfactant (a) SEM micrographs (b) UV-vis spectra

3.4.2 Alcohols

Alcohols may have influence in the AuNP nucleation and growth [12] as well as in the development of *m*SiO_2 [39–41] for which we expect an increase of the pore size. The role of increasing the alcohol chain length from C2 to C4 in the final calcined particles was explored. When butanol was used, no purple color was detected, and large *m*SiO_2 particles were formed, as observed by DLS (Table 3.3). With isopropanol (IPA), large (150-500 nm) yet polydisperse *m*SiO_2 particles were obtained, which featured polydisperse AuNPs (10-20 nm) at their surface (Figure 3.18).

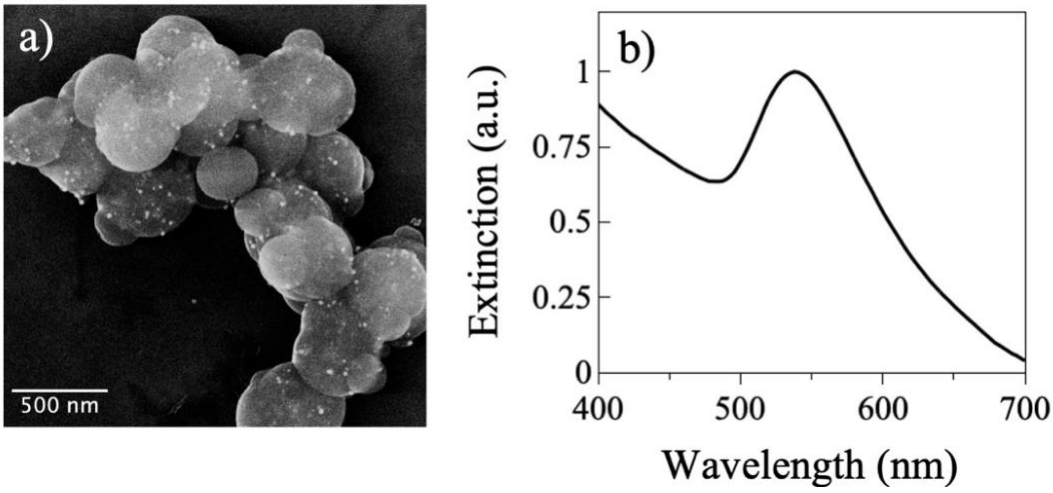

Figure 3.18. Au@*m*SiO_2 obtained by *one-pot* method using Brij C10:CTAC (1:5) as surfactant and 28% isopropanol-water as solvent (a) SEM micrographs (b) UV-vis spectra

Table 3.3. Characterization data of Au@*m*SiO_2 obtained with Brij C10:CTAB (1:5) and different alcohols

Alcohol	**[a]D_{part} (nm)**	**[a]D_{Au} (nm)**	**[b]DLS (nm)**
Ethanol	86 ± 6	15±5	159
Butanol	-	ND	761
Isopropanol	150-500	10-20	209

[a]Diamenter obtained from SEM microscopies

[b]Hydrodynamic diameter

To better understand the evolution of the reaction in IPA, we compared the reaction's color development with that in ethanol. The emergence of the typical red color of AuNPs is much slower in IPA than in ethanol. Before triggering the reaction with NaOH, both reactions exhibited the same yellow color corresponding to the [X_4Au^-—CTA^+] complex, and the pH of both reactions was 5, indicating that the gold species were the same. After triggering the reaction with NaOH, both reactions reached pH 9.5. However, the typical color development associated with the formation of AuNPs was significantly slower in the reaction with isopropanol. In ethanol, the yellow color of the precursor turned dark purple within the first 10 seconds, whereas in isopropanol, the dark purple color had

not developed even after 180 seconds of monitoring. After 2 hours of reaction, both solutions had developed the characteristic purple color of AuNPs (Figure 3.19).

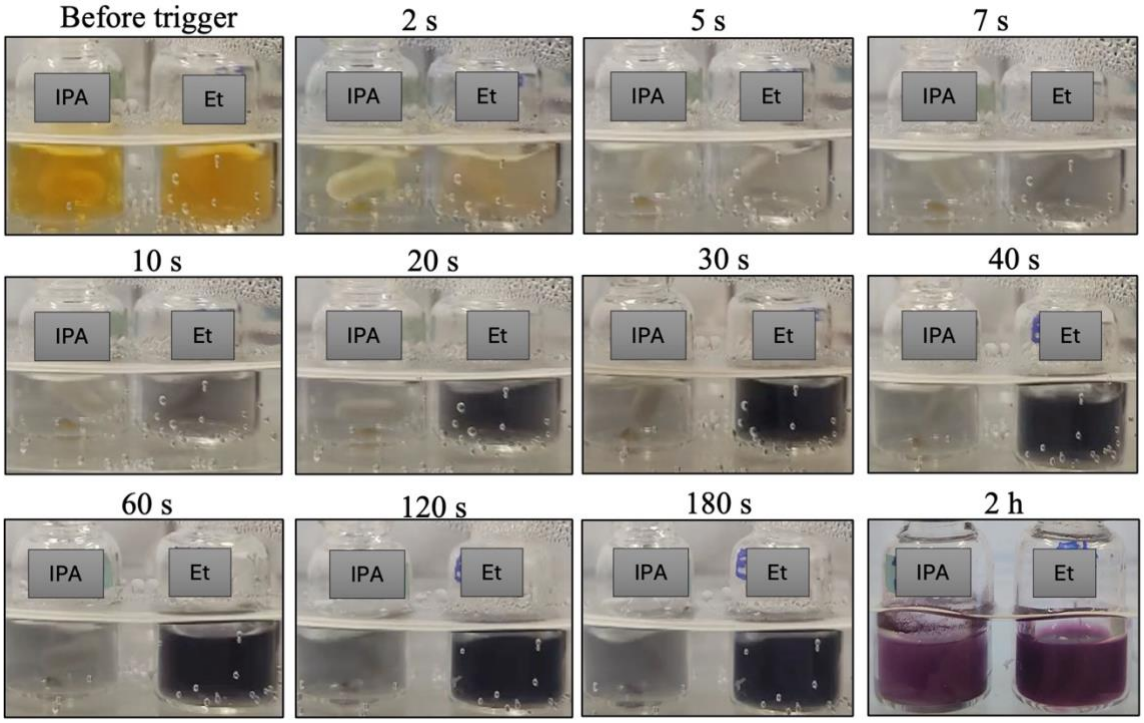

Figure 3.19**.** Photographs of the reaction at various times during the 3 mL synthesis of Au@*m*SiO_2 using Brij C10: CTAB (1:5) as surfactant in (left) 28% isopropanol:water (IPA) and (right) 28% ethanol:water (Et). The first photograph shows the color of the solution just before triggering the reaction.

Regarding silica, the hydrolysis of TEOS, monitored by pH decrease, occurs in both systems at similar rates (Figure 3.20), indicating that the initial kinetics of *m*SiO_2 formation is not altered when switching from ethanol to IPA.

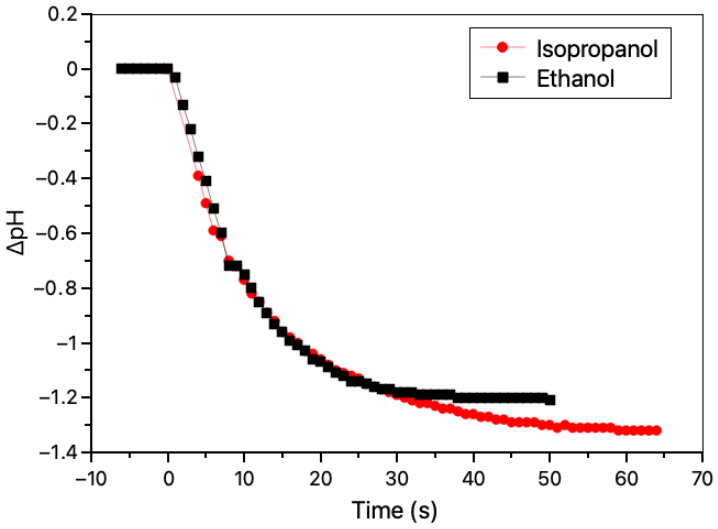

Figure 3.20. Reaction kinetics monitored by pH evolution in solution containing TEOS, water, CTAB, Brij C10 and ethanol (black) or isopropanol (red).

The p*Ka* of the alcohol determines the concentration of alcoholate available to transfer an electron to Au(III). The p*Ka* of the alcohols increases from ethanol to butanol, which explains the lower reactivity towards Au(III) reduction observed for isopropanol and butanol. Additionally, gold reduction requires an alcoholate to enter the solvation sphere of the Au complex and replace one of the ligands, a process that is kinetically controlled by steric and diffusion factors [12]. Consequently, the lower nucleation and growth rates of AuNPs in isopropanol compared to ethanol result in the nucleation of *m*SiO_2 units occurring first, leading to polydisperse *m*SiO_2 particles decorated with AuNPs (Figure 3.18).

3.4.3 Base source

The base used to trigger the reaction (Figure 3.1 step 4) defines the pH, the ionic strength, and may introduce steric factors controlling the interactions between particles. The pH affects the kinetics of *m*SiO_2 hydrolysis and condensation, as well as Au(III) speciation and reduction. As the optimal pH for the synthesis of mesoporous silica particles falls in the range 8.5-10.5 [42], we

analyzed the effects of sodium tetraborate and triethanolamine (TEOA) maintaining the pH of the reaction nearly constant.

Triggering the reaction with borax at pH 9.0 led to a bimodal distribution with Au@*m*SiO_2 particles having D_{part} = 120±9 nm and *m*SiO_2 particles without gold core (D_{part} 62±9 nm) (Figure 3.21c). Borax alters the nucleation and growth of AuNPs and develops large gold cores (35±6 nm). Despite nearly the same amount of Au(III) being reduced, fewer gold nuclei were formed that grew into large particles, probably because borax introduces steric hindering for gold nucleation. In this scenario, the nucleation of silicate oligomers occurs both homogeneously and heterogeneously on AuNPs, giving the bimodal distribution of particles.

Triethanolamine is a weak base that regulates silica hydrolysis and condensation by the formation of atrane species, allowing control of particle size and often leading to well-dispersible nano-objects [42, 43]. Triggering the reaction at pH 8.5 with TEOA (p*Ka* = 7.8) instead of NaOH (Figure 3.21 d) results in 60±8 nm *m*SiO_2 particles without a gold core and predominantly triangular gold nanoplates with a *m*SiO_2 shell (D_{part} = 106 ± 9 nm). The triangular gold shape was corroborated by the presence of two broad plasmon bands at 550 and 590 nm (Figure 3.21f). The development of triangular nanoplates indicates that in addition to triggering the reaction, TEOA acts as a gold shape-directing agent. This aligns well with previous reports where triangular gold nanoplates were obtained by using CTAB/TEOA mixtures [44]. However, the lack of enough AuNP acting as seeds makes that *m*SiO_2 forms through both homogeneous and heterogeneous nucleation.

The molecular structure of the base used for triggering the reaction influences the particle evolution in *Stage I*, even when the same initial pH is reached. Either Borax or TEOA introduce steric perturbations in the nucleation and growth of AuNP, resulting in respectively larger spheroidal or triangular nanoplates AuNPs. In the case of Borax (Figure 3.21c) larger AuNPs are a consequence of few nuclei growing fast, reducing the availability of Au seeds for

mSiO_2 nucleation. Consequently, the sample contains Au@*m*SiO_2 particles, as well as *m*SiO_2 particles without Au cores. In the case of TEOA, it also guides the growth of the nanoparticles into a defined structure *ie* triangular nanoplates [45, 46].

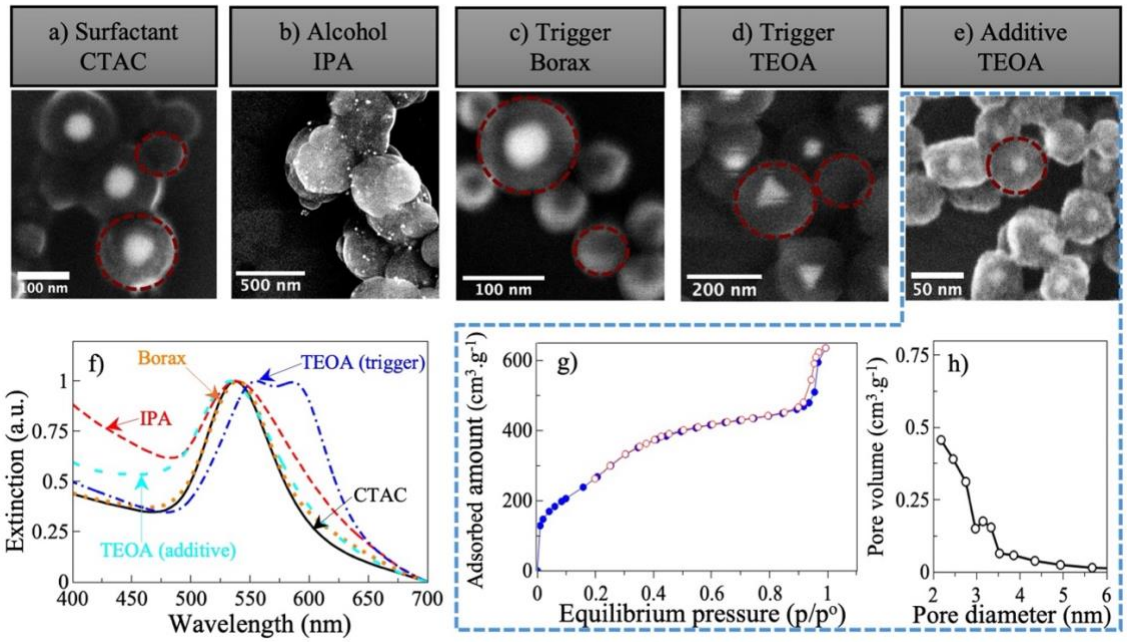

Figure 3.21. Characterization of Au@*m*SiO_2 with different synthesis parameters. SEM micrographs of Au@*m*SiO_2 synthesized with a) Brij C10:CTAC (1:5) instead of CTAB. b) IPA instead of ethanol. c) sodium tetraborate instead of NaOH. d) TEOA instead of NaOH. e) TEOA as additive added 1 min after triggering the reaction with NaOH. f) Normalized UV-vis spectra calcined Au@*m*SiO_2. g) N_2 adsorption (red line) /desorption (blue line) isotherms and (h) BJH pore size distribution of calcined Au@*m*SiO_2 synthesized using NaOH as reaction trigger and TEOA as additive.

Taking advantage of the complexation of Si(IV) by TEOA, we performed the usual pathway using NaOH in step 4 (Figure 3.1) and added TEOA 1 minute after triggering the reaction, so that TEOA would act as a complexant instead of a base. Interestingly, small, monodisperse Au@*m*SiO_2 were obtained (D_{part} = 50 nm) while conserving the 15 nm gold cores and maintaining the characteristic SPR band (Figure 3.21e). The D_{part} of these particles is nearly the same as when the reaction is triggered by TEOA alone (compare Figure 3.21d and e), indicating that TEOA interacts only with the *m*SiO_2 shell already formed on the Au core. N_2 sorption analysis reveals a broader pore distribution between 2.0 and 3.5 nm (Figure 3.21g

and Table 3.4) that suggests dissolution of silica from the pores walls, as reported for mesoporous films in weak basic media [47].

Table 3.4. Characterization data and textural parameters of Au@*m*SiO_2 synthesized by the *one-pot* method and using TEOA as complexant.

[a]D_{part} (nm)	[a]D_{Au} (nm)	[b]DLS (nm)	SBET (m2/g)	[c]Mesopore volume (cm3/g)	[c]BJH Pore diameter (nm)	[c]Gurwich pore diameter (nm)
50±8	15±5	166	988	0.64	2.0-3.0	2.6

[a]Diamenter obtained from SEM

[b]Hydrodynamic diameter

[c]Textural parameters derived from the N_2-sorption isotherm

The presence of TEOA as complexant did not induce significant changes in the hydrolysis kinetics curves, and the cloud point was similar to that of the reaction with CTAB alone. This indicates that TEOA does not alter the hydrolysis kinetics of TEOS under the given reaction conditions (Figure 3.22).

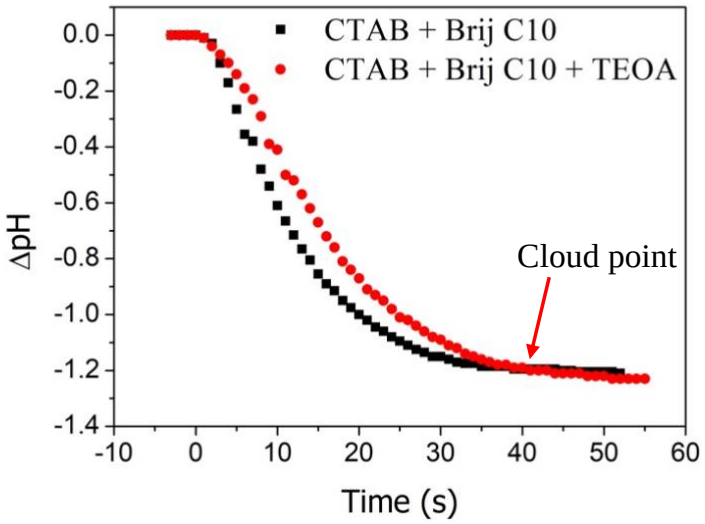

Figure 3.22. Reaction kinetics monitored by pH evolution in solution containing TEOS, ethanol, and water, CTAB, and Brij C10. Reaction performed (black) in the absence of TEOA and (red) in the presence of TEOA.

The addition of complexants that adsorb on the surface modifies the particle surface at *Stage II.* TEOA may form "surface-atranes" [43, 48, 49] on the surface, thus blocking the possibility of condensation between silica building blocks. It should be noted that the surface complexation of TEOA undergoes a fast adsorption kinetics and quenches growth at the size achieved before its addition. SEM micrographs reveals that the timing of TEOA addition in *Stage II* determines the final size of the shell. When TEOA is added 10 minutes after triggering the reaction, the particles have already reached a D_{part} of 103 ± 12 nm, and they maintain that size until the end of the reaction (Figure 3.23 a). Conversely, if TEOA is added one minute after triggering, the final D_{part} is 60 ± 7 nm, as the growth of the shell stops after one minute, transitioning to *Stage III* (Figure 3.23b).

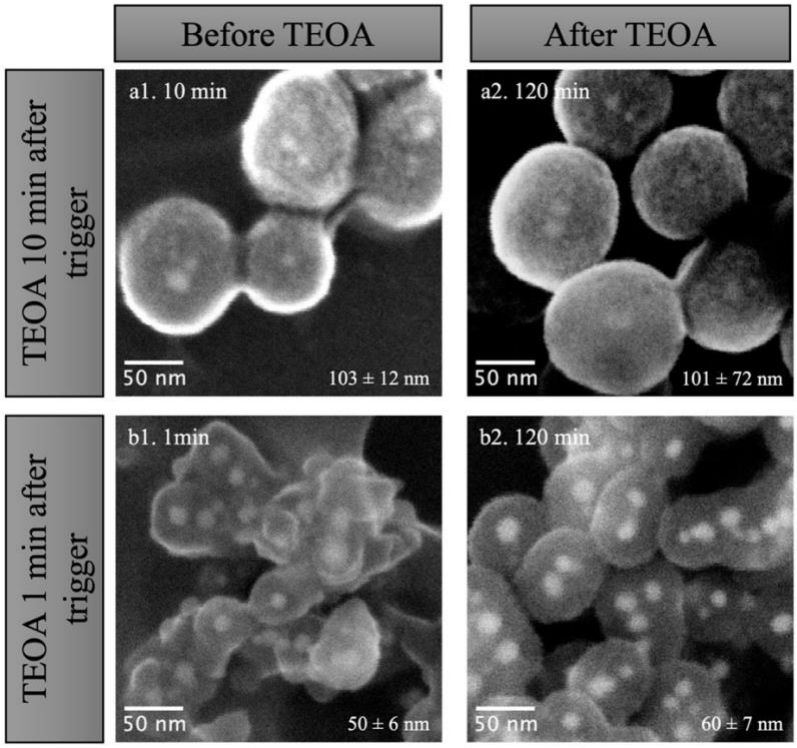

Figure 3.23. SEM micrographs of aliquots taken during the synthesis of Au@*m*SiO_2 (1) before and (2) after the addition of TEOA. The upper panel (a) shows the micrographs of the Au@*m*SiO_2 synthesized when TEOA was added after 10 minutes of triggering the reaction. The lower panel (b) shows the micrographs of the Au@*m*SiO_2 synthesized when TEOA was added after 1 minute of triggering the reaction.

3.4.4 Temperature and gold salt concentration

Other parameters, such as reaction temperature and gold precursor concentration were analyzed. The temperature was systematically varied within the range of 50 to 80 ˚C, resulting in negligible variations in the characteristics of the calcined Au@*m*SiO_2 particles (Figure 3.24).

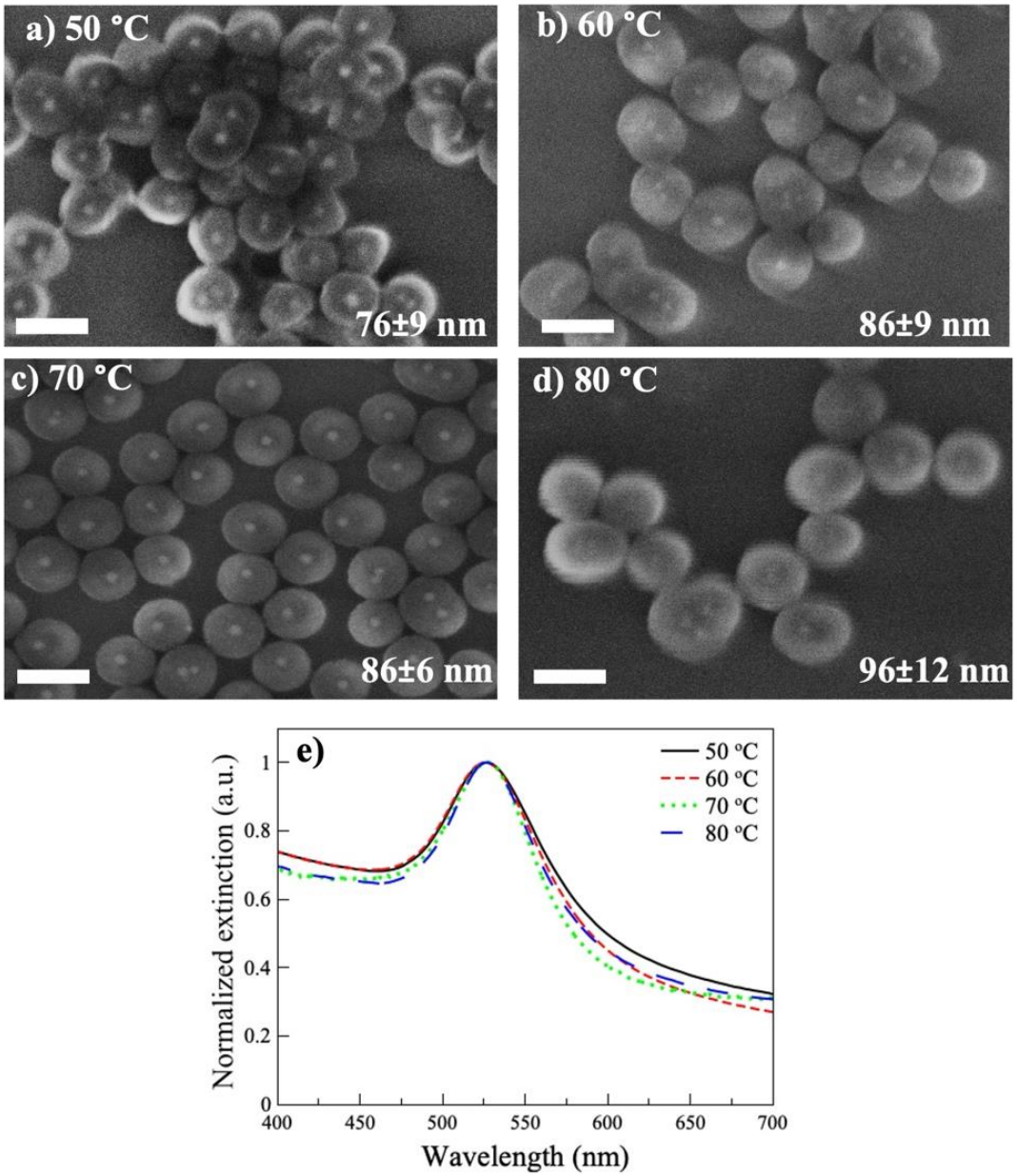

Figure 3.24. Au@*m*SiO_2 synthesized with Brij C10: CTAB (1:5) at different temperatures (a) 50 ˚C, (b) 60 ˚C, (c) 70 ˚C, (d) 80 ˚C. (e) UV-spectra. Scale bar = 100 nm.

Regarding the concentration of the gold precursor, there were no differences in D_{part} or D_{Au}, however, two types of particles were observed when the precursor concentration was halved, yielding both Au@*m*SiO_2 and empty *m*SiO_2 particles (Figure 3.25).

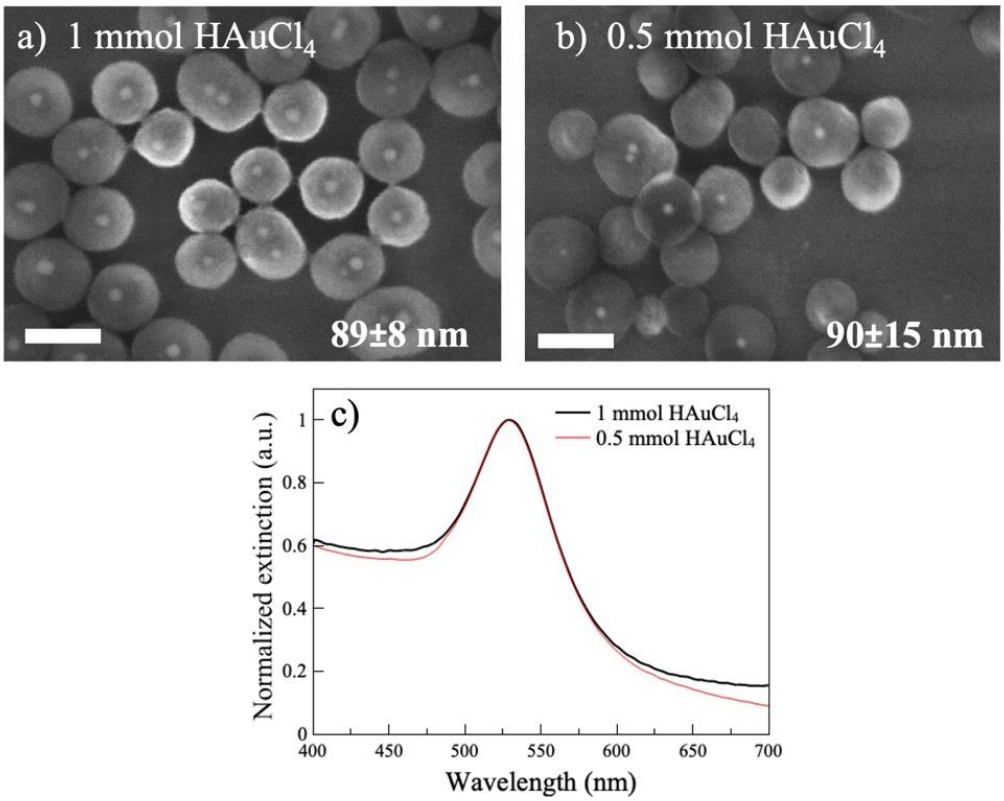

Figure 3.25. Au@*m*SiO_2 synthesized with Brij C10:CTAB (1:5) using (a) 1 mmol $HAuCl_4$ and (b) using 0.5 mmol $HAuCl_4$ (c) UV-spectra. Scale bar = 100 nm.

3.5 Conceptualization

The overall Au@*m*SiO_2 synthesis can be described by considering two independent reaction trajectories: the transformation of Au(III) to AuNPs (gold trajectory) and the conversion of TEOS to *m*SiO_2 (silica trajectory). These trajectories intersect in the reaction space as schematized in Figure 3.26. The starting point of this process is the precursor state, which consists of Au(III)X_4^- (X = Cl, Br, OH), TEOS, and surfactant mixtures in alcohol-water. TEOS and AuX_4^-

are the main players; surfactants are assembled into micelles that act as anchoring points for either mSiO$_2$ building blocks and Au clusters and primary particles, *i.e.* as templates for mSiO$_2$ and capping for AuNPs.

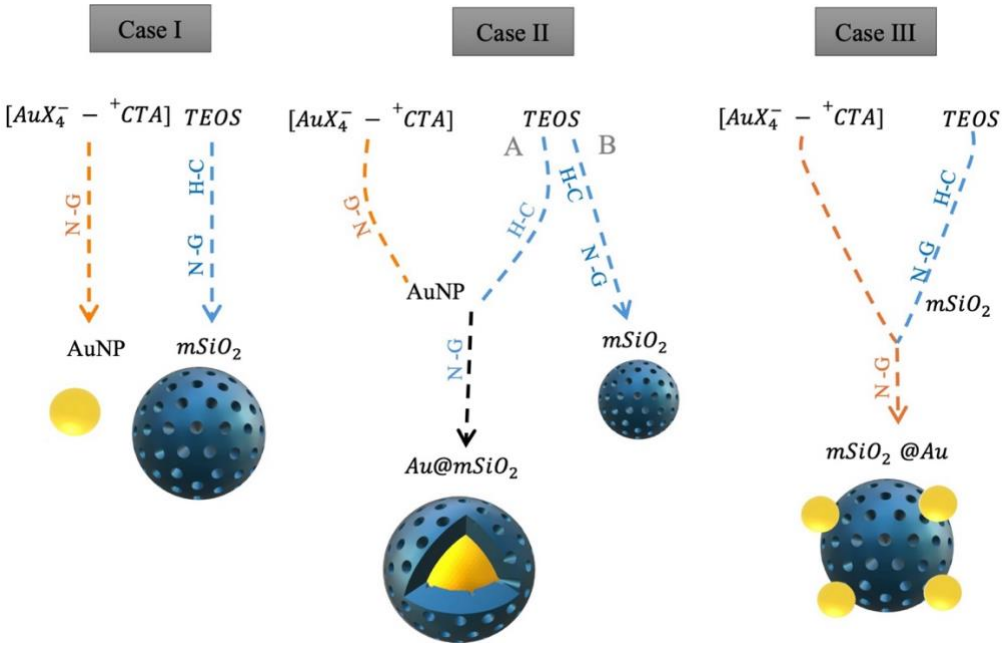

Figure 3.26. Schematic of the possible reaction trajectories in the *one-pot* synthesis of Au@mSiO$_2$. The gold trajectory comprising nucleation and growth (N-G) is shown in orange, the silica trajectory comprising hydrolysis and condensation (H-C) and nucleation and growth (N-G) is shown in blue. Case I: gold and silica trajectories do not intersect. Case II: two scenarios are possible (A) gold trajectory develops before the intersection with silica trajectory leading to core-shell structures; (B) concomitant homogeneous and heterogeneous nucleation of mSiO$_2$ leading to two nanoparticle populations. Case III: gold trajectory develops after the intersection with silica trajectory.

In a limit case where gold and silica trajectories would not intersect, the final state would consist in a collection of independent AuNPs and mSiO$_2$ particles (Figure 3.26, case I). This scenario can be disregarded since micelles interact with hydrolyzed TEOS and AuX_4^- or Au primary particles. When the trajectories of gold and silica intersect, various outcomes are possible, as shown for some particular cases in Figures 3.26, cases II and III.

In case II, the intersection occurs when metastable AuNPs are already formed and there is an incipient evolution of TEOS hydrolysis and condensation:

the gold seeds formed *in situ* are then immediately surrounded by the mesoporous layer (Figure 3.26A). This path requires an appropriate AuNPs/TEOS relationship since insufficient AuNPs leads to *m*SiO_2 particles without gold cores (Figure 3.26B). In case III, trajectories intersect after homogeneous nucleation and growth of the *m*SiO_2 shell (Figure 3.26, case III). Thus, at the crossing point AuNPs either form on the silica surface (heterogeneous nucleation) or in solution (homogeneous nucleation) and are incorporated into *m*SiO_2.

The ideal conditions of case IIA open up several possibilities to tune the size and shape of the core by employing other Au(III) ligands that operate as structure and size directing agents [25, 45, 46, 50]. In this way one could obtain cores with LSPR in the NIR and edges or tips that enhance the electromagnetic field yielding a higher temperature rise at the surface of the particle [51]. The choice of Au(III) ligands should be such that they do not interfere with the growth of the mesoporous layer on the core.

The thickness of the mesoporous layer can also be adjusted by adding surface modifiers that lead to higher colloidal stability [52]. However, these stabilizers should be added after the crossover point, when the processes leading to the development of the mesoporous layer prevail.

3.6 Conclusions

In this chapter, the synthesis of mesoporous silica nanoparticles containing one or more gold cores with a tunable shell thickness was developed on a 200 mg scale by modifying a *one-pot* method [2]. Compared to previous reports, this method enables the preparation of appreciable amounts of nanoparticles which all feature at least a gold core, by contrast to previous reports which afford nanoparticles on milligram scales with a large number of gold-free nanoparticles.

From the proposed mechanism, the key for controlling the overall process – and to achieve reproducible synthesis- is to reach a well-defined precursor state

composed by non-hydrolyzed TEOS, gold complexes and clusters bound to the micelles. In *Stage I* the base triggers the production of enough alcoholate for gold (III) reduction and NP growth so that AuNPs develop in less than 6 s together with first hydrolysis of TEOS. In *Stage II,* TEOS condensation occurs, forming the mesoporous layer, which becomes detectable after 60 seconds. During this phase, the mesoporous silica shell continues to grow until *Stage III,* where the particles stabilize in size, and the percentage of reduced gold increases from 30% to 70% of the initial Au(III), with the gold nanoparticles becoming more spherical and monodisperse.

The mechanism drawn from our results and the wide knowledge on *m*SiO_2 and AuNPs synthesis account for the role of Au@*m*SiO_2 synthesis parameters. This mechanism is described from the individual trajectories Au(III) →AuNP and TEOS→*m*SiO_2 which cross at some point in the reaction space. The crossover point would define the conditions under which the core-shell particles are built-up. This scenario allows to draw criteria for modifying the size and shape of the core, as well as the thickness of the shell. Within this framework, and considering also the dispersability of particles in aqueous solutions, the BrijC10:CTAB (1:5) was considered as optimal and will be used in chapter 5 for the analysis of protein loading (*sp*-Au@*m*SiO_2).

Attempts to widen pores with surfactants or co-solvents forming bigger micelles, as usually reported in templated sol-gel methods, alters the precursor state leading to nanoparticles with large gold cores or gold located at the surface of silica particles. These examples highlight how such parameters can affect the chemistry of gold species. Nevertheless, the core-shell Au@*m*SiO_2 particles with a thin mesoporous silica shell can act as seeds to promote the formation of an additional layer of silica with large pores (8-13 nm) able to carry large biomolecules, as demonstrated in Chapter 4.

3.7 References

1. Anastas PT, Warner JC (2000) Green Chemistry: Theory and Practice, online edn. Oxford

2. Croissant J, Zink JI (2012) Nanovalve-Controlled Cargo Release Activated by Plasmonic Heating. J Am Chem Soc 134:7628–7631. https://doi.org/10.1021/ja301880x

3. Kamiya K, Yoko T (1986) Synthesis of SiO2 glass fibres from Si(OC2Hs)4-H20-C2HsOH-HCI solutions through sol-gel method

4. Cheng W, Dong S, Wang E (2003) Synthesis and Self-Assembly of Cetyltrimethylammonium Bromide-Capped Gold Nanoparticles. Langmuir 19:9434–9439. https://doi.org/10.1021/la034818k

5. Fenger R, Fertitta E, Kirmse H, et al (2012) Size dependent catalysis with CTAB-stabilized gold nanoparticles. Physical Chemistry Chemical Physics 14:9343–9349. https://doi.org/10.1039/c2cp40792b

6. Pastoriza-Santos I, Pérez-Juste J, Liz-Marzán LM (2006) Silica-coating and hydrophobation of CTAB-stabilized gold nanorods. Chemistry of Materials 18:2465–2467. https://doi.org/10.1021/cm060293g

7. Chen J, Zhang R, Han L, et al (2013) One-pot synthesis of thermally stable gold@mesoporous silica core-shell nanospheres with catalytic activity. Nano Research 6:871–879. https://doi.org/10.1007/s12274-013-0363-1

8. Gao C, Lyu F, Yin Y (2021) Encapsulated Metal Nanoparticles for Catalysis. Chemical Reviews 121:834–881. https://doi.org/10.1021/acs.chemrev.0c00237

9. Zuo B, Li W, Wu X, et al (2020) Recent Advances in the Synthesis, Surface Modifications and Applications of Core-Shell Magnetic Mesoporous Silica Nanospheres. Chemistry - An Asian Journal 15:1248–1265. https://doi.org/10.1002/asia.202000045

10. Cattoën X, Kodjikian S, Trens P (2023) Periodic mesoporous organosilica nanoparticles: Morphology control and sorption properties. Colloids and Surfaces A: Physicochemical and Engineering Aspects 677:132325–132325. https://doi.org/10.1016/j.colsurfa.2023.132325

11. Alvarado Meza R, Santori T, Cattoën X (2023) A kinetic approach to the mechanism of formation of mesoporous silica nanoparticles. Journal of Sol-Gel Science and Technology. https://doi.org/10.1007/s10971-023-06130-w

12. Quinson J, Aalling-Frederiksen O, Dacayan WL, et al (2023) Surfactant-Free Colloidal Syntheses of Gold-Based Nanomaterials in Alkaline Water and Mono-alcohol Mixtures. Chemistry of Materials 35:2173–2190. https://doi.org/10.1021/acs.chemmater.3c00090

13. Grün M, Lauer I, Unger KK (1997) The synthesis of micrometer- and submicrometer-size spheres of ordered mesoporous oxide MCM-41. Advanced Materials 9:254–257. https://doi.org/10.1002/adma.19970090317

14. Liu S, Lu L, Yang Z, et al (2006) Further investigations on the modified Stöber method for spherical MCM-41. Materials Chemistry and Physics 97:203–206. https://doi.org/10.1016/j.matchemphys.2005.09.003

15. Goia DV, Matijevic (1999) Tailoring the particle size of monodispersed colloidal gold. Colloids Surf A: Physicochem Eng Asp 146:139–152

16. Durović MD, Puchta R, Bugarčić ŽD, Van Eldik R (2014) Studies on the reactions of [AuCl4]- with different nucleophiles in aqueous solution. Dalton Transactions 43:8620–8632. https://doi.org/10.1039/c4dt00247d

17. Usher A, McPhail DC, Brugger J (2009) A spectrophotometric study of aqueous Au(III) halide-hydroxide complexes at 25-80 °C. Geochimica et Cosmochimica Acta 73:3359–3380. https://doi.org/10.1016/j.gca.2009.01.036

18. Khan MN, Khan TA, Al-Thabaiti SA, Khan Z (2015) Spectrophotometric evidence to the formation of AuCl4-CTA complex and synthesis of gold nano-flowers with tailored surface textures. Spectrochimica Acta - Part A: Molecular and Biomolecular Spectroscopy 149:889–897. https://doi.org/10.1016/j.saa.2015.04.088

19. Khan Z, Singh T, Hussain JI, Hashmi AA (2013) Au(III)-CTAB reduction by ascorbic acid: Preparation and characterization of gold nanoparticles. Colloids and Surfaces B: Biointerfaces 104:11–17. https://doi.org/10.1016/j.colsurfb.2012.11.017

20. Pérez-Juste J, Pastoriza-Santos I, Liz-Marzán LM, Mulvaney P (2005) Gold nanorods: Synthesis, characterization and applications. Coord Chem Rev 249:1870–1901. https://doi.org/10.1016/j.ccr.2005.01.030

21. Rodríguez-Fernández J, Pérez-Juste J, Mulvaney P, Liz-Marzán LM (2005) Spatially-Directed Oxidation of Gold Nanoparticles by Au(III)−CTAB Complexes. J Phys Chem B 109:14257–14261. https://doi.org/10.1021/jp052516g

22. Tang J, Huang J, Man SQ (2013) Preparation of gold nanoparticles by surfactant-promoted reductive reaction without extra reducing agent. Spectrochimica Acta - Part A: Molecular and Biomolecular Spectroscopy 103:349–355. https://doi.org/10.1016/j.saa.2012.10.049

23. Echeverría JC, Moriones P, Arzamendi G, et al (2018) Kinetics of the acid-catalyzed hydrolysis of tetraethoxysilane (TEOS) by 29Si NMR spectroscopy and mathematical modeling. Journal of Sol-Gel Science and Technology 86:316–328. https://doi.org/10.1007/s10971-018-4637-7

24. Sanchez J, McCormick A (1992) 5) Birks, J. B. Photophysics of Aromatic Molecules. Wiley-Interscience. ISBN 9780471074205.

25. Wuithschick M, Birnbaum A, Witte S, et al (2015) Turkevich in New Robes: Key Questions Answered for the Most Common Gold Nanoparticle Synthesis. ACS Nano 9:7052–7071. https://doi.org/10.1021/acsnano.5b01579

26. Turkevich J, Stevenson PC, Hillier J (1951) A study of the nucleation and growth processes in the synthesis of colloidal gold. Discuss Faraday Soc 11:55–75. https://doi.org/10.1039/DF9511100055

27. Frens G (1973) Controlled Nucleation for the Regulation of the Particle Size in Monodisperse Gold Suspensions. Nature Physical Science 241:20–22. https://doi.org/10.1038/physci241020a0

28. Hendel T, Wuithschick M, Kettemann F, et al (2014) In Situ Determination of Colloidal Gold Concentrations with UV–Vis Spectroscopy: Limitations and Perspectives. Anal Chem 86:11115–11124. https://doi.org/10.1021/ac502053s

29. Scarabelli L, Sánchez-Iglesias A, Pérez-Juste J, Liz-Marzán LM (2015) A "Tips and Tricks" Practical Guide to the Synthesis of Gold Nanorods. Journal of Physical Chemistry Letters 6:4270–4279. https://doi.org/10.1021/acs.jpclett.5b02123

30. Hargittai M, Schulz A, Réffy B, Kolonits M (2001) Molecular Structure, Bonding, and Jahn−Teller Effect in Gold Chlorides: Quantum Chemical Study of AuCl3, Au2Cl6, AuCl4-, AuCl, and Au2Cl2 and Electron Diffraction Study of Au2Cl6. J Am Chem Soc 123:1449–1458. https://doi.org/10.1021/ja003038k

31. Bogush GH, Zukoski Iv CF (1991) Uniform Silica Particle Precipitation: An Aggregative Growth Model. Journal of Colloid and Interface Science 142:19–34. https://doi.org/10.1016/0021-9797(91)90030-C

32. Wang F, Richards VN, Shields SP, Buhro WE (2014) Kinetics and Mechanisms of Aggregative Nanocrystal Growth. Chem Mater 26:5–21. https://doi.org/10.1021/cm402139r

33. Kankala RK, Han YH, Na J, et al (2020) Nanoarchitectured Structure and Surface Biofunctionality of Mesoporous Silica Nanoparticles. Advanced Materials 32:. https://doi.org/10.1002/adma.201907035

34. Oh JH, Lee JS (2018) One-Pot Photochemical Synthesis of Gold Nanoplates Using Nonionic Diblock Copolymers and their Surface Functionalization. Bulletin of the Korean Chemical Society 39:1165–1170. https://doi.org/10.1002/bkcs.11569

35. Chakraborty T, Ghosh S, Moulik SP (2005) Micellization and related behavior of binary and ternary surfactant mixtures in aqueous medium: Cetyl pyridinium chloride (CPC), Cetyl trimethyl ammonium bromide (CTAB), and polyoxyethylene (10) cetyl ether (Brij-56) derived system. Journal of Physical Chemistry B 109:14813–14823. https://doi.org/10.1021/jp044580o

36. Meng H, Xue M, Xia T, et al (2011) Use of size and a copolymer design feature to improve the biodistribution and the enhanced permeability and retention effect of doxorubicin-loaded

mesoporous silica nanoparticles in a murine xenograft tumor model. ACS Nano 5:4131–4144. https://doi.org/10.1021/nn200809t

37. Mohanan S, Sathish CI, Ramadass K, et al (2023) Design and Synthesis of Cabazitaxel Loaded Core-Shell Mesoporous Silica Nanoparticles with Different Morphologies for Prostate Cancer Therapy. Small. https://doi.org/10.1002/smll.202303269

38. Yoon S, Kim C, Lee B, Lee JH (2019) From a precursor to an etchant: Spontaneous inversion of the role of Au(iii) chloride for one-pot synthesis of smooth and spherical gold nanoparticles. Nanoscale Advances 1:2157–2161. https://doi.org/10.1039/c9na00157c

39. Bari AH, Jundale RB, Kulkarni AA (2020) Understanding the role of solvent properties on reaction kinetics for synthesis of silica nanoparticles. Chemical Engineering Journal 398:. https://doi.org/10.1016/j.cej.2020.125427

40. Mine E, Nagao D, Kobayashi Y, Konno M (2005) Solvent Effects on Particle Formation in Hydrolysis of Tetraethyl Orthosilicate. J Sol-Gel Sci Technol 35:197–201. https://doi.org/10.1007/s10971-005-2289-x

41. Liu S, Cool P, Collart O, et al (2003) The Influence of the Alcohol Concentration on the Structural Ordering of Mesoporous Silica: Cosurfactant versus Cosolvent. J Phys Chem B 107:10405–10411. https://doi.org/10.1021/jp034410w

42. Qiao ZA, Zhang L, Guo M, et al (2009) Synthesis of mesoporous silica nanoparticles via controlled hydrolysis and condensation of silicon alkoxide. Chemistry of Materials 21:3823–3829. https://doi.org/10.1021/cm901335k

43. Möller K, Kobler J, Bein T (2007) Colloidal suspensions of nanometer-sized mesoporous silica. Advanced Functional Materials 17:605–612. https://doi.org/10.1002/adfm.200600578

44. Miranda A, Malheiro E, Skiba E, et al (2010) One-pot synthesis of triangular gold nanoplates allowing broad and fine tuning of edge length. Nanoscale 2:2209–2216. https://doi.org/10.1039/C0NR00337A

45. Qin X, Gu C, Wang M, et al (2018) Triethanolamine-Modified Gold Nanoparticles Synthesized by a One-Pot Method and Their Application in Electrochemiluminescent Immunoassy. Analytical Chemistry 90:2826–2832. https://doi.org/10.1021/acs.analchem.7b04952

46. Tu X, Li X, Liu B, et al (2024) Facile one-pot synthesis of triethanolamine-functionalized AuNPs-GO-UiO-66-NH2 nanocomposites for simultaneous electrochemical detection of Cd(II), Pb(II), and Cu(II). J Solid State Electrochem 28:433–444. https://doi.org/10.1007/s10008-023-05697-2

47. Onna D, Marchi MC, Martínez Ricci ML, Bilmes SA (2022) Loading insoluble sulfides in mesoporous oxide films from precursors in solution. J Sol-Gel Sci Technol 102:264–278. https://doi.org/10.1007/s10971-021-05718-4

48. Cabrera SL, Haskouri JE, Guillem C, et al (2000) Generalised syntheses of ordered mesoporous oxides: the atrane route. Solid State Sci 2:405–420. https://doi.org/10.1016/S1293-2558(00)00152-7

49. Garrido MD, El Haskouri J, Vie D, et al (2022) Generalized “one-pot” preparative strategy to obtain highly functionalized silica-based mesoporous spherical particles. Microporous and Mesoporous Materials 337:111942. https://doi.org/10.1016/j.micromeso.2022.111942

50. Kapil N, Cardinale F, Weissenberger T, et al (2021) Gold nanoparticles with tailored size through ligand modification for catalytic applications. Chemical Communications 57:10775–10778. https://doi.org/10.1039/D1CC04165G

51. Agarwal NR, Ossi PM, Trusso S (2019) Driving electromagnetic field enhancements in tailored gold surface nanostructures: Optical properties and macroscale simulations. Applied Surface Science 466:19–27. https://doi.org/10.1016/j.apsusc.2018.09.251

52. Semeykina V, Zharov I (2022) Medium controlled aggregative growth as a key step in mesoporous silica nanoparticle formation. Journal of Colloid and Interface Science 615:236–247. https://doi.org/10.1016/j.jcis.2022.01.166

Chapter 4

Two-steps synthesis of large-pores Au@*m*SiO_2

4.1. Introduction

Au@*m*SiO_2 nanoparticles represent a promising class of mesoporous materials that combine the unique optical properties of gold nanoparticles with the capacity of mesoporous silica nanoparticles (MSN) to efficiently retain and transport various molecules. To facilitate the on-demand delivery of large molecular weight biomolecules, such as proteins, using the gold photothermal effect as a trigger, it is crucial to focus on enlarging the pore size of the Au@*m*SiO_2 particle shell. While numerous Au@*m*SiO_2 particles have been synthesized predominantly through stepwise methods, and a few through *one-pot* methods, there has been only marginal progress in tuning the pore size, with reported pore sizes smaller than 4 nm (See Table A1 and A2 in Appendix). This limitation is presumably due to a lack of understanding of the complex synthesis mechanism.

For MSN, various synthesis strategies have been reported to enlarge the pores from 2 to 50 nm [1–12]. However, controlling pore size and particle size

while maintaining well-dispersed, uniform, and colloidally stable particles remains a challenge [10]. The use of additional agents to enlarge pores often alters both the hydrolysis and condensation rates of the silica sources, significantly affecting the size distribution of the MSNs. In the synthesis of Au@*m*SiO_2, which involves a more complex mechanism, the use of agents to enlarge pores can also lead to problems with gold nucleation, thus making it impractical to apply the same strategies used for MSN under a *one-pot* approach. For instance, in Chapter 3, it was demonstrated that adding pore-expanding agents, solvents, or co-solvents alters the precursor state of Au@*m*SiO_2, leading to undesired results that affect the core-shell structure.

To address the challenges of enlarging the pores of MSN, seed-growth methods have been proposed to obtain uniform, well-dispersed particles with controlled size and pore size through a step-by-step preparation of MSNs [13–17]. A similar approach may thus be used for the synthesis of Au@*m*SiO_2, where well-consolidated particles containing a gold core and a thin mesoporous silica shell would be used as starting seeds. The silica shells could then be grown using strategies to enlarge pores without altering the already formed gold cores. In general, two synthetic approaches have been developed for the synthesis of large-pore MSN using seed-growth methods. The first one involves growing the seed with pore-expanding agents that form larger micelles, thus enlarging the template [18]. The second one involves a growth by biphasic stratification using an oil-based microemulsion approach [6].

One of the main advantages of using MSNs in the development of nanocarriers for drug delivery is their ability to degrade through hydrolysis under physiological conditions. To harness this property in Au@*m*SiO_2, the mesoporous shell must strike a balance between stability and biodegradability to ensure safe transport of proteins to the target site while also minimizing toxicity through biodegradation. The degradation rate of silica is mainly determined by two factors: structural-textural characteristics (such as morphology, porosity, condensation degree of the silica network, and surface

chemistry) and medium conditions (including pH, concentration, and additives) [19–22]. As a result, the degradation time of MSNs can range from a few hours to several weeks, depending on their physicochemical properties.

AuNPs are typically regarded as relatively non-toxic due to their inert properties, enabling their retention in tissues over prolonged periods without substantial adverse effects. Nonetheless, long-term studies indicate that AuNPs may recrystallize into biopersistent clusters, which raises potential concerns regarding accumulation and toxicity [23, 24]. While numerous studies have explored how these parameters influence the stability of MSNs and AuNPs, there is currently no information on the stability and degradation behavior of Au@*m*SiO_2.

This chapter presents the adaptation and optimization of seed-growth methods using both the pore-expanding agents and biphasic stratification approaches. Both methods start with Au@*m*SiO_2 seeds that have a particle diameter (D_{part}) of ~50 nm, consisting of a 15 nm gold core and an 18 nm thick silica shell with mesopores of 3 nm. These particles, referred to as *seed*-Au@*m*SiO_2, were synthesized using a combination of BrijC10:CTAB:TEOS:$HAuCl_4$:NaOH:TEOA in the ratio (1:5:12.8:0.42:3.4:4.1). The seed growth methods produce large-pore Au@*m*SiO_2 (*lp*-Au@*m*SiO_2), achieving pores sizes up to 8 nm with pore-expanding agents and up to 20 nm using the biphasic stratification approach. The stability of the synthesized particles was analyzed, revealing a direct relationship between the synthesis method and particle concentration on nanoparticle stability.

4.2. Growth with pore-expanding agents

In this section, we detail the synthesis of Au@*m*SiO_2 with tunable porosities using *seed*-Au@*m*SiO_2, CTAB as a template, triisopropylbenzene (TIPB) as a pore-expanding agent, and tetra *n*-propyl orthosilicate (TPOS) as a silica source (Figure 4.1). TPOS has slower hydrolysis kinetics compared to the commonly used tetraethyl orthosilicate (TEOS). This leads to low supersaturation of hydrolyzed silicates in solution, which can then preferentially add on the existing NPs rather than form new nuclei. The mesoporosity of the final Au@*m*SiO_2 can be tailored depending on the amount of TIPB added during shell growth. This growth method was adapted from a synthesis procedure reported by Kuroda's group for pore-expanded MSN with controlled size [18], and used recently by V Guerrero-Florez in our group [22]. Hereafter the particles synthesized with this method are referred to as *e*-Au@*m*SiO_2, where the prefix "***e***" denotes the use of pore-expanding agents in the seed growth process.

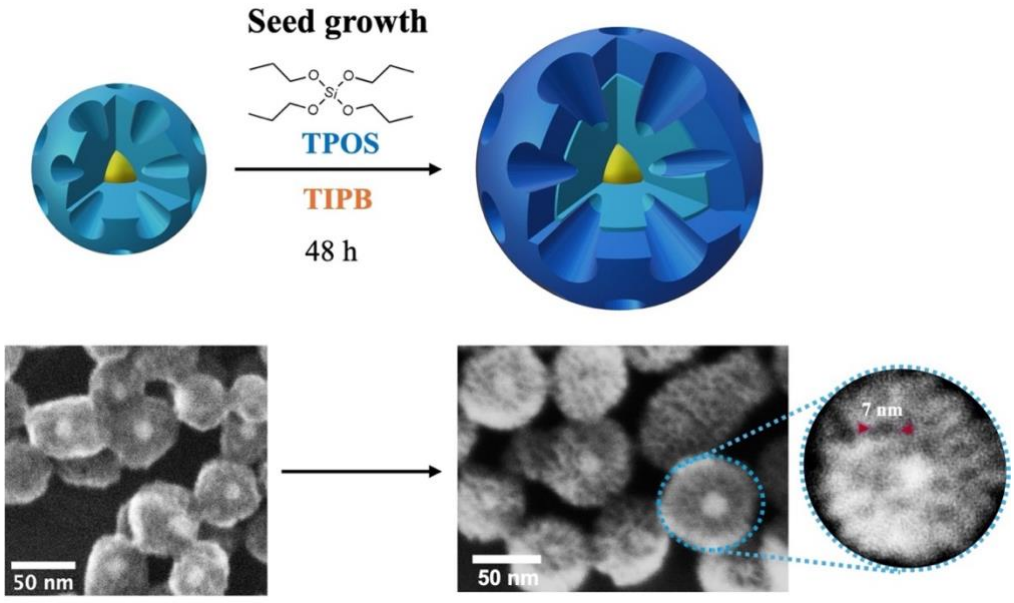

Figure 4.1. Top: Schematic illustration of the preparation of monodisperse *e*-Au@*m*SiO_2 by seed growth using TIPB as pore expanding agent and TPOS as silica source. Gold core in yellow, seed silica shell in light blue, and grown silica shell in blue. Bottom: SEM characterization of the *seed*-Au@*m*SiO_2 and the final *e*-Au@*m*SiO_2 for a 2*y* TIPB concentration.

The *e*-Au@*m*SiO_2 particles, with diameters ranging from 60 to 90 nm, exhibited good dispersibility. Their pore size could be tuned by varying the concentration of TIPB from 0 to 2*y*, corresponding to 0, 0.6, 1.2, 2, 3 and 6.2 mM TIPB in solution (Figure 4.2 and Table 4.1). No significant changes in the size or morphology of AuNPs were observed after the seed growth process, as confirmed by UV-vis spectroscopy (Figure 4.2g). There was no apparent correlation between the amount of TIPB and the particle size. Regardless of the TIPB concentration, the particles maintained monodispersity and good dispersibility, yielding between 100 and 150 mg of *e*-Au@*m*SiO_2. For a reaction volume of 140 mL, this represents a yield of 20-35%. SEM micrographs indicated that TIPB concentrations enabled the synthesis of *e*-Au@*m*SiO_2 particles with pores up to 7 nm in diameter.

Table 4.1. Characterization data of *e*-Au@*m*SiO_2 obtained with different TIPB concentrations. Particle diameters (D_{part}) and nanoparticle percentages were determined from SEM micrographs. Hydrodynamic diameters were measured using DLS.

TIPB (*y*)	**D_{part} (nm)**	**Hydrodynamic diameter (nm)**	**% NP without Au core**	**% NP with >1 Au cores**	**% NP with 1 Au core**
0	89 ± 10	190	27.6	22.2	50.2
0.2	79 ± 9	209	14.6	30.6	54.8
0.4	65 ± 7	76	29.6	24.8	45.6
0.6	80 ± 9	168	28.5	20	51.5
1	59 ± 8	218	41.7	18.8	39.5
2	61 ± 8	176	24.7	7.3	68

For a more precise characterization of the textural parameters of these particles, N_2-sorption measurements were conducted on *e*-Au@*m*SiO_2 synthesized with 0.4*y* TIPB, whose TEM image is shown in Figure 4.2i. The sorption isotherms obtained exhibited Type IV characteristics according to the IUPAC classification, which is typical for CTAB-templated materials (Figure 4.2h). The *t*-plot analysis of the sorption isotherms excluded the presence of micropores in significant amounts. The specific surface area obtained was 908 m^2/g. The main sorption uptake takes place over a wide range between $p/p^\circ = 0.3$ and 0.5, indicating the presence of mesopores with a broad size distribution. Indeed, according to the BJH analysis, the pore size distribution ranges from 2 to approximately 5 nm, with average pore diameters of 3.5 nm (see Table 4.2). The mesopores filling at around $0.2 < p/p^0 < 0.5$ is reversible, which strongly suggests that the largest mesopores exhibit a conical shape [25]

Table 4.2. Textural parameters derived from the N_2-sorption isotherms for *e*-Au@*m*SiO_2 synthesized with 0.4*y* TIPB.

TIPB (*y*)	**SBET (m^2/g)**	**Mesopore volume (cm^3/g)**	**BJH Pore diameters (nm)**
0.4	908	0.71	2—5

The observed size variations among particles synthesized with different TIPB concentrations can be attributed to aggregation, coalescence, and Ostwald ripening processes during the seed growth stage. These phenomena was also reported by Kuroda's group, when the same approach was used to synthesize large-pore MSN particles [18]. In the synthesis of *e*-Au@*m*SiO_2, the size variation is more pronounced because the *seed*-Au@*m*SiO_2 suspension contains not only the Au@*m*SiO_2 seeds but also uncoated AuNPs, as evidenced by the recovery of a violet-colored supernatant upon particle centrifugation. When the entire mixture

is introduced into the growth medium, silica nucleates using both the *seed*-Au@*m*SiO_2 and the remaining AuNPs as nuclei. This uneven silica shell growth results in the formation of *e*-Au@*m*SiO_2 particles of varying sizes.

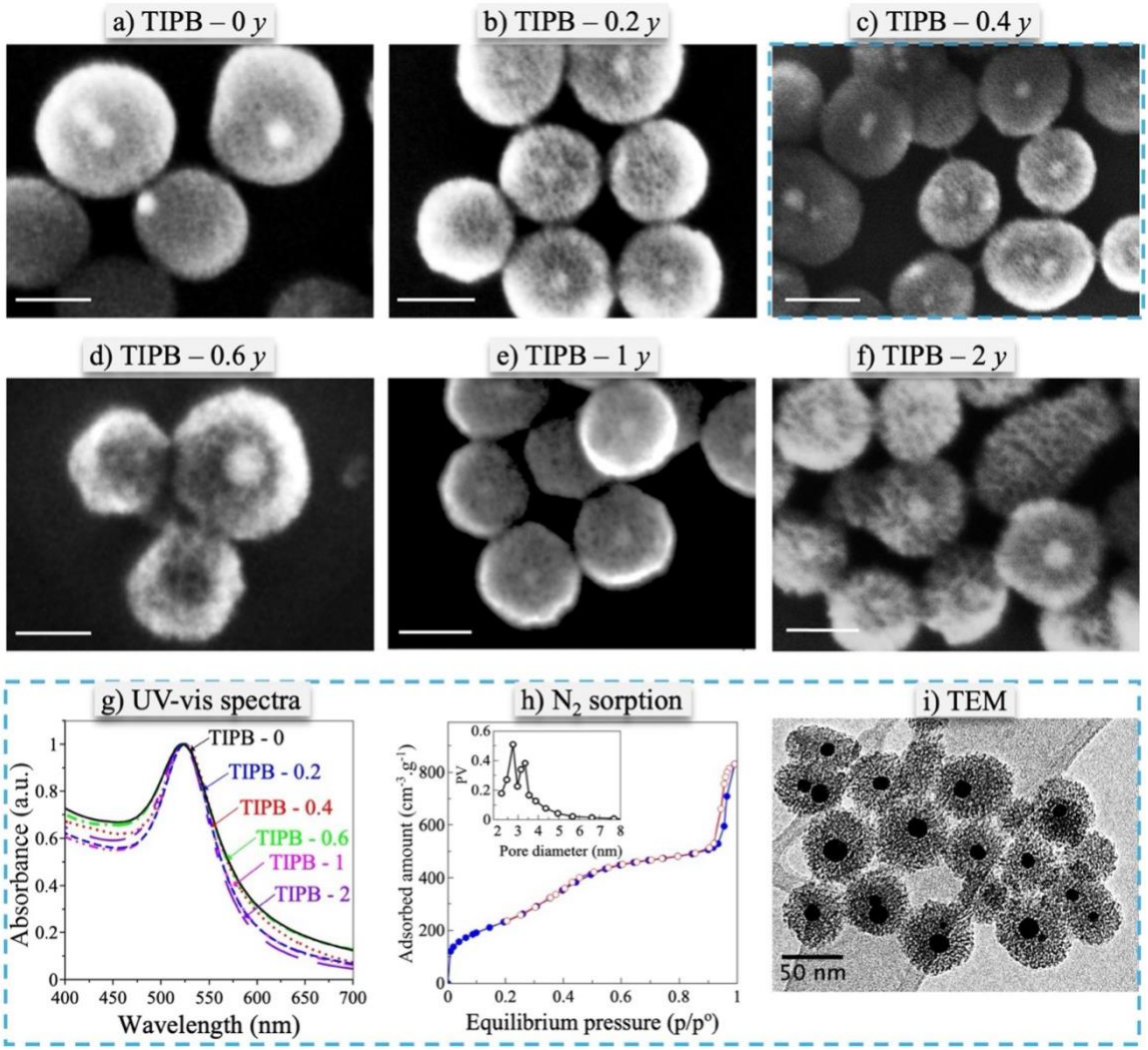

Figure 4.2. Characterization of *e*-Au@*m*SiO_2 obtained with different TIPB concentrations. SEM micrographs of *e*-Au@*m*SiO_2 synthesized with a) 0*y* TIPB, b) 0.2*y* TIPB, c) 0.4*y* TIPB, d) 0.6*y* TIPB, e) 1*y* TIPB, and f) 2*y* TIPB (Scale bar = 100 nm). g) Normalized UV-vis spectra for *e*-Au@*m*SiO_2 obtained with different TIPB concentrations. h) N_2 adsorption (blue line) /desorption (red line) isotherms for 0.4*y* TIPB, the inset shows the BJH pore size distribution. i) TEM micrographs for 0.4*y* TIPB.

Regardless of TIPB concentration, between 15% to 42% of MSN particles without a gold core were also observed (Table 4.1). This is likely due to the spontaneous generation of nuclei during seed formation or shell growth. To optimize this parameter, *e*-Au@*m*SiO_2 synthesis was performed with variations in the seed synthesis procedure.

The analysis of Au@*m*SiO_2 synthesis parameters, as detailed in Chapter 3, Section 3.4.4, revealed that the [TEOS]:[Au] ratio significantly affects the formation of either empty silica particles or particles with a gold core. Specifically, a lower concentration of the gold precursor resulted in a higher proportion of MSNs without a gold core. To address this, we adjusted the TEOS concentration during seed synthesis, preparing Au@*m*SiO_2 seeds with 1*x*, 0.5*x*, 0.25*x*, and 0.2*x* TEOS (were 1*x* represents the previously used TEOS amount). SEM images of these seeds, taken directly from the reaction medium before washing and growth, are presented in Figure 4.3 for the samples synthesized with 1*x*, 0.25*x*, and 0.2*x* TEOS. The micrographs reveal that when 1*x* TEOS is used, both uncoated AuNPs and empty MSNs are present. By contrast, the seeds synthesized with 0.25*x* and 0.2*x* TEOS show no empty MSNs, and instead, several particles containing multiple Au cores are observed.

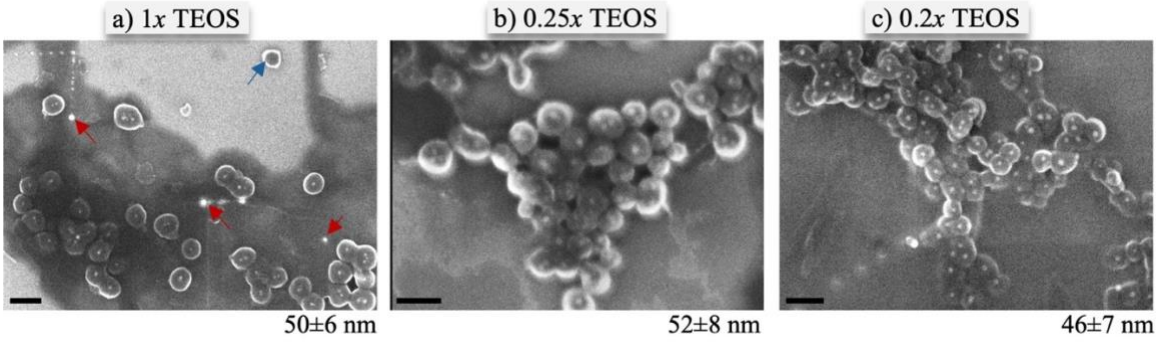

Figure 4.3. SEM micrographs of Au@*m*SiO_2 seeds synthesized with a) 1*x*, b) 0.25*x*, and c) 0.2*x* TEOS. Red arrows indicate AuNPs that are not coated with a silica shell, while blue arrow point MSN that lack a gold core. Scale bar = 50 nm.

Based on this observation, to improve the synthesis yield and maximize the number of Au@*m*SiO_2 particles containing at least one gold core while minimizing the formation of empty MSNs, we synthesized *e*-Au@*m*SiO_2 using seeds produced with 1*x*, 0.5*x*, or 0.2*x* TEOS while the shell growth was performed with 2*y* TIPB. The corresponding SEM micrographs and UV-Vis spectra of these particles are shown in Figure 4.4.

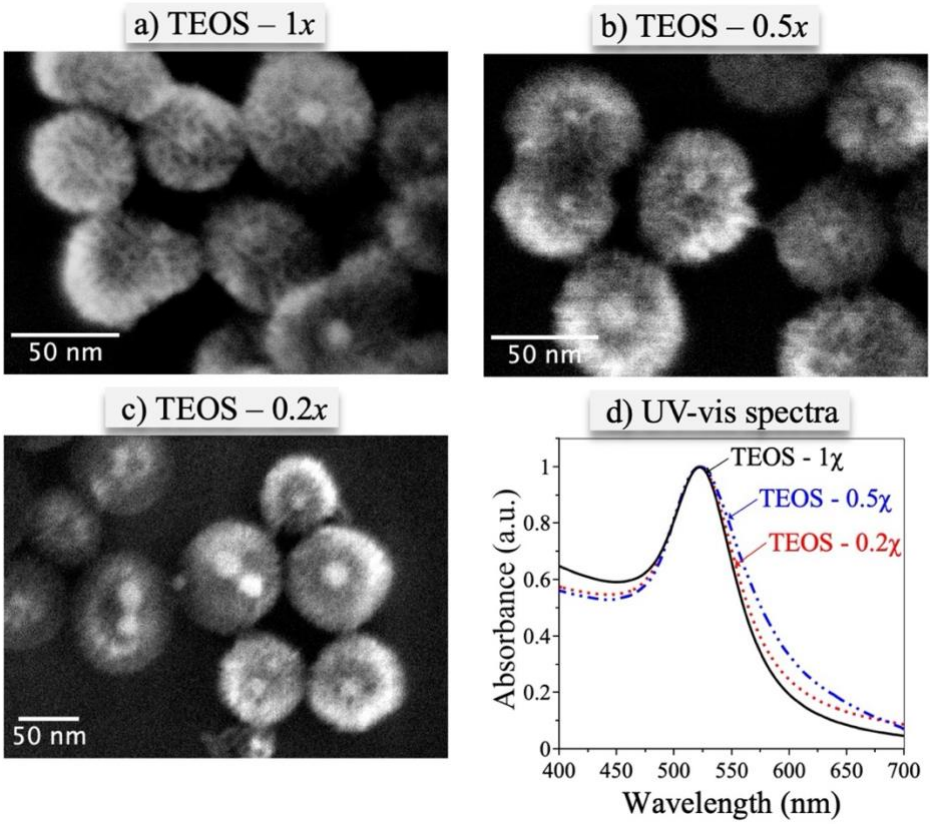

Figure 4.4. SEM micrographs of *e*-Au@*m*SiO_2 synthesized with 2*y* TIPB during shell growing and seeds obtained with a) 1*x*, b) 0.5*x*, and c) 0.2*x* TEOS. Normalized UV-vis spectra of the final *e*-Au@*m*SiO_2 particles.

e-Au@*m*SiO_2 synthesized with 1*x* TEOS had 25% MSN particles without a gold core. Reducing TEOS to 0.5*x* decreased the proportion of MSN particles to 9%, while further reducing TEOS to 0.2*x* eliminated MSN particles entirely. However, with 0.5*x* and 0.2*x* TEOS, the proportion of particles with two or more cores increased significantly, reaching 46% and 80.6%, respectively (Table 4.3).

Notably, *e*-Au@*m*SiO_2 synthesized with 0.2*x* TEOS exhibited the highest D_{part}, suggesting coalescence of particles during shell growth that lead to the synthesis of *e*-Au@*m*SiO_2 with multiple cores (Figure 4.4c). This coalescence is also suggested by the increase in diameter from 60 to 90 nm when *x* is reduced.

Table 4.3. Characterization data of *e*-Au@*m*SiO_2 synthesized with 2*y* TIPB during shell growing and seeds obtained with 1*x*, 0.5*x* and 0.2*x* TEOS. Particle diameters (D_{part}) and nanoparticle percentages were determined from SEM micrographs. Hydrodynamic diameters were measured using DLS.

TEOS (x)	D_{part} (nm)	Hydrodynamic diameter (nm)	% NP without Au core	% NP with Au core >1	% NP with Au core = 1
1*x*	61 ± 8	176	24.7	7.3	68.0
0.5*x*	65 ± 8	121	9.4	46.0	44.6
0.2*x*	90 ± 11	267	0	80.6	19.4

In summary, seed growth using TIPB as pore-expanding agent an TPOS as silica source allowed to obtain Au@*m*SiO_2 with tunable porosities. The pore size can be adjusted by varying the TIPB concentration during synthesis, without affecting the AuNPs. Additionally, modifying the TEOS concentration during seed synthesis effectively controls the number of gold cores per particle and eliminates unwanted empty MSNs.

4.3. Growth by Biphasic stratification

The biphasic stratification process has been reported as a method of choice to synthesize monodisperse dendritic MSNs with pore diameters ranging from 4 nm to 12−15 nm [6]. In this method, the particles form through a biphasic mediated process. The process develops at the interface between a bottom aqueous phase, containing a base and a surfactant, usually CTAC, and an upper organic phase, containing the silica precursor dissolved in a hydrophobic solvent. The surfactant concentration exceeds the critical micelle concentration, leading

to the formation of spherical micelles [26] (Figure 4.5b). When TEOS reaches the interface, it undergoes hydrolysis-condensation reactions and the silicic acid oligomers associate with the positively charged CTAC mesophase (Figure 4.5c). The low surface tension of the developing CTAC-silica assembly facilitates the transformation of the lamellar phase to a higher curvature droplet phase as an invaginated interfacial structure (Figure 4.5d-f) that works as template for silica growth and results in the formation of dendritic MSN (Figure 4.5h) [6, 27, 28]. Hereafter the particles synthesized with this method are referred to as *b*-Au@*m*SiO_2, where the prefix "***b***" denotes the use of biphasic stratification in the seed growth process.

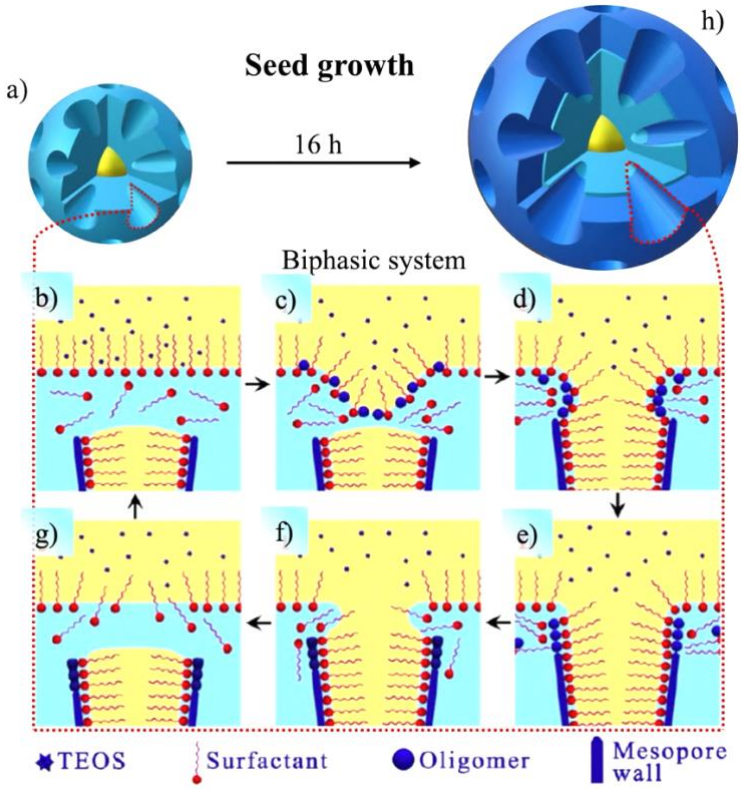

Figure 4.5. Schematic illustration of the mechanism of formation for large pores *b*-Au@*m*SiO_2 particles using a biphasic stratification method. Adapted from [6].

To grow silica on the *seed*-Au@*m*SiO_2 particles using the biphasic approach, a cyclohexane layer containing TEOS was added onto the as-obtained Au@*m*SiO_2 seeds suspension after the addition of CTAC, according to Method A (See Chapter 2, section 2.1.2.3). This process resulted in *b*-Au@*m*SiO_2 with large pores containing one or more gold cores, with a D_{part} of 98±12 nm (Figure 4.6 a and Table 4.4). However, similarly to the growth process with TIPB described in Section 4.2, a significant percentage (48%) of empty MSN particles were observed.

To improve the synthesis and achieve a higher yield of Au@*m*SiO_2 -without empty MSN- the biphasic growth was performed using *seed*-Au@*m*SiO_2 particles synthesized with reduced TEOS concentrations: 1*x*, 0.5*x*, 0.25*x*, and 0.2*x* (See SEM micrographs of seeds in Figure 4.3). Regardless of the seed type, the synthesis resulted in 60-100 mg of *b*-Au@*m*SiO_2, corresponding to a yield of 20-25%. The percentage of gold-free MSN decreased as the TEOS concentration in the seed synthesis was reduced (Table 4.4), indicating that a 0.2*x* concentration is optimal for achieving a [TEOS]:[Au] ratio that favors the formation of MSN nucleating on AuNPs.

No direct relationship was observed between the amount of TEOS used in the *seed*-Au@*m*SiO_2 synthesis and the size of the resulting nanoparticles, which ranged from 58 to 109 nm (Figure 4.6 and Table 4.4). Similarly to the synthesis of Au@*m*SiO_2 using TIPB as a pore expander, the observed variation in particle sizes is attributed to the presence of uncoated AuNPs in the seed solution that remain in the reaction medium. This leads to uneven growth of the silica shell, resulting in Au@*m*SiO_2 particles of varying sizes.

However, reducing the amount of TEOS in the seeds does affect the pore size, resulting in larger pores with seeds synthesized using 0.2*x* TEOS, as inferred from SEM micrographs and N_2-sorption characterization. The sorption isotherms obtained for *b*-Au@*m*SiO_2 synthesized with seeds obtained with 0.5*x*, 0.2*x*, and 0.25*x* TEOS exhibit similar characteristics but differ in some aspects (Figure 4.6

d-f). All isotherms belong to type IV according to IUPAC classification, showing high nitrogen uptake at intermediate relative pressures. Specific surface areas are near 700 $m^2.g^{-1}$ for all the *b*-Au@*m*SiO_2 (Table 4.4). Application of the *t*-plot method to these isotherms excludes the presence of micropores.

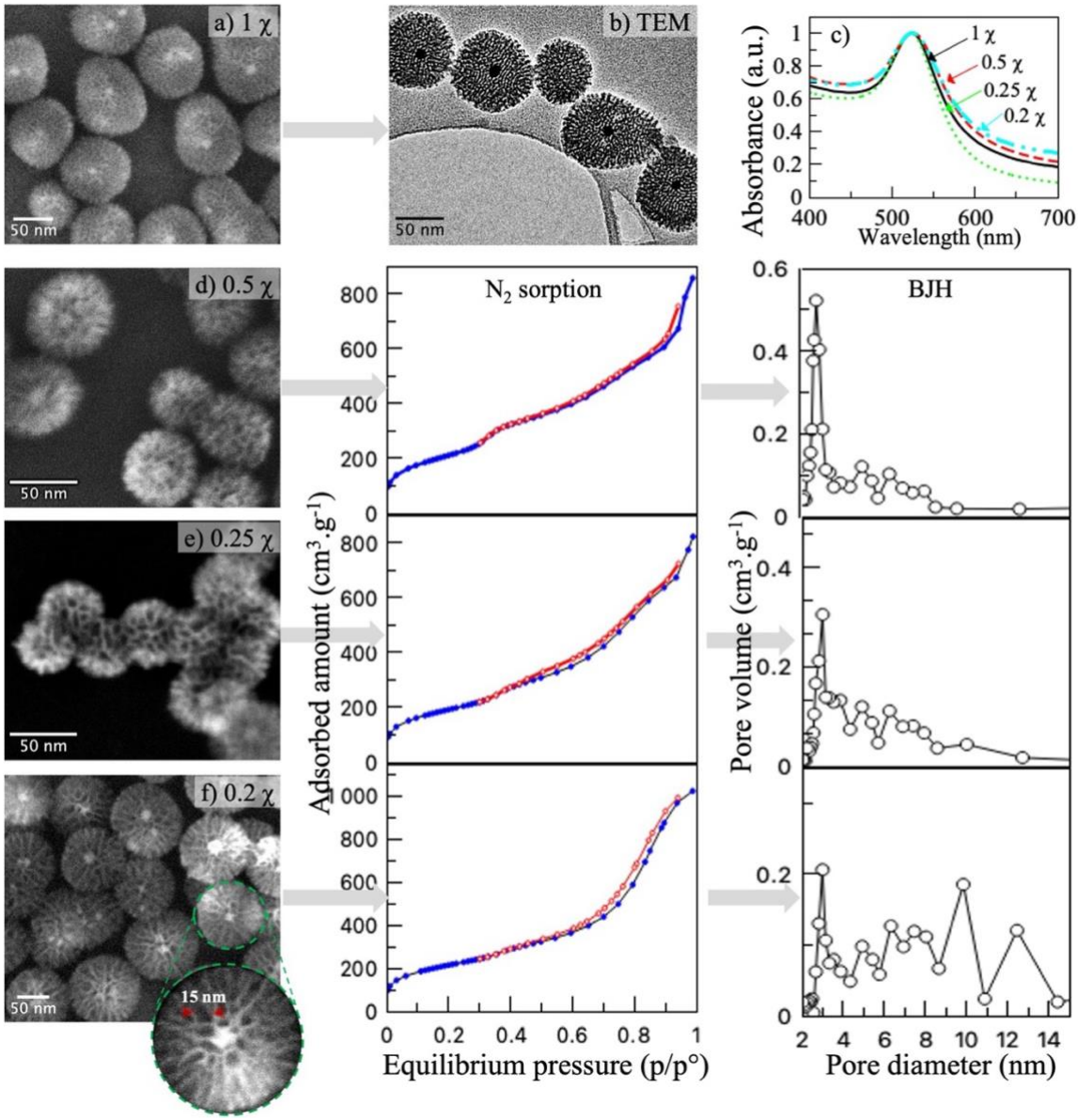

Figure 4.6. Characterization of *b*-Au@*m*SiO_2 obtained with seeds synthesized with 1*x*, 0.5*x*, 0.25*x*, and 0.2*x* TEOS (Method A). a) SEM and b) TEM micrographs of *b*-Au@*m*SiO_2 obtained with seeds synthesized with 1x TEOS. c) Normalized UV-vis spectra for all *b*-Au@*m*SiO_2. SEM micrographs, N_2-sorption and BJH pore size distribution of *b*-Au@*m*SiO_2 obtained with seeds synthesized with d) 0.5*x*, e) 0.25*x*, and f) 0.2*x* TEOS.

Table 4.4. Characterization data of *b*-Au@*m*SiO_2 obtained with seeds synthesized with 1*x*, 0.5*x*, 0.2*x*, and 0.25*x* TEOS (Method A). Particle diameters (D_{part}) and nanoparticle percentages were determined from SEM micrographs. Hydrodynamic diameters were measured using DLS. The textural parameters were derived from the N_2-sorption isotherms showed in Figure 4.6

TEOS in seed	Hydrodynamic diameter (nm)	D_{part} (nm)	% NP without Au core	% NP with >1 Au cores	% NP with 1 Au core	S_{BET} (m^2/g)	Mesopore volume (cm^3/g)	BJH Pore diameters (nm)
1*x*	243	98 ± 12	48.3	17.9	33.8	ND	ND	ND
0.5*x*	117	58 ± 7	30.8	12	57.2	772	0.51	2.7 & 7
0.25*x*	240	60 ± 6	17.5	30	52.5	695	0.47	3.0 & 7
0.2*x*	130	109 ± 14	3.1	54.7	42.2	778	0.52	3.0 & 8

The three particles were identified as mesoporous materials, evidenced by three distinct sub-steps observed during the sorption process. The precise positions determined using the first derivative of the isotherms (Appendix 3) align with the pore size distributions (Figure 4.6). Each particle exhibits a sorption uptake at a relative pressure of approximately $p/p^\circ = 0.4$, indicating the presence of small mesopores around 3 nm (see Table 4.4). Additionally, there is progressive and significant adsorption starting from $p/p^\circ = 0.5$, indicating the presence of larger, heterogeneous pores with sizes of approximately 5-10 nm. Notably, for the *b*-Au@*m*SiO_2 synthesized with 0.2*x* seeds, an inflection is observed at $p/p^\circ = 0.9$, suggesting the filling of larger mesopores of varying sizes with pores up to 14 nm. The isotherms for all three types of particles exhibit a very narrow hysteresis loop, characteristic of pores with one closed aperture as previously reported for mesoporous materials with conical pores [29, 30]. These observations align with SEM observations and support the conclusion that the larger pores are conical mesopores. Thus, these particles exhibit two distinct populations of mesopores: (i) a uniform population of small mesopores around 3 nm in size, probably originated from the seed particles, and (ii) conical mesopores with diameters ranging from 5 to 10 nm for *b*-Au@*m*SiO_2 synthesized

with 0.5*x* and 0.25*x* seeds, and up to 13 nm for *b*-Au@*m*SiO_2 synthesized 0.2*x* seeds particles (see Table 4.4).

According to the literature, in the biphasic growth approach, the pore size can be enlarged up to 15 nm by applying various growth stages or reducing the TEOS concentration [6, 31]. Using this approach and maintaining the seed synthesized with 0.2*x* TEOS, three methods were employed, referred to as Methods B, C, and D (for details, see Chapter 2, Section 2.1.2.3). In Method B, the TEOS concentration used during the seed growth was halved (0.5*z* TEOS). The resulting nanoparticles, with a D_{part} of 70 ± 7 nm, displayed similar textural characteristics to those produced with 1*z* TEOS (compare with Figure 4.6). The first derivative of the isotherms reveals three sub-steps during the sorption process, indicating three distinct mesopore populations (Appendix 3). The first population consists of small pores ranging from 3 to 5 nm, the second population ranges from 5 to 10 nm, and the third population consists of the largest pores, attributed to interparticular voids between NPs (Figure 4.7, Method B and Table 4.5).

In Method C, two consecutive growth steps were performed, resulting in larger particles with a D_{part} of 91 ± 10 nm, accompanied by an increase in pore size (Figure 4.7, Method C and Table 4.5). N_2 sorption results indicate that, unlike other *b*-Au@*m*SiO_2 particles, those synthesized with two layers do not have small mesopores, as their sorption isotherm does not show a nitrogen uptake substep below $p/p^\circ = 0.4$. These findings align well with the single sub-step revealed by the first derivative of the isotherms (Appendix 3) and the BJH analysis, which shows that these particles primarily contain large mesopores ranging from 4 to 10 nm, with a predominant size around 5 nm.

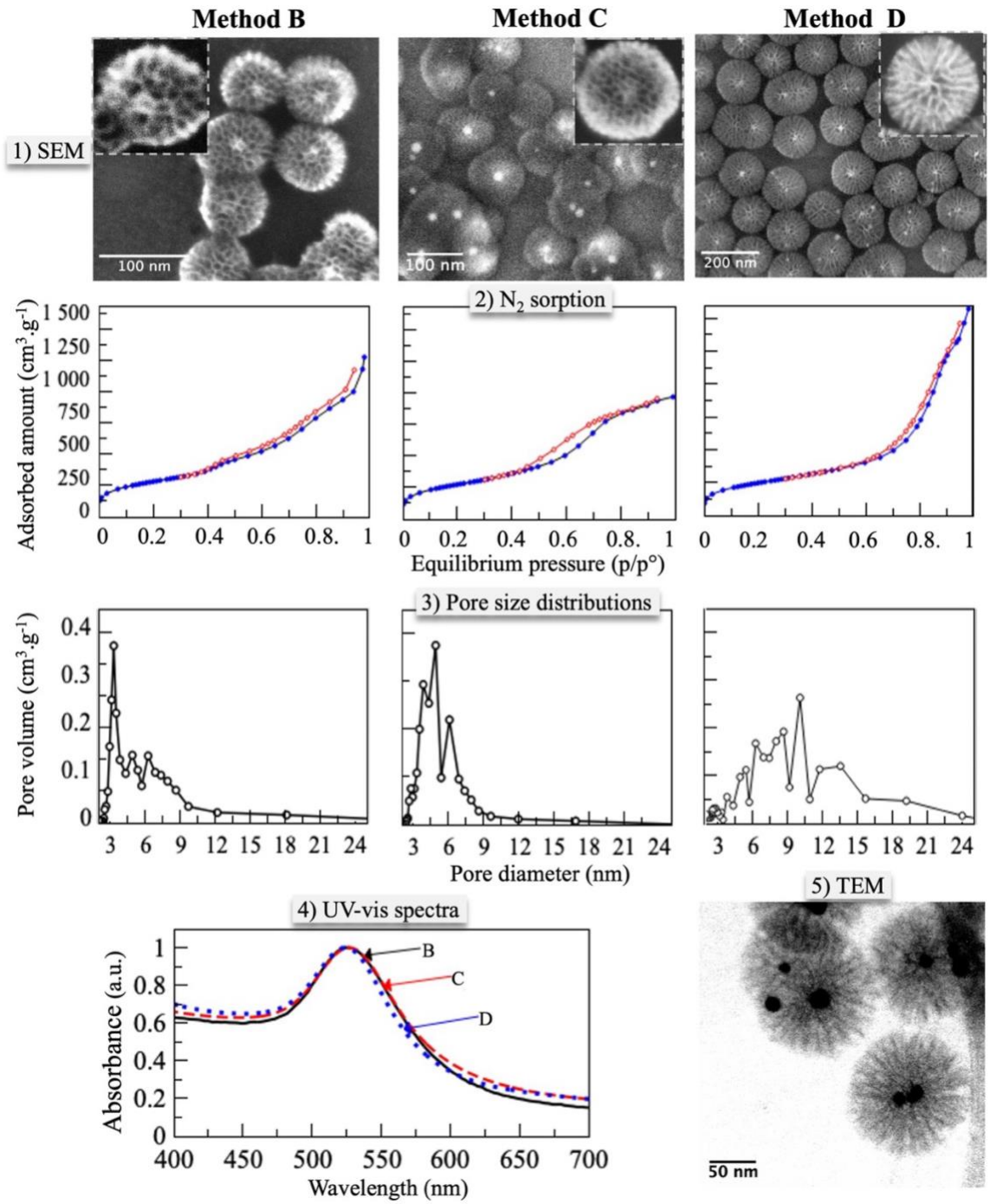

Figure 4.7. Characterization of *b*-Au@*m*SiO_2 nanoparticles synthesized with seeds produced using 0.2*x* TEOS and shell growth employing different biphasic stratification methods: Method B: shell growth using half the concentration of TEOS (0.5*z*), Method C: two consecutive shell growth steps using 1*z* TEOS each time, Method D: isolation of seed particles before shell growth, followed by shell growth with 0.3*z* TEOS. 1) SEM micrographs, 2) N_2 sorption isotherms, 3) BJH pore size distribution, 4) Normalized UV-vis spectra for *b*-Au@*m*SiO_2 synthesized with (B) Method B, (C) Method C, and (D) Method D, 5) TEM micrograph of *b*-Au@*m*SiO_2 obtained with Method D

Table 4.5. Characterization data of *b*-Au@*m*SiO_2 nanoparticles synthesized with seeds produced using 0.2*x* TEOS and shell growth employing different biphasic stratification methods: Method B: shell growth using half the concentration of TEOS (0.5*z*), Method C: two consecutive shell growth steps using 1*z* TEOS each time, Method D: isolation of seed particles before shell growth, followed by shell growth with 0.3*z* TEOS. Particle diameter (D_{part}) and nanoparticle percentages were determined from SEM micrographs. Hydrodynamic diameters were measured using DLS. The textural parameters were derived from the N_2-sorption isotherms showed in Figure 4.7

Method	Hydrodynamic diameter (nm)	D_{part} (nm)	% NP without Au core	% NP with >1 Au cores	% NP with 1 Au core	S_{BET} (m^2/g)	Mesopore volume (cm^3/g)	Average BJH Pore diameter (nm)
Method B	244	70 ± 7	12.2	32.9	54.9	818	0.62	3.3 & 7
Method C	245	91 ± 10	12.1	28.6	59.3	796	0.93	5.3
Method D	222	120 ± 11	0	76.6	23.4	823	1.82	10.7

Finally, Method D was investigated to avoid uneven growth of the silica shell caused by the seed polydispersity. This method used a reduced TEOS concentration (0.3*z* TEOS) during seed growth. Additionally, seed nanoparticles were isolated from the reaction medium by centrifugation prior to growth in the biphasic media. As a result, monodisperse particles with D_{part} = 120 ± 11 nm were obtained, all containing one or more gold cores (Figure 4.7, Method D and Table 4.5). These particles demonstrated excellent dispersibility, as evidenced by SEM micrographs (Figure 4.7.1)

Remarkably, the particles synthesized using Method D exhibited the largest pore sizes, as inferred from SEM and N_2 sorption. The sorption isotherm shows no nitrogen uptake substep below p/p° = 0.4, indicating the absence of small pores, but an inflection is observed at p/p° = 0.9, suggesting the filling of larger mesopores of varying sizes. As shown by the BJH plots (Figure 4.7, Method D and Table 4.5), these materials contain large mesopores up to 24 nm, with a predominant size around 10 nm. These findings are consistent with the single sub-step revealed by the first derivative of the isotherms (Appendix 3). The sorption isotherm has a very narrow hysteresis loop, indicative of pores with a

single closed aperture. This suggests the presence of conical pores, a conclusion that aligns with the observations from SEM micrographs.

To further investigate the pore structure of *b*-Au@*m*SiO_2, we employed AFM in tapping mode using silicon probes with a 2 nm tip radius. This work was carried out in collaboration with Lia Pietrasanta and Silvio Ludueña (CMA, UBA). Although AFM offers high spatial resolution, its use for characterizing mesopores in nanoparticles is challenging due to the need for a flat surface. To address this, we prepared the nanoparticles to form a homogeneous monolayer on a flat silicon substrate, made possible by the high dispersibility of the *b*-Au@*m*SiO_2, suspension (for detailed sample preparation, see Chapter 2, section 2.2.4). AFM imaging successfully revealed that the *b*-Au@*m*SiO_2, nanoparticles possess open pores large enough to be detected by the 4 nm AFM tip, and these pores are uniformly distributed across the nanoparticles (Figure 4.8). To our knowledge, these AFM images provide the first detailed observation of mesopores in silica nanoparticles.

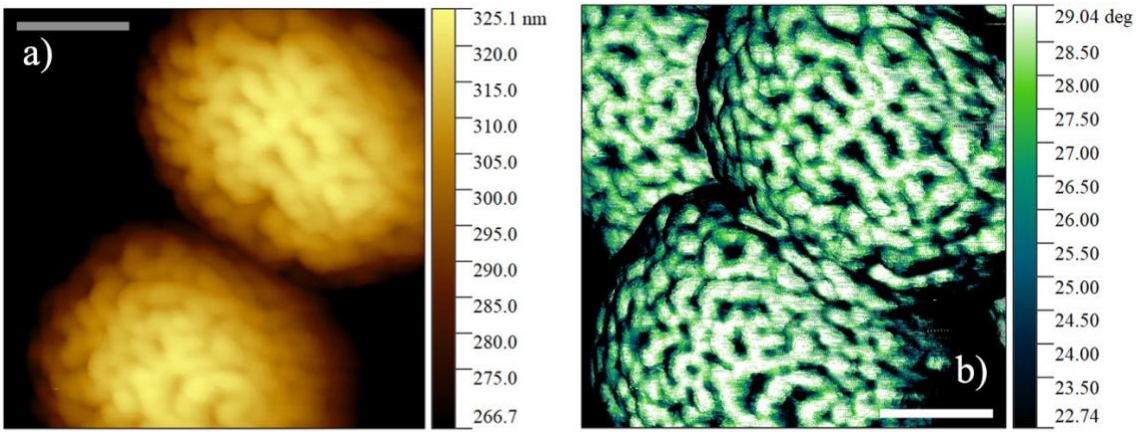

Figure 4.8. AFM micrographs of *b*-Au@*m*SiO_2 acquired in tapping mode over a 200 × 200 nm² area. (a) topography channel indicating height variation on the surface of the particles. (b) phase channel showing variations in the mechanical properties of the particle's outer surface and within the pores. Horizontal scale bar = 50 nm.

In summary, the use of biphasic stratification for seed growth enabled the synthesis of Au@*m*SiO_2 nanoparticles with mesopores up to 24 nm in diameter, which are open and evenly distributed. Adjusting the TEOS concentration during seed synthesis effectively controls the number of gold cores per particle and eliminates undesired empty MSNs. Furthermore, the pore size distribution can be optimized through multi-step shell growth. The largest pores and the best particle dispersibility were achieved by isolating the seeds from the reaction medium before introducing them into the biphasic system.

4.4. Au@*m*SiO_2 particles stability

To evaluate the hydrolytic stability of Au@*m*SiO_2 particles and assess the effects of particle concentration and textural characteristics, the morphology of calcined Au@*m*SiO_2 particles was monitored in saline aqueous medium. Suspensions with concentrations of 1 mg/mL and 0.1 mg/mL were incubated in PBS 1×, and their morphological evolution was tracked daily or hourly using SEM. These conditions were chosen based on the silica solubility limit (SSL), which is approximately 0.15 mg/mL in PBS 1× at 37 °C [21]. Thus, the silica has to dissolve fully into silicic acid in the case of a starting concentration of 0.1 mg/mL, though for 1 mg/mL, only a small fraction (*ca* 15%) should get dissolved.

The particles evaluated in this study included *e*-Au@*m*SiO_2 synthesized using seeds with 1*x* TEOS and grown with 2*y* TIPB; *b*-Au@*m*SiO_2 synthesized using method D as previously described; and small-pore Au@*m*SiO_2 (*sp*-Au@*m*SiO_2) obtained via the *one-pot* methodology detailed in Chapter 3. *e*-Au@*m*SiO_2 exhibit conical pores with a diameter of up to 7 nm, *b*-Au@*m*SiO_2 has conical pores reaching up to 12 nm, and *sp*-Au@*m*SiO_2 displayed cylindrical pores with a diameter of 2.5 nm.

The degradation profiles of the studied particles align with those previously reported for MSNs. These profiles are influenced by two main factors: structural characteristics, which are determined by the synthesis conditions [6, 32, 33], and particle concentration [21, 33, 34]. It has been established that when MSN are suspended above the silica solubility limit (SSL), dissolution-reprecipitation processes occur among the silicate species, altering the pore structure and surface area of particles. Below the solubility limit of silica, MSN particles undergo full hydrolysis, resulting in total dissolution into silicic acid and oligomers [20].

4.4.1. Morphological evolution upon incubation in phosphate buffer

4.4.1.1. *e*-Au@*m*SiO_2

In the 1 mg/mL *e*-Au@*m*SiO_2 suspension, dissolution-reprecipitation resulted in the formation of two distinct particle populations: (i) the original *e*-Au@*m*SiO_2 particles, which retained their gold core and exhibited a smaller silica shell (D_{part} ~ 53 nm), and (ii) swollen *e*-Au@*m*SiO_2, characterized by widened pore openings. These particle types coexisted for two days, with a noticeable increase in the proportion of swollen *e*-Au@*m*SiO_2 at the expense of the original *e*-Au@*m*SiO_2, which had a D_{part} ~ 39 nm by day two. By the third day, predominantly *e*-Au@*m*SiO_2 particles with moderately increased size and altered morphology were observed. By the fifth and sixth days, particles with larger pores and multiple gold cores were identified, indicating potential coalescence of neighboring *e*-Au@*m*SiO_2 particles (Figure 4.9a-g).

As expected for suspensions above the silica solubility limit (SSL), complete hydrolysis of silica into silicic acid did not occur. Instead, dissolution-

reprecipitation processes resulted in particles with altered morphology, characterized by a polymorphic mesoporous silica shell, with AuNPs located at both the center and edges of the particles. Notably, the AuNPs do not change in size or morphology; rather, their positions shift as the silica reprecipitates.

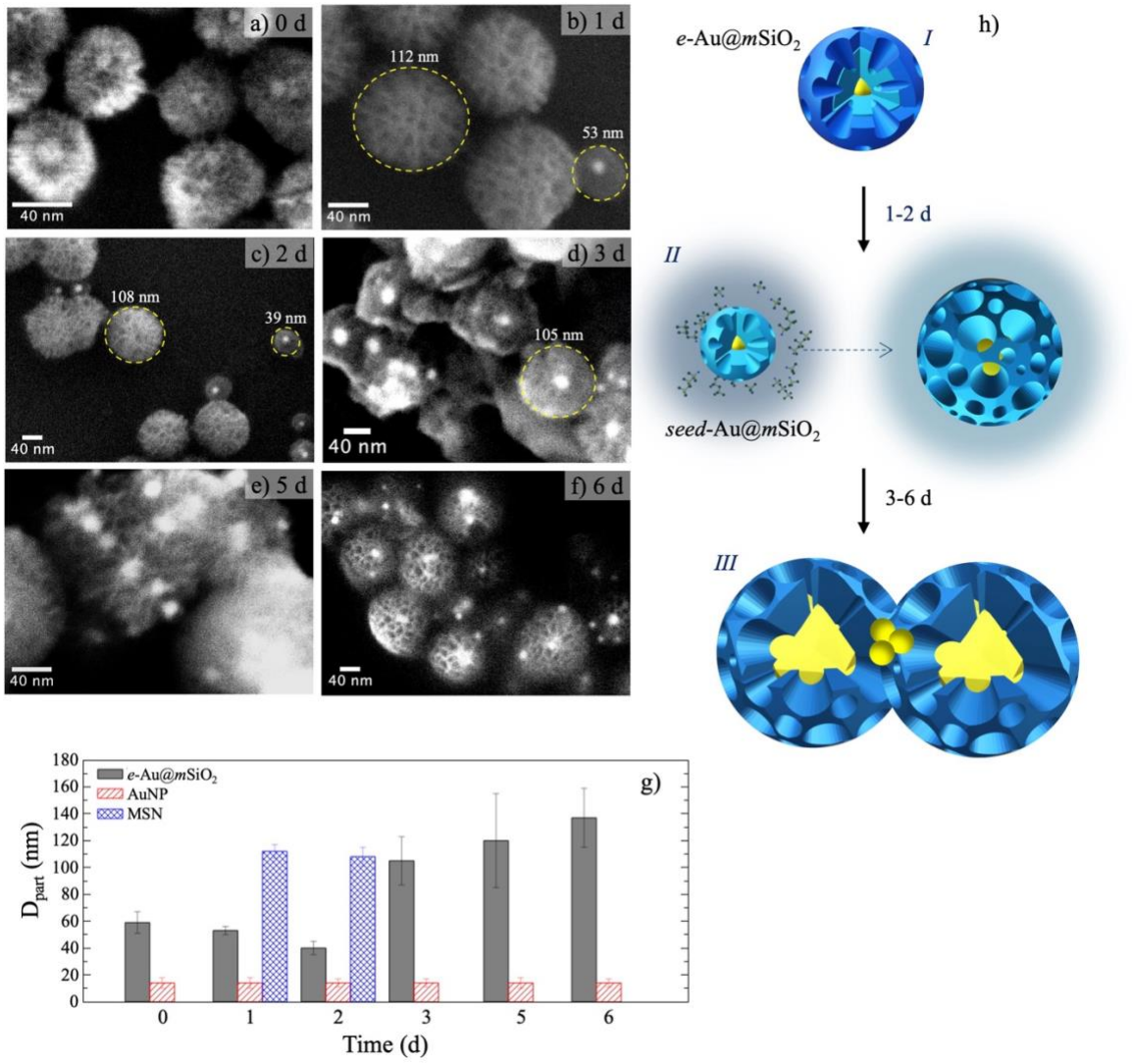

Figure 4.9. Morphological evolution over time of a 1 mg/mL *e*-Au@*m*SiO_2 suspension in PBS 1×. a-f) SEM micrographs. g) Proposed mechanism for *e*-Au@*m*SiO_2 dissolution when the particle concentration exceeds the solubility limit of silica. h) Particle size of the three distinct particle populations as function of degradation time determined by SEM.

SEM micrographs suggest a degradation mechanism for *e*-Au@*m*SiO_2 at concentrations above the SSL in PBX 1× involving a particle lifetime of less than a day. The degradation process begins with the hydrolysis of the outer silica layer synthesized during the seed growth phase. The resulted dissolved silica fragments reprecipitate, forming swollen *e*-Au@*m*SiO_2 with large pores that serve as intermediates in the degradation process (Figure 4.9h-II). Subsequently, large-pore MSN particles with embedded AuNPs, at both the center and periphery, are formed. This observed morphology likely arises from the dissolution and reprecipitation of both the seed *e*-Au@*m*SiO_2 and the swollen intermediates, with AuNPs acting as nucleation sites (Figure 4.9h-III).

A different degradation profile was observed for the 0.1 mg/mL suspension of *e*-Au@*m*SiO_2, *ie* under the SSL. SEM analysis revealed that after one day of incubation, only the seeds used for the preparation of *e*-Au@*m*SiO_2 particles, featuring a reduced shell thickness (D_{part} ~ 40 nm) remained, and these particles were aggregated with no other particle types detected. By the second day, complete dissolution of the silica was evident, likely resulting in undetectable silicic acid, leaving only aggregated AuNPs visible (Figure 4.10 a-c). It is important to note that aggregation was already present at t=0, which may be attributed to the sample preparation process. Specifically, the high salinity of PBS 1× is detrimental to the colloidal stability of *e*-Au@*m*SiO_2.

At *e*-Au@*m*SiO_2 concentrations below the silica solubility limit (SSL), the dissolution process does not result in detectable intermediate species, as silica reprecipitation is not thermodynamically favored. If reprecipitation occurs, it is likely confined to localized regions—such as within the nanoparticle—where the silicate concentration might briefly exceed the SSL. The particles exhibit a lifetime of less than one day. Initially, the external silica layer synthesized during the seed growth process undergoes hydrolysis (see Figure 4.10d-II). Following this, the silica shell of the seed itself is hydrolyzed, leaving only the AuNPs

(Figure 4.10d-III). These AuNPs tend to aggregate due to the absence of a stabilizing coating.

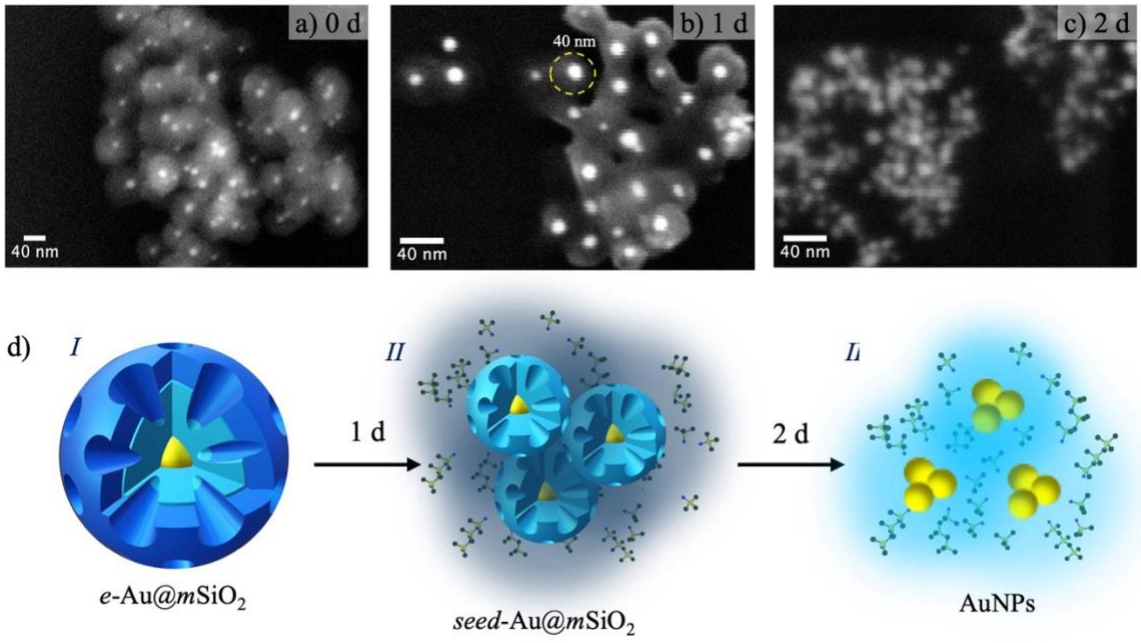

Figure 4.10. Morphological evolution over time of a 0.1 mg/mL *e*-Au@*m*SiO_2 suspension in PBS 1×. a-c) SEM micrographs. d) Proposed mechanism for *e*-Au@*m*SiO_2 dissolution when the particle concentration is under the SSL.

The degradation mechanism proposed for *e*-Au@*m*SiO_2 is analogous to that previously reported for large-pore MSNs synthesized via the seed-growth method utilizing TIPB and TPOS, but without the gold core [22]. In the referenced work, the degradation of MSNs at concentrations below the SSL was investigated using SEM and DLS on an hourly basis in pure water over the course of a day. The degradation began with the formation of intermediate altered particles with interconnected pores, which were observed early in the process. After one day of incubation, the particles became swollen and agglomerated, and their number significantly decreased. This mechanism closely mirrors the one observed in this study for concentrations above the SSL (Figure 4.9), with the primary difference

being the observation of the same two particle populations over an extended time scale. These findings suggest that, at concentrations below the SSL, the formation of short-lived intermediates (lasting less than one day) may also be an integral part of the degradation mechanism. However, it is important to note that in the referenced study, the particles were not calcined, which could result in a different degree of condensation, significantly affecting the stability of the MSNs [35].

4.4.1.2. *b*-Au@*m*SiO_2

SEM analysis reveals that *b*-Au@*m*SiO_2 particles are less prone to morphological changes. At a concentration of 1 mg/mL, *ie* above the SSL, the nanoparticles maintain their morphology intact for the initial two days when suspended in 1× PBS. Between days three and five, minor modifications in pore shape and particle roughness are observed, likely attributed to dissolution-reprecipitation processes involving silica. Additionally, increased particle aggregation is noted during this period. By day six, the changes in pore morphology become more pronounced, with pores enlarging and losing their conical shape (refer to Figure 4.11a-h). This alteration appears to be the result of silica reprecipitation forming a mesoporous shell, with AuNPs acting as nucleation sites.

These observations suggest that *b*-Au@*m*SiO_2 particles, when suspended at concentrations above the SSL, possess a lifetime of at least 2 days in 1× PBS, maintaining their morphology during this timeframe. Beyond this period, degradation begins without the formation of detectable intermediates, indicating that dissolution-reprecipitation processes occur gradually. By day six, significant changes in the particle shell are evident (see Figure 4.11 i).

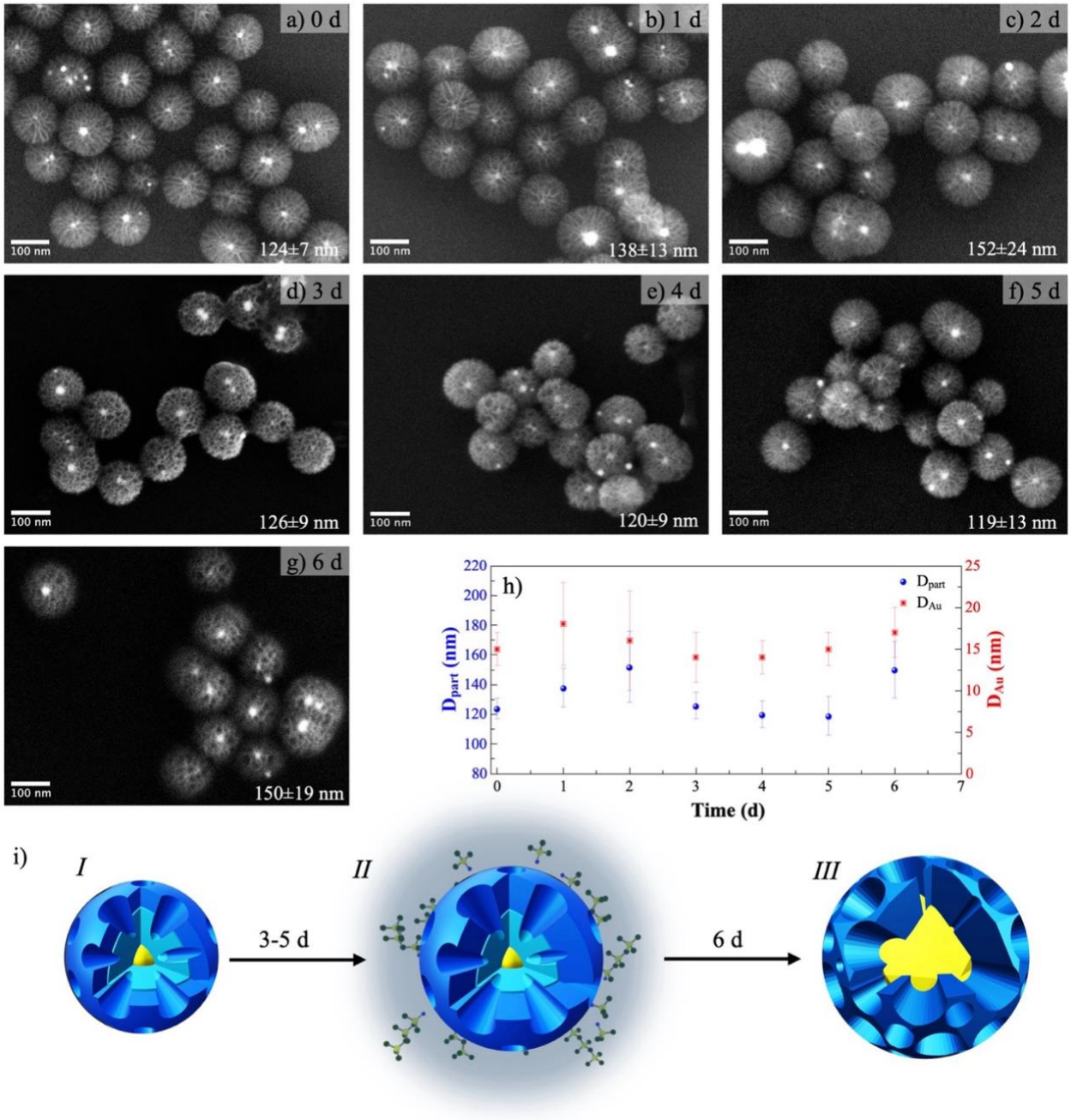

Figure 4.11. Morphological evolution over time of a 1 mg/mL *b*-Au@*m*SiO_2 suspension in PBS 1×. a-g) SEM micrographs. h) Particle size of *b*-Au@*m*SiO_2 (D_{part}) and gold core (D_{Au}) as function of degradation time determined by SEM. i) Proposed mechanism for *b*-Au@*m*SiO_2 dissolution when the particle concentration exceeds the solubility limit of silica.

At a concentration of 0.1 mg/mL, below the SSL, *b*-Au@*m*SiO_2 nanoparticles retain their morphology for up to two days when incubated in 1× PBS (Figure 4.12). It is noteworthy that at *t*=0, the particles are already aggregated, as a result of the high salinity of the medium. After two days, between days 3 and 5, changes in the pore size and surface roughness of the silica shell become apparent. The particles slightly decrease in size and form larger aggregates (Figure 4.12h). By day six, the particles are completely dissolved, and no silica residues are visible.

Thus, below the SSL, *b*-Au@*m*SiO_2 particles have a lifetime of about 2 days. After this period, the external shell undergoes hydrolysis, causing the surface to change significantly. Eventually, the entire shell dissolves into silicic acid, which cannot be detected by SEM. The result is the aggregation of AuNPs, as there is no stabilizing coating to prevent this aggregation (Figure 4.12i).

The degradation behavior of large-pore MSNs synthesized via biphasic stratification has been characterized in the literature as a two-step process, with degradation progressing from the outside to the inside of the particle [6]. Initially, the outer layer of large-pore MSNs degrades rapidly, followed by a slower degradation of the inner small-pore MSN layer, with the entire process completing in 72 hours. However, the particle concentration was not specified in the study. Notably, the lifetime of *b*-Au@*m*SiO_2 particles, irrespective of concentration, exceeds 72 hours. This extended stability may be attributed to the different template removal methods employed: calcination for *b*-Au@*m*SiO_2 versus ammonium nitrate extraction for MSNs. The method of template removal likely influences the degree of condensation of the final particles, contributing to their differing stabilities.

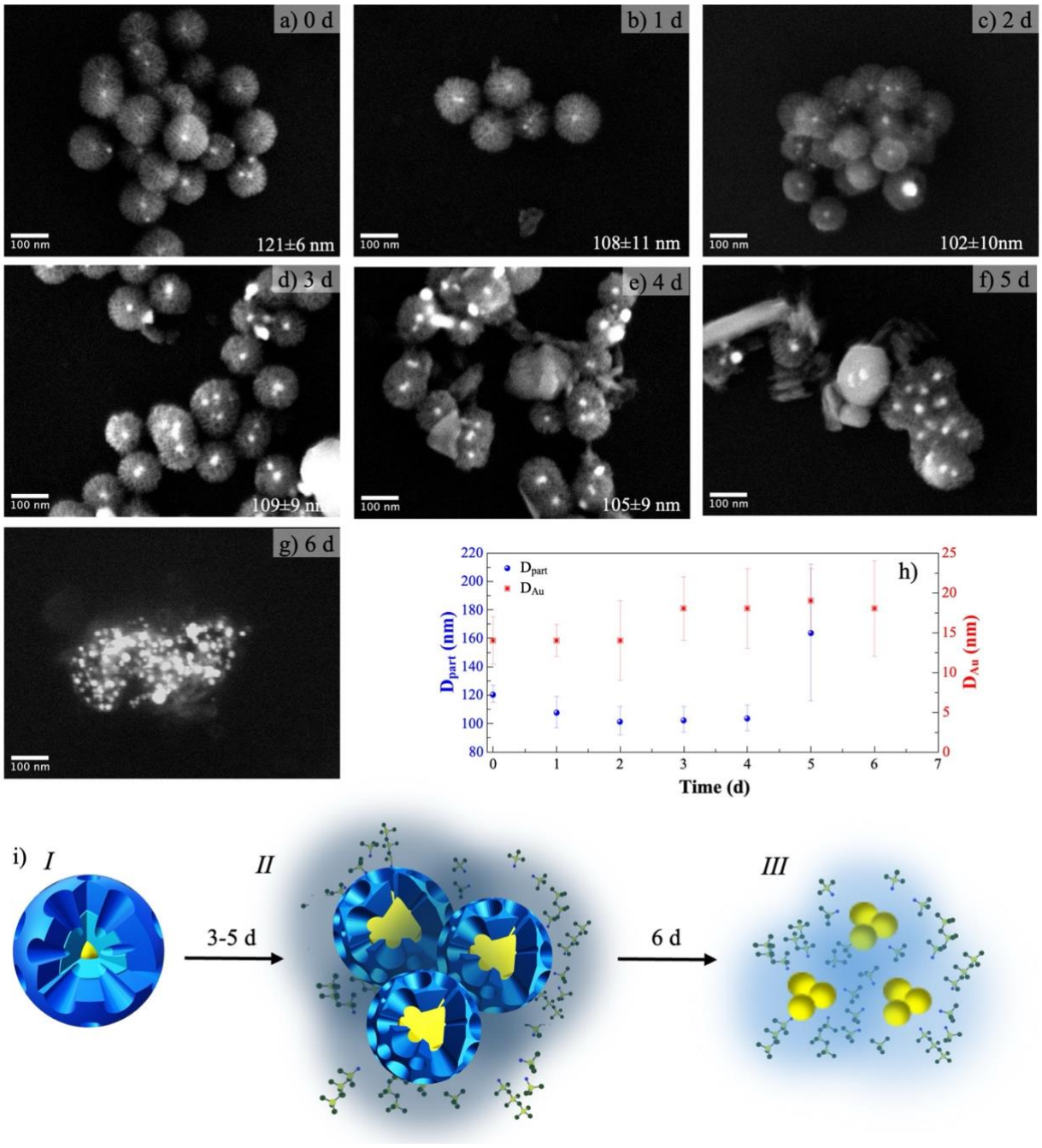

Figure 4.12. Morphological evolution over time of a 0.1 mg/mL *b*-Au@*m*SiO_2 suspension in PBS 1×. a-g) SEM micrographs. h) Particle size of *b*-Au@*m*SiO_2 (D_{part}) and gold core (D_{Au}) as function of degradation time determined by SEM. i) Proposed mechanism for *b*-Au@*m*SiO_2 dissolution when the particle concentration is under the SSL.

4.4.1.3. *sp*-Au@*m*SiO_2

The degradation behavior of *sp*-Au@*m*SiO_2 particles reveals distinct temporal characteristics compared to *e*-Au@*m*SiO_2 and *b*-Au@*m*SiO_2 particles. Specifically, the morphological changes in *sp*-Au@*m*SiO_2 occur over a shorter time frame, within hours.

In a 1 mg/mL *sp*-Au@*m*SiO_2 suspension, after four hours, the dissolution-reprecipitation process led to the formation of two distinct particle populations: (i) the original *sp*-Au@*m*SiO_2 particles (D_{part} = 106 ± 10 nm) and (ii) *sp*-Au@*m*SiO_2 particles with expanded pores (D_{part} = 115 ± 5 nm). However, the latter particle type exists for less than one hour, as by the fifth hour, the original *sp*-Au@*m*SiO_2 particles are observed embedded in a mesoporous matrix, likely formed by the dissolution of the expanded *sp*-Au@*m*SiO_2 particles. After 24 hours, the porous matrix disappears, leaving only the original *sp*-Au@*m*SiO_2 particles, which retain their initial size (Figure 4.13a). These particles were monitored for up to 10 days, with no significant changes in size, pore structure, or morphology observed (See Chapter 5, Figure 5.19). Importantly, the size of the gold particles remained unchanged throughout the process.

At concentrations above the silica solubility limit (SSL) in PBS 1×, the degradation process for *sp*-Au@*m*SiO_2 particles occurs from the inside out. Initially, the pore walls dissolve, leading to the formation of short-lived intermediates with expanded pores. These intermediates dissolve completely within an hour, and after 24 hours, only the original particles are observed.

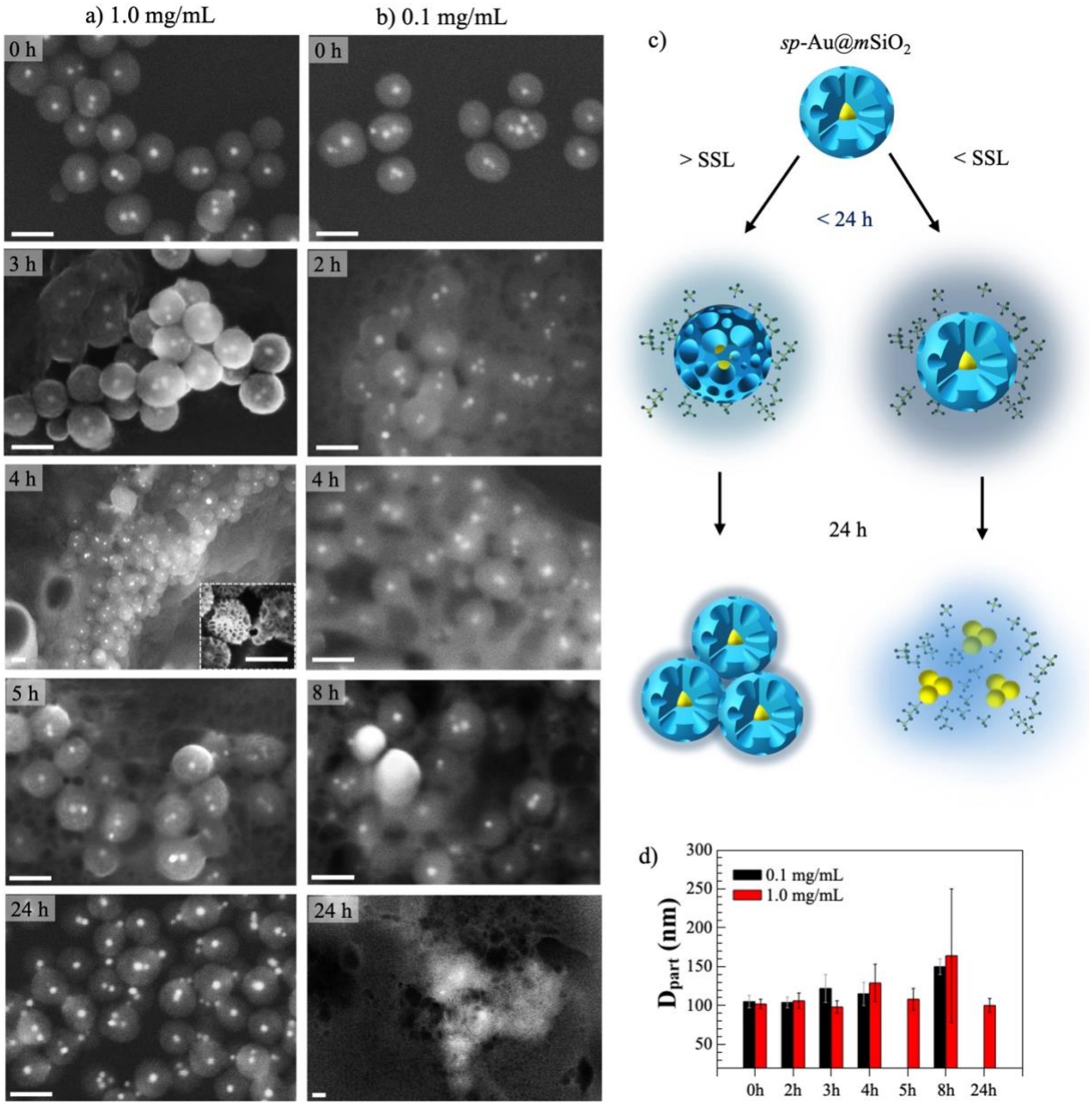

Figure 4.13. Morphological evolution of *sp*-Au@*m*SiO_2, monitored by SEM of a) 0.1 mg/mL *sp*-Au@*m*SiO_2 suspension and b) 1.0 mg/mL *sp*-Au@*m*SiO_2 suspension in PBS 1×. c) Proposed mechanism for *sp*-Au@*m*SiO_2 dissolution: (left) below the SSL and (right) above the SSL d) Particle size of *sp*-Au@*m*SiO_2 (D_{part}) as function of degradation time determined by SEM.

In the 0.1 mg/mL *sp*-Au@*m*SiO_2 suspension, no intermediate particles were observed during degradation. Instead, a porous matrix was noted in the background. The particles maintained their morphology for up to 8 hours, although they became agglomerated, and silica re-precipitation was evident in the bottle necks of the particles. After one day, complete dissolution of the silica was observed, leaving only AuNPs embedded in a silica matrix (Figure 4.13).

Given that no variation in particle size was observed and that the particles appeared to be embedded in a mesoporous matrix during the degradation process, it can be inferred that, similarly to the 0.1 mg/mL suspension, the dissolution occurs from within the pores.

Irrespective of the particle concentration, the particles exhibit a lifetime of less than one day. This behavior is consistent with previously reported results for MCM-48 particles with a size of 150 nm and cylindrical pores of 3.2 nm, which start to disintegrate after 5 hours of incubation in 1× PBS [20].

4.5. Summary of Au@*m*SiO_2 particle stability

The stability and degradation of Au@*m*SiO_2 particles depend on both concentration and synthesis method. When the particle suspension is above the SSL, the particles dissolve slowly. During this process, reprecipitation leads to changes in particle morphology, resulting in aggregated particles with enlarged pores that contain one or more gold cores at the center and edges. For *e*-Au@*m*SiO_2 the degradation occurs more rapidly and involves the formation of intermediates with larger pores. This happens because the more porous external shell dissolves first and then reprecipitates to form swollen *e*-Au@*m*SiO_2. For *b*-Au@*m*SiO_2 particles degrade more slowly. Intermediate particle formation, if it occurs, is brief. The reprecipitation process alters the original core-shell

particles, increasing their porosity and roughness to form more porous *b*-Au@*m*SiO_2 particles. For *sp*-Au@*m*SiO_2, total particle disintegration was not observed even after 10 days, however the observation of immediate larger pore particles suggests that the dissolution-reprecipitation process is constantly taking place.

When the concentration is below the SSL, the particles dissolve quickly. The silica shell hydrolyzes completely into silicic acid or small oligomers. As a result, only naked gold AuNPs remain, which tend to aggregate due to the absence of a stabilizing coating. For *e*-Au@*m*SiO_2, the dissolution process begins with the dissolution of the more porous external shell, followed by the dissolution of the seed shell. For *b*-Au@*m*SiO_2, the process is slower. The external shell initially becomes more porous but maintains its size, then the particles aggregate, and finally, the entire shell undergoes complete hydrolysis. For *sp*-Au@*m*SiO_2, the dissolution is faster and does not result in changes in particle size.

It was observed that *e*-Au@*m*SiO_2 particles dissolve more rapidly than *b*-Au@*m*SiO_2, both above and below the SSL. The *e*-Au@*m*SiO_2 particles, characterized by medium-sized mesopores possess a larger surface area compared to *b*-Au@*m*SiO_2. The impact of surface area on degradation rate is well-documented; an increased surface area accelerates the degradation process due to enhanced interaction with water at the particle interfaces [32]. This relationship is further supported by observations of a significant increase in the degradation rate of mesoporous silica nanoparticles with larger surface areas increased from 280 to 960 $m^2\ g^{-1}$ [33]. Moreover, thinner walls may also fragilize MSNs towards hydrolysis for the same surface area [22].

The dissolution of *sp*-Au@*m*SiO_2 particles at a concentration below the SSL, was observed to be significantly faster compared to *lp*-Au@*m*SiO_2 particles. This faster dissolution may be attributed to differences in specific properties, such as pore size and geometry. Specifically, *sp*-Au@*m*SiO_2 particles feature small

cylindrical pores, while *lp*-Au@*m*SiO_2 particles have conical large pores. However, the role of pore geometry in the dissolution process requires further investigation to establish any definitive correlation.

A critical factor affecting the degradability of MSN is the degree of condensation. This parameter is determined by the ratio of siloxane (Si-O-Si) bonds to silanol (Si-OH) bonds within the silica network. A higher proportion of siloxane bonds signifies a more condensed and highly connected mesoporous silica network [35]. Differences in the degree of condensation between nanoparticles may arise from variations in the synthesis method and pore size. It has been reported that calcined, non-porous silica nanoparticles degrade slowly, with only 30% degradation observed after 15 days. In contrast, non-calcined MSNs can degrade completely in less than 48 hours [19]. Studies on the degree of connectivity of the silica framework should be conducted on the particles presented in this chapter using ^{29}Si NMR. This analysis will help evaluate how the synthesis strategy affects the framework's connectivity and, in turn, the overall stability of the nanoparticles.

4.6. Conclusions

Au@*m*SiO_2 particles with tunable pore sizes and controllable particle sizes were successfully synthesized using seed growth methods. The method employing pore-expanding agents was effective in producing Au@*m*SiO_2 particles with diameters lower than 90 nm, with pore sizes adjustable by varying the TIPB amount, achieving conical pores of approximately 7 nm at the highest TIPB concentration. The biphasic stratification method yielded Au@*m*SiO_2 particles with even larger conical pores, ranging from 3 to 10 nm. Notably, when monodisperse seed nanoparticles were isolated before growth, a broader pore size distribution was achieved, with pores up to 24 nm and particle sizes of 120 nm. For both seed growth methods, starting with monodisperse and

homogeneous seeds containing a single gold core per particle was crucial for obtaining monodisperse particles that retained the core-shell morphology.

The stability and degradation behavior of large-pore Au@*m*SiO_2 particles are highly dependent on their concentration and synthesis method. When above the SSL, *e*-Au@*m*SiO_2 particles exhibit rapid degradation, forming MSN intermediates due to the dissolution and reprecipitation of the more porous external shell. By contrast, *b*-Au@*m*SiO_2 particles degrade more slowly, with a brief formation of intermediates and gradual changes in porosity and roughness. Below the SSL, all particles dissolve quickly into silicic acid or small oligomers, with *e*-Au@*m*SiO_2 particles dissolving in a two-step process and *b*-Au@*m*SiO_2 particles degrading more slowly.

The degradation behavior of large-pore Au@*m*SiO_2 differs notably from that of *sp*-Au@*m*SiO_2. Specifically, *sp*-Au@*m*SiO_2 particles degrade more rapidly when the concentration is below the SSL. Conversely, at concentrations above the SSL, *sp*-Au@*m*SiO_2 particles maintain their size and morphology for up to 10 days. However, the formation of short-lived intermediate particles is observed early in the degradation process.

These findings underscore the critical role of synthesis methods and particle concentration in influencing the stability and potential cytotoxicity of Au@*m*SiO_2 particles, which is essential for their suitability in biological applications.

4.7. References

1. Du X, Qiao SZ (2015) Dendritic Silica Particles with Center-Radial Pore Channels: Promising Platforms for Catalysis and Biomedical Applications. Small 11:392–413. https://doi.org/10.1002/smll.201401201

2. Niu D, Liu Z, Li Y, et al (2014) Monodispersed and Ordered Large-Pore Mesoporous Silica Nanospheres with Tunable Pore Structure for Magnetic Functionalization and Gene Delivery. Advanced Materials 26:4947–4953. https://doi.org/10.1002/adma.201400815

3. Zhang K, Xu L-L, Jiang J-G, et al (2013) Facile Large-Scale Synthesis of Monodisperse Mesoporous Silica Nanospheres with Tunable Pore Structure. J Am Chem Soc 135:2427–2430. https://doi.org/10.1021/ja3116873

4. Nandiyanto ABD, Kim S-G, Iskandar F, Okuyama K (2009) Synthesis of spherical mesoporous silica nanoparticles with nanometer-size controllable pores and outer diameters. Microporous and Mesoporous Materials 120:447–453. https://doi.org/10.1016/j.micromeso.2008.12.019

5. Moon D-S, Lee J-K (2012) Tunable synthesis of hierarchical mesoporous silica nanoparticles with radial wrinkle structure. Langmuir 28:12341–12347. https://doi.org/10.1021/la302145j

6. Shen D, Yang J, Li X, et al (2014) Biphase stratification approach to three-dimensional dendritic biodegradable mesoporous silica nanospheres. Nano Lett 14:923–932. https://doi.org/10.1021/nl404316v

7. Gai S, Yang P, Ma P, et al (2012) Uniform and size-tunable mesoporous silica with fibrous morphology for drug delivery. Dalton Trans 41:4511–4516. https://doi.org/10.1039/C2DT11552B

8. Gao F, Botella P, Corma A, et al (2009) Monodispersed Mesoporous Silica Nanoparticles with Very Large Pores for Enhanced Adsorption and Release of DNA. J Phys Chem B 113:1796–1804. https://doi.org/10.1021/jp807956r

9. Wu M, Meng Q, Chen Y, et al (2015) Large-Pore Ultrasmall Mesoporous Organosilica Nanoparticles: Micelle/Precursor Co-templating Assembly and Nuclear-Targeted Gene Delivery. Advanced Materials 27:215–222. https://doi.org/10.1002/adma.201404256

10. Yamada H, Ujiie H, Urata C, et al (2015) A multifunctional role of trialkylbenzenes for the preparation of aqueous colloidal mesostructured/mesoporous silica nanoparticles with controlled pore size, particle diameter, and morphology. Nanoscale 7:19557–19567. https://doi.org/10.1039/C5NR04465K

11. Fuentes KM, Onna D, Rioual T, et al (2021) Copper upcycling by hierarchical porous silica spheres functionalized with branched polyethylenimine: Antimicrobial and catalytic applications. Microporous and Mesoporous Materials 327:111391. https://doi.org/10.1016/j.micromeso.2021.111391

12. Coria-Oriundo LL, Battaglini F, Wirth SA (2021) Efficient decolorization of recalcitrant dyes at neutral/alkaline pH by a new bacterial laccase-mediator system. Ecotoxicology and Environmental Safety 217:112237. https://doi.org/10.1016/j.ecoenv.2021.112237

13. Lin Y-S, Lu C-YD, Hung Y, Mou C-Y (2009) Uniform Mesoporous Silica Hexagon and Its Two-Dimensional Colloidal Crystal. ChemPhysChem 10:2628–2632. https://doi.org/10.1002/cphc.200900251

14. Cauda V, Schlossbauer A, Kecht J, et al (2009) Multiple Core−Shell Functionalized Colloidal Mesoporous Silica Nanoparticles. J Am Chem Soc 131:11361–11370. https://doi.org/10.1021/ja809346n

15. Nakamura T, Mizutani M, Nozaki H, et al (2007) Formation Mechanism for Monodispersed Mesoporous Silica Spheres and Its Application to the Synthesis of Core/Shell Particles. J Phys Chem C 111:1093–1100. https://doi.org/10.1021/jp0648240

16. Yano K, Nakamura T (2006) Synthesis of Highly Monodispersed Core/Shell Mesoporous Silica Spheres. Chemistry Letters 35:1014–1015. https://doi.org/10.1246/cl.2006.1014

17. Lin Y-S, Tsai C-P, Huang H-Y, et al (2005) Well-Ordered Mesoporous Silica Nanoparticles as Cell Markers. Chem Mater 17:4570–4573. https://doi.org/10.1021/cm051014c

18. Yamamoto E, Mori S, Shimojima A, et al (2017) Fabrication of colloidal crystals composed of pore-expanded mesoporous silica nanoparticles prepared by a controlled growth method. Nanoscale 9:2464–2470. https://doi.org/10.1039/C6NR07416B

19. Croissant JG, Fatieiev Y, Khashab NM (2017) Degradability and Clearance of Silicon, Organosilica, Silsesquioxane, Silica Mixed Oxide, and Mesoporous Silica Nanoparticles. Advanced Materials 29:1604634. https://doi.org/10.1002/adma.201604634

20. Lin C-Y, Yang C-M, Lindén M (2022) Dissolution and morphology evolution of mesoporous silica nanoparticles under biologically relevant conditions. Journal of Colloid and Interface Science 608:995–1004. https://doi.org/10.1016/j.jcis.2021.09.164

21. Spitzmüller L, Nitschke F, Rudolph B, et al (2023) Dissolution control and stability improvement of silica nanoparticles in aqueous media. J Nanopart Res 25:40. https://doi.org/10.1007/s11051-023-05688-4

22. Guerrero-Florez V, Barbara A, Kodjikian S, et al (2024) Dynamic Light Scattering Unveils Stochastic Degradation in Large-pore Mesoporous Silica Nanoparticles. J Colloid Interface Sci 676:1098–1108. https://doi.org/10.1016/j.jcis.2024.07.151

23. McCarrick S, Midander K, Krausová M, et al (2021) Gold Nanoparticles Dissolve Extracellularly in the Presence of Human Macrophages. Int J Nanomedicine 16:5895–5908. https://doi.org/10.2147/IJN.S314643

24. Balfourier A, Luciani N, Wang G, et al (2020) Unexpected intracellular biodegradation and recrystallization of gold nanoparticles. Proceedings of the National Academy of Sciences 117:103–113. https://doi.org/10.1073/pnas.1911734116

25. Robens E (1999) Adsorption by powders and porous solids. F. Rouquerol, J. Rouquerol, K. Sing, Academic Press, San Diego 1999, ISBN: 0-12-598920-2, 467 S. £79.95. Vakuum in Forschung und Praxis 11:191–191. https://doi.org/10.1002/vipr.19990110317

26. Henriksson U, Blackmore ES, Tiddy GJT, Soederman O (1992) Intermediate liquid crystalline phases in the binary system C16TACl-H2O: an NMR and low-angle x-ray diffraction study. J Phys Chem 96:3894–3902. https://doi.org/10.1021/j100188a059

27. Bahadur J, Maity A, Sen D, et al (2021) Origin of the Hierarchical Structure of Dendritic Fibrous Nanosilica: A Small-Angle X-ray Scattering Perspective. Langmuir 37:6423–6434. https://doi.org/10.1021/acs.langmuir.1c00368

28. Nemec S, Kralj S (2021) A Versatile Interfacial Coassembly Method for Fabrication of Tunable Silica Shells with Radially Aligned Dual Mesopores on Diverse Magnetic Core Nanoparticles. ACS Appl Mater Interfaces 13:1883–1894. https://doi.org/10.1021/acsami.0c17863

29. Bruschi L, Mistura G, Negri F, et al (2018) Adsorption on alumina nanopores with conical shape. Nanoscale 10:18300–18305. https://doi.org/10.1039/C8NR06265J

30. Nguyen PTM, Do DD, Nicholson D (2013) Simulation study of hysteresis of argon adsorption in a conical pore and a constricted cylindrical pore. Journal of Colloid and Interface Science 396:242–250. https://doi.org/10.1016/j.jcis.2012.12.057

31. Noureddine A, Hjelvik EA, Croissant JG, et al (2019) Engineering of large-pore lipid-coated mesoporous silica nanoparticles for dual cargo delivery to cancer cells. J Sol-Gel Sci Technol 89:78–90. https://doi.org/10.1007/s10971-018-4772-1

32. Yamada H, Urata C, Aoyama Y, et al (2012) Preparation of Colloidal Mesoporous Silica Nanoparticles with Different Diameters and Their Unique Degradation Behavior in Static Aqueous Systems. Chem Mater 24:1462–1471. https://doi.org/10.1021/cm3001688

33. He Q, Shi J, Zhu M, et al (2010) The three-stage *in vitro* degradation behavior of mesoporous silica in simulated body fluid. Microporous and Mesoporous Materials 131:314–320. https://doi.org/10.1016/j.micromeso.2010.01.009

34. Mendez N, Liberman A, Corbeil J, et al (2017) Assessment of in vivo systemic toxicity and biodistribution of iron-doped silica nanoshells. Nanomedicine: Nanotechnology, Biology, and Medicine 13:933–942. https://doi.org/10.1016/j.nano.2016.10.018

35. da Cruz Schneid A, Albuquerque LJC, Mondo GB, et al (2022) Colloidal stability and degradability of silica nanoparticles in biological fluids: a review. J Sol-Gel Sci Technol 102:41–62. https://doi.org/10.1007/s10971-021-05695-8

Chapter 5

Protein loading on Au@*m*SiO_2 nano-vehicles

5.1. Introduction

Protein delivery using nano-vehicles requires meeting three key criteria: (i) the nano-vehicles must retain the protein efficiently, (ii) the proteins must remain stable and functional; and (iii) the nanoparticles must maintain their stability under physiological conditions, preserving their integrity until they reach the target site. This chapter aims to address these criteria to evaluate the potential of the designed Au@*m*SiO_2 nano-vehicles for protein transport. We begin by examining the loading capacity of Au@*m*SiO_2 nanoparticles and evaluating the impact of pore size on this capacity. Next, we investigate the proteins location on nanoparticles—whether they are encapsulated within the pores or adsorbed on the external surface. We also assess the stability of the retained proteins by analyzing changes in their conformational structure and functionality. Finally, we evaluate the stability of the protein-loaded nanoparticles using a methodology similar to that presented in Chapter 4.

Protein adsorption on silica nanoparticles is primarily driven by the particle-protein interaction and structural characteristics of each protein [1, 2].

Since the interaction is predominantly long-range van der Waals forces, the surface charges of proteins are critical in determining their adsorption behavior. Proteins containing positively charged amino acids are more likely to interact with the negatively charged silica surface [3]. Apart from the *N*-terminus, which is typically buried within the protein, only arginine and lysine have positively charged groups at physiological pH. The presence of these amino acids significantly enhances the protein's affinity for the silica surface [3].

The structural stability of proteins also plays a crucial role in their adsorption behavior. Based on Norde's pioneering research, proteins can be classified as either 'hard' or 'soft,' depending on their structural stability during adsorption [4–7]. 'Hard' proteins maintain their structure with minimal changes upon adsorption, resulting in transient interactions where the desorbed proteins retain their native structure. By contrast, 'soft' proteins undergo significant structural alterations upon adsorption, spreading out on the surface, which can lead to irreversible adsorption. However, many proteins exhibit intermediate behaviors, possessing both well-structured and flexible regions. Some proteins also contain intrinsically disordered regions, which lack stable secondary structures [8] and show a high affinity for silica surfaces [9] but the underlying reasons for this affinity remain unclear.

Surface properties like pore size and structure, and particle size significantly influence protein adsorption on silica nanoparticles. Adsorption is generally more effective when the protein size matches or is smaller than the pore size [10–13]. Pore structure plays a crucial role in protein adsorption due to confinement effects [14], which can limit the available space, making it difficult for proteins to form a densely packed monolayer with favorable orientation and conformation. Furthermore, the surface curvature impacts the structure and function of adsorbed proteins. For certain proteins, such as BSA [15], and cytochrome C [16], a higher surface curvature better preserves their structure and function. However, in the case of RNase A, the degree of denaturation increases with the curvature [17].

The stability of protein adsorbed on nanoparticles is linked to the conformational changes that occur due to protein-nanoparticle interactions [18, 19]. These structural changes vary: some proteins like RNase A and lysozyme lose structure and function upon adsorption on silica surfaces [20, 21] while others, such as cytochrome c, exhibit enhanced activity due to alterations in their heme environments when interacting with silica nanoparticles [16].

Regarding the stability of protein-loaded nanoparticles, information is quite limited, with existing studies primarily focusing on MSN suspended in albumin solutions rather than MSN loaded with the protein [22–24]. These studies suggest that albumin can significantly impact the stability of MSN. Specifically, albumin-MSN exhibit improved colloidal stability [23], a reduced rate of silica dissolution [22], and a different dissolution mechanism compared to nanoparticles without protein [24].

Despite numerous studies on protein adsorption onto silica nanoparticles, there is a lack of comprehensive information regarding the key variables influencing protein loading and the stability of both the particles and proteins. Most research has focused on dense silica nanoparticles or those with small pores, where protein adsorption is primarily superficial [10-11,13]. Consequently, there is limited knowledge about the behavior of proteins loaded into nanoparticles with larger pores and the effects on protein and particle stabilities remain poorly understood.

To address these knowledge gaps, this chapter investigates the loading of three model proteins—bovine serum albumin (BSA), *m*Cherry, and horseradish peroxidase (HRP)— onto different types of nanoparticles: large-pore Au@*m*SiO_2 (*lp*-Au@*m*SiO_2), small-pore Au@*m*SiO_2 (*sp*-Au@*m*SiO_2), and non-porous silica nanoparticles (SNPs). These proteins were selected for their distinct sizes, isoelectric point, structural stability, and functionalities, making them ideal for studying how different nanoparticle architectures influence protein adsorption. This study aims to elucidate how these nanoparticle systems influence protein adsorption and to evaluate the stability of both the proteins and the particles in

saline medium. Ultimately, this research seeks to enhance our understanding of the factors that govern protein interactions with Au@*m*SiO_2 nanoparticles.

This chapter presents the results of several characterization techniques, including circular dichroism (CD) to assess protein stability upon loading onto nanoparticles, and atomic force microscopy (AFM) and *cryo*-electron microscopy (*cryo*-EFTEM) to determine protein location. All these techniques were optimized for this study (refer to Chapter 2 for details). Notably, to the best of our knowledge, this study presents the first use of AFM and *cryo*-EF-TEM specifically to characterize protein adsorption on silica nanoparticles [25], offering new insights into protein-nanoparticle interactions.

It is important to highlight that the results presented in this chapter are the outcome of collaborative work with various institutions, laboratories, and researchers. CD spectra of adsorbed proteins were obtained in collaboration with the Laboratorio Nacional de Luz Sincrotrón (LNLS, CNPEM, Brazil). AFM microscopy was conducted in collaboration with the Centro Avanzado de Microscopia (CMA, UBA, Argentina). *Cryo*-EF-TEM microscopy was performed in collaboration with the Laboratorio Nacional de Nanotecnología (LNNano, CNPEM, Brazil). The *m*Cherry protein was cloned and purified at the Instituto de Biociencias, Biotecnologia y Biologia translacional (iB3, UBA, Argentina). Enzymatic activity and proteins quantification assays were conducted in collaboration with the Laboratorio de Agrobiotecnología (UBA, Argentina) and the Chemistry for the Recognition and Study of Biological Assemblies Laboratory (CREAB, SyMMES, France).

5.2. The particles explored

Three types of nanoparticles with varying pore sizes were used: large-pore Au@*m*SiO_2 (*lp*-Au@*m*SiO_2) from Chapter 4 (see also Chapter 2, Section 2.1.2.3), small-pore Au@*m*SiO_2 (*sp*-Au@*m*SiO_2) from Chapter 3, and non-porous silica particles (SNP) synthesized as described in Chapter 2, Section 2.1.3. Figure 5.1

summarizes the characteristics of these particles. Electron microscopy images show that Au@*m*SiO_2 particles have a gold core of 15±5 nm and size distributions with averages around 100 nm (Figure 5.1 a-f and Table 5.1). The UV-vis spectra shows that Au@*m*SiO_2 exhibit a typical SPR absorption peak at 530 nm (Figure 5.1 i). The SNP are dense particles of 100±10 nm and lack a gold core (Figure 5.1 g-h).

The textural parameters of the nanoparticles were obtained by N_2 sorption and AFM analyses and are summarized in Figure 5.1 and Table 5.1. For *sp*-Au@*m*SiO_2 particles, a detailed description is provided in Chapter 3, while for *lp*-Au@*m*SiO_2, it is covered in Chapter 4. The *lp*-Au@*m*SiO_2, exhibit a specific surface area of 908 $m^2\ g^{-1}$, whit large conical mesopores ranging from 10 and 20 nm (Figure 5.1j). The *sp*-Au@*m*SiO_2 have a specific surface area of 790 $m^2\ g^{-1}$ and a pore size distribution centered around 2.5 nm Figure 5.1k. AFM images of *sp*-Au@*m*SiO_2 shows that the smaller pore size results in the pores appearing as uniform surface roughness rather than distinct holes, due to the tip's limited ability to access the pore depth (Figure 5.1e). For SNP, SEM and AFM analysis shows no porosity (Figure 5.1g-h).

The zeta potential values (ζ-potential) of Au@*m*SiO_2 are presented in Figure 5.1 l, as a function of pH. The hydroxyl groups on Au@*m*SiO_2 surfaces are deprotonated over a wide pH range (3 – 7.5), as observed by the ζ-potential variation (0 to −27 mV). It should be noted that this is an average parameter as the surface may exhibit patches with variable charge density depending on the curvature.

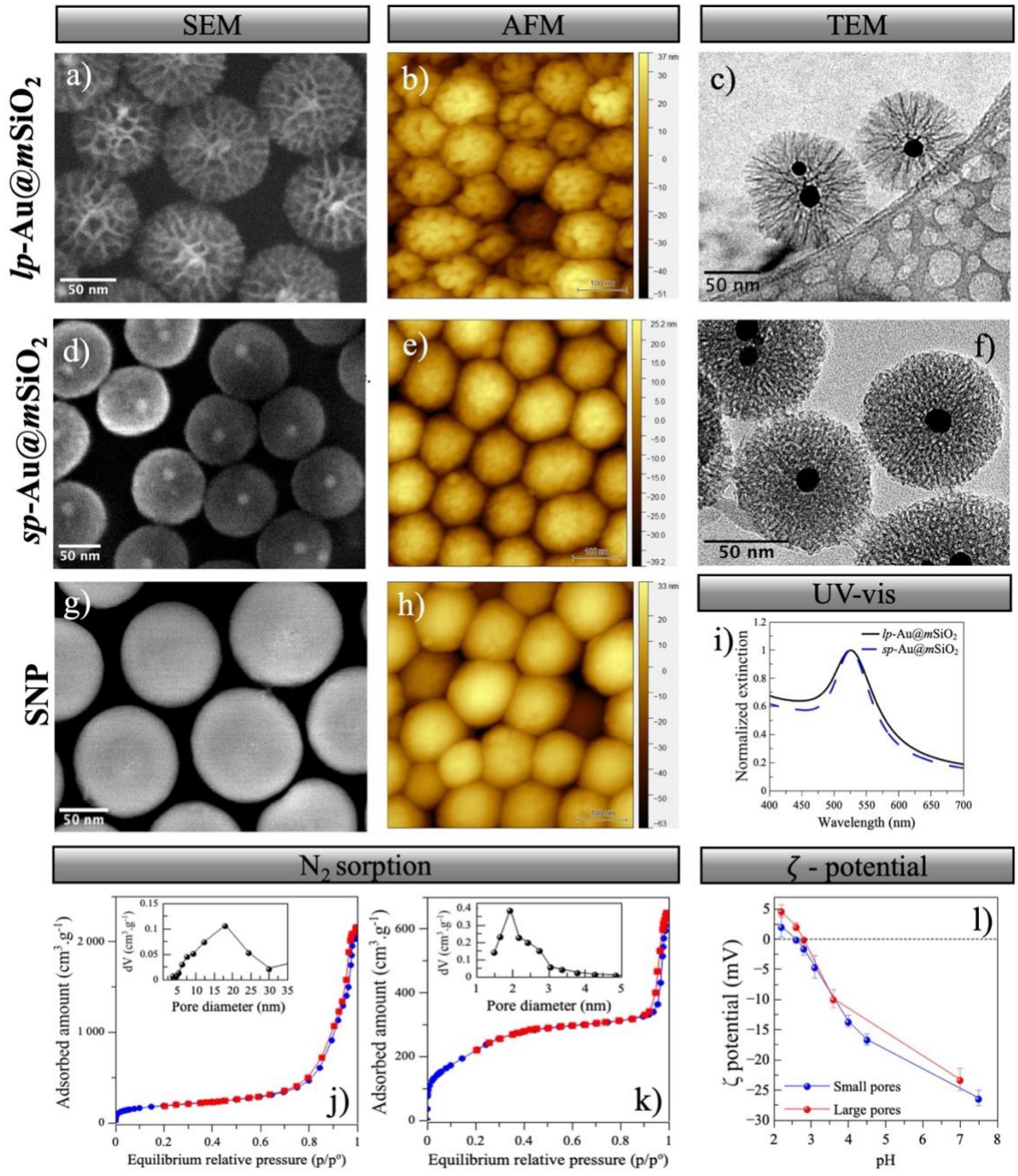

Figure 5.1. Characterization of *lp*-Au@*m*SiO_2 (a-c), *sp*-Au@*m*SiO_2 (d-f), and SNP (g-h). The left panel present SEM micrographs, the middle panel present AFM micrographs acquired in tapping mode in the topography channel over a 500 × 500 nm² area, and the right panel present TEM micrographs. (i) UV-vis spectra of *lp*-Au@*m*SiO_2 (black line) and *sp*-Au@*m*SiO_2 (blue line). (j) and (k) N_2 adsorption (blue line) /desorption (red line) isotherms of *lp*-Au@*m*SiO_2 and *sp*-Au@*m*SiO_2 respectively, with BJH pore size distribution in the insets (l) ζ-potential of particles as a function of pH.

Table 5.1. Characterization data of Au@*m*SiO_2 and SNP. Particle diameters (D_{part}) were determined from SEM and AFM micrographs. Hydrodynamic diameters were measured using DLS. The surface area and mesopore volume were derived from the N_2-sorption isotherms showed in Figure 5.1. The pore diameter was determined from BJH and AFM micrographs. For SNP, the surface area was calculated considering a sphere with a diameter of 110 nm.

Particle	SEM D_{part} (nm)	AFM D_{part} (nm)	Hydrodynamic diameter (nm)	Surface area (m^2/g)	Mesopore volume (cm^3/g)	BJH Pore diameter (nm)	AFM Pore diameter (nm)
lp-Au@*m*SiO_2	95 ± 12	103±8	123±3	908	0.52	17	10±4
sp-Au@*m*SiO_2	93 ± 7	103±7	116±4	790	0.45	2.3	-
SNP	110 ± 10	110±12	-	23	-	-	-

5.3. The proteins explored

The protein loading capacity of Au@*m*SiO_2 particles was evaluated using three model proteins: BSA, *m*Cherry, and HRP. These proteins were carefully selected based on their structural stability, with BSA classified as a 'soft' protein [26] and *m*CHerry and HRP classified as 'hard' proteins [27, 28]. Among the hard proteins, HRP and *m*Cherry differ significantly in terms of dimensions, secondary structure, and surface charge, as illustrated in Figure 5.2 and detailed in Table 5.2, which present their physicochemical properties and crystallographic structures, respectively. HRP was also selected for its measurable enzymatic activity, enabling the assessment of enzyme activity when loaded into particles.

BSA, is the most prevalent protein in blood and is known for its globular structure and conformational adaptability. Structurally, BSA consists of a single large globular protein chain made up of 583 amino acid residues that is divided into three homologous but structurally distinct domains. Protein's secondary structure is predominantly α-helical, with flexible regions between subdomains [29, 30]. BSA has an isoelectric point around 4.5–4.8 [31] and exhibits an asymmetric surface charge distribution (Figure 5.2).

*m*Cherry is a luminescent, monomeric protein with a fluorescent chromophore. It is composed of 236 amino acids folded in 11 β-strands arranged in a barrel shape known as a β-can, which provides the structural rigidity. A single central helix runs through the middle of this β-can, with three amino acid residues forming the chromophore [32]. *m*Cherry has an isoelectric point of 5.8 [33]. The surface charge distribution of *m*Cherry reveals the presence of both negative and positive charge patches, evenly distributed across the protein surface (Figure 5.2).

HRP is a monomeric plant enzyme that catalyzes the oxidation of aromatic compounds by hydrogen peroxide or alkyl hydroperoxide. Its structure consists of a single polypeptide chain, a heme group, and two Ca^{2+} ions that maintain the enzyme's conformation [35, 36]. HRP is a globular molecule with a predominantly α-helical secondary structure. The heme group, acts as the active site and has a planar structure conformation, with the heme moiety securely placed between two structurally rigid domains, contributing to the overall structural stability of HRP [37]. HRP exists in various isoenzymic forms, with isoelectric points ranging from 3.0 to 9.0 [38].

In summary, BSA, *m*Cherry, and HRP were selected to provide a range of protein types with distinct structures, sizes, stabilities, and isoelectric points. This diverse selection allows for a thorough evaluation of how different proteins interact with the Au@*m*SiO_2 particles.

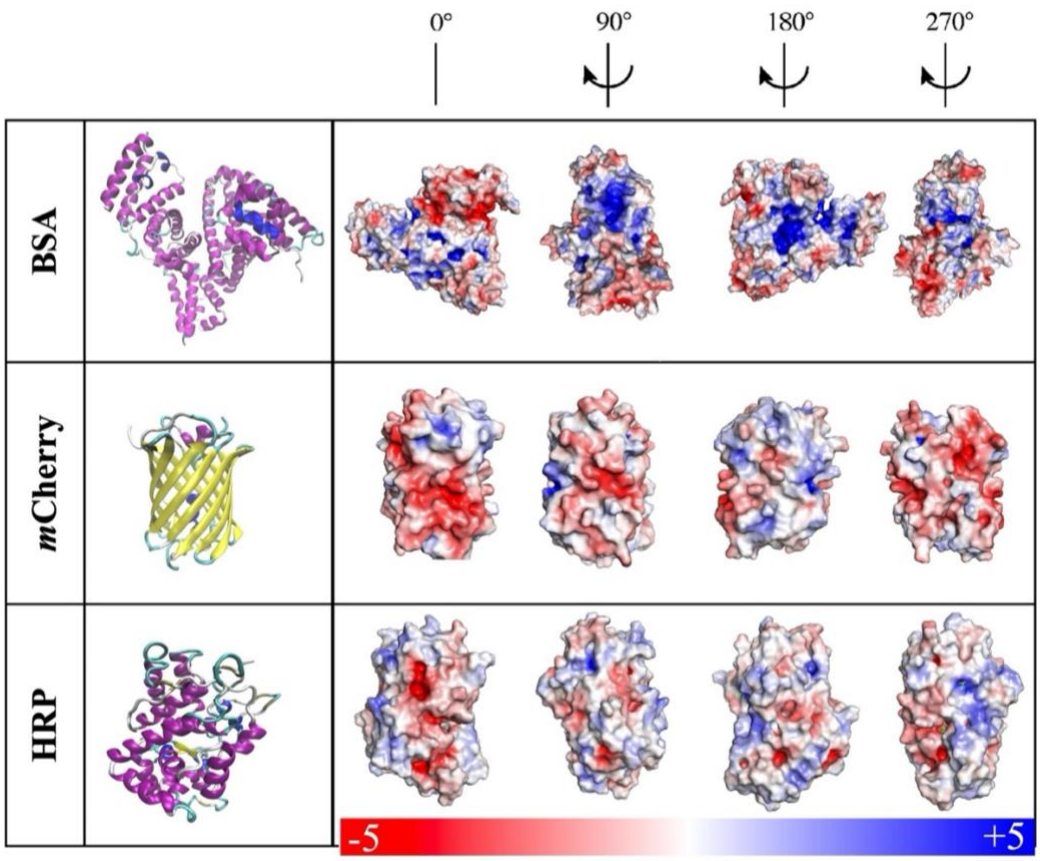

Figure 5.2. Crystallographic structures of BSA, *m*Cherry, and HRP obtained from the Protein Data Bank (PDB) with respective PDB codes: 4f5s, 2vad, and 1hch. In the left panel the proteins are shown in New Cartoon representation, with secondary structures color-coded as follows: Alpha-helix (violet), 3_{10}-helix (blue), turn (cyan), beta-strand (yellow), and coil (white). The right panel show the surface of each protein colored by electrostatic potential. The scale bar shows the range of electrostatic potential from -5.0 kcal/mol (red) to +5.0 kcal/mol (blue). Images were generated using the Adaptive Poisson-Boltzmann Solver (APBS) in Pymol [34]

Table 5.2. Physical Properties of the adsorbed proteins

Protein	**[a]Mw (kDa)**	**[a]Dimensions (nm^3)**	**Isoelectric point**	**[b]Ads max ($nmol.m^{-2}$)**
BSA	66	8 × 8 × 3.5	4.5–4.8	60
*m*Cherry	32	4 × 3 × 3	5.8	32
HRP	44	11.7 × 4 × 6.7	3 – 9	10

[a]The molecular weight and geometric dimensions of these proteins come from the Protein Data Bank. PDB codes: 4f5s, 1atj, and 4zin.

[b]Amount of the proteins adsorbed per m2 was calculated based on the molecular dimensions for a closed-packed monolayer.

5.4. Protein loading on nanoparticles

This section delves into the protein loading behavior on nanoparticles, beginning with an analysis of how pores influence loading capacity. We then estimate the maximum loading capacity for each protein on *lp*-Au@*m*SiO_2. Subsequently, AFM and *cryo*-EF-TEM microscopy techniques are employed to visualize the distribution of proteins on the nanoparticles. Finally, we assess the conformational stability of the adsorbed proteins and explore the role of pore size in maintaining this stability.

To evaluate the loading capacity, the particles were incubated with each protein under the following conditions: 2 mg of nanoparticles with 0.2 mg protein for BSA and HRP, and 0.3 mg of nanoparticles with 10 µg protein for *m*Cherry, all in phosphate buffer 10 mM (pH 7) for two hours. After incubation, unadsorbed proteins were removed by centrifugation, followed by three washes with water. Given the variations in size, volume, and surface area among the three types of particles (Table 5.1), the protein loading capacity was evaluated by calculating the effective specific adsorption, *ie*, the number of protein molecules per nanoparticle unit. Additionally, to evaluate the effective area that the protein occupies on the nanoaprticle surface -packing density- the loading capacity is expressed as nmol of protein per m^2 of nanoparticle.

To quantitatively describe the maximum loading on *lp*-Au@*m*SiO_2, the adsorption of protein onto *lp*-Au@*m*SiO_2 was further studied at 20 ˚C by varying the initial protein concentration. Adsorption equilibria data was analyzed using the Langmuir [39], Freundlich [40], Temkin-Pyzhev [41], and Dubinin-Radushkevich [42] equations. Although protein adsorption often deviates from the assumptions of these classic models [7, 43], these models were employed for

estimation and comparison purposes due to their widespread use in the literature for describing protein adsorption.

5.4.1. Bovine serum albumin

5.4.1.1. Comparative BSA loading on nanoparticle variants

Figure 5.3 and Table 5.3 display the results of BSA adsorption onto the three types of nanoparticles, demonstrating that adsorption occurs across all nanoparticle types studied. At pH 7, BSA has an overall negative effective charge, estimated to be around −8 [44] resulting from the combined charges of its amino acid residues. However, the protein's surface charge is not uniform, leading to local variations that can differ significantly from the overall charge (Figure 5.2). The loading of BSA onto the negatively charged silica surface is likely driven by electrostatic interactions, either due to positively charged regions on the protein's surface or charge regulation effects [45, 46]. This indicates that the global charge of the protein is not the most critical factor in predicting its adsorption onto nanoparticles.

Molecular dynamics simulations of BSA adsorption on a flat silica surface at pH 7 [47] have shown that the process is driven by electrostatic interactions between the lysine residues on the protein surface and the silica. During adsorption, BSA reorients to expose lysine residues on the surface while keeping negatively charged domains away. Thus, the adsorption of BSA on silica particles can be explained by electrostatic interactions between specific positive residues and the negative moieties on the particle surface.

The highest BSA effective adsorption was observed on *lp*-Au@*m*SiO_2. For *sp*-Au@*m*SiO_2 and SNP it is comparable, with slightly higher adsorption on SNP (Figure 5.3a), despite it has the lower surface area (Table 5.1). This observation aligns with previous findings that silica nanoparticles with pore sizes between 2

and 3 nm, as well as non-porous silica nanoparticles, tend to adsorb proteins larger than the pore sizes [48]. Given that BSA dimensions ($8 \times 8 \times 3.5$ nm^3) exceed the pore sizes of *sp*-Au@*m*SiO_2 (~2.5 nm), BSA likely interacts with the external surface of the particles and the pore gates forming a protein corona, a phenomenon well-documented for various porous and non-porous silica nanoparticle systems [49].

Table 5.3. Protein loading capacity of particles expressed as effective specific adsorption, *ie*, the number of protein molecules per nanoparticle unit (molecules/NP) and as protein nmol per particle square meter. The loading experiment was conducted at 25°C in 10 mM PB, pH 7 with initial protein molecule counts of 1.8 x 10^{15} for BSA, 5.2 x 10^{12} for *m*Cherry, and 2.7 x 10^{18} for HRP, and particle counts of 1.1 x 10^{12} for *lp*-Au@*m*SiO_2, 1.8 x 10^{12} for *sp*-Au@*m*SiO_2, and 1 x 10^{12} for SNP.

Particle	BSA		*m*Cherry		HRP	
	Molecules/NP	nmol/m² NP	Molecules/NP	nmol/m² NP	Molecules/NP	nmol/m² NP
lp-Au@*m*SiO_2	1267±103	1.8±0.14	939±4	1.29±0.1	1643±34	2.3±0.05
sp-Au@*m*SiO_2	603±104	1.2±0.2	389±11	0.74±0.02	897±16	1.7±0.03
SNP	877±210	32±10	15±8	0.56±0.32	1546±87	56.8±3

For *lp*-Au@*m*SiO_2 since the pores of these particles are larger (15-20 nm) than BSA, protein adsorption can occur both on the external surface of the particles and within the pores. The combination of these adsorption sites results in a high adsorption uptake per particle (Figure 5.3a). When the results are normalized by the specific surface area, the amount adsorbed in the case of non-porous particles is much higher than for Au@*m*SiO_2. The outer surface seems to be used to create a corona of proteins. For *lp*- and *sp*-Au@*m*SiO_2, only a small part of the surface area is available to interact with the proteins. In the case of

sp-Au@*m*SiO_2, this includes the outer surface and pore entrances, while for *lp*-Au@*m*SiO_2, it comprises the outer surface and the fraction of conical mesopores with an appropriate diameter for protein adsorption.

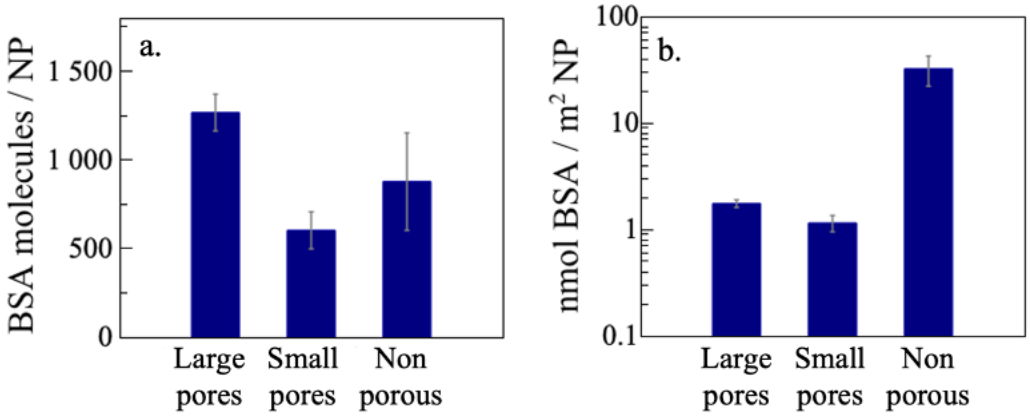

Figure 5.3. a) BSA effective adsorption showed in number of protein molecules per particle unit. b) Particles loading capacity expressed in nmol of protein per m^2 of particle. Error bars represent standard deviation (n=3). The loading experiment was conducted at 25°C in 10 mM PB, pH 7 with initial protein molecule counts of 1.8 x 10^{15} for BSA and particle counts of 1.1 x 10^{12} for *lp*-Au@*m*SiO_2, 1.8 x 10^{12} for *sp*-Au@*m*SiO_2, and 1 x 10^{12} for SNP.

5.4.1.2. Adsorption equilibria of BSA on *lp*-Au@*m*SiO_2

Based on the determination coefficients (R^2) obtained from the fitting analysis (Appendix 4), the adsorption behavior of BSA on *lp*-Au@*m*SiO_2 is best described by the Langmuir equation (R^2 = 0.978), outperforming the other models studied (Freundlich R^2 = 0.962, Temkin R^2 = 0.936, and Dubinin-Radushkevich R^2 = 0.711).

The results indicate that in a saturated state, each nanoparticle accommodates approximately up to ten thousand BSA molecules (Q_m = 10 136 BSA molecules/NP) (Figure 5.4 b). If we approximate the large pores of *lp*-Au@*m*SiO_2 as uniformly conical with an external diameter of 17 nm, each nanoparticle is estimated to have around 700 pores. Given the dimensions of a

BSA molecule (8 × 8 × 3.5 nm^3), and a pore height of 25 nm, up to 20 BSA molecules could theoretically fit in each pore. This gives a theoretical maximum of 8400 BSA molecules that could fit within the pores of each particle. These estimation suggest that in a saturated state, BSA not only fills the pores but also covers the outer surface, forming a stable "hard corona" (strongly bound protein layer) [49] that remains even after particle washing.

The maximum loading of BSA on *lp*-Au@*m*SiO_2 is higher than that reported in other studies using nanoparticles with pores between 2 and 40 nm (See Appendix 5). This high adsorption capacity may be attributed to the excellent colloidal and hydrolytic stability of the nanoparticles (See Chapter 4), a factor that has been scarcely studied in the current literature.

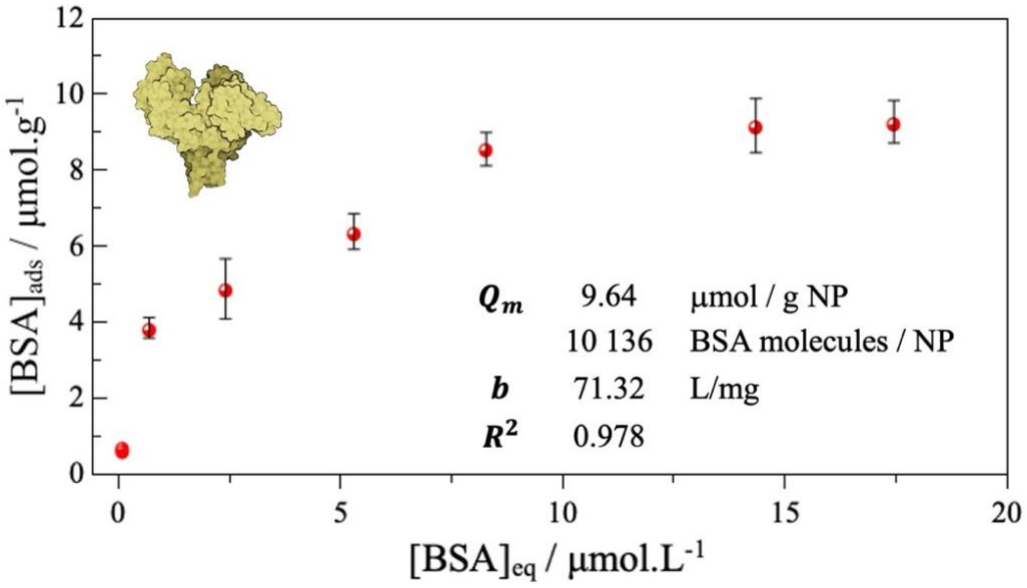

Figure 5.4. Amount of BSA adsorbed per gram of *lp*-Au@*m*SiO_2 as a function of free protein concentration in solution. Error bars are the standard deviation from independent measurements. The parameters derived from the Langmuir equation are shown: (Q_m) the maximum amount of protein adsorbed expressed in µmol BSA per gram of nanoparticle, and the number of BSA molecules per nanoparticles (*b*) "Langmuir constant" for adsorbate-adsorbent equilibrium.

5.4.1.3. BSA location on nanoparticles

To characterize BSA location on each type of particle, AFM and *cryo*-EF-TEM microscopy under cryogenic conditions were employed. AFM micrographs (Figure 5.5) showed an increase in particle diameter of 12±7 nm, 16±8 nm, and 11±8 nm for *lp*-Au@*m*SiO_2, *sp*-Au@*m*SiO_2, and SNP, respectively, upon BSA loading (Table 5.4).

From *cryo*-EF-TEM microscopy, which maps carbon from the protein and silicon from the particles (as detailed in Chapter 2, section 2.4.4), showed a carbon layer surrounding the silicon signal of *lp*-Au@*m*SiO_2 and *sp*-Au@*m*SiO_2 particles (Figure 5.6). The thickness of this carbon layer was consistent with the diameter increase observed by AFM (Table 5.4). These results indicate that the observed increase in particle size by AFM, along with the carbon layer detected by *cryo*-EF-TEM, is due to the formation of a protein corona on the surface of the nanoparticles.

Table 5.4. Protein corona thickness representing the adsorbed protein layer on the external surface of the particles. The AFM-measured corona thickness was determined by the difference in particle size with and without BSA. The *cryo*-EF-TEM-measured corona thickness was obtained by measuring the thickness of the carbon signal in Figure 5.5.

Sample	**AFM corona thickness (nm)**	**EF-TEM thickness (nm)**
lp-Au@*m*SiO_2	12±7	15±9
sp-Au@*m*SiO_2	16±8	25±5
SNP	11±8	ND

In the case of SNP, the maximum BSA adsorption as a monolayer can be calculated by considering the native heart-shaped structure of BSA, which can be approximated to a triangular prism. On a dense flat surface, the maximum amount of BSA that can be adsorbed is about 12 nmol/m² (Table 5.2). Given that adsorption is typically higher on curved surfaces, the amount of BSA adsorbed on spherical particles should exceed 12 nmol/m². Indeed, adsorption twice this

value was observed on SNP (Figure 5.3b). This finding, along with the increase in diameter observed by AFM, indicates that BSA forms at least a monolayer around SNP.

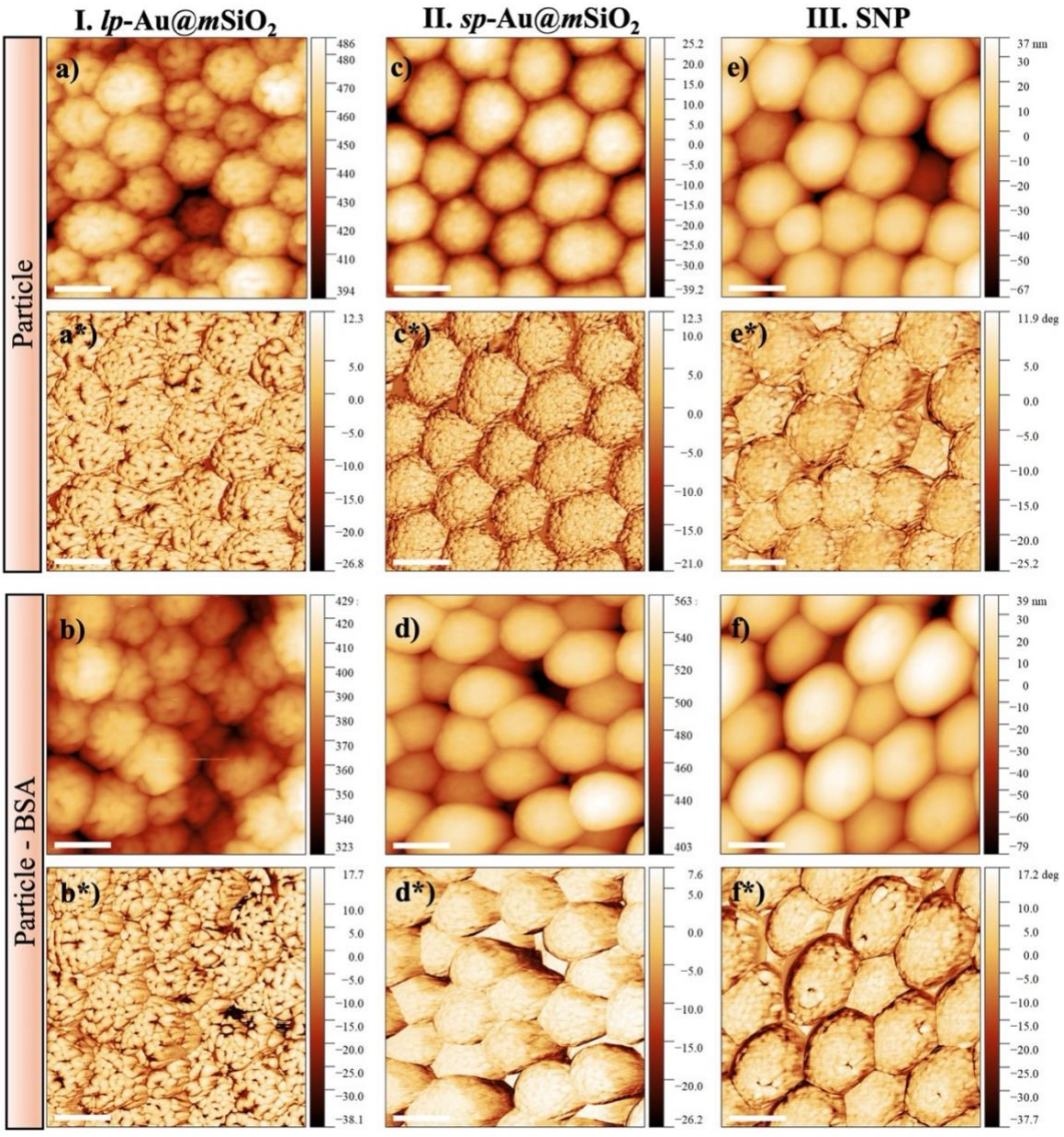

Figure 5.5. AFM micrographs of I. *lp*-Au@mSiO$_2$, II. *sp*-Au@mSiO$_2$, and III.SNP with BSA (bottom panel) and without BSA (upper panel). The micrographs were acquired in tapping mode in the topography and phase (*) channel over a 500 × 500 nm² area. Horizontal scale bar = 100 nm.

In addition to measuring the size of the protein corona adsorbed on the external surface of the three types of particles, AFM also allowed for the analysis of particle roughness through phase images. For *lp*-Au@*m*SiO_2, a slight decrease in pore size and depth was observed (Table 5.5), which can be attributed to BSA adsorption on the outer surface of nanoparticles. In the case of *sp*-Au@*m*SiO_2 and SNP, the particle roughness seems to be lower, making the particles appear smoother in the presence of BSA (Figure 5.5 c*- d* and e*-f*). This suggests that BSA forms a more compact layer on these particles, likely due to a larger interaction area with the particle's external surface.

Table 5.5. Parameters obtained from the characterization of particles with and without BSA, as determined by AFM in tapping mode.

Sample	***lp*-Au@*m*SiO_2**		***sp*-Au@*m*SiO_2**		**SNP**	
	No BSA	**BSA**	**No BSA**	**BSA**	**No BSA**	**BSA**
AFM D_{part} (nm)	102±3	114±4	101±4	117±4	105±5	116±3
AFM pore size (nm)	10±4	8.7±4	-	-	-	-
AFM pore depth (nm)	6.7±4	4.6±3	-	-	-	-

In addition, the silicon and carbon maps determined by *cryo*-EF-TEM (Figure 5.5) showed significant differences in protein localization. For *lp*-Au@*m*SiO_2, carbon signals due to BSA were intense and distributed homogeneously within and outside the particles, represented by the silicon signal. By contrast, for *sp*-Au@*m*SiO_2 carbon signals were predominantly distributed around the particles, with merged micrographs showing a silicon

signal surrounded by a carbon layer. Altogether, these results demonstrate that BSA is located both inside and outside the pores for *lp*-Au@*m*SiO_2, while for *sp*-Au@*m*SiO_2 BSA adsorbs mainly as a protein corona outside the particle rather than inside the pores. Furthermore, these results highlight that *core-loss cryo*-EF-TEM is an effective technique for visualizing and characterizing protein adsorption on silica particles.

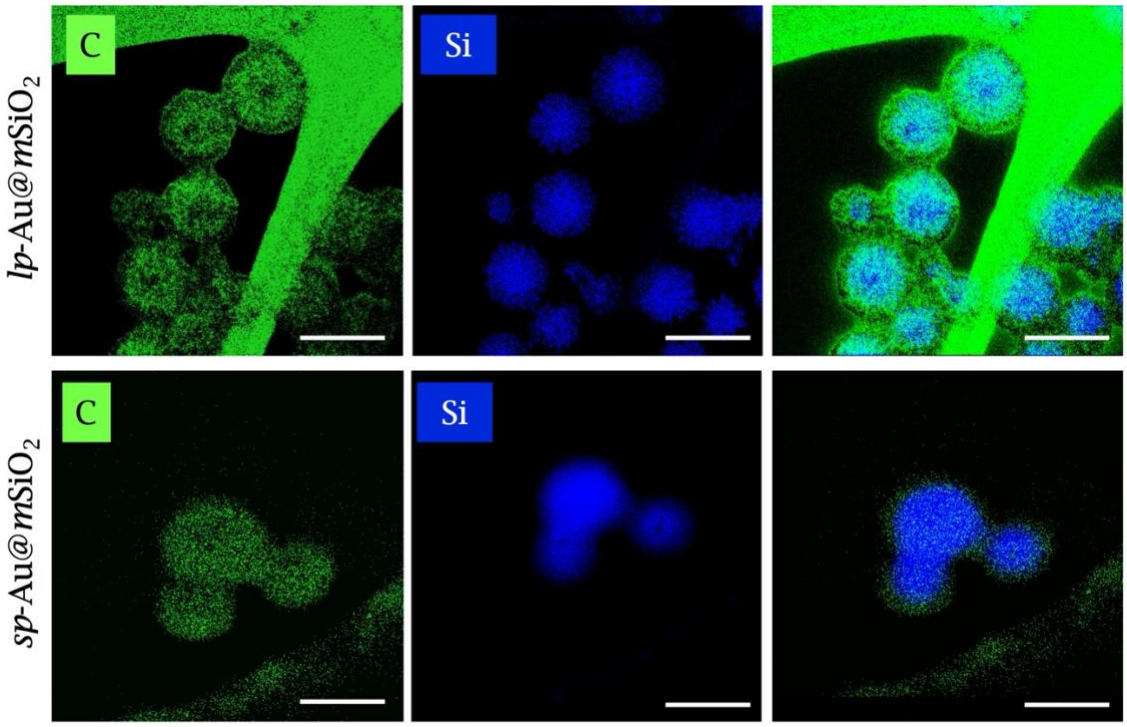

Figure 5.6. *cryo*-EFTEM micrographs of the C (green signal) and Si (blue signal) elements corresponding to (top) *lp*-Au@*m*SiO_2 + BSA and (bottom) *sp*-Au@*m*SiO_2 + BSA. The last panel shows the merged image of Si and C signals. The sample was prepared on a lacey carbon grid (green signal) under cryogenic conditions. Scale bar = 100 nm

5.4.1.4. Structural Stability of BSA loaded on particles

Most proteins experience a loss of secondary structure upon adsorption [4, 5]. The origin of this destructuration is unclear, but conformational changes

likely enhance protein-surface interactions. To analyze the stability of proteins adsorbed in Au@*m*SiO_2, secondary structure changes were studied by circular dichroism for proteins immobilized on *lp*-Au@*m*SiO_2 and *sp*-Au@*m*SiO_2.

The spectrum of free BSA (Figure 5.7a, left panel) exhibits the typical characteristics for BSA reported in the literature, with a positive maximum at 192 nm and two negative minima at 208 and 222 nm [50, 51]. As the temperature increases, these signals diminish in intensity primarily due to significant conformational changes favoring unordered secondary motifs [52]. When BSA is adsorbed on *sp*-Au@*m*SiO_2, characteristic bands of free BSA in solution are preserved, but their intensity drops abruptly, indicating a substantial alteration in secondary structure. For BSA adsorbed on *lp*-Au@*m*SiO_2, the overall intensity of the spectrum is maintained, but there is an inversion in the intensity of the negative minima at 208 and 222 nm, favoring the latter. In both cases, for BSA adsorbed on *sp*-Au@*m*SiO_2 and *lp*-Au@*m*SiO_2, the increase in temperature results in a smaller decrease in intensity compared to the free protein.

The secondary structure of free BSA derived from CD spectra (Figure 5.7b, left panel) exhibit a thermal stability profile consistent with the mechanism of BSA denaturation reported in the literature [52, 53]. Indeed, for free BSA at 50 ˚C, a thermal transition is observed with a slight loss of α-helices and an increase in disordered structures (others and turns). These conformational changes are reversible and do not alter protein function [53]. Increasing the temperature above 50 ˚C results in more substantial conformational changes; the decreasing number of α-helices becomes more pronounced, leading to an increase in disordered structures. This change involves domain unfolding, and at this point, structural changes are only partially reversible [52, 53]. When heated to 70 ˚C, there is also a slight increase in β-strands percentage due to formation of intermolecular associations between partially unfolded proteins, eventually forming a molten globule [52].

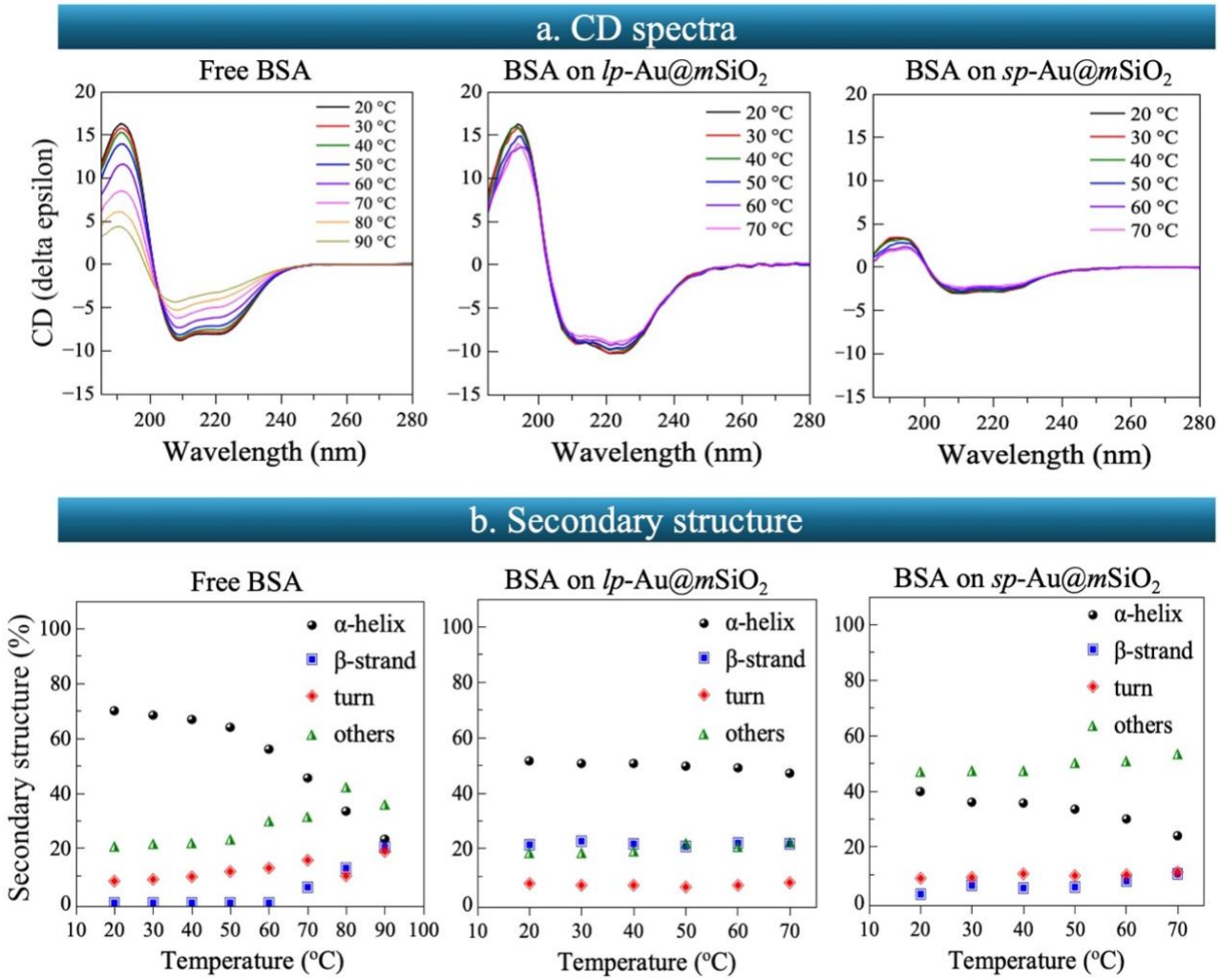

Figure 5.7. CD of BSA before and after loading on *lp*- and *sp*- Au@*m*SiO_2 a) UV-CD spectra of BSA free in water (left), BSA loaded on *lp*-Au@*m*SiO_2 (middle) and *sp*-Au@*m*SiO_2 particles (right) over a temperature range from 20 ˚C to 70 ˚C. b) Secondary structure derived from CD spectra for free BSA, BSA on *lp*-Au@*m*SiO_2, and BSA on *sp*-Au@*m*SiO_2.

BSA adsorbed on *sp*-Au@*m*SiO_2 exhibits a loss of nearly 30% of α-helices, accompanied by a gain of disordered structures and β-sheet domains, suggesting significant conformational changes upon adsorption (Figure 5.7a, middle panel). The thermal stability profile follows a trend similar to that observed for free BSA, albeit with the transition temperature shifted to 60 ˚C and lower decrease of the number of α-helices with increasing temperature, indicative of increased thermostability. The loss of secondary structure following adsorption on *sp*-

Au@*m*SiO_2 is attributed to BSA adopting a perturbed state (P state). This observation is consistent with reports of BSA adsorption on negatively charged surfaces, where conformational changes are proposed as the primary driving force for adsorption even under unfavorable electrostatic interactions [6, 52].

When BSA is adsorbed on *lp*-Au@*m*SiO_2, the P state implies a loss of only about 18% of α-helices, with a predominant gain in β-sheets (Figure 5.7a, right panel). The reduced loss of α-helices indicates that the proteins are lodged within the large pores and encapsulated, leading to minimal disturbance in their secondary structures. The transition from α-helix to β-sheet upon heating typically involves intermolecular associations, such as the aggregation of multiple BSA molecules [52, 54], consistent with the estimation that at least three BSA molecules can reside in a pore. Remarkably, there is nearly no loss of α-helices up to 70 °C, suggesting that the proteins adsorbed on *lp*-Au@*m*SiO_2 exhibit greater thermostability compared to free BSA and BSA adsorbed on *sp*-Au@*m*SiO_2. Importantly, in BSA on *lp*-Au@*m*SiO_2, there is no increase in disordered structures, indicating the absence of transition from the P state to the denatured state observed in free BSA and BSA on *sp*-Au@*m*SiO_2. This underscores the protective role of the pore walls.

5.4.2. *m*Cherry

5.4.2.1. Comparative *m*Cherry loading on particle variants

*m*Cherry adsorption was predominantly observed on porous particles (Figure 5.8). The protein's isoelectric point is 5.8 [33], indicating that at pH 7, *m*Cherry has a net negative charge. Visualization of *m*Cherry's electrostatic surface also shows that it is predominantly composed of negative charges (Figure 5.2), making electrostatic interactions with the negatively charged silica surface

unfavorable. Additionally, *m*Cherry's "hard" structure resists conformational change upon adsorption. This inherent rigidity, combined with unfavorable electrostatic interactions, leads to poor adsorption on SNPs, consistent with previous findings for its closely related GFP mutant [9, 55].

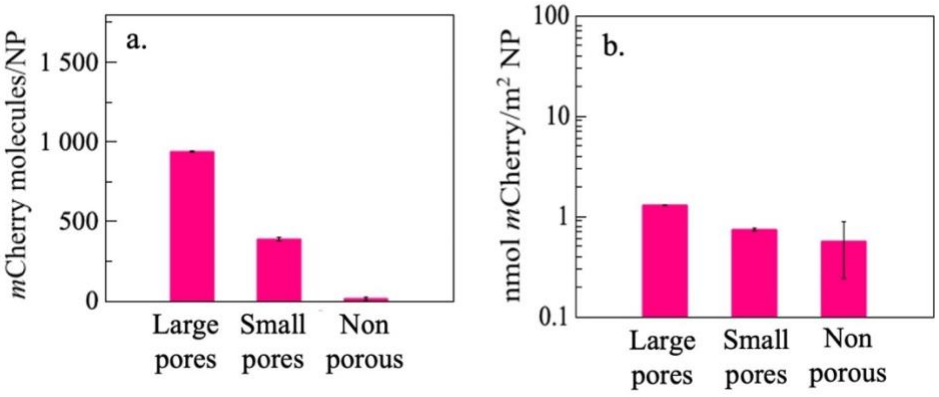

Figure 5.8. a) *m*Cherry effective adsorption showed in number of protein molecules per particle unit. b) Particles loading capacity expressed in nmol of protein per m^2 of particle. Error bars represent standard deviation (n=3). The loading experiment was conducted at 25 ˚C in 10 mM PB, pH 7 with initial protein molecule counts of 5.2 x 10^{12} and particle counts of 3 x 10^{11} for *lp*-Au@*m*SiO_2, 5.4 x 10^{11} for *sp*-Au@*m*SiO_2, and 3 x 10^{11} for SNP.

Effective *m*Cherry adsorption was primarily observed on *sp*-Au@*m*SiO_2 and *lp*-Au@*m*SiO_2 particles (Figure 5.8). Given that *m*Cherry is smaller than the pores of *lp*-Au@*m*SiO_2 and similar in size to those of *sp*-Au@*m*SiO_2, it is likely that *m*Cherry undergoes encapsulation within the pores of *lp*-Au@*m*SiO_2 and partial encapsulation within the pores of *sp*-Au@*m*SiO_2. In addition to electrostatic interactions, hydrophobic interactions between the nonpolar side chains of the protein's amino acids and the particle surface may also play a significant role in the adsorption process [4]. According to the literature, at pH 7, a fraction of the silanol groups could remain protonated [56], which may reduce the repulsive electrostatic forces and allow for hydrophobic interactions. Given that the nanoparticles are calcined, the surface likely contains a high proportion of siloxane groups, further promoting hydrophobic interactions. The increase in entropy associated with these hydrophobic interactions can outweigh the effects

of electrostatic repulsion, irrespective of the overall charge on the surface and the protein. This effect is particularly pronounced in porous particles, where a larger surface area facilitates greater interaction with proteins.

5.4.2.2. Adsorption equilibria of *m*Cherry on *lp*-Au@*m*SiO_2

The adsorption behavior of *m*Cherry on *lp*-Au@*m*SiO_2 is best described by the Langmuir equation, as indicated by the highest determination coefficient (R^2 = 0.966) among the models tested (Freundlich R^2 = 0.964, Temkin R^2 = 0.886, and Dubinin-Radushkevich R^2 = 0.894) (Appendix 4). Based on the Langmuir equation, each particle can accommodate up to 1277 *m*Cherry molecules (Q_m = 1277 *m*Cherry molecules/NP) (Figure 5.9). Notably, this value is ten times lower than that observed for BSA. Also, the Langmuir constant was significantly lower for *m*Cherry (b = 0.25 L/mg) compared to BSA (b = 71 L/mg), indicating that *m*Cherry has a lower affinity for silica particles than BSA.

Interestingly, the maximum loading of *m*Cherry on *lp*-Au@*m*SiO_2 is higher than the reported adsorption of GFP on SBA15-type particles of 250 nm in diameter and 6 nm pores, which can adsorb up to 6 nmol of GFP per gram of particle [57]. These findings indicate that the large internal surface area provided by the large pores is crucial for the adsorption of *m*Cherry.

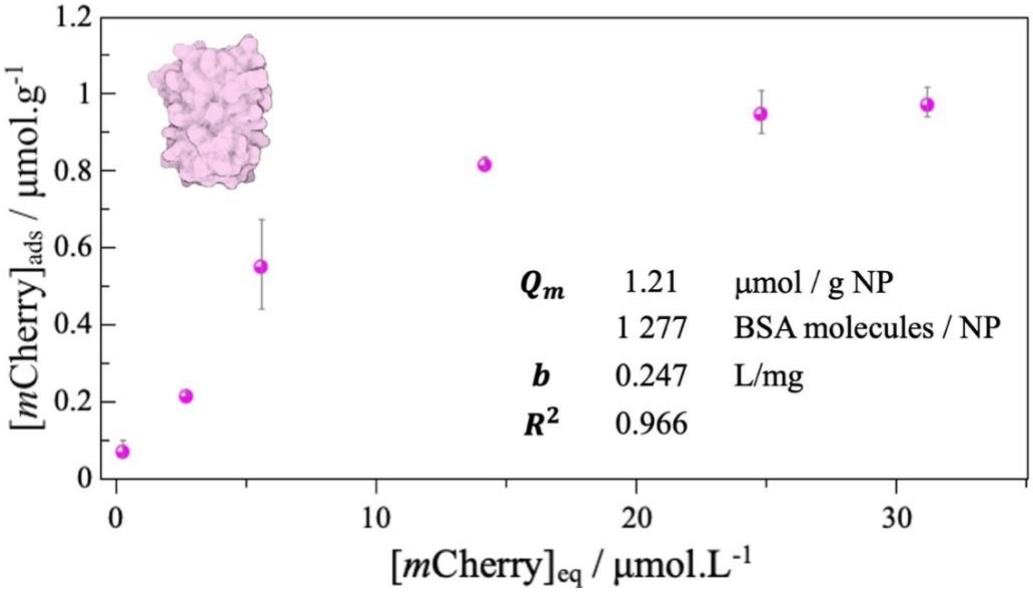

Figure 5.9. Amount of *m*Cherry adsorbed per gram of *lp*- Au@*m*SiO_2 as a function of free *m*Cherry concentration in solution. Error bars are the standard deviation from independent measurements. The parameters derived from the Langmuir equation are shown: (Q_m) the maximum amount of protein adsorbed expressed in µmol *m*Cherry per gram of nanoparticle, and the number of *m*Cherry molecules per nanoparticles (*b*) Langmuir constant for adsorbate-adsorbent equilibrium.

5.4.2.3. *m*Cherry location on nanoparticles

AFM measurements indicated that after *m*Cherry adsorption, the *lp*-Au@*m*SiO_2 particles exhibited an increased diameter, suggesting the presence of a protein corona approximately 30 nm thick (see Figure 5.10 and Table 5.6), however with very large uncertainties. *Cryo*-EF-TEM carbon maps revealed a significantly thinner protein corona, around 7 ± 3 nm.

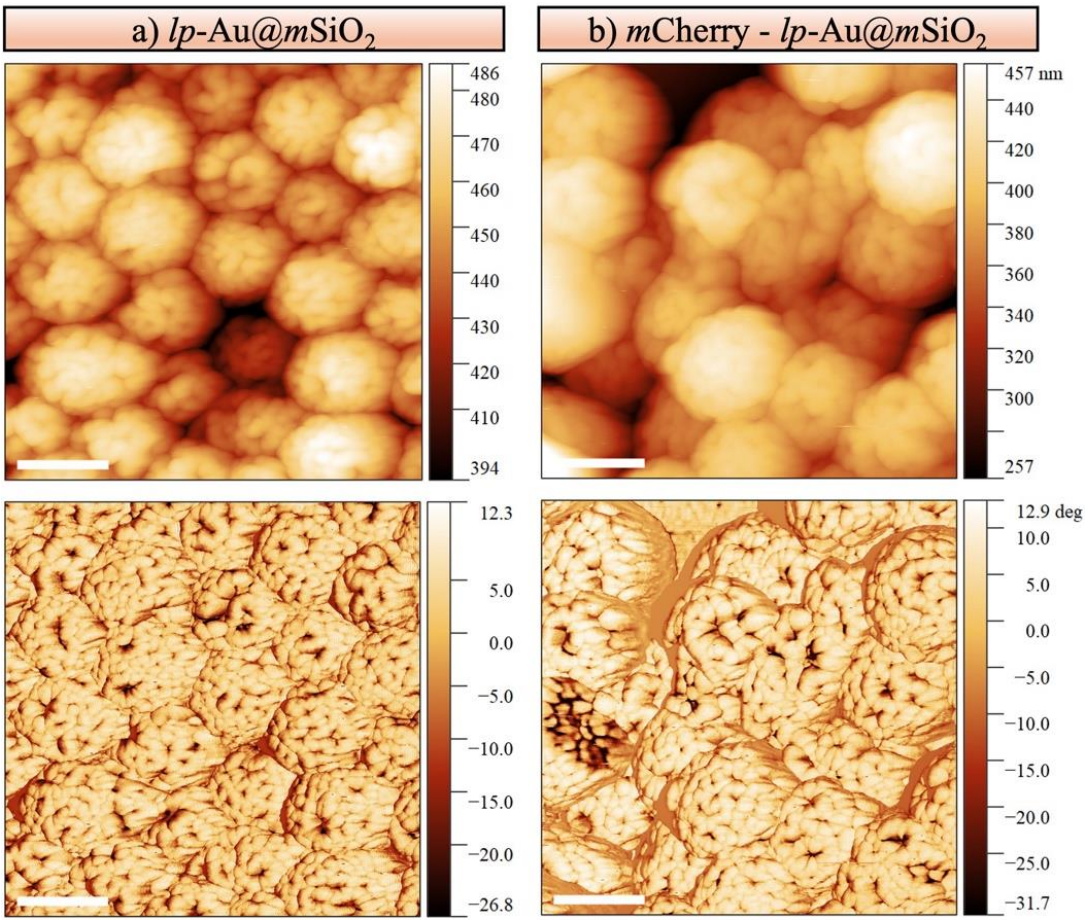

Figure 5.10. AFM micrographs of (a) *lp*-Au@*m*SiO_2 and (b) *m*Cherry adsorbed on *lp*-Au@*m*SiO_2. Micrographs were acquired in tapping mode in the topography (upper panel) and phase (bottom panel) channel over a 500 × 500 nm² area. Horizontal scale bar = 100 nm.

Both AFM and *cryo*-EF-TEM micrographs demonstrate significant particle aggregation upon *m*Cherry loading. This observation was further corroborated by an observed increase in hydrodynamic diameter from 184 nm to 243 nm after *m*Cherry adsorption (Table 5.9).

Table 5.6. Parameters obtained from the characterization of particles with and without *m*Cherry, as determined by AFM in tapping mode and EF-TEM.

Sample	***lp*-Au@*m*SiO$_2$**	***m*Cherry-*lp*-Au@*m*SiO$_2$**
AFM D_{part} (nm)	103±8	133±7
AFM pore size (nm)	10±4	8.2±4
AFM pore depth (nm)	6.7±4	8.3±6
AFM corona thickness (nm)	-	30±15
EF-TEM corona thickness (nm)	-	7±3

Cryo-EF-TEM results (Figure 5.11) show the silicon and carbon maps for *m*Cherry retained in *lp*-Au@*m*SiO$_2$ and *sp*-Au@*m*SiO$_2$. For *lp*-Au@*m*SiO$_2$, the carbon signal was less intense than in the BSA- *lp*-Au@*m*SiO$_2$ case and was distributed on the outer surface and on the inside of the particles. For *sp*-Au@*m*SiO$_2$, the carbon signal was even weaker than that observed for *lp*-Au@*m*SiO$_2$ and was found both within the particles and on their external surface. These findings suggest that *m*Cherry is primarily localized inside the pores of *lp*-Au@*m*SiO$_2$ and *sp*-Au@*m*SiO$_2$, as well as on their external surfaces.

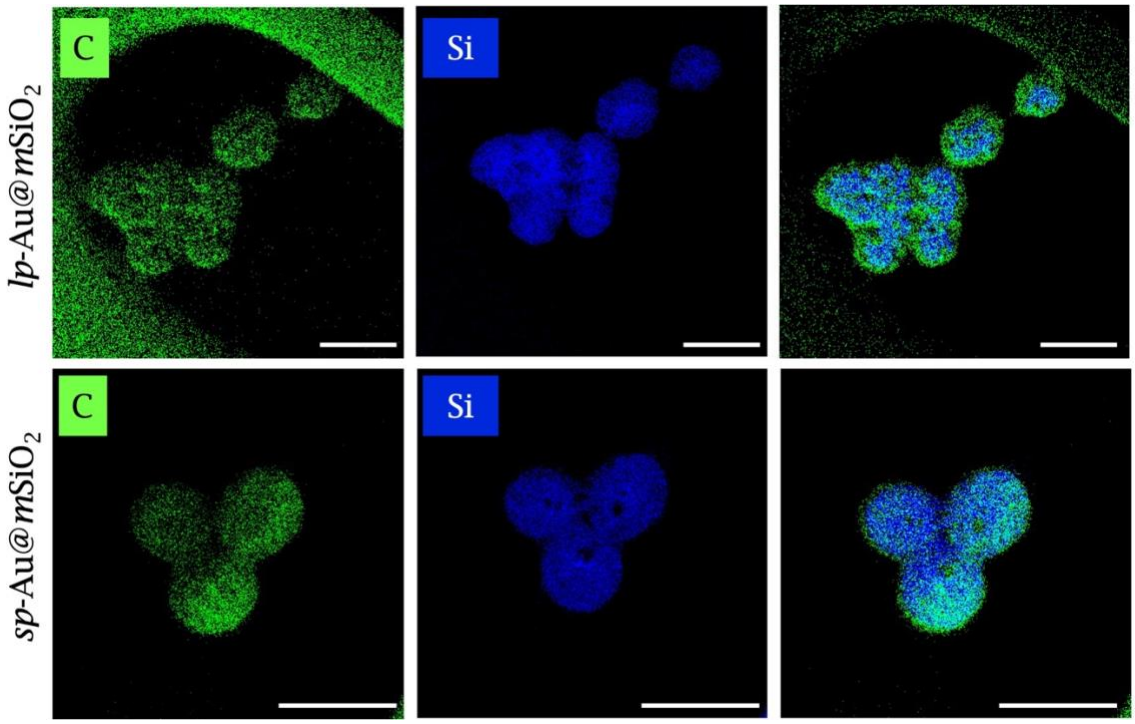

Figure 5.11. *cryo*-EF-TEM core-loss micrographs of the C (green signal) and Si (blue signal) elements corresponding to (top) *lp*-Au@*m*SiO_2 - *m*Cherry and (bottom) *sp*-Au@*m*SiO_2 - *m*Cherry. The last panel shows the merged image of Si and C signals. The sample was prepared on a lacey carbon grid (green signal) under cryogenic conditions. Scalebar = 100 nm

5.4.2.4. Structural Stability of *m*Cherry loaded on nanoparticles

Despite sharing only 25% homology with GFP [58], *m*Cherry exhibits a nearly identical folding pattern, as demonstrated by the structure alignment (see alignment in Appendix 6). Consequently, the far-UV CD spectra of these proteins are expected to be comparable. Indeed, the CD spectrum of free *m*Cherry (Figure 5.12a, left panel) shows characteristics akin to those reported for GFP, with a positive maximum at 198 nm and a negative maximum at 219 nm, indicative of a high β-sheet content [59–61].

Upon increasing temperature, the 219 nm band undergoes some changes, most notably a decrease in the 198 nm band, implying a reduction in helices by approximately 4%, while other components remain nearly unaltered (Figure 5.12

b, left panel). This is consistent with the high thermal stability reported for GFP, with a melting temperature (the temperature at which 50% of the protein denatures) of 83 ˚C [62].

When *m*Cherry is adsorbed on *sp*-Au@*m*SiO_2 or *lp*-Au@*m*SiO_2, a red shift in the spectrum of 10 nm and 5 nm, respectively, is observed. Additionally, there is a decrease in the positive band's intensity for *m*Cherry adsorbed on *sp*-Au@*m*SiO_2 (Figure 5.12a, right panel). Despite these spectral changes, fluorescence emission and excitation spectra of *m*Cherry adsorbed on *lp*-Au@*m*SiO_2 show no significant alterations compared to the free protein in solution (Appendix 7). This indicates that, although there are structural variations upon adsorption, they do not impact the chromophore's fluorescence.

The calculated secondary structure of *m*Cherry in *sp*-Au@*m*SiO_2 (Figure 5.12b) shows that the fraction of disordered structures (% of other structures) decreases by 7%, and the helix fraction decreases by 5% at the expense of an increase in β-strands. Conversely, the structure of *m*Cherry in *lp*-Au@*m*SiO_2 exhibits a 6% reduction in disordered structures and a 2% reduction in helices, also compensated by an increase in β-strands. In both cases, increasing temperature does not significantly alter the secondary structure. This is in good agreement with the rigid structure characteristic of GFP and its derivatives, where rigidity is important for maintaining the protein's fluorescent behavior [63].

Due to the rigid structure of this family of fluorescent proteins, they exhibit a denaturation model different from other globular proteins like BSA [64, 65]. Thus, during adsorption, a P state is not formed, and only minor changes in the secondary structure of *m*Cherry, such as slight increases in β-strands, are observed. The more significant increase in β-strands for *m*Cherry adsorbed on *sp*-Au@*m*SiO_2 suggests that confinement within the small pores induces a conformational change. It is well documented that the solvent plays a key role in protein folding, and specifically for fluorescent proteins with a β-can, as the interaction of water molecules inside the β-can is crucial for maintaining the

structure [64]. A possible explanation for the increase in β-strands could be that when the protein is confined in a pore that is approximately the same size, water becomes less accessible, leading to rearrangements in the protein structure. In contrast, within the larger pores of *lp*-Au@*m*SiO_2, *m*Cherry is less confined, which allows greater water access and leads to fewer conformational changes.

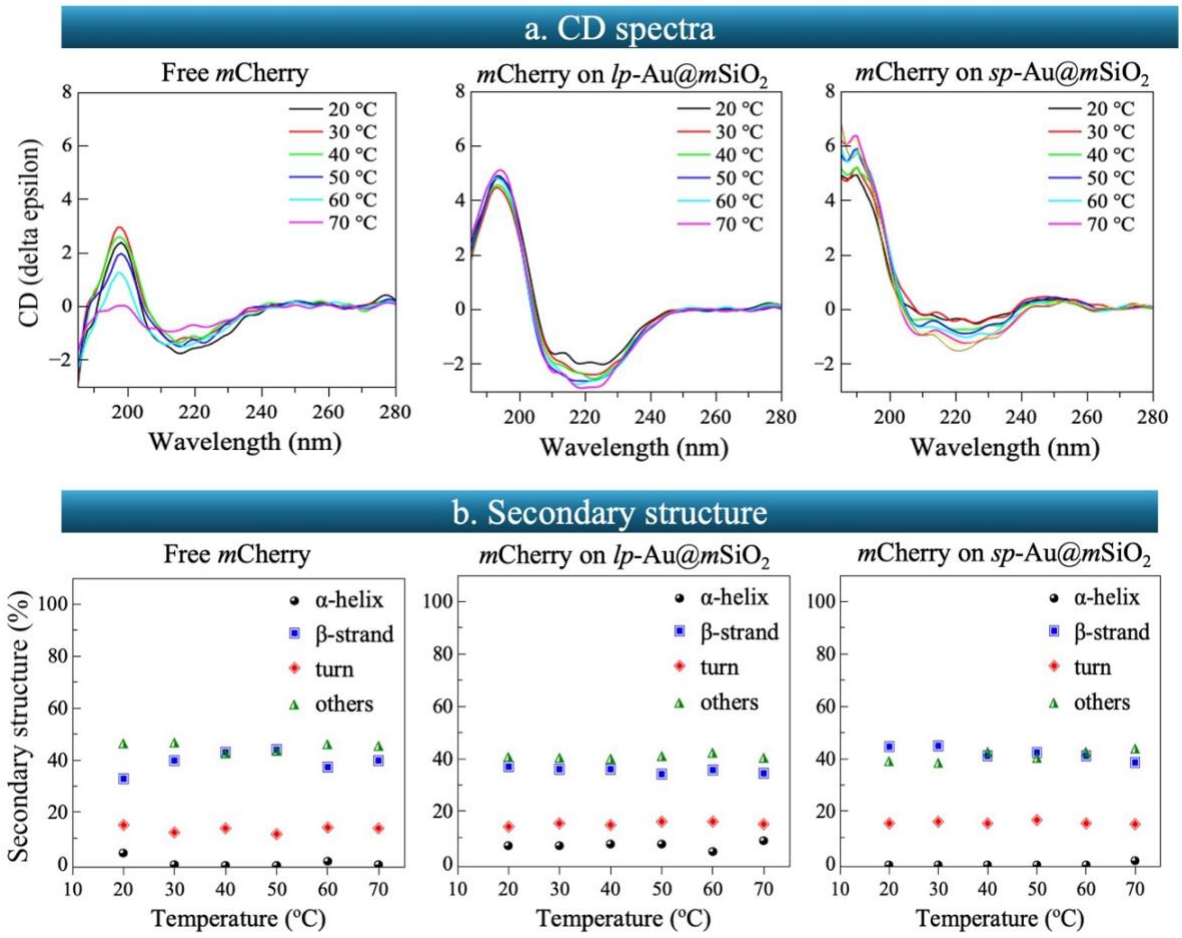

Figure 5.12. CD of *m*Cherry before and after loading on *lp*- and *sp*- Au@*m*SiO_2 a) UV-CD spectra of *m*Cherry free in water (left), and *m*Cherry loaded on *lp*-Au@*m*SiO_2 (middle) and *sp*-Au@*m*SiO_2 particles (right) over a temperature range from 20 ˚C to 70 ˚C. b) Secondary structure derived from CD spectra for free *m*Cherry, *m*Cherry on *lp*-Au@*m*SiO_2, and *m*Cherry on *sp*-Au@*m*SiO_2.

5.4.3. Horseradish Peroxidase

5.4.3.1. Comparative HRP loading on nanoparticle variants

The HRP adsorption on negatively charged surfaces is known to be pH-dependent, with maximum adsorption typically occurring below the isoelectric point of the protein [66]. According to the supplier of the enzyme, the HRP used in this thesis is a mixture of isoenzymes each one with a different isoelectric point ranging from 3.0 to 9.0. Therefore, the average isoelectric point of the enzyme employed is uncertain.

The crystallographic structure of HRP reveals several exposed lysine and arginine residues, which are positively charged amino acids. These residues have been shown to significantly influence the adsorption of other proteins on silica surfaces [3]. Thus, it can be suggested that these positively charged residues also contribute to the adsorption of HRP on Au@*m*SiO_2 and SNP.

The effective adsorption of HRP on *lp*-Au@*m*SiO_2 is comparable to that on SNP, but higher than on *sp*-Au@*m*SiO_2 (Figure 5.13). Its predominant adsorption on SNP and *lp*-Au@*m*SiO_2 might be related to higher availability of anchoring points, *i.e.* silanols exposed, to interact with the positively charged amino acid, of the protein. Due to the large pore sizes of *lp*-Au@*m*SiO_2, HRP can lodge within the pores and interact with the silanols on the pore walls. Also, SNP provides a denser surface with a higher density of exposed silanols compared to small porous particles.

The dependency of HRP adsorption on pore size has been previously reported, showing higher adsorption on MSN with pore dimensions larger than HRP and lower adsorption on MSN with pore dimensions smaller than HRP [10,

11]. Furthermore, another study also observed high HRP adsorption on flat silicon surfaces (56 nmol/m²), comparable to what was observed in this study for SNP [67].

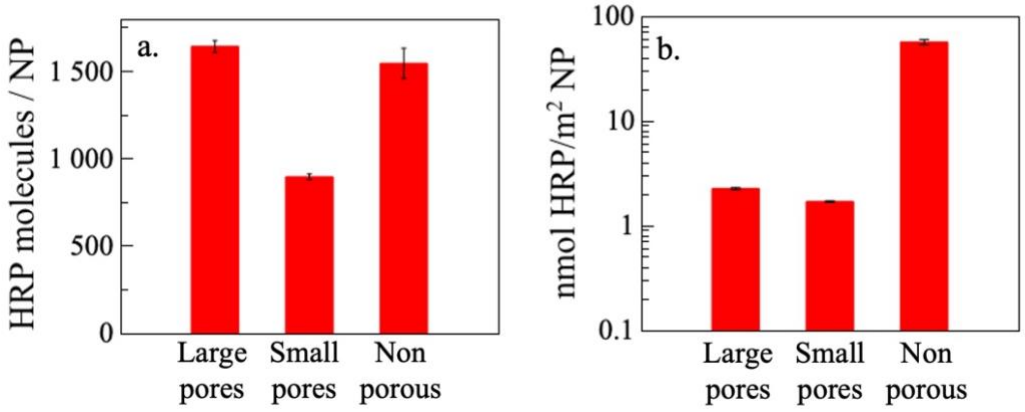

Figure 5.13. a) HRP effective adsorption showed in number of protein molecules per particle unit. b) Particles loading capacity expressed in nmol of protein per m^2 of particle. Error bars represent standard deviation (n=3). The loading experiment was conducted at 25°C in 10 mM PB, pH 7 with initial protein molecule counts of 2.7 x 10^{18} for HRP, and particle counts of 1.1 x 10^{12} for *lp*-Au@*m*SiO_2, 1.8 x 10^{12} for *sp*-Au@*m*SiO_2, and 1 x 10^{12} for SNP.

5.4.3.2. Adsorption equilibria of HRP on *lp*-Au@*m*SiO_2

Among the adsorption models tested, the Langmuir equation provided the best fit for describing the adsorption behavior of HRP on *lp*-Au@*m*SiO_2 (Langmuir R^2 = 0.983, Freundlich R^2 = 0.971, Temkin R^2 = 0.894, and Dubinin-Radushkevich R^2 = 0.914) (Appendix 4). The maximum effective adsorption of HRP on *lp*-Au@*m*SiO_2, calculated using the Langmuir equation shows that each nanoparticle may accommodate up to two thousand HRP molecules (Q_m = 2080 HRP molecules/NP) (Figure 5.18b). Considering the dimensions of HRP (Table 5.2), a maximum of 7 native HRP molecules can fit within a single *lp*-Au@*m*SiO_2 pore. Assuming each particle contains approximately 700 pores of 17 nm in diameter, the theoretical maximum adsorption capacity should be 4900 HRP molecules that

could fit within the pores of each particle. These calculations suggest that, in a fully saturated state, HRP does not entirely occupy all the pores of *lp*-Au@*m*SiO_2.

Interestingly, the maximum loading of HRP on *lp*-Au@*m*SiO_2 is higher than that of *m*Cherry (Q_m = 1277 *m*Cherry molecules/NP) but significantly lower than that of BSA (Q_m = 10136 BSA molecules/NP). Also, the Langmuir constant for HRP is the lowest among the three proteins, with a value of b = 0.02 L/mg, compared to 0.25 L/mg for *m*Cherry and 71 L/mg for BSA. This suggest that the rigidity of HRP could play a major role in its adsorption behavior.

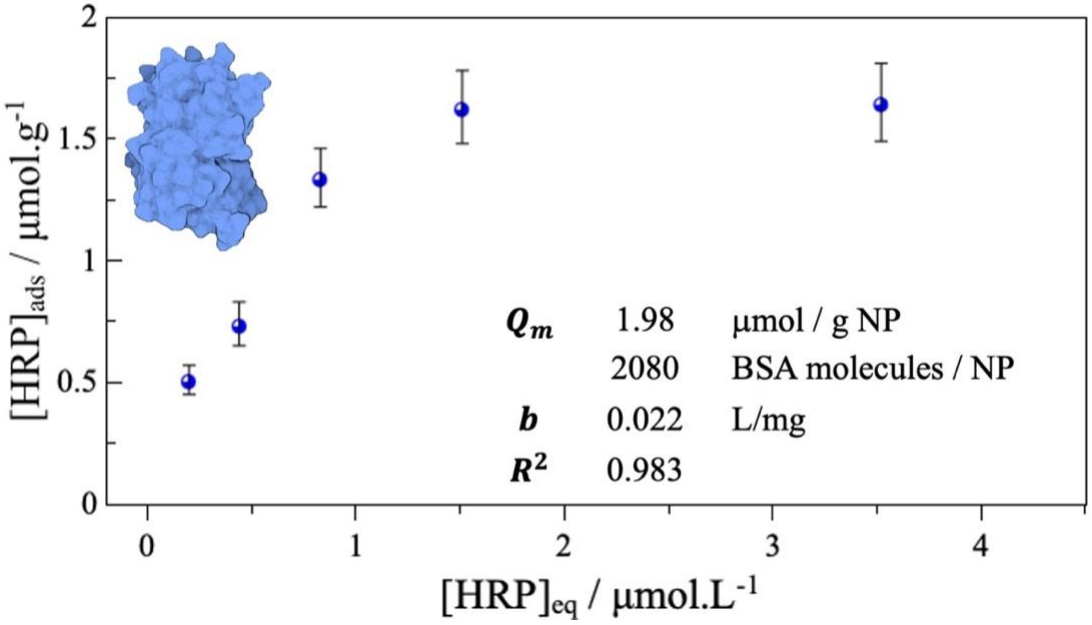

Figure 5.14. a) Amount of HRP adsorbed per gram of *lp*-Au@*m*SiO_2 as a function of free protein concentration in solution. Error bars are the standard deviation from independent measurements. The parameters derived from the Langmuir equation are shown: (Q_m) the maximum amount of protein adsorbed expressed in µmol HRP per gram of nanoparticle, and the number of HRP molecules per nanoparticles (*b*) Langmuir constant for adsorbate-adsorbent equilibrium.

5.4.3.3. HRP location on nanoparticles

The localization of HRP on *lp*-Au@*m*SiO_2 particles was investigated using AFM. AFM measurements indicated an increase in the diameter of *lp*-Au@*m*SiO_2 particles following HRP adsorption, suggesting the formation of a protein corona with an estimated thickness of approximately 29 nm (Figure 5.15, Table 5.7), though with large uncertainties.

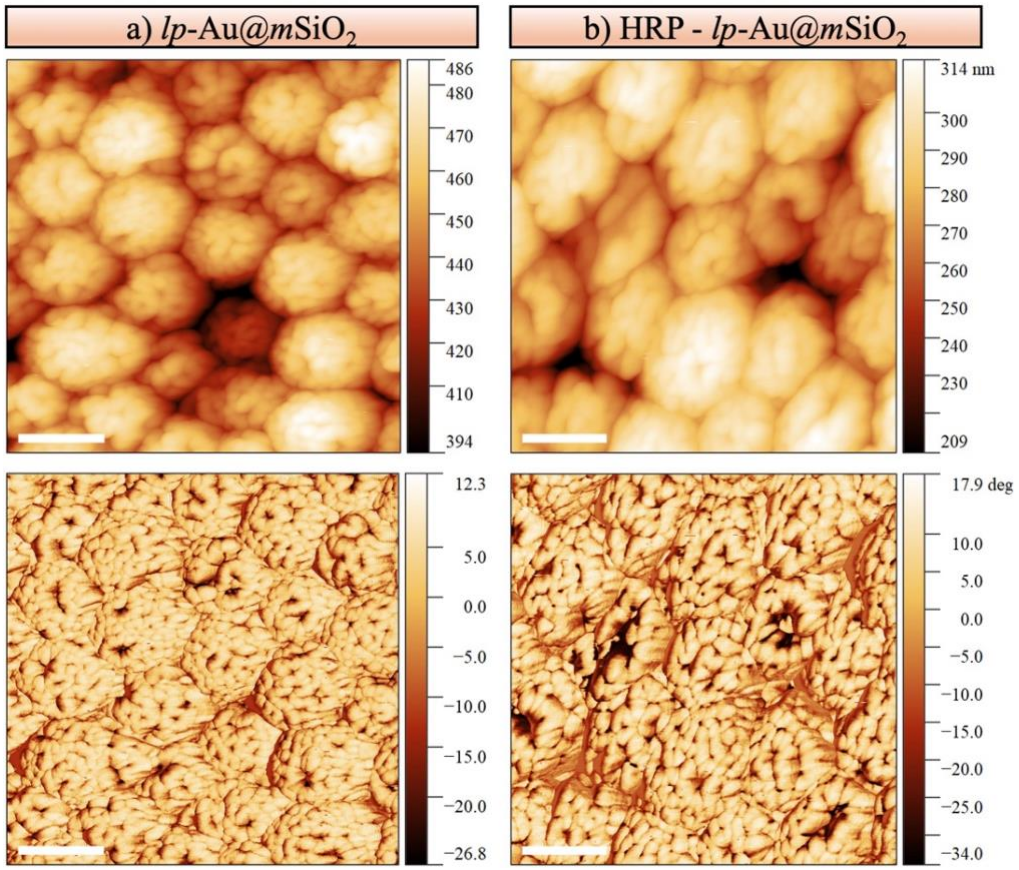

Figure 5.15. AFM micrographs of *lp*-Au@*m*SiO_2 (left) and HRP adsorbed on *lp*-Au@*m*SiO_2 (right). The micrographs were acquired in tapping mode in the topography channel over a 500 x 500 nm² area.

Table 5.7. Parameters obtained from the characterization of particles with and without HRP, as determined by AFM in tapping mode.

Sample	***lp*-Au@*m*SiO$_2$**	**HRP-*lp*-Au@*m*SiO$_2$**
AFM D_{part} (nm)	103±8	132±26
AFM pore size (nm)	10±4	8.6±4
AFM pore depth (nm)	6.7±4	7±5
AFM corona thickness (nm)	-	29±34

The native structure of HRP can be approximated as an ellipsoid, leading to a maximum adsorption of 10 nmol/m² on a dense surface. This is approximately six times less than the observed HRP adsorption on SNP (57 nmol/m²). This indicate that HRP forms more than one layer on the SNP, validating HRP's capability to form multilayers on *lp*-Au@*m*SiO$_2$ under the experimental conditions studied.

Unfortunately, *cryo*EF-TEM imaging could not be performed during the experimental time provided at LNNano. However, a sample of HRP-*lp*-Au@*m*SiO$_2$ has been prepared and will be analyzed soon. This experiment will be crucial to ascertain the location of the HRP.

5.4.3.4. Structural Stability of HRP loaded on nanoparticles

The stability of adsorbed HRP was evaluated by examining its secondary structure through CD spectra and by assessing its enzymatic activity, measured by the enzyme's ability to oxidize ABTS (see Chapter 2, section 2.4.3 for more details).

The spectrum of free HRP (Figure 5.16a) exhibits characteristics similar to those reported in the literature, with a positive maximum at 191 nm and two negative minima at 208 and 221 nm [68]. The secondary structure obtained is typical of heme peroxidases, with a higher proportion of α-helices (30%) than β-sheets (12%), consistent with the reported crystallographic structure [68, 69] containing 10-11 α-helices linked by turns, while β-strands constitute a minor component.

As the temperature increases, the positive and negative bands diminish in intensity, primarily due to a decrease in the percentage of α-helix and an increase in β-strands (Figure 5.16b). This effect is more pronounced after 60 °C, coinciding with the HRP melting temperature [70].

When HRP is adsorbed on *sp*-Au@*m*SiO_2, the intensity of the positive band and the negative band at 221 nm decreases, leading to a 9% increase in β-sheet and 6% increase in disordered structures (other) at the expense of a 17% decrease in α-helix. This increase in disordered structures and β-strands might suggest aggregation, which has been reported for other peroxidases in response to denaturing conditions [71].

For HRP adsorbed on *lp*-Au@*m*SiO_2, the intensity of the positive band increases, and the signal of the two negative bands decreases. Although there is also a decrease in α-helix content and an increase in β-strands, the secondary structure is closer to the observed for free HRP. This suggests that adsorption on

lp-Au@*m*SiO_2 results in less significant conformational changes compared to adsorption on *sp*-Au@*m*SiO_2.

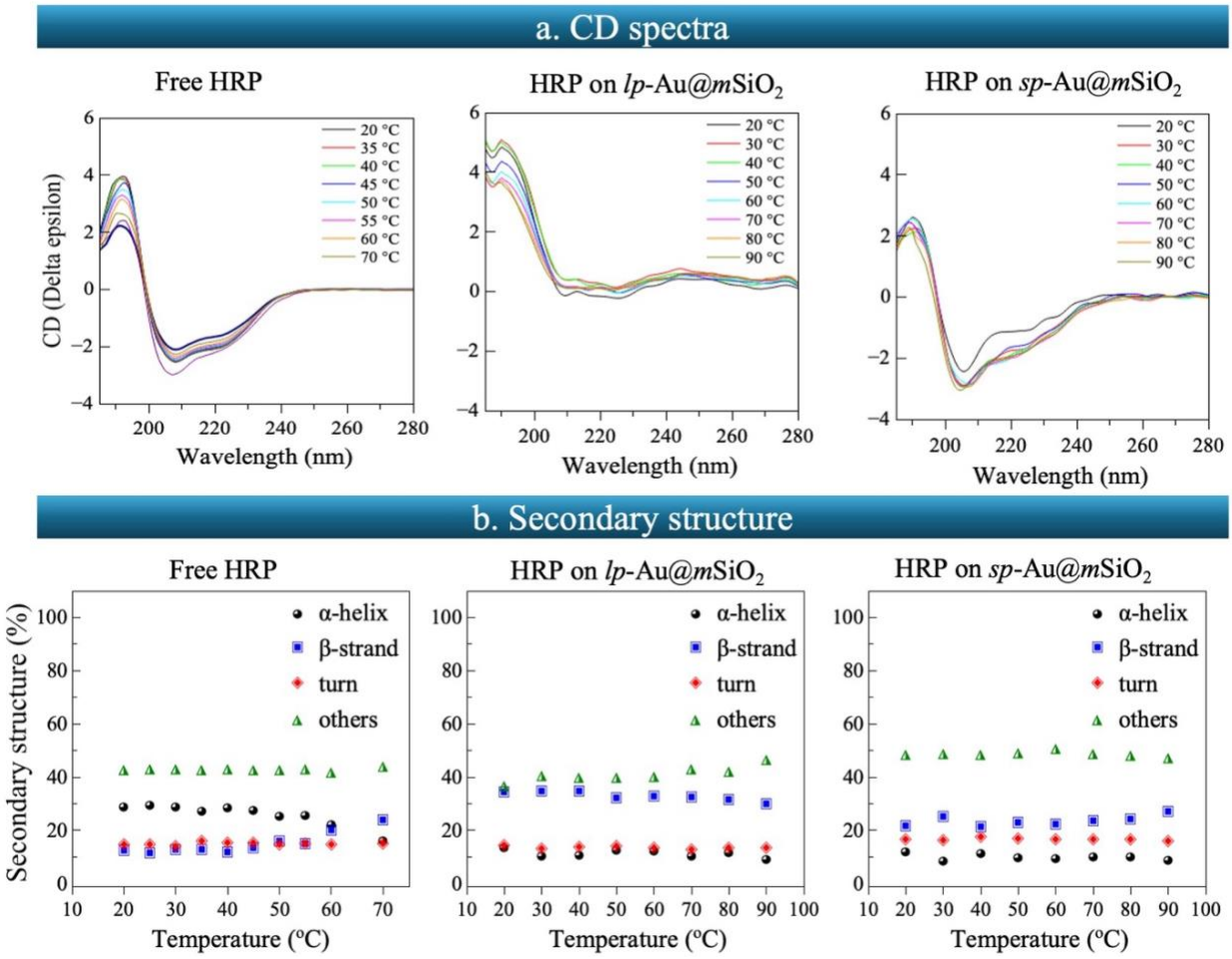

Figure 5.16. CD of HRP before and after loading on *lp*- and *sp*- Au@*m*SiO_2 a) UV-CD spectra of HRP in free in water (left), and HRP loaded on *lp*-Au@*m*SiO_2 (middle) and *sp*-Au@*m*SiO_2 particles (right) over a temperature range from 20 ˚C to 70 ˚C. b) Secondary structure derived from CD spectra for free HRP, HRP on *lp*-Au@*m*SiO_2, and HRP on *sp*-Au@*m*SiO_2.

5.4.3.5. HRP activity

HRP has been shown to lose activity after adsorption on various substrates such as graphite, polyaniline composites, and titanate compounds [72–74]. This loss of activity has been primarily attributed to conformational changes in the proteins that make the heme group less accessible. The activity of free HRP and HRP adsorbed on *lp*-Au@*m*SiO_2 against ABTS in McIlvaine buffer (citrate-phosphate buffer) of different pH was compared. As expected for free HRP [75], the highest enzymatic generation of the ABTS chromogenic product was observed at pH 4. A similar result was observed for HRP adsorbed on *lp*-Au@*m*SiO_2, showing that the enzymatic activity remains consistent across a pH range of 2 to 8 (Figure 5.17). This suggests that HRP is adsorbed without altering its conformational structure and in a location where mass transport to the active site of the protein is feasible. These results align with those observed for HRP adsorption in MSN with different pore diameters, where the protein's activity is the highest when retained in pores with dimensions similar to the protein (14 nm) and decreases as the pore size decreases to 3 nm [10].

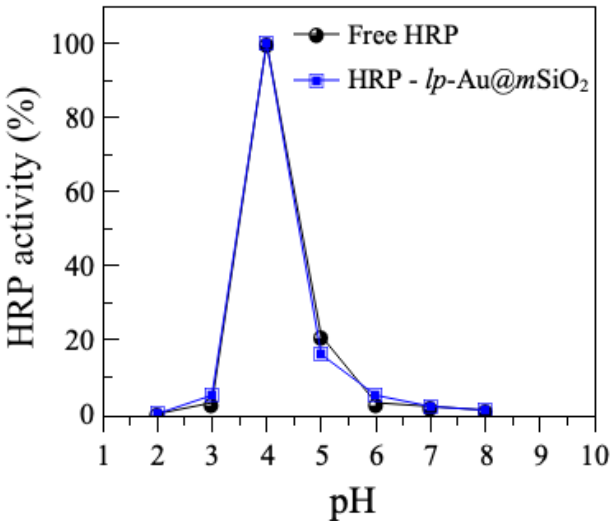

Figure 5.17. Effect of pH on the activity of Free HRP (black) and HRP adsorbed on *lp*-Au@*m*SiO_2 (blue) measured by ABTS assay at 25 °C in McIlvaine buffer.

5.4.4. Summary of protein loading

BSA adsorbs onto all three types of nanoparticles studied—*sp*-Au@*m*SiO_2, *lp*-Au@*m*SiO_2, and SNP. This broad adsorption capability is attributed to BSA's classification as a soft protein, which allows it to adsorb onto silica surfaces even under unfavorable electrostatic conditions at pH 7, where both the protein and the nanoparticles are negatively charged. This phenomenon can be explained by the protein's ability to undergo conformational changes that expose positively charged residues, enabling interaction with the silica. This observation is consistent with the secondary structure analysis of the adsorbed BSA.

On *sp*-Au@*m*SiO_2, BSA primarily adsorbs on the surface, forming a protein corona, leading to protein adsorption levels similar to those observed for SNP. This suggests that adsorption on *sp*-Au@*m*SiO_2 is largely driven by conformational changes, as evidenced by the observed loss of secondary structure. In contrast, BSA adsorption on *lp*-Au@*m*SiO_2 occurs both on the surface and within the pores, leading to lower conformational changes compared to *sp*-Au@*m*SiO_2. The confinement within the pores restricts the protein's ability to rearrange its structure, thus maintaining a conformation closer to that of the free protein. Furthermore, BSA encapsulated within the pores exhibits greater resistance to thermal denaturation, likely due to the protective and confining environment provided by the pores.

The adsorption of *m*Cherry onto silica nanoparticles is less favorable compared to BSA (Table 5.8). At pH 7, *m*Cherry carries a negative surface charge and is a rigid protein, which resists major secondary structure alterations upon adsorption. As a result, the adsorption process is governed by different forces than those influencing BSA adsorption. In this case, electrostatic interactions are not favored, and hydrophobic interactions between the hydrophobic amino acids on the protein surface and the nanoparticle surface predominate. Due to the larger surface area of porous particles, *m*Cherry adsorption is greater on these particles, with the protein adsorbing onto both the pores and the surface.

HRP, despite being a rigid protein, adsorbs onto SNP and Au@*m*SiO_2 to a much lesser extent than BSA (Table 5.8). The adsorption of HRP appears to be primarily of electrostatic nature, and it is likely that the positive amino acids on the surface of the protein play a crucial role. Similar to *m*Cherry and BSA, HRP forms a protein corona when adsorbed onto *lp*-Au@*m*SiO_2. Importantly, the enzymatic activity of HRP remains unaffected when adsorbed onto *lp*-Au@*m*SiO_2, indicating that the protein retains its functional integrity.

Table 5.8. Summary of the protein loading results in *lp*- and *sp*-Au@*m*SiO_2 nanoparticles, including the maximum loading (Q_m), Langmuir constant (b), protein localization (I= inside the pores / O = outer surface) and corona thickness as determined by *cryo*-EFTEM, and protein conformation assessed through CD analysis (+ moderate change, ++ high change, - no change)

Nanoparticle	**Protein**	**Protein nature**	Q_m ($mg.g^{-1}NP$)	b ($L.mg^{-1}$)	**Protein Location**	**Conformation upon loading**	**Corona thickness (nm)**
lp-Au@*m*SiO_2	BSA	Soft	640	71	I/O	+	15±9
	*m*Cherry	Hard	40	0.25	I/O	_	7±3
	HRP	Hard	85	0.02	ND	_	ND
sp-Au@*m*SiO_2	BSA	Soft	ND	ND	O	++	25±5
	*m*Cherry	Hard	ND	ND	I/O	-	11±4
	HRP	Hard	ND	ND	ND	-	ND

5.5. Particle stability

The stability of nanoparticles loaded with protein was assessed by monitoring changes in particle morphology over time. To achieve this, the particle-protein pellet, which underwent several washings to remove unadsorbed proteins, was resuspended in 1× PBS buffer to obtain a colloidal suspension with

a concentration of 1 mg/mL (above the SSL, as discussed in Chapter 4). Aliquots were taken daily and diluted in water for SEM analysis, with a control sample incubated in PBS but unloaded with proteins.

The following sections present the findings from SEM monitoring. First, the results of *lp*-Au@*m*SiO_2 and *sp*-Au@*m*SiO_2 nanoparticles loaded with BSA are discussed. Subsequently, the data for nanoparticles loaded with *m*Cherry and HRP are presented.

5.5.1. Stability of nanoparticles loaded with BSA

Previous studies have shown that BSA coating improves the colloidal stability of MSN with pore sizes of 3-4 nm [23, 24]. This increased stability has been attributed to the adsorbed proteins slowing down the transport of dissolved silica and water into and out of the particles [22]. This phenomenon aligns well with observations made for Au@*m*SiO_2 nanoparticles, though the protective mechanism of BSA differs depending on whether large or small pores are involved.

SEM analysis revealed that BSA-coated *lp*-Au@*m*SiO_2 (BSA-*lp*-Au@*m*SiO_2) particles are less susceptible to morphological changes than their uncoated counterparts (Figure 5.18). At a concentration of 1 mg/mL, above the SSL, BSA-*lp*-Au@*m*SiO_2 particles maintain their morphology for the first six days after suspension in 1× PBS. By contrast, particles without BSA coating began to show morphological changes by day 3, primarily manifesting as more open pores and increased aggregation due to silica dissolution and reprecipitation (as discussed in Chapter 4). It is noteworthy that aggregation was observed in both BSA-coated and uncoated particles from day 0, corresponding to the particles immediately after the loading process. However, as no aggregation was detected by DLS (Table 5.8), it is suggested that the aggregation observed by SEM occurred during sample preparation.

After 10 days, the dissolution-reprecipitation of *lp*-Au@*m*SiO_2 particles became more apparent, with a noticeable reduction in particle size and pore morphology remaining relatively unchanged (Figure 5.18f), indicating that the dissolution process occurs from the outside inwards. Interestingly, BSA-*lp*-Au@*m*SiO_2 particles after 10 days exhibited significant agglomeration, with an evident layer enveloping the particles (Figure 5.18e), corresponding to the BSA exposed on the surface, which burns under the electron beam during SEM analysis. In addition to agglomeration, pore size was enlarged, leading to the formation of a large-pore matrix.

For *sp*-Au@*m*SiO_2 particles, the presence of BSA induced silica dissolution and reprecipitation in two distinct manners. First, by day 1, flower-like particles were observed, suggesting that dissolution and reprecipitation start from the inside and progress outward (Figure 5.19). This finding aligns with previous studies on MCM-48 particles in BSA-containing media [24]. Second, by day 3, particle fusion was observed, leading to the formation of larger particles with multiple gold cores. Therefore, it can be concluded that in *sp*-Au@*m*SiO_2 particles, dissolution occurs both on the surface and within the particle structure.

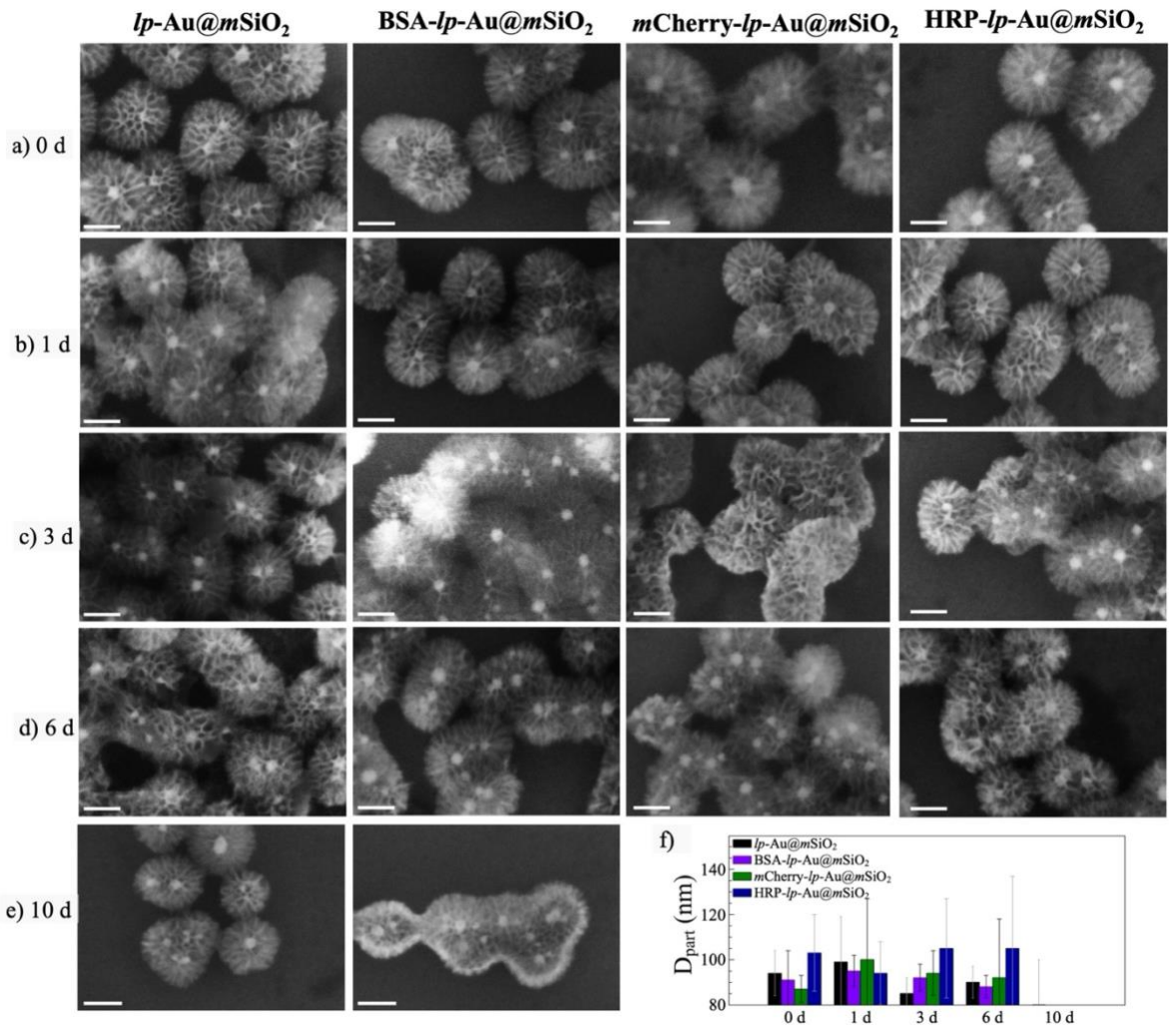

Figure 5.18. a-e) SEM micrographs showing the morphological evolution over time of a 1 mg/mL *lp*-Au@*m*SiO_2 particles with and without BSA, *m*Cherry, and HRP suspended in PBS 1×, scalebar = 50 nm. (f) Particle size (D_{part}) of *lp*-Au@*m*SiO_2 and *lp*-Au@*m*SiO_2 loaded with protein as function of degradation time determined by SEM.

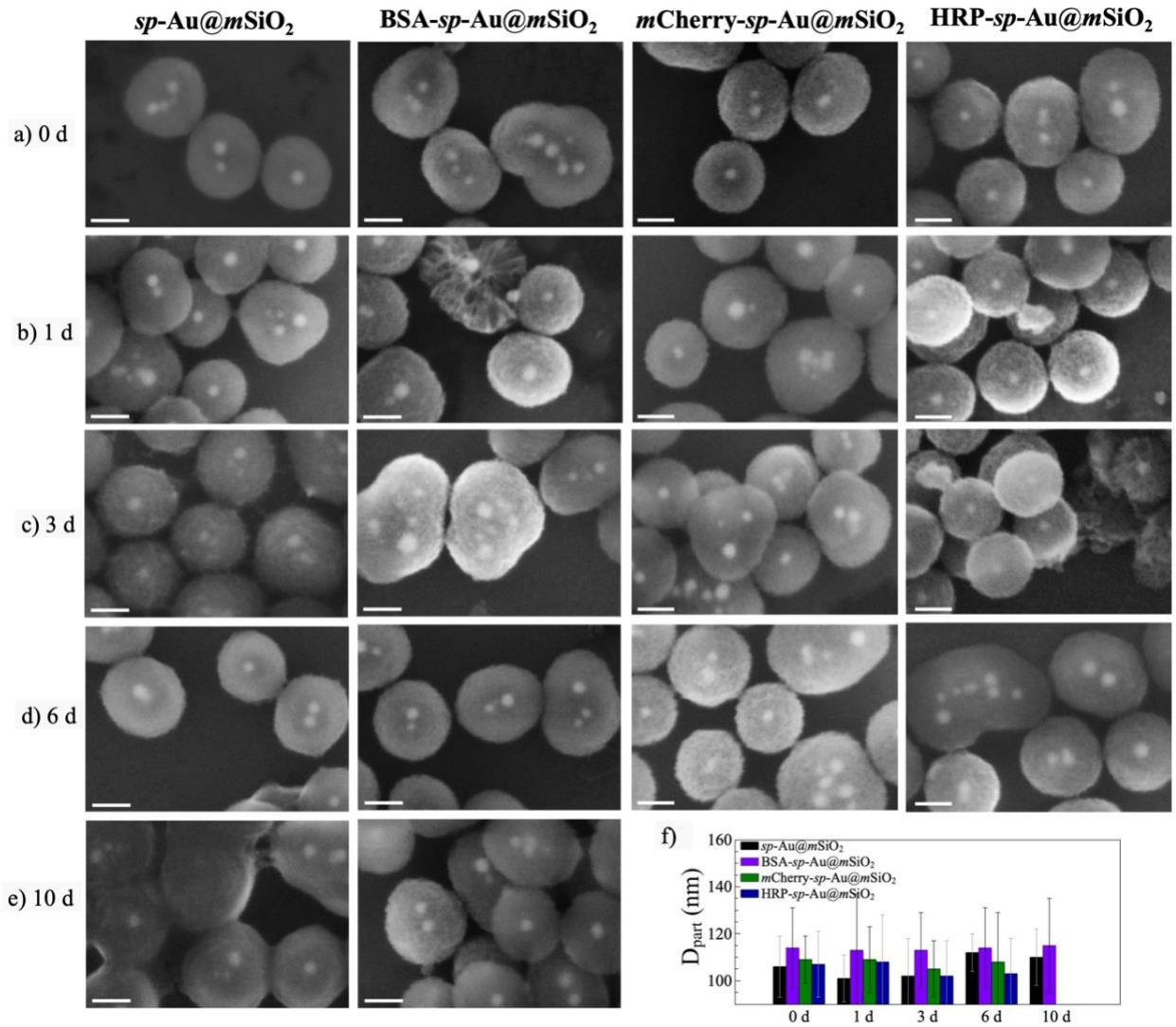

Figure 5.19. a-e) SEM micrographs showing the morphological evolution over time of a 1 mg/mL *sp*-Au@*m*SiO_2 particles with and without BSA, *m*Cherry, and HRP suspended in PBS 1×, scalebar = 50 nm. (f) Particle size (D_{part}) of *sp*-Au@*m*SiO_2 and *sp*-Au@*m*SiO_2 loaded with protein as function of degradation time determined by SEM.

In summary, for *lp*-Au@*m*SiO_2 particles, dissolution occurs from the outside inward because the proteins are encapsulated within the pores, shielding them from dissolution. This phenomenon can be explained as follows (depicted in Figure 5.20): BSA adsorbs within the pores and on the particle surface. The BSA molecules inside the pores maintain their secondary structure close to the native state, as evidenced by circular dichroism analysis. However, surface-adsorbed BSA undergoes conformational changes [7]. Proteins that do not

undergo significant conformational changes to adapt to the surface are more likely to desorb over time [7]. As a result, proteins within the pores gradually desorb, leaving behind protein-free spaces that are prone to dissolution and reprecipitation, ultimately leading to the formation of a porous matrix surrounded by protein.

In contrast, for BSA- *sp*-Au@*m*SiO_2 particles, this matrix formation is not observed, even after 10 days. This lack of matrix formation is likely due to the more homogeneous surface of *sp*-Au@*m*SiO_2 (which is less rough than *lp*-Au@*m*SiO_2). In this case, proteins tend to adapt to the surface and bind irreversibly [7].

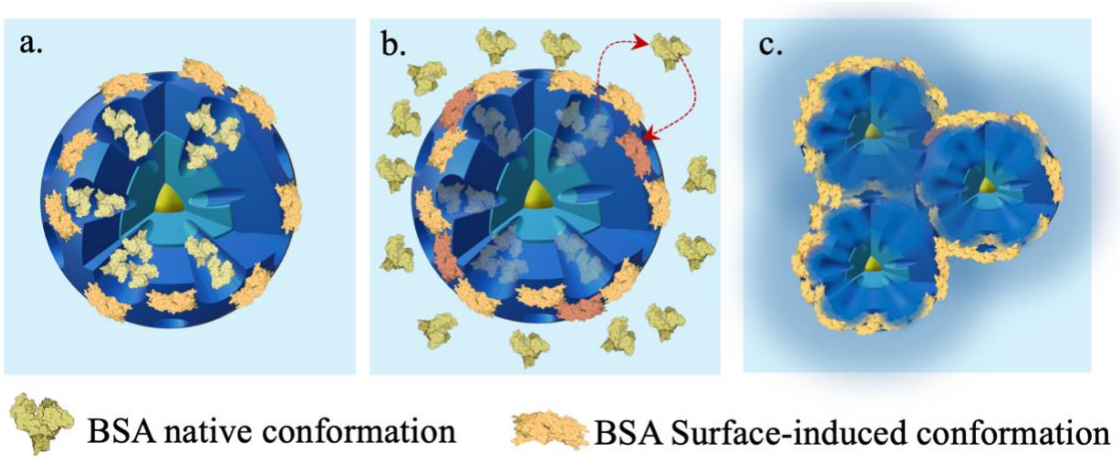

Figure 5.20. Proposed mechanism for *lp*-Au@*m*SiO_2 dissolution upon adsorption of BSA. a) BSA molecules adsorb inside the mesopores, retaining their native structure, while those adsorbed on the outer surface undergo structural changes. b) Proteins inside the pores are more susceptible to desorption, creating protein-free spaces within the nanoparticles that become more vulnerable to silica dissolution and reprecipitation. c) The dissolution and reprecipitation of silica in these protein-free spaces promote particle aggregation.

Table 5.9. Hydrodynamic diameters and ζ-potential of Au@*m*SiO_2 before and after protein loading

Particle type	Protein Adsorbed	Hydrodynamic diameter (nm)	ζ-potential (mV)
lp-Au@*m*SiO_2	-	184	-27
	BSA	172	-28
	*m*Cherry	243	-29
	HRP	176	-25
sp-Au@*m*SiO_2	-	167	-33
	BSA	168	-29
	*m*Cherry	186	-31
	HRP	159	-20

5.5.2. Stability of nanoparticles loaded with *m*Cherry and HRP

Both *lp*-Au@*m*SiO_2 and *sp*-Au@*m*SiO_2 particles loaded with the hard proteins *m*Cherry or HRP at a colloid concentration of 1 mg/mL in 1× PBS, exhibit similar degradation behavior to particles without protein (Figures 5.18 and 5.19). For *sp*-Au@*m*SiO_2 loaded with *m*Cherry or HRP, the evolution of particle morphology closely resembles that observed in particles without any protein. For *lp*-Au@*m*SiO_2, in both particles with and without protein, a significant alteration of the mesopores is observed after 3 days, accompanied by particle aggregation.

The rigidity of *m*Cherry and HRP, as observed through circular dichroism, prevents it from adapting its conformation to the adsorbent. Therefore, these

proteins cannot protect the particles as BSA does and the dissolution-reprecipitation processes occur as if there were no protein.

5.6. Summary and conclusions

The study presented in this chapter was conducted with the objective of evaluating the potential application of Au@*m*SiO_2 nanoparticles as nano-vehicles for protein delivery. At the beginning of the chapter, three key criteria were established that these nano-vehicles should meet. The following discussion addresses how the experimental findings contribute to determining whether Au@*m*SiO_2 nanoparticles fulfill these criteria.

i) The nano-vehicles retain the protein efficiently

The experimental data indicate that Au@*m*SiO_2 nanoparticles are capable of effectively retaining proteins even under unfavorable electrostatic conditions. For instance, *m*Cherry, a hard protein with a negative charge at pH 7, was successfully retained by these nanoparticles. This suggests that hydrophobic interactions play a significant role in the adsorption process. Importantly, the *m*Cherry retained its secondary structure after adsorption and is then expected to desorb relatively easily.

When electrostatic interactions are favorable and the protein is hard, as in the case of HRP, adsorption occurred even on non-porous silica particles. HRP retained both its secondary structure and enzymatic activity when loaded onto *lp*-Au@*m*SiO_2 nanoparticles.

When electrostatic interactions are unfavorable and the protein is soft, as in the case of BSA, adsorption was observed on all nanoparticle types. Adsorption on the outer surface of nanoparticles resulted in a loss of secondary structure,

whereas adsorption within the pores of *lp*-Au@*m*SiO_2 preserves a structure close to that of the free protein.

In summary, Au@*m*SiO_2 nanoparticles demonstrate efficiency in protein loading. However, to ensure their functionality as nano-vehicles, it is crucial that protein adsorption occurs with sufficient energy to prevent premature desorption, yet not so strong as to result in irreversible binding. Post-adsorption, the protein-loaded nanoparticles underwent multiple washing steps to remove unadsorbed or weakly bound proteins. The fact that proteins remained bound after these washes suggests that the adsorption occurred with sufficient energy to keep the proteins attached during transport. Nevertheless, further investigation is required to assess the efficiency of protein desorption.

ii) The proteins remain stable and functional upon adsorption

Protein stability was closely linked to the protein's inherent softness or hardness. BSA, a soft protein, exhibited the most significant alteration in secondary structure upon adsorption; however, this effect was mitigated when BSA was encapsulated within *lp*-Au@*m*SiO_2 nanoparticles. Additionally, encapsulation appeared to protect BSA from thermal denaturation. In contrast, the hard proteins *m*Cherry and HRP, due to their rigidity, maintained secondary structures upon adsorption similar to the free protein. Notably, the emission and excitation spectra of *m*Cherry adsorbed on *lp*-Au@*m*SiO_2 were not significantly altered compared to the free protein in solution, indicating preservation of its optical properties. Furthermore, HRP retained its enzymatic activity post-adsorption, comparable to that of the free protein. These findings confirm that encapsulation within the large pores of *lp*-Au@*m*SiO_2 allows proteins to retain both their structural integrity and functional activity.

iii) The nanoparticles maintain their stability

The stability of the nanoparticles in phosphate buffer saline was similarly influenced by the protein's softness or hardness. Nanoparticles loaded with BSA exhibited greater resistance to morphological changes compared to their

unloaded counterparts, suggesting that BSA plays a protective role against silica dissolution and reprecipitation processes. When loaded with hard proteins like *m*Cherry and HRP, the nanoparticles maintained their morphology, indicating that protein adsorption did not compromise nanoparticle stability. These tests were conducted at nanoparticle concentrations above the silica solubility limit, which has implications for the storage of nanovehicles. However, further studies on the stability of nanovehicles at concentrations below the silica solubility limit are necessary to better simulate conditions relevant to protein therapy applications.

In conclusion, *lp*-Au@*m*SiO_2 nanoparticles demonstrate potential as nanovehicles, satisfying the criteria established for protein loading, stability, and nanoparticle integrity. The large pores of *lp*-Au@*m*SiO_2 provide proteins with an environment that allows for electrostatic or hydrophobic interactions, without loss of structure or function. However, further research is necessary to optimize the desorption process, particularly for proteins like BSA, which may exhibit irreversible adsorption. Conversely, hard proteins such as HRP and *m*Cherry show promise for delivery applications due to their stability and propensity for easier desorption.

5.7. References

1. Ikeda T, Kuroda A (2011) Why does the silica-binding protein “Si-tag” bind strongly to silica surfaces? Implications of conformational adaptation of the intrinsically disordered polypeptide to solid surfaces. Colloids and Surfaces B: Biointerfaces 86:359–363. https://doi.org/10.1016/j.colsurfb.2011.04.020

2. Shemetov AA, Nabiev I, Sukhanova A (2012) Molecular Interaction of Proteins and Peptides with Nanoparticles. ACS Nano 6:4585–4602. https://doi.org/10.1021/nn300415x

3. Mathé C, Devineau S, Aude J-C, et al (2013) Structural Determinants for Protein adsorption/non-adsorption to Silica Surface. PLOS ONE 8:e81346. https://doi.org/10.1371/journal.pone.0081346

4. Norde W (2008) My voyage of discovery to proteins in flatland ...and beyond. Colloids Surf B Biointerfaces 61:1–9. https://doi.org/10.1016/j.colsurfb.2007.09.029

5. Norde W, Lyklema J (2012) Interfacial behaviour of proteins, with special reference to immunoglobulins. A physicochemical study. Advances in Colloid and Interface Science 179–182:5–13. https://doi.org/10.1016/j.cis.2012.06.011

6. Norde W, Favier JP (1992) Structure of adsorbed and desorbed proteins. Colloids and Surfaces 64:87–93. https://doi.org/10.1016/0166-6622(92)80164-W

7. Norde W, Horbett TA, Brash JL (2012) Proteins at Interfaces III: Introductory Overview. In: Proteins at Interfaces III State of the Art. American Chemical Society, pp 1–34

8. Uversky VN (2011) Intrinsically disordered proteins from A to Z. Int J Biochem Cell Biol 43:1090–1103. https://doi.org/10.1016/j.biocel.2011.04.001

9. Klein G, Devineau S, Aude JC, et al (2016) Interferences of Silica Nanoparticles in Green Fluorescent Protein Folding Processes. Langmuir 32:195–202. https://doi.org/10.1021/acs.langmuir.5b03890

10. Chouyyok W, Panpranot J, Thanachayanant C, Prichanont S (2009) Effects of pH and pore characters of mesoporous silicas on horseradish peroxidase immobilization. Journal of Molecular Catalysis B: Enzymatic 56:246–252. https://doi.org/10.1016/j.molcatb.2008.05.009

11. Takahashi H, Li B, Sasaki T, et al (2000) Catalytic Activity in Organic Solvents and Stability of Immobilized Enzymes Depend on the Pore Size and Surface Characteristics of Mesoporous Silica. Chem Mater 12:3301–3305. https://doi.org/10.1021/cm000487a

12. Tárraga WA, Picco AS, Longo GS (2024) Understanding protein adsorption on silica mesoporous materials through thermodynamic simulations. Surfaces and Interfaces 52:104870. https://doi.org/10.1016/j.surfin.2024.104870

13. Zampini G, Matino D, Quaglia G, et al (2019) Experimental evidences on the role of silica nanoparticles surface morphology on the loading, release and activity of three proteins.

Microporous and Mesoporous Materials 287:220–227. https://doi.org/10.1016/j.micromeso.2019.06.005

14. Beitzinger B, Schmid R, Jung C, et al (2024) Confinement and Polarity Effects on the Peptide Packing Density on Mesoporous Silica Nanoparticles. Langmuir 40:4294–4305. https://doi.org/10.1021/acs.langmuir.3c03513

15. Roach P, Farrar D, Perry CC (2006) Surface tailoring for controlled protein adsorption: effect of topography at the nanometer scale and chemistry. J Am Chem Soc 128:3939–3945. https://doi.org/10.1021/ja056278e

16. Shang W, Nuffer JH, Muñiz-Papandrea VA, et al (2009) Cytochrome C on silica nanoparticles: influence of nanoparticle size on protein structure, stability, and activity. Small 5:470–476. https://doi.org/10.1002/smll.200800995

17. Shang W, Nuffer JH, Dordick JS, Siegel RW (2007) Unfolding of Ribonuclease A on Silica Nanoparticle Surfaces. Nano Lett 7:1991–1995. https://doi.org/10.1021/nl070777r

18. Zoungrana T, Findenegg GH, Norde W (1997) Structure, Stability, and Activity of Adsorbed Enzymes. Journal of Colloid and Interface Science 190:437–448. https://doi.org/10.1006/jcis.1997.4895

19. Devineau S, Zanotti J-M, Loupiac C, et al (2013) Myoglobin on Silica: A Case Study of the Impact of Adsorption on Protein Structure and Dynamics. Langmuir 29:13465–13472. https://doi.org/10.1021/la4035479

20. Wei Y, Thyparambil AA, Wu Y, Latour RA (2014) Adsorption-Induced Changes in Ribonuclease A Structure and Enzymatic Activity on Solid Surfaces. Langmuir 30:14849–14858. https://doi.org/10.1021/la503854a

21. Vertegel AA, Siegel RW, Dordick JS (2004) Silica nanoparticle size influences the structure and enzymatic activity of adsorbed lysozyme. Langmuir 20:6800–6807. https://doi.org/10.1021/la0497200

22. Möller K, Bein T (2019) Degradable Drug Carriers: Vanishing Mesoporous Silica Nanoparticles. Chem Mater 31:4364–4378. https://doi.org/10.1021/acs.chemmater.9b00221

23. Schneid A da C, Silveira CP, Galdino FE, et al (2020) Colloidal Stability and Redispersibility of Mesoporous Silica Nanoparticles in Biological Media. Langmuir 36:11442–11449. https://doi.org/10.1021/acs.langmuir.0c01571

24. Lin C-Y, Yang C-M, Lindén M (2022) Dissolution and morphology evolution of mesoporous silica nanoparticles under biologically relevant conditions. Journal of Colloid and Interface Science 608:995–1004. https://doi.org/10.1016/j.jcis.2021.09.164

25. Galdino FE, Picco AS, Capeletti LB, et al (2021) Inside the Protein Corona: From Binding Parameters to Unstained Hard and Soft Coronas Visualization. Nano Lett 21:8250–8257. https://doi.org/10.1021/acs.nanolett.1c02416

26. Efimova YM, Haemers S, Wierczinski B, et al (2007) Stability of globular proteins in H2O and D2O. Biopolymers 85:264–273. https://doi.org/10.1002/bip.20645

27. Alkaabi KM, Yafea A, Ashraf SS (2005) Effect of pH on thermal- and chemical-induced denaturation of GFP. Appl Biochem Biotechnol 126:149–156. https://doi.org/10.1385/ABAB:126:2:149

28. Kondo A, Murakami F, Higashitani K (1992) Circular dichroism studies on conformational changes in protein molecules upon adsorption on ultrafine polystyrene particles. Biotechnol Bioeng 40:889–894. https://doi.org/10.1002/bit.260400804

29. Peters T (1995) 2 - The Albumin Molecule: Its Structure and Chemical Properties. In: Peters T (ed) All About Albumin. Academic Press, San Diego, pp 9–II

30. Majorek KA, Porebski PJ, Dayal A, et al (2012) Structural and immunologic characterization of bovine, horse, and rabbit serum albumins. Molecular Immunology 52:174–182. https://doi.org/10.1016/j.molimm.2012.05.011

31. Rezwan K, Meier LP, Rezwan M, et al (2004) Bovine Serum Albumin Adsorption onto Colloidal Al2O3 Particles: A New Model Based on Zeta Potential and UV−Vis Measurements. Langmuir 20:10055–10061. https://doi.org/10.1021/la048459k

32. Strongin DE, Bevis B, Khuong N, et al (2007) Structural rearrangements near the chromophore influence the maturation speed and brightness of DsRed variants. Protein Engineering, Design and Selection 20:525–534. https://doi.org/10.1093/protein/gzm046

33. Smigielski L, Aguilar GB, Kwaaitaal M, et al (2019) The isoelectric point of proteins influences their translocation to the extrahaustorial matrix of the barley powdery mildew fungus. Cellular Microbiology 21:e13091. https://doi.org/10.1111/cmi.13091

34. Dolinsky TJ, Nielsen JE, McCammon JA, Baker NA (2004) PDB2PQR: an automated pipeline for the setup of Poisson–Boltzmann electrostatics calculations. Nucleic Acids Research 32:W665–W667. https://doi.org/10.1093/nar/gkh381

35. Chattopadhyay K, Mazumdar S (2000) Structural and Conformational Stability of Horseradish Peroxidase: Effect of Temperature and pH. Biochemistry 39:263–270. https://doi.org/10.1021/bi990729o

36. Colonna S, Gaggero N, Richelmi C, Pasta P (1999) Recent biotechnological developments in the use of peroxidases. Trends in Biotechnology 17:163–168. https://doi.org/10.1016/S0167-7799(98)01288-8

37. Gajhede M, Schuller DJ, Henriksen A, et al (1997) Crystal structure of horseradish peroxidase C at 2.15 Å resolution. Nat Struct Mol Biol 4:1032–1038. https://doi.org/10.1038/nsb1297-1032

38. Welinder KG (1979) Amino Acid Sequence Studies of Horseradish Peroxidase. European Journal of Biochemistry 96:483–502. https://doi.org/10.1111/j.1432-1033.1979.tb13061.x

39. Langmuir I (1918) THE ADSORPTION OF GASES ON PLANE SURFACES OF GLASS, MICA AND PLATINUM. Journal of the American Chemical Society. https://doi.org/10.1021/ja02242a004

40. Freundlich H (1906) Over the adsorption in solution. JPhysChem 57U:385–470. https://doi.org/10.1515/zpch-1907-5723

41. Temkin M. and Pyzhev V (1940) Kinetics of ammonia synthesis on promoted iron catalysts. Acta Physiochim URSS 12:327–356

42. M. M. Dubinin, E. D. Zaverina, L. V. Radushkevich (1947) Sorption and Structure of Active Carbons I. Adsorption of Organic Vapors. 21:1351–1362

43. Latour RA (2015) The langmuir isotherm: A commonly applied but misleading approach for the analysis of protein adsorption behavior. Journal of Biomedical Materials Research Part A 103:949–958. https://doi.org/10.1002/jbm.a.35235

44. Böhme U, Scheler U (2007) Effective charge of bovine serum albumin determined by electrophoresis NMR. Chemical Physics Letters 435:342–345. https://doi.org/10.1016/j.cplett.2006.12.068

45. Boubeta FM, Soler-Illia GJAA, Tagliazucchi M (2018) Electrostatically Driven Protein Adsorption: Charge Patches versus Charge Regulation. Langmuir 34:15727–15738. https://doi.org/10.1021/acs.langmuir.8b03411

46. Hartvig RA, van de Weert M, Østergaard J, et al (2011) Protein adsorption at charged surfaces: the role of electrostatic interactions and interfacial charge regulation. Langmuir 27:2634–2643. https://doi.org/10.1021/la104720n

47. Kubiak-Ossowska K, Jachimska B, Mulheran PA (2016) How Negatively Charged Proteins Adsorb to Negatively Charged Surfaces: A Molecular Dynamics Study of BSA Adsorption on Silica. J Phys Chem B 120:10463–10468. https://doi.org/10.1021/acs.jpcb.6b07646

48. Clemments AM, Botella P, Landry CC (2015) Protein Adsorption From Biofluids on Silica Nanoparticles: Corona Analysis as a Function of Particle Diameter and Porosity. ACS Appl Mater Interfaces 7:21682–21689. https://doi.org/10.1021/acsami.5b07631

49. Kopac T (2021) Protein corona, understanding the nanoparticle–protein interactions and future perspectives: A critical review. International Journal of Biological Macromolecules 169:290–301. https://doi.org/10.1016/j.ijbiomac.2020.12.108

50. Beychok S (1966) Circular dichroism of biological macromolecules. Science 154:1288–1299. https://doi.org/10.1126/science.154.3754.1288

51. Moffitt W (1956) THE OPTICAL ROTATORY DISPERSION OF SIMPLE POLYPEPTIDES. II. Proc Natl Acad Sci U S A 42:736–746

52. Giacomelli CE, Norde W (2001) The Adsorption-Desorption Cycle. Reversibility of the BSA-Silica System. J Colloid Interface Sci 233:234–240. https://doi.org/10.1006/jcis.2000.7219

53. Flora K, Brennan JD, Baker GA, et al (1998) Unfolding of acrylodan-labeled human serum albumin probed by steady-state and time-resolved fluorescence methods. Biophys J 75:1084–1096

54. van Stokkum IHM, Linsdell H, Hadden JM, et al (1995) Temperature-Induced Changes in Protein Structures Studied by Fourier Transform Infrared Spectroscopy and Global Analysis. Biochemistry 34:10508–10518. https://doi.org/10.1021/bi00033a024

55. Singh NK, Pushpavanam K, Radhakrishna M (2024) Tuning Electrostatic Interactions To Control Orientation of GFP Protein Adsorption on Silica Surface. ACS Appl Bio Mater 7:596–608. https://doi.org/10.1021/acsabm.3c00125

56. Rosenholm JM, Czuryszkiewicz T, Kleitz F, et al (2007) On the Nature of the Brønsted Acidic Groups on Native and Functionalized Mesoporous Siliceous SBA-15 as Studied by Benzylamine Adsorption from Solution. Langmuir 23:4315–4323. https://doi.org/10.1021/la062450w

57. Tumbiolo S, Caputo FCG, Coluccia S (2008) Fluorescent mesoporous hybrid materials based on GFP adsorbed into SBA-15. In: Gédéon A, Massiani P, Babonneau F (eds) Studies in Surface Science and Catalysis. Elsevier, pp 763–768

58. Wall MA, Socolich M, Ranganathan R (2000) The structural basis for red fluorescence in the tetrameric GFP homolog DsRed. Nat Struct Mol Biol 7:1133–1138. https://doi.org/10.1038/81992

59. Nolles A, Dongen NJE van, Westphal AH, et al (2017) Encapsulation into complex coacervate core micelles promotes EGFP dimerization. Phys Chem Chem Phys 19:11380–11389. https://doi.org/10.1039/C7CP00755H

60. Raghunathan G, Sokalingam S, Soundrarajan N, et al (2013) A comparative study on the stability and structure of two different green fluorescent proteins in organic co-solvent systems. Biotechnol Bioproc E 18:342–349. https://doi.org/10.1007/s12257-012-0579-z

61. Visser NV, Hink MA, Borst JW, et al (2002) Circular dichroism spectroscopy of fluorescent proteins. FEBS Letters 521:31–35. https://doi.org/10.1016/S0014-5793(02)02808-9

62. Nagy A, Málnási-Csizmadia A, Somogyi B, Lőrinczy D (2004) Thermal stability of chemically denatured green fluorescent protein (GFP): A preliminary study. Thermochimica Acta 410:161–163. https://doi.org/10.1016/S0040-6031(03)00397-6

63. Zimmer M (2002) Green Fluorescent Protein (GFP): Applications, Structure, and Related Photophysical Behavior. Chem Rev 102:759–782. https://doi.org/10.1021/cr010142r

64. Melnik BS, Molochkov NV, Prokhorov DA, et al (2011) Molecular mechanisms of the anomalous thermal aggregation of green fluorescent protein. Biochimica et Biophysica Acta (BBA) - Proteins and Proteomics 1814:1930–1939. https://doi.org/10.1016/j.bbapap.2011.07.017

65. Nishiyama K, Watanabe T, Hoshino T, Ohdomari I (2005) Analysis of Interactions between Green Fluorescent Protein and Silicon Substrates Using Molecular Dynamics Simulations. Jpn J Appl Phys 44:8210. https://doi.org/10.1143/JJAP.44.8210

66. Klint D, Eriksson H (1997) Conditions for the Adsorption of Proteins on Ultrastable Zeolite Y and Its Use in Protein Purification. Protein Expression and Purification 10:247–255. https://doi.org/10.1006/prep.1997.0729

67. Naves AF, Carmona-Ribeiro AM, Petri DFS (2007) Immobilized horseradish peroxidase as a reusable catalyst for emulsion polymerization. Langmuir 23:1981–1987. https://doi.org/10.1021/la061884o

68. Strickland EH, Kay E, Shannon LM, Horwitz J (1968) Peroxidase Isoenzymes from Horseradish Roots: III. Circular Dichroism of Isoenzymes and Apoisoenzymes. Journal of Biological Chemistry 243:3560–3565. https://doi.org/10.1016/S0021-9258(19)34177-8

69. Banci L (1997) Structural properties of peroxidases. Journal of Biotechnology 53:253–263. https://doi.org/10.1016/S0168-1656(97)01677-5

70. Carvalho ASL, Melo EP e, Ferreira BS, et al (2003) Heme and pH-dependent stability of an anionic horseradish peroxidase. Archives of Biochemistry and Biophysics 415:257–267. https://doi.org/10.1016/S0003-9861(03)00275-3

71. Saud Al-Bagmi M, Shahnawaz Khan M, Alhasan Ismael M, et al (2019) An efficient methodology for the purification of date palm peroxidase: Stability comparison with horseradish peroxidase (HRP). Saudi Journal of Biological Sciences 26:301–307. https://doi.org/10.1016/j.sjbs.2018.04.002

72. Caramori SS, Fernandes KF (2004) Covalent immobilisation of horseradish peroxidase onto poly(ethylene terephthalate)–poly(aniline) composite. Process Biochemistry 39:883–888. https://doi.org/10.1016/S0032-9592(03)00188-2

73. Ferapontova E, Puganova E (2002) Effect of pH on direct electron transfer between graphite and horseradish peroxidase. Journal of Electroanalytical Chemistry 518:20–26. https://doi.org/10.1016/S0022-0728(01)00692-1

74. Nicolini JV, de Resende NS, Ferraz HC (2015) Adsorption of horseradish peroxidase onto titanate nanowires. Journal of Chemical Technology & Biotechnology 90:739–746. https://doi.org/10.1002/jctb.4369

75. Drozd M, Pietrzak M, Parzuchowski PG, Malinowska E (2016) Pitfalls and capabilities of various hydrogen donors in evaluation of peroxidase-like activity of gold nanoparticles. Anal Bioanal Chem 408:8505–8513. https://doi.org/10.1007/s00216-016-9976-z

Chapter 6

Au@*m*SiO_2 light-induced heating

6.1. Introduction

Chapter 5 demonstrated that the Au@*m*SiO_2 nanoparticles developed in this thesis effectively encapsulate proteins while maintaining the stability of both the proteins and nanoparticles, thereby meeting the criteria for use as nanovehicles. In addition, to their application as nanovehicles, this thesis explores their potential for on-demand delivery. To this end, the nanoparticles were designed with a gold core to enable plasmonic heating, facilitating the controlled release of the encapsulated proteins. A critical aspect of this system is its ability to efficiently convert light into heat, with the resulting temperature increase being sufficient to trigger protein release. This chapter investigates the photothermal properties of Au@*m*SiO_2 nanoparticles, focusing on the characterization of photothermal heating and quantification of the corresponding temperature increment.

The conversion of photon energy into heat within a metallic nanoparticle can be described in three main stages. First, when the nanoparticle absorbs a photon, its electrons become excited, leading to a plasmon resonance that rapidly thermalizes (~100 fs). Next, the energy from these excited electrons is transferred

to the particle's atomic lattice in a process known as electron-phonon thermalization, which occurs over a few picoseconds. At this point, the nanoparticle reaches a uniform internal temperature, but it is still not in thermal equilibrium with the surrounding environment, which remains at room temperature. The final stage is the transfer of heat from the nanoparticle to the surrounding medium. This thermal diffusion happens over a much longer timescale compared to the previous stages, typically taking tens to hundreds of picoseconds, depending on the medium's heat capacity and thermal conductivity [1–3].

Theoretical models have been developed to study the light-induced heating at the level of a single particle [4–6]. Additionally, macroscopic photothermal effects in gold nanoparticles and core-shell particles like Au@*m*SiO_2 has been described through experimental calculations [7–9]. Specifically, previous research conducted by Croissant & Zink [10] demonstrated that Au@*m*SiO_2 nanoparticles (D_{part} ~100 nm, D_{Au} = 15 nm, 76% porosity), allow the release of small molecules by light-induced heating. In this study, the nanoparticles were functionalized with *N*-(6-aminohexyl) aminomethyltriethoxysilane stalks, loaded with rhodamine B, and the pores were closed using cucurbit[6]uril (CB[6]). Rhodamine release occurs upon supplying sufficient energy to the system to break the two hydrogen bonds between the stalk and the CB[6] ring, as well as the hydrophobic interactions between the alkyl chain of the stalk and the CB[6] core. This energy is supplied by irradiating the particle suspension with a 514 nm laser at 15 mW, which heats the system. The authors report that the release mechanism is driven by local internal heat generated through photothermal conversion of light energy, rather than a bulk temperature increase. This finding raises several research questions about the thermoplasmonic behavior of the Au@*m*SiO_2 system. Thus, it is essential to characterize the photothermal efficiency and determine the potential temperature increase the system can achieve. This understanding is crucial for assessing whether this on-demand release mechanism could work with larger molecules, such as proteins, which may require higher temperatures than smaller molecules like rhodamine B.

Additionally, it is important to investigate how morphological factors like particle size and porosity affect the photothermal effect. This knowledge will help optimize Au@*m*SiO_2-based nanovehicles by identifying key parameters that enhance their photothermal performance.

In this chapter, we evaluate the photothermal heating of Au@*m*SiO_2 particles using two distinct approaches. The first approach involves experimentally measuring the maximum temperature increase after irradiating the particles with a 532 nm continuous wave laser, focusing on the effects of particle concentration and laser power on photothermal efficiency. The second approach applies theoretical models, initially developed for naked AuNPs, to predict the photothermal response of these core-shell particles at the nanoscale level. These models have been adapted to study how factors such as particle size, porosity, and the number of gold cores per particle influence the light-induced heating of Au@*m*SiO_2.

6.2. Theoretical bases of photothermal heating at the macroscale

As outlined by Roper et al [8] and Penelas et al [7], the heat flow balance for the suspension can be written as:

$$m\, C_p \frac{dT}{dt} = \sum Q_i = Q_{irr} + Q_{cond} + Q_{rad} \qquad (1)$$

where m is the weight of the suspension, C_p is the specific heat capacity of the suspension, T is the temperature, Q_{irr} is the energy transferred to the system

upon irradiation, Q_{cond} is the energy transferred by conduction and Q_{rad} the energy transferred by radiation. In a good approximation, the green light is only absorbed by the nanoparticles, which leads to:

$$Q_{irr} = I.(1 - 10^{-A}).\eta \qquad (2)$$

where I is the incident light power, A is the absorbance of the sample, and η the photothermal conversion efficiency that quantifies the effectiveness of converting light into heat and is defined as the ratio of absorption to extinction, accounting for the energy loss due to scattering during photothermal heating.

For 1.0 mg/mL and a path length of 2.0 cm, the coefficient A in our experiments is near 3, which means that $10^{-A} \ll 1$. Thus $Q_{irr} = I.\eta$ (3)

By definition, $Q_{cond} = -K.\Delta T$ (4),

with K a proportionality constant and $\Delta T = T - T_{amb}$.

and $Q_{rad} = -L.(T^4 - T_{amb}^4) = \Delta T\,(T + T_{amb})(T^2 + T_{amb}^2).$ (5)

with L a proportionality constant. Owing to the low temperature variation, $(T^4 - T_{amb}^4)$ can be considered proportional to ΔT at first order approximation. The error on this approximation is within 15% from 293 to 320 K.

Thus,

$$m\,C_p\frac{dT}{dt} = m\,C_p\frac{d\Delta T}{dt} = I.\eta - B.\Delta T \qquad (6)$$

Where B is a constant to be determined for the system. When the equilibrium is reached, $\frac{dT}{dt} = 0$, thus

$$I.\eta = B.\Delta T_{max} \qquad (10).$$

When there is no more heating (no illumination), the temperature decreases in the dark after the plasmonic heating, so $I = 0$, and the equation can be written as:

$$m\,C_p\frac{d\Delta T}{dt} = -B.\Delta T \qquad (7)$$

the temperature can thus be fitted with a monoexponential decay curve,

$$\Delta T = \Delta T_{max}.e^{-\frac{t}{\tau}} \qquad (8)$$

where $\tau = \frac{m.C_p}{B}$, represents the characteristic time of temperature decay.

Equation (6) can be solved by the function:

$$\Delta T = \Delta T_{max}.\left(1 - e^{-\frac{t}{\tau}}\right) \qquad (11)$$

with $\tau = \frac{m.C_p}{B}$ and $I.\eta = B.\Delta T_{max}$

Based on these theoretical principles, a temperature increment is expected during particle´s irradiation, according to Equation (11), reaching an asymptotic value at T_{max}. After irradiation, the temperature will then exhibit an exponential decay, as described by Equation (8). Thus, experimental measurements of temperature changes during and after irradiation can be used to determine the photothermal efficiency (η).

6.3. Characterization of the Au@*m*SiO_2 heating at the macroscale

The experiments on Au@*m*SiO_2 light-induced heating presented here were conducted with Corinne Felix and Veronique Boutou from Institut Néel, who set up the experiment. The light-induced heating was characterized in aqueous suspensions of *sp*-Au@*m*SiO_2 and *lp*-Au@*m*SiO_2, with the specific characteristics of these particles outlined in Table 6.1. First, two milliliters of a *sp*-Au@*m*SiO_2 suspension in water were placed in a quartz cuvette and irradiated with a collimated laser beam (2.3 mm in diameter) at a wavelength of 532 nm to excite the surface plasmon of the metallic cores. The particle concentration was varied using suspensions of 0.25, 0.5, and 1 mg/mL, corresponding to 4.7×10^{11}, 9.5×10^{11}, and 1.9×10^{12} nanoparticles, respectively. The laser power was also adjusted at 280, 500, and 800 mW. The temperature changes were monitored over time during both the heating and cooling phases using a thermocouple immersed in the suspension. Upon ceasing the irradiation at t_l = 8 min, the temperature decreased according to a monoexponential decay as described previously [4, 7, 8]. A detailed description of the experimental protocol is provided in Chapter 2.

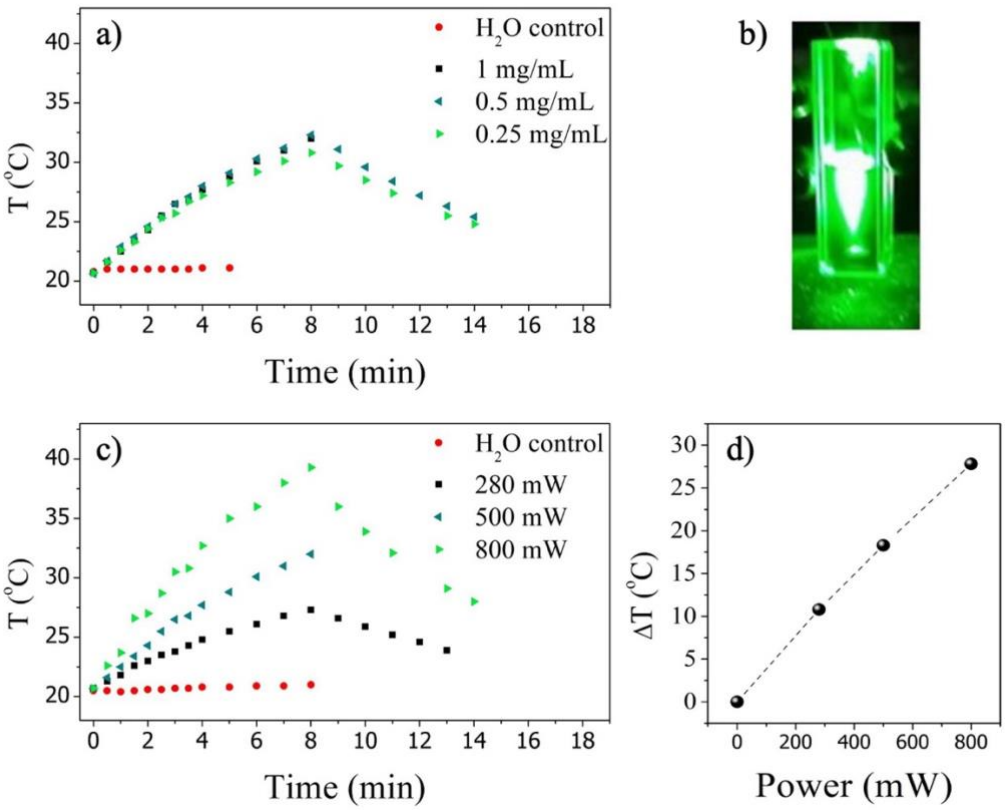

Figure 6.1. a) Temperature variation of a *sp*-Au@*m*SiO_2 colloid at 500 mW under a collimated 532 nm laser irradiation for 8 min for different concentrations. (red dots) 0 mg/mL; (green right triangles) 0.25 mg/mL; (blue left triangles) 0.5 mg/mL; (black squares) 1.0 mg/mL. b) The picture shows the scattered green light during the heating experiment with the exciting beam coming from the top of the cuvette containing 2 mL of a 1.0 mg/mL colloid solution. c) Temperature variation of a 1 mg/mL *sp*-Au@*m*SiO_2 colloid at (black squares) 280 mW; (blue left triangles) 500 mW; (green right triangles) 800 mW; (Red dots): pure water control at 500 mW. d) Temperature increment as a function of laser power.

Based on the temperature profile as a function of irradiation time and after turning off the excitation source (Figure 6.1a and c), it is evident that irradiating the colloid leads to a significant macroscopic temperature increase. Under the test conditions, a suspension of 1 mg/mL at 800 mW resulted in a temperature rise of approximately 28 ˚C, raising the system's temperature from room temperature to around 40 ˚C. This temperature range is highly suitable for biomedical applications, as it aligns with physiological temperature ranges.

Table 6.1. Key Parameters of the nanoparticle suspensions studied. Particle diameters (D_{part}) were determined from TEM micrographs, while textural parameters such as pore volume and pore diameter were derived from N_2-sorption isotherms. Porosity (*f*) is calculated as the ratio of the porous volume to the total volume of the particle.

Sample	**Vol_{susp} (mL)**	**Number of particles**	**D_{Au} (nm)**	**D_{part} (nm)**	**Pore size (nm)**	**Pore volume ($cm^3.g^{-1}$)**	***f* (%)**
AuNP	1	2.7×10^{13}	15	15	-	-	-
lp-Au@*m*SiO_2	1	5.7×10^{11}	15±5	92±6	20	2	80
sp-Au@*m*SiO_2	2	1.8×10^{12}	15±5	112±8	3	1.7	76

The maximum temperature is nearly independent of the concentration in the 0.25-1.0 mg/mL range (Figure 6.1a), which can be understood as most of the incident light is absorbed by the sample through the 20 mm of solution as seen in the cuvette photograph. Moreover, the cuvette used and the water itself could not absorb light, leading to a negligible temperature increase when no Au@*m*SiO_2 were used. The maximum temperature increase after 8 minutes of irradiation was proportional to the incident power (Figure 6.1d), in accordance to what has been described in the literature [7]. These experiments confirm the potential of Au@*m*SiO_2 as strong absorbers for photothermal therapy or photothermal release of cargo molecules retained in the mesopores.

To investigate the effect of the silica shell and its porosity, we also examined the plasmonic heating of *lp*-Au@*m*SiO_2 and naked AuNPs. Table 6.1 presents the size, porosity, concentration, and number of particles used in the experiment. Due to equipment constraints, we were limited to laser power of 51, 78, and 117 mW. This restriction led to smaller temperature increase compared to that observed for *sp*-Au@*m*SiO_2 irradiated at higher power levels (Figure 6.2a and b). However, similarly to the *sp*-Au@*m*SiO_2, the maximum temperature increase after irradiation was proportional to the incident power (Figure 6.2c and d).

The temperature increase observed is due to heat transfer within the liquid system, governed by factors like specific heat capacity, thermal diffusivity, and experimental conditions such as the volume surrounding the irradiated area. These results demonstrate that irradiating Au@*m*SiO_2 induces significant macroscopic heating through the photothermal effect, which can be precisely modulated by adjusting the irradiation power.

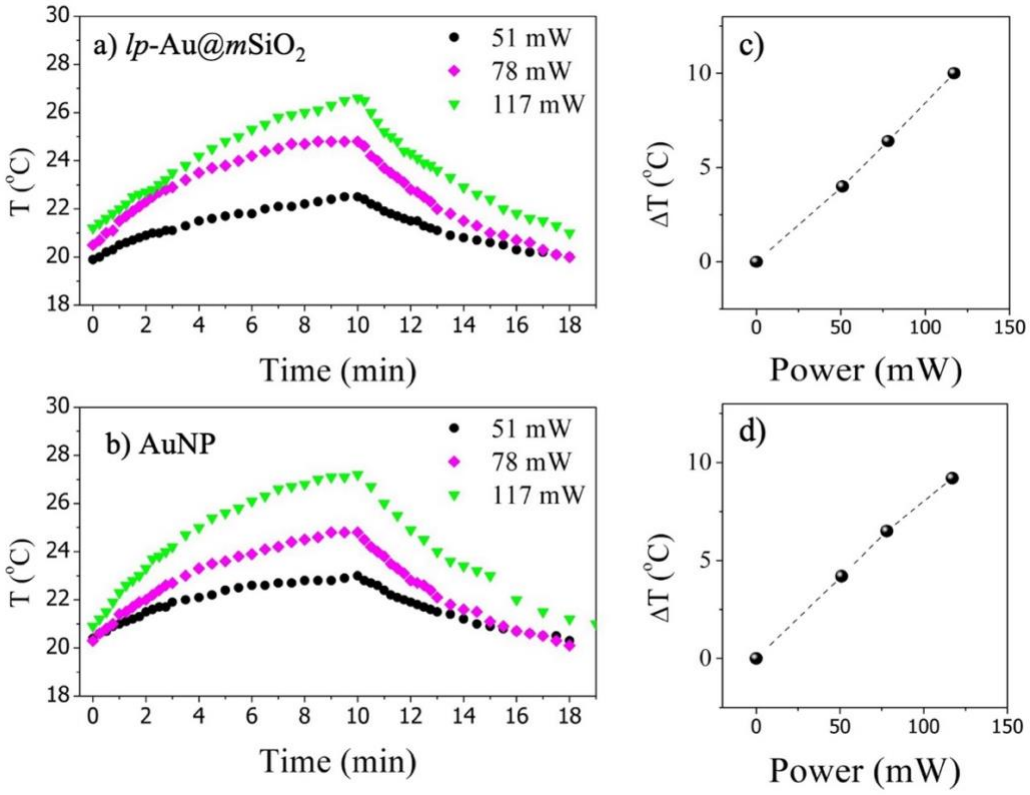

Figure 6.2. Left: Temperature variation of (a) *lp*-Au@*m*SiO_2 and (b) AuNP colloid at 1.0 mg/mL under a collimated 532 nm laser irradiation for (black dots) 51 mW; (magenta diamonds) 78 mW; (green triangles) 117 mW. Right: Temperature increase as a function of laser power.

6.3.1. Photothermal efficiency calculation

The temperature monitoring experiments allow to calculate the photothermal efficiency using the heat flow balance method described in section 6.2

τ and ΔT_{max}were obtained from the experimental results according to equations [9] and [11], and the results are summarized in Table 6.2, together with the photothermal efficiency values η.

Table 6.2. Relevant thermal parameters extracted from the photothermal experiment

Particle	I (mW)	V_{susp} (mL)	τ (s)[a]	τ (s)[b]	ΔT_{max} (K) [b]	η [c]
sp-Au@*m*SiO_2	280	2	nd	513	10.8	0.75
	500	2	440	470	18.3	0.71
	800	2	391	430	27.8	0.68
lp-Au@*m*SiO_2	51	1	310	357	4	1.10
	78	1	301	253	6.4	1.33
	117	1	306	502	10	1.06
AuNP	51	1	286	287	4.2	1.49
	78	1	293	304	6.5	1.37
	117	1	379	247	9.2	1.04

[a] determined from the temperature decay curve. [b] determined from the temperature increase curve; [c]taking $\tau = 280\ s$ for AuNP, $\tau = 430\ s$ for *sp*-Au@*m*SiO_2, and $\tau = 305\ s$ for *lp*-Au@*m*SiO_2.

For the AuNP suspension, the conversion efficiency value was approximately 1 for a laser power of 117 mW, consistent with reported values in the literature [7]. However, at lower laser powers, for AuNPs and *lp*-Au@*m*SiO_2, the efficiency reached values higher than 1 (Table 6.2), which has no physical meaning. This apparent increase in efficiency at lower powers might be due to

the experimental conditions, specifically the use of a lower volume of suspension, which results in much more important contribution of the heat losses by the cuvette, which heat capacity is not considered in the model. Such effect is more pronounced at lower laser powers, leading to an overestimation of the efficiency by about 30%.

For the *sp*-Au@*m*SiO_2 suspension, the photothermal efficiency was approximately 0.7 (Table 6.2), which is consistent with studies on Au@SiO_2 particles with a dense silica shell [7]. This lower efficiency compared to what is described for naked AuNPs highlights the significant scattering effect caused by the silica shell. The photothermal efficiency analysis shows that, despite the AuNPs being coated with a silica shell, they are still effective at heating up when exposed to light, although there is a 30% loss in efficiency due to increased light scattering from the shell. However, to make definitive conclusions, it is essential to conduct further experiments where all three types of particles are tested under the same conditions (volume, laser power, geometry). This will ensure a more accurate comparison and understanding of how shell porosity affects photothermal performance.

6.4. Theoretical modelling of the plasmonic heating at the nanoscale

Theoretical calculations presented here were performed by María Luz Martínez Ricci (DQIAQF, Argentina) and Guillermo Ortiz (Universidad Nacional del Nordeste, Argentina). In this modelling work, we aim to establish the temperature profile at the nanoscale when a silica-coated gold nanoparticle suspended in water at a fixed bulk temperature is irradiated within its plasmon band.

The physical basis for photothermal conversion for pure AuNPs is well known [5]. To calculate the photothermal response of core-shell particles we have adapted previous results [6] to consider a spherical Au metal core of diameter D_{Au} and thermal conductivity K_0, surrounded by a porous mSiO$_2$ shell of diameter D_{part} and thermal conductivity K_1^{eff}. As the shell is mesoporous, both refractive index and effective conductivity of the mSiO$_2$ part have been calculated applying effective medium approximations (EMA) models [11, 12] considering the porosity of the shell. Pores were considered to host water as well as the surrounding environment. In all cases, $K_0 > K_1^{eff} \geq K_2$ where K_2 is the thermal conductivity of the external aqueous medium. This system is schematized in Figure 6.3a.

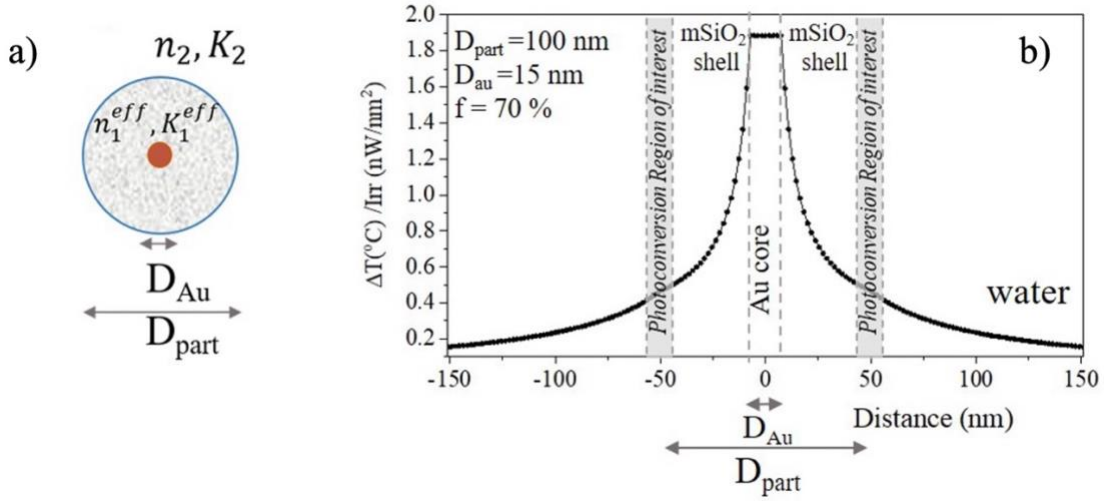

Figure 6.3. a) Scheme of the Au@mSiO$_2$ particles and parameters used in simulations, b) ΔT profile per irradiance ($\frac{nW}{nm^2}$) for an Au@mSiO$_2$ with D_{Au} = 15 nm, D_{part} = 100 nm, and f = 70%, b) ΔT at the surface as a function of D_{part}, with D_{Au} = 15 nm, and f = 70%, error bars correspond to the variation inside the photoconversion region of interest.

For a single Au NP core inside a shell as the one schemed in Figure 6.3a, the temperature as a function of distance can be obtained analytically, as a solution of the Poisson equation for the metal core: $\nabla^2 T(r) = -\frac{q(r)}{K}$, where K is the thermal conductivity of the surrounding medium and $q(r)$ is the heat power density that comes from the Joule effect, $q(r) = \frac{1}{2} Re[\boldsymbol{J}^*(r) \cdot \boldsymbol{E}(\boldsymbol{r})]$ with $\boldsymbol{J}(r)$ the

current density and $\boldsymbol{E}(\boldsymbol{r})$ the electric field. For Au@mSiO$_2$ it is also necessary to apply bounding conditions at $r = D_{Au}/2$ and at $r = \frac{D_{part}}{2}$. The solutions for the increment in temperature relative to T_{amb} at each region become:

$$\begin{cases} T_0 = \dfrac{Q}{4\pi}\left(\dfrac{1}{K_1^{eff} D_{Au}} + \dfrac{1}{K_2 D_{part}} - \dfrac{1}{K_1^{eff} D_{part}}\right), & \text{for} \quad r \le \dfrac{D_{Au}}{2} \\ T(r) = \dfrac{Q}{4\pi}\left(\dfrac{1}{K_1^{eff} r} + \dfrac{1}{K_2 D_{part}} - \dfrac{1}{K_1^{eff} D_{part}}\right), & \text{for} \dfrac{D_{Au}}{2} \le r \le \dfrac{D_{part}}{2} \\ T(r) = \dfrac{Q}{4\pi}\dfrac{1}{K_2 r} & \text{for} \quad r \ge \dfrac{D_{part}}{2} \end{cases}$$

where $Q = C_{abs} Irr$ with C_{abs} the absorption cross section for core-shell particles. The effective conductivity K_1^{eff} was calculated using the Maxwell effective method that follows the equation $\frac{K^{eff}}{K_{SiO_2}} = 1 + \frac{3f}{\frac{K_{H_2O}+2K_{SiO_2}}{K_{H_2O}-K_{SiO_2}} - f}$,with $K_{H_2O} = 0.59\frac{W}{mK}$ and $K_{SiO_2} = 1.1 - 1.2\frac{W}{mK}$ for SiO_2 nanoparticles [13].

Figure IV-3b exhibits the photothermal response as a function of distance for the systems used in the photothermal experiment using *sp*-Au@mSiO$_2$. At the surface of the particle (d = D$_{\text{part}}$) for an irradiance of $Irr = 1\, nW\, nm^{-2}$, we calculated $\Delta T \approx 0.35\,°C$. It is worth noticing that the irradiance used for the photothermal experiments was below 0.2 $W\, mm^{-2}$, *ie* $2 \times 10^{-4}\, nW\, nm^{-2}$. Under this irradiance, the expected temperature increase for $D_{part} = 100\, nm$ is $\Delta T \approx 7\, x\, 10^{-5}\,°C$ under isothermal conditions. Therefore, the macroscopic rise in temperature observed in the experimental characterization can only be explained by a collective heating of the medium by numerous nanoparticles.

To understand how different morphological parameters affect temperature, simulations were conducted to examine the impact of shell

thickness, porosity, gold core diameter, and the number of gold cores per particle.

As expected, the temperature increase decreases with thicker shells (Figure 6.4a). The temperature increase could be adjusted within a range of 2 ˚C nm² nW⁻¹ by modulating the shell thickness. For porosity, simulations reveal that particles with a dense silica shell (f = 0) experience a higher temperature rise compared to particles with a porous silica shell (f = 100%) for those with a diameter of D_{part} = 100 nm (Figure 6.4c). Temperature increment could be controlled within a range of 0.15 ˚C nm² nW⁻¹ by adjusting the porosity. Regarding Au core size, more important differences could be observed for larger Au cores which could raise up to $\Delta T \approx 5\ °C\ nm^2\ nW^{-1}$ for particles of D_{Au} = 30 nm (Figure 6.4b).

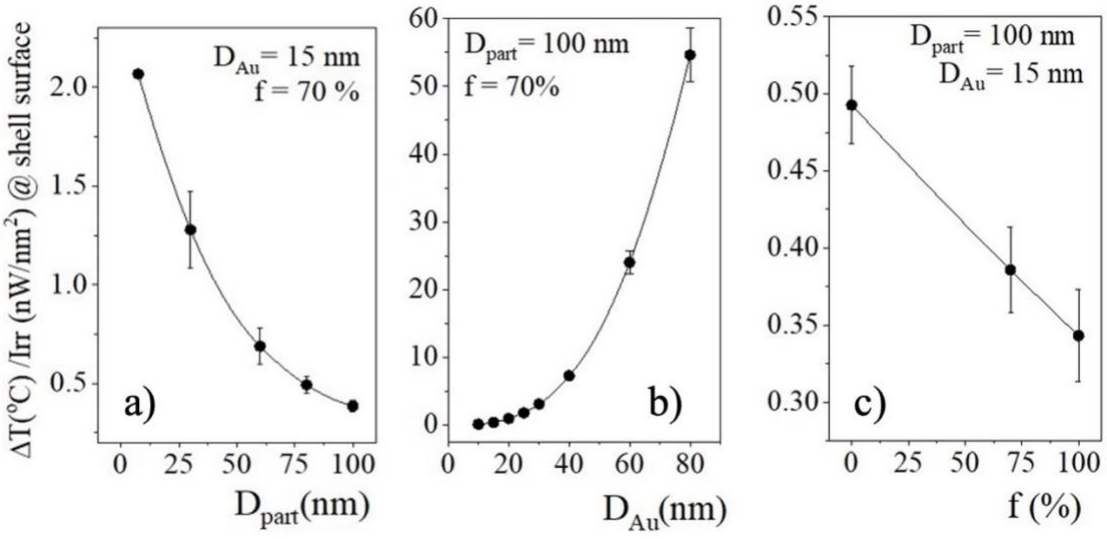

Figure 6.4. ΔT at the surface as a function of (a) $D_{part,}$ with D_{Au} = 15 nm, and f = 70%, (b) D_{Au} with $D_{part} = 100\ nm$ and f = 70%, (c) f% with $D_{part} = 100\ nm$ and with $D_{Au} = 15\ nm$. Error bars correspond to the variation inside the photoconversion region of interest.

From TEM images of the core-shell particles (Figure 6.5 insets), some particles exhibit 2 or more cores. From microscopy statistical analysis on the *sp*-Au@*m*SiO_2 sample, 61% of the NPs exhibit a single core while 39% have multiple cores. To understand the role of multi-core NPs in the photothermal response, simulations have been performed using *Photonic open source code* [14]. Particles with 2 and 3 cores have been considered since they are statistically more frequent in the samples, with a mean distance between cores of d_c = 7±3 nm, as measured in TEM micrographs.

For the multicore simulations, the heat power density expression results proportional to the electric field density $|E|^2$. Therefore, for each of the configurations we have calculated the $|E|^2$ distribution in the 3D space for polarization in x, y and z directions since the morphology is no longer isotropic. To show the behaviour of $|E|^2$, we have selected x-axis profile for x polarization, for 1, 2 and 3 cores at two different d_c distances in-between the measured d_c values. Figure IV-5a shows the dipolar distribution of $|E|^2$ for 1 core where the EM field is concentrated in the neighborhood of the metal surface. For 2 cores $|E|^2$ distribution is very sensible to the inter-core distances considered. Figure IV-5b and c show the $|E|^2$profile in x-axis for d_c = 3.5 nm and d_c = 7 nm respectively. In both cases the 2D x-y distribution is included showing a clear hot spot for the shortest distance, with high energy concentration at the center of the particles of almost one order of magnitude respect to $|E|^2$ in Figure IV-5c. Particles composed of 3 cores show the same behavior for d_c = 3.5 nm (Figure IV-5d), where $|E|^2$ is more localized and intense than for d_c = 7 nm (Figure IV-5e), which can also be observed in the corresponding 2D x-y $|E|^2$ distributions. $|E|^2$ has also been performed for the other 2 polarization cases. To calculate the temperature at the surface of the Au@*m*SiO_2 particle it is necessary to consider all the $q(r)$ contributions to the $\Delta T(r = \frac{D_{part}}{2})$. To take into consideration all contributions, temperature variations can be calculated as $\Delta T\left(\frac{D_{part}}{2}\right) = \int G\left(r, \frac{D_{part}}{2}\right) q(r) dr$, where $G\left(r, \frac{D}{2}\right)$ represents the Green function associated to the Poisson equation.

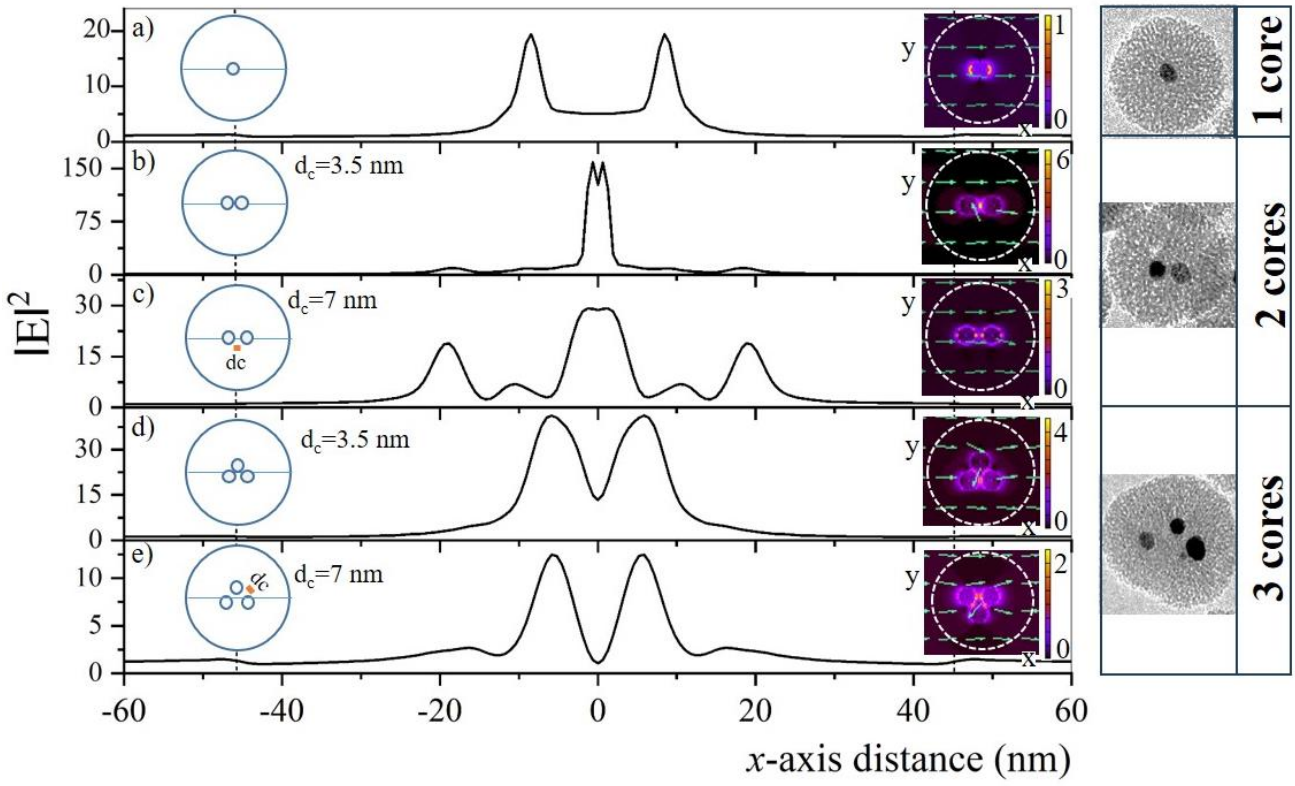

Figure 6.5. $|E|^2$profile at x axis for x polarization case for Au@mSiO$_2$ particles with (a) 1 core, (b) 2 cores with an intercore distance d_c = 3.5 nm, (c) 2 cores with d_c = 7 nm, (d) 3 cores with d_c = 3.5 nm and (d) 3 cores with d_c = 7 nm. Each case considered, shows the corresponding scheme (left inset), TEM image (right inset) and 2D x-y $|E|^2$ distribution (normalized to the maxium of the $|E_{1NP}|^2$ case for x polarization).

To understand if the number of cores modifies the temperature at $r = \frac{d_{D_{part}}}{2}$, the rate $\sigma = \frac{\Delta T}{\Delta T_1}$ has been calculated for each of the configurations of Figure IV-5, where ΔT_1 represents the variation of temperature for only 1 core. As a first approach, σ has been calculated using a 1D Green function at axis x, y and z as privileged directions of the system, due to the configurations of cores at the center. As the $|E|^2$distribution is higher at those axes, they are expected to be upper bounds for the temperature. Table 6.3a shows the values obtained for σ in particular for the 2 cores with d_c = 3.5 nm case for the 3 axes in the 3 polarization cases. Due to the distribution of the $|E|^2$density in x-polarization (which can be

observed in the corresponding 2D graph) it is possible to observe a clear increment of the temperature with respect to the 1 core case, while in y and z polarizations, this effect does not occur and in fact it represents less temperature for some axes contributions. Although the expected anisotropic response is found, photothermal experiments have been done with unpolarized light and with randomly distributed particles, which implies averaging in polarization states and directions. These averages imply a temperature increment with $\sigma = 1.7$ in particular for the 2 cores with $d_c = 3.5$ nm. For all other multi-core particles studied, the average values are depicted in Table 6.3b. For all cases where hot spots are present ($d_c = 3.5$ nm) ΔT is higher than for cores that are separated 7 nm. For this case $d_c = 7$ nm, there is almost no increment in ΔT since σ is close to 1.

Simulations thus show that it is possible to increment photothermal conversion for certain multi-core Au@mSiO$_2$ particles, in particular for those that exhibit a morphology compatible with hot spots. However, the frequency at which particles with this morphology appear in a sample is low and so no relevant change is expected for a photothermal experiment as the one done in Figure 6.4. As regards multi-core NPs with more separated cores, they do not exhibit a representative variation in temperature at the surface of the shell respect to 1 core Au@mSiO$_2$ NPs.

Table 6.3. Calculated σ values from simulated $|E|^2$ data from Figure 6.5. (a) Discriminated σ values for each polarization direction calculated along the 3 main axes. The last column represents the average for unpolarized light. (b) Average values in polarization states and direction for 2 and 3 cores, considering d_c = 3.5 nm and d_c = 7 nm.

a)

2 cores - σ ($d_c = 3.5\ nm$)					
		polarization			UnPolarized
		x	y	z	
axis	x	2.9	1.1	1.1	1.7
	y	4.3	0.4	0.4	1.7
	z	4.3	0.5	0.4	1.7

b)

	2 cores		3 cores	
	$d_c = 3.5nm$	$d_c = 7\ nm$	$d_c = 3.5nm$	$d_c = 7\ nm$
σ	1.7	1.1	2.4	1.3

6.5. Conclusions

Experimental measurements revealed that irradiating Au@mSiO$_2$ nanoparticles in suspension with a 532 nm laser induced a notable macroscopic temperature increase. For instance, suspensions at a concentration of 1 mg/mL and a laser power of 800 mW achieved a temperature elevation of 28 ˚C with an efficiency of *ca* 70%. However, due to the strong dependence of these measurements on the experimental setup, it is essential to perform the experiments under highly controlled conditions to be able to compare different systems. Simulations show that such nanoparticles exhibit a temperature increase of *ca* 0.35 ˚C at their surface under isothermal conditions for a continuous irradiance of 1 nW/nm^2. This elevated irradiance necessary to heat demonstrates that the observed temperature increase of the suspension under excitation mostly results from the collective heating by a large number of nanoparticles (~10^{11} NP/mL), each of them providing a small heating effect. A key challenge in comparing macroscopic and theoretical heating at the nanoscale is

the difficulty in directly measuring the temperature of individual nanoparticles during irradiation.

Theoretical calculations provided additional insights into how particle morphology affects photothermal response. Simulations suggested that changes in shell thickness, porosity, or the presence of multiple cores result in only marginal differences in temperature increase, with the gold core size having the most significant impact. Despite this, the individual temperature increases (ΔT) are too small to trigger a photothermally stimulated release of guests at the irradiance levels typically used in experiments (< 1 W/mm²). However, the cumulative effect of numerous nanoparticles may contribute to a larger overall temperature rise, as many nanoparticles can be optically stimulated simultaneously.

These results are therefore in contradiction with those reported by Croissant & Zink [10] who stipulate that Au@*m*SiO_2 nanoparticles can individually elevate their temperature by 35 °C at less than 1 W/mm², within a medium at constant temperature. In that study, the particles were positioned as a pellet in a corner of the cuvette, where the collective effects of aggregated particles surely contributed significantly to the observed temperature increase, resulting in bulk heating. This scenario, however, is unrealistic for nanovehicles, which are expected to be suspended and dispersed throughout the medium.

The temperature increase is directly proportional to the laser power used. Therefore, irradiating nanoparticle suspensions with higher-powered lasers, or using pulsed lasers in the nanosecond or picosecond range, could result in higher temperature increases. For example, it has been calculated that 20 nm gold nanoparticles exposed to picosecond pulsed lasers can heat to their melting point, causing them to dissolve, while nanosecond lasers can raise particle temperatures to around 80 °C [3]. Nevertheless, the laser power must be carefully optimized for the specific application of the nanovehicle. In practical applications, the maximum heating power is often limited to prevent thermal damage to biomolecules, such as protein denaturation [15]. Therefore, the

heating capability of the nanovehicle needs to be thoroughly investigated and optimized for safe and effective use.

6.6. References

1. Hodak JH, Henglein A, Hartland GV (1999) Size dependent properties of Au particles: Coherent excitation and dephasing of acoustic vibrational modes. The Journal of Chemical Physics 111:8613–8621. https://doi.org/10.1063/1.480202

2. Hu M, Hartland GV (2002) Heat Dissipation for Au Particles in Aqueous Solution: Relaxation Time versus Size. J Phys Chem B 106:7029–7033. https://doi.org/10.1021/jp020581+

3. Hodak JH, Henglein A, Giersig M, Hartland GV (2000) Laser-Induced Inter-Diffusion in AuAg Core−Shell Nanoparticles. J Phys Chem B 104:11708–11718. https://doi.org/10.1021/jp002438r

4. Richardson HH, Carlson MT, Tandler PJ, et al (2009) Experimental and theoretical studies of light-to-heat conversion and collective heating effects in metal nanoparticle solutions. Nano Lett 9:1139–1146. https://doi.org/10.1021/nl8036905

5. Baffou G, Quidant R, Girard C (2010) Thermoplasmonics modeling: A Green's function approach. Phys Rev B 82:165424. https://doi.org/10.1103/PhysRevB.82.165424

6. Baffou G, Quidant R (2013) Thermo-plasmonics: using metallic nanostructures as nano-sources of heat. Laser & Photonics Reviews 7:171–187. https://doi.org/10.1002/lpor.201200003

7. Penelas MJ, Arenas GF, Trabadelo F, et al (2022) Importance of the Structural and Physicochemical Properties of Silica Nanoshells in the Photothermal Effect of Silica-Coated Au Nanoparticles Suspensions. Langmuir 38:3876–3886. https://doi.org/10.1021/acs.langmuir.2c00127

8. Roper DK, Ahn W, Hoepfner M (2007) Microscale Heat Transfer Transduced by Surface Plasmon Resonant Gold Nanoparticles. J Phys Chem C Nanomater Interfaces 111:3636–3641. https://doi.org/10.1021/jp064341w

9. Palermo G, Pagnotto D, Ricciardi L, et al (2017) Thermoplasmonic Effects in Gain-Assisted Nanoparticle Solutions. J Phys Chem C 121:24185–24191. https://doi.org/10.1021/acs.jpcc.7b08186

10. Croissant J, Zink JI (2012) Nanovalve-Controlled Cargo Release Activated by Plasmonic Heating. J Am Chem Soc 134:7628–7631. https://doi.org/10.1021/ja301880x

11. Sihvola A (2001) Two Main Avenues Leading To the Maxwell Garnett Mixing Rule. Journal of Electromagnetic Waves and Applications 15:715–725. https://doi.org/10.1163/156939301X00968

12. Pietrak K, Wiśniewski T (2015) A review of models for effective thermal conductivity of composite materials. Journal of Power Technologies Vol. 95:

13. Chen W, Feng Y, Qiu L, Zhang X (2020) Scanning thermal microscopy method for thermal conductivity measurement of a single SiO2 nanoparticle. International Journal of Heat and Mass Transfer 154:119750. https://doi.org/10.1016/j.ijheatmasstransfer.2020.119750

14. Mochán WL, Ortiz, Mendoza B s, Pérez-Huerta JS (2016) Photonic. A perl package for calculations on photonics and metamaterials.

15. Pustovalov VK (2023) Heating of nanoparticles and their environment by laser radiation and applications. Nanotechnology and Precision Engineering 7:015001. https://doi.org/10.1063/10.0022560

Chapter 7

Conclusions and Outlooks

This thesis presents a fundamental study for the design of nanovehicles for protein delivery. Au@*m*SiO_2 particles featuring a gold core and a mesoporous silica shell are optimizaed to serve as a platform for protein loading and delivery triggered by photothermal conversion. Their tunable properties make them well-suited for potential on-demand protein delivery, particularly in topical applications.

The first stage of this work was focused on achieving a reproducible and robust synthesis with high yield, particle diameter less than 100 nm for a facile penetration in a cell, and pores with diameter enough to lodge proteins. A *one-pot* synthesis method was employed to construct these nanovehicles. This approach was selected for its alignment with green chemistry principles, and potential scalability. This allowed the development of a molecular description of the synthesis mechanism, which was mapped into two trajectories: (i) from the gold precursor to the formation of AuNPs, and (ii) from the silica precursor to the formation of the mesoporous shell. These trajectories intersect at a critical point in the reaction space at an specific point that is defined by the precursor state before triggering AuNP formation and TEOS hydrolysis and condensation. If these conditions are met, it becomes possible to modify the size and shape of the core and shell thickness, yielding monodisperse nanoparticles.

Particle diameter control was achieved with a mixture of CTAB and Brij C10 (1:5). However, pore size modification was not feasible by the *one-pot* method, as pore-enlarging strategies disrupted the timing of the reaction trajectories,

leading to undesired products. To achieve large-pore nanoparticles, a two-step synthesis was undertaken. This pathway requires: : (i) synthesizing small core-shell nanoparticles (45 nm diameter) using the optimized *one-pot* method, and (ii) growing a second, silica shell with large pores. Two methods were adapted for this: the use of pore-expanding agents and a biphasic stratification process. The latter method enabled the production of Au@*m*SiO_2 particles with large pores (up to 20 nm) and improved stability for up to three days under *saline* conditions. This approach marks the first reported synthesis and detailed stability characterization of large-pore Au@*m*SiO_2 particles.

The second part of this study focused on understanding how pore size and protein structure influence protein loading, location, and structural changes. AFM and *cryo*-EF-TEM analyses showed that in large-pore nanoparticles, proteins were found both inside the pores and on the outer surface. In small-pore nanoparticles, protein location was size-dependent: larger proteins predominantly adsorbed on the outer surface, whereas proteins closer in size to the pores adsorbed both within the pores and on the outer surface.

The structural changes observed in proteins upon adsorption also vary depending on their nature and the pore size of the nanoparticles. Soft proteins undergo conformational changes compared to their free form and exhibit increased thermal stability when loaded into large-pore nanoparticles. This enhanced stability is less evident when these proteins are adsorbed on the surface of small-pore nanoparticles. In contrast, 'hard' proteins like *m*Cherry maintain the native conformation, experiencing minimal structural changes, regardless of the pore size. This emphasizes the importance of both pore size and protein structure in preserving the structural integrity of adsorbed proteins.

To explore the potential for on-demand protein delivery, the light-induced heating of Au@*m*SiO_2 nanoparticles was assessed both macroscopically, through temperature monitoring under laser irradiation, and at the nanoscale, via

computational modeling. Results showed that individual nanoparticles exhibit very small temperature increases under practical laser power. However, when considering the collective effect of many nanoparticles, temperature increases contribute to a larger overall rise, as a myriad of particles can be optically stimulated simultaneously. These observations challenge earlier reports, which claimed that individual nanoparticles could achieve sufficiently high temperatures to produce significant thermal effects (1).

In summary, this thesis provides several key contributions to the field of nanovehicles for protein delivery. It contributes to the development of Au@*m*SiO_2 nanoparticles with precise control over size, pore size, and polydispersity, while providing a deeper understanding of the synthesis mechanism. It also introduces potentially scalable methodologies, crucial for the large-scale production of advanced nanomaterials for high-performance applications. Additionally, the results demonstrate the potential of Au@*m*SiO_2 for protein delivery application and improve our understanding of how selecting the appropriate protein and pore size can predict protein stability during transport. A particularly noteworthy contribution is the integration of advanced techniques, such as AFM and EF-TEM, to precisely characterize the localization of proteins within and around the nanoparticles, providing a deeper understanding of their behavior in nanocarrier systems.

The findings presented in this thesis open new research directions, with significant implications for the future development of Au@*m*SiO_2 nanoparticles. First, the detailed mechanistic understanding of nanoparticle synthesis presented here offers a unique opportunity to explore the fabrication of Au@*m*SiO_2 structures with anisotropic gold cores, such as nanoprims, nanostars, or nanorods. These anisotropic nanoparticles possess a larger absorption cross-section than their spherical counterparts, enabling more efficient light absorption and heat conversion. Furthermore, their tunable localized surface plasmon resonance peaks can be designed to match specific wavelengths of light,

notably in the infrared, allowing precise control over the heating effects that trigger protein release.

Second, while this work demonstrates promising results for protein stability in saline conditions, further investigation is essential to determine nanoparticle behavior in more complex, physiologically relevant environments. It is imperative to evaluate stability in media that closely mimic biological fluids, such as serum or blood plasma, to better understand how Au@*m*SiO_2 nanoparticles perform *in vivo*. These studies are crucial for translating these materials into practical applications, especially in biomedical settings.

Third, although this thesis establishes the cability of Au@*m*SiO_2 nanoparticles to retain proteins, the mechanisms governing protein release remain unexplored and represent a critical area for future research. Key questions that need to be addressed include the nature of protein-nanoparticle interactions and the efficacy of plasmonic heating in triggering protein release. Recent *in silico* simulations have provided valuable insights into protein adsorption on silica surfaces (2–4). By combining these advanced models with the experimental data presented in this thesis, it is possible to simulate the effects of temperature on protein adsorption and predict how nanoparticles respond to thermal stimuli. This integrated approach will be instrumental in guiding the development of more effective protein delivery systems.

Additionally, understanding the temperature profiles generated by nanoparticle irradiation is essential for optimizing protein release. Ongoing research by Maria Luz Martinez Ricci and Aude Barbara within our groups is addressing this issue through experimental measurements of the temperatures reached at the surface of individual Au@*m*SiO_2. These measurements will provide critical data for estimating the thermal conditions within the system, thus refining the design of nanoparticle-based delivery systems.

Moreover, quantifying protein release under experimental conditions remains a necessary step in fully realizing the potential of Au@*m*SiO_2

nanoparticles. Concentrating the laser energy in short periods of time using pulsed lasers, should allow to reach elevated temperatures specifically within individual nanoparticles. Such strategies could lead to more efficient energy transfer, maximizing the temperature rise and improving the efficacy of protein delivery.

Finally, the stability and versatility of Au@*m*SiO_2 nanoparticles indicate that their applications may extend well beyond biomedical fields. Notably, the potential of these nanoparticles in plant protein delivery presents an exciting, largely unexplored frontier. Current approaches to penetrate plant cell walls are often inefficient and can cause cellular damage (5). However, preliminary studies suggest that metal-based nanomaterials, including Au@*m*SiO_2, can internalize within walled cells without causing harm (5–7). This opens up promising application for these nanoparticles in agricultural biotechnology, paving the way for innovative solutions in plant science.

7.1. References

1. Croissant J, Zink JI. Nanovalve-Controlled Cargo Release Activated by Plasmonic Heating. J Am Chem Soc. 2012 May 9;134(18):7628–31.

2. Ozboyaci M, Kokh DB, Corni S, Wade RC. Modeling and simulation of protein–surface interactions: achievements and challenges. Quarterly Reviews of Biophysics. 2016 Jan;49:e4.

3. Tárraga WA, Picco AS, Longo GS. Understanding protein adsorption on silica mesoporous materials through thermodynamic simulations. Surfaces and Interfaces. 2024 Sep 1;52:104870.

4. Giussani L, Tabacchi G, Coluccia S, Fois E. Confining a Protein-Containing Water Nanodroplet inside Silica Nanochannels. International Journal of Molecular Sciences. 2019 Jan;20(12):2965.

5. Wang JW, Cunningham FJ, Goh NS, Boozarpour NN, Pham M, Landry MP. Nanoparticles for protein delivery *in planta*. Current Opinion in Plant Biology. 2021 Apr 1;60:102052.

6. Wu H, Li Z. Nano-enabled agriculture: How do nanoparticles cross barriers in plants? Plant Communications. 2022 Nov 14;3(6):100346.

7. Etxeberria E, Gonzalez P, Baroja-Fernández E, Romero JP. Fluid Phase Endocytic Uptake of Artificial Nano-Spheres and Fluorescent Quantum Dots by Sycamore Cultured Cells: Evidence for the Distribution of Solutes to Different Intracellular Compartments. Plant Signaling & Behavior. 2006 Jul 1;1(4):196–200.

Appendix

Appendix 1. Stepwise methods for the synthesis of Au@*m*SiO_2

In stepwise methods, AuNPs are first synthesized using the Turkevich-Frens method or similar approaches to create spherical particles. Once formed, these AuNPs are transferred into a new reaction mixture, where a silicon precursor is added to grow the mesoporous silica shell. The silicon precursor undergoes hydrolysis and then condenses around the gold core, forming the silica layer using the AuNPs as nucleation sites.

Table A1. Compilation of reported Au@*m*SiO_2 stepwise synthesis.

Ref	Coating-Solvent	Stabilizing agent	Shell formation Trigger	pH	Silica source	T (°C)	Reaction time (h)	D_{part} (nm)	D_{Au} (nm)	Pore size (nm)
[1]	Isopropanol	PVP	NH_3	10	C18TMS/ TEOS	RT	30	~100	20	3.7
[2]	H_2O	TTAB	NaOH	11.4 to 11.1	TEOS	25C	22	32 to 42	5	2.0 to 2.7
[3]	Ethanol	CTAB	NH_3	10	TEOS	60C	48	~100	ND	2.1
[4]	H_2O	CTAB	NH_3	10	TEOS	25C	12	~100	50	2.1
[5]	H_2O	CTAB	NaOH	ND	TEOS/ sodium silicate	80C	2	100 to 231	10 to 68	ND
[6]	Ethanol	CTAB	NH_3	ND	TEOS	ND	30	40	10	2 and 5
[7]	Ethanol/ H_2O	APTMS	NaOH	ND	TEOS	RT	72	100 to 140	15 to 30	3.5

C18TMS: octadecyltrimethoxysilane
TTAB: tetradecyltrimethylammonium bromide
APTMS: 3-aminopropyltrimethoxysilane

Appendix 2. Methods for the *One-pot* synthesis of Au@*m*SiO_2

The Au@*m*SiO_2 formation principle consists in the synthesis of gold cores by reducing a gold (III) precursor ($HAuCl_4$ or $KAuCl_4$) to generate NPs with a diameter between 5 and 40 nm. These AuNPs are then generally stabilized with the cetyltrimethylammonium bromide (CTAB) surfactant which prevents aggregation and acts as a template for further porous silica growth. To synthesize the porous shell, a silica precursor is added to promote hydrolysis and condensation. Finally, the CTAB template is removed by calcination or acidic extraction. Table A2 details the one-pot methods for Au@*m*SiO_2 synthesis reported so far.

Table A2. Compilation of reported Au@*m*SiO2 *one-pot* synthesis

Ref	Solvent	Au(III) reductor	Template	Trigger	pH	Gold source	Silica source	T (°C)	Reaction time (h)	D_{part} (nm)	D_{Au} (nm)	Pore size (nm)	Core-shell morphology	Application
[8]	28% ethanol-water	Ethanol	CTAB	NaOH	ND	$HAuCl_4$	TEOS	70	2	150	20	2	Several AuNPs per particle	Nanovalve
[9]	H2O	Sodium citrate	CTAB	NaoH	10	$HAuCl_4$	TEOS	RT	6	100	20	2.5	Single core	ND
[10]	H2O	Formaldehyde	CTAB	NaOH	ND	$HAuCl_4$	TEOS	80	1	~100	25 to 40	2.5	Single core	Catalysis
[11]	H2O	Sodium citrate	CTAB	NH_3	8-9	$HAuCl_4$	TEOS	35	24	70	No data	2.4	Single core	Cell imaging
[12]	H2O	Ethylene glycol	DTAB	ND	12	Au(I) complex	TMOS	60	12	155 to 360	4 to 8	2.3	Several AuNPs per particle	Biosensing
[13]	H2O	Sodium Borohydride	CTAB	NaOH	ND	$HAuCl_4$	TEOS	90	8	~60	5 to 8	3	Several AuNPs per particle	Catalysis
[14]	13% ethanol-water	2-methylaminoethanol	CTAB	2-methylaminoethanol	pH 11	$HAuCl_4$	TEOS	80	0.5	~50 to 80	21	4.17	Single core	Fluorescence enhancement
[15]	13% ethanol-water	2-methylaminoethanol	CTAB	2-methylaminoethanol	ND	$HAuCl_4$	TEOS	80	1.5	~100	22	3.4	Single core	Catalysis
[16]	13% ethanol-water	formaldehyde	CTAC	Amomonia	ND	$HAuCl_4$	TEOS	80/RT	1	64, 73, 68	17 to 22	ND	Single bimetallic core	Fluorescence enhacement
[17]	13% ethanol-water	formaldehyde	CTAB	NaOH	ND	$HAuCl_4$	TEOS	80	1	50±8	10	ND	Several bimetallic cores	Catalysis

Appendix 3. First derivatives of the sorption isotherms of *b*-Au@*m*SiO_2

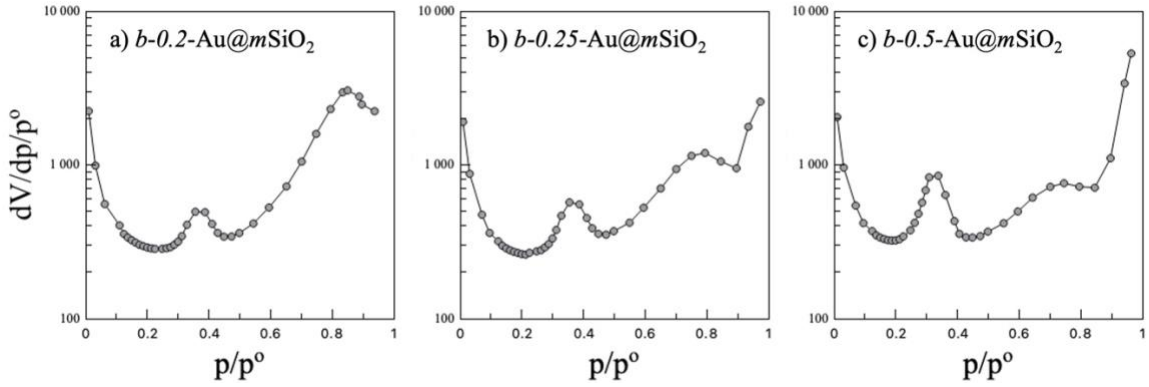

Figure A1. First derivatives of the adsorption branches of the sorption isotherms of *b*-Au@*m*SiO_2 nanoparticles synthesized with seeds using varying concentrations of TEOS: a) 0.2*x*, b) 0.25*x*, and c) 0.5*x*.

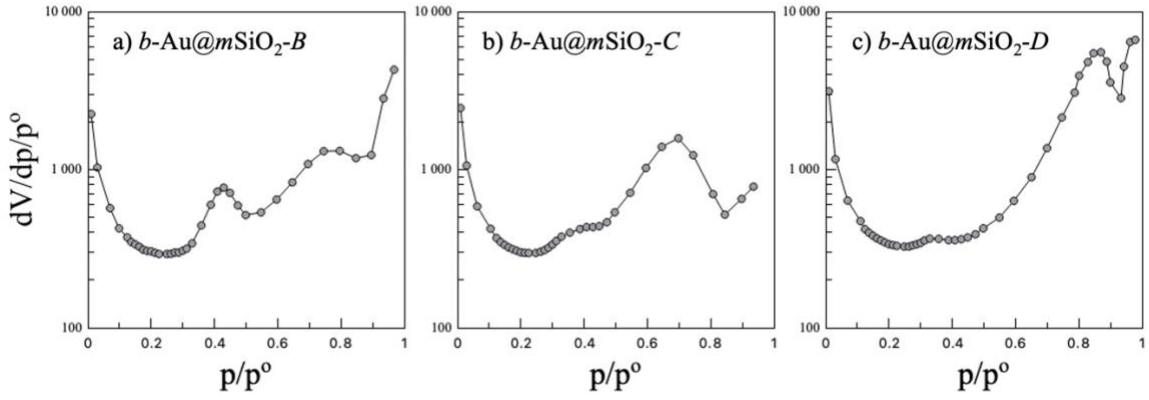

Figure A2. First derivatives of the adsorption branches of the sorption isotherms of *b*-Au@*m*SiO_2 nanoparticles synthesized with methods B, C, and D

Appendix 4. Linearized forms and parameters obtained from adsorption isotherms of BSA, *m*Cherry, and HRP adsorbed on *lp*-Au@*m*SiO_2

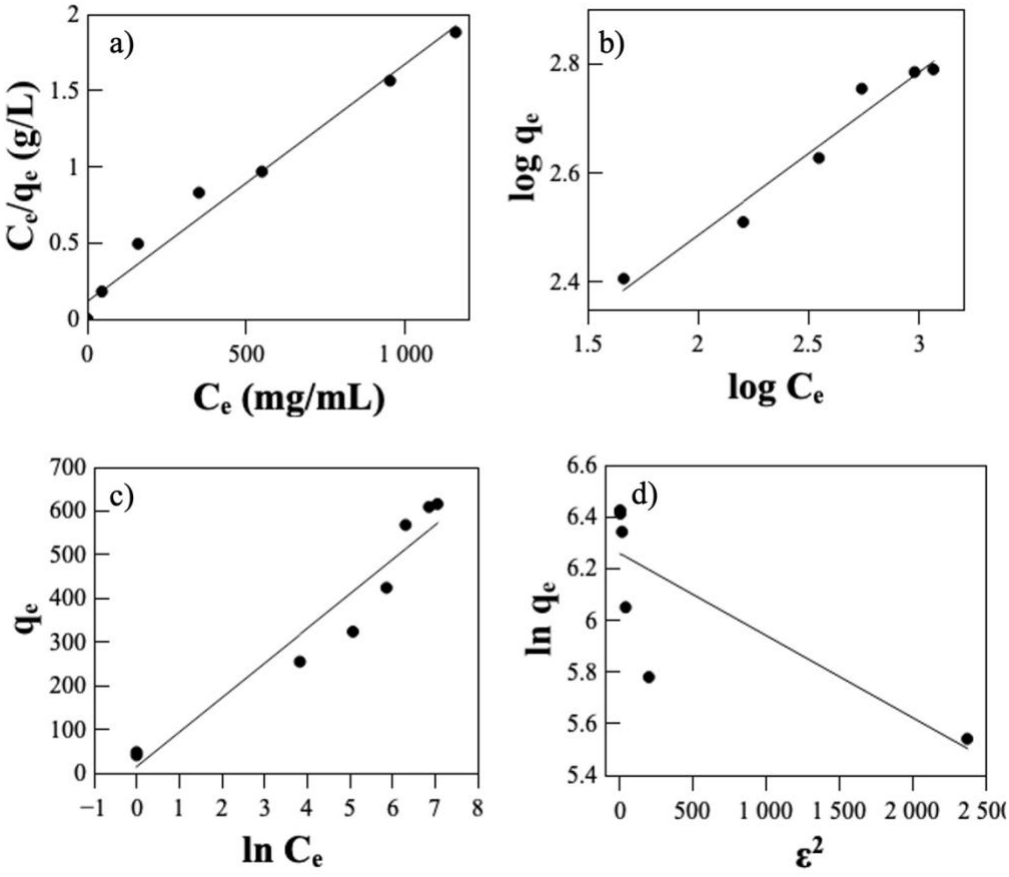

Figure A3. Linear fit of experimental data of BSA adsorption on *lp*-Au@*m*SiO_2 obtained using (a) Langmuir, (b) Freundlich, (c) Temkin, and (d) Dubinin-Radushkevich.

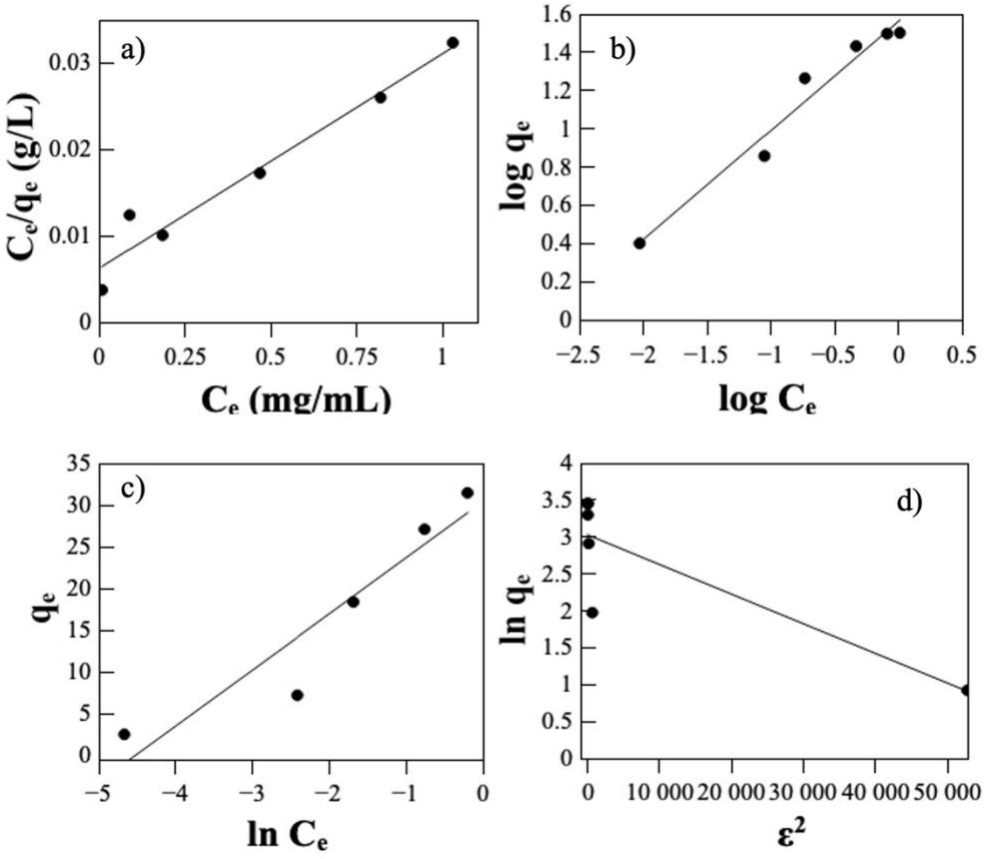

Figure A4. Linear fit of experimental data of *m*Cherry adsorption on *lp*-Au@*m*SiO_2 obtained using (a) Langmuir, (b) Freundlich, (c) Temkin, and (d) Dubinin-Radushkevich

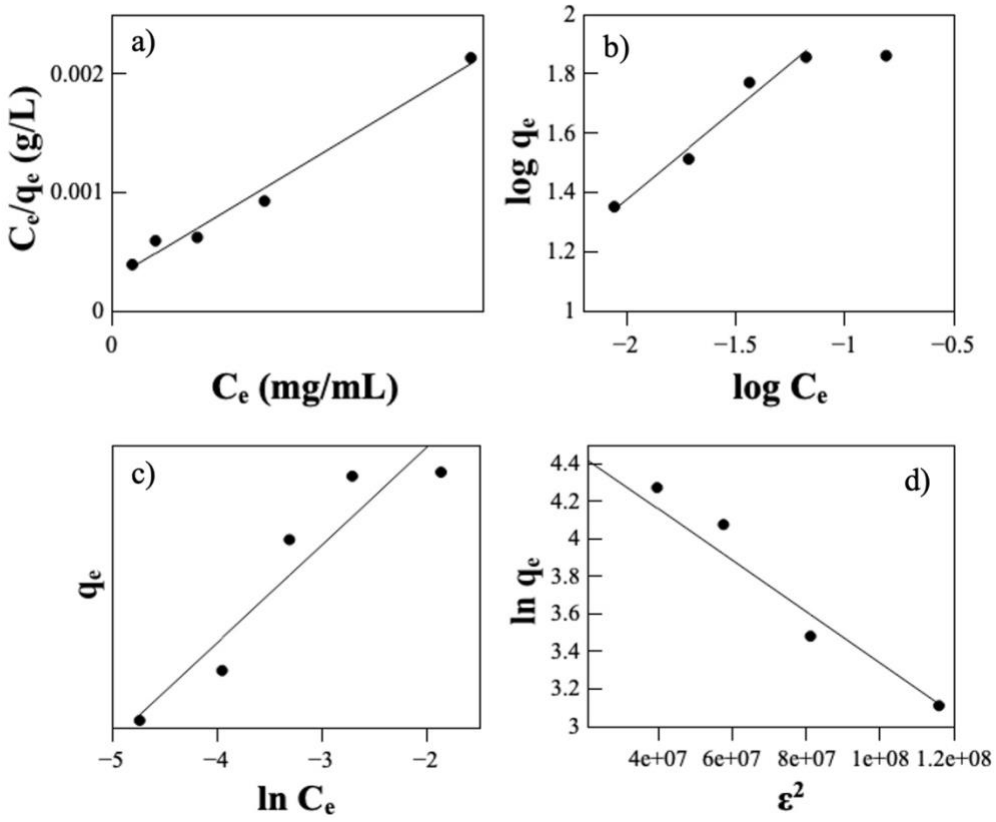

Figure A5. Linear fit of experimental data of HRP adsorption on *lp*-Au@*m*SiO_2 obtained using (a) Langmuir, (b) Freundlich, (c) Temkin, and (d) Dubinin-Radushkevich.

Table A3. Protein adsorption on *lp*-Au@*m*SiO_2 isotherm parameters

Isotherm	Equation	BSA	mCherry	HRP
Langmuir	$\frac{C_e}{q_e} = \frac{1}{Q_m b} + \frac{1}{Q_m} C_e$	$Q_m = 640.5\ mg.g^{-1}NP$ $b = 71.32\ L.mg^{-1}$ $R^2 = 0.978$	$Q_m = 40.09\ mg.g^{-1}NP$ $b = 0.247\ L.mg^{-1}$ $R^2 = 0.966$	$Q_m = 84.85\ mg.g^{-1}NP$ $b = 0.022\ L.mg^{-1}$ $R^2 = 0.983$
Freundlich	$\log(q_e) = \log K_f + \frac{1}{n} \log C_e$	$K_f = 6.62$ $n = 3.37$ $R^2 = 0.962$	$K_f = 4.76$ $n = 1.74$ $R^2 = 0.965$	$K_f = 13.35$ $n = 1.647$ $R^2 = 0.971$
Temkin	$q_e = B \ln A + B \ln C_e$	$B = 78.75$ $A = 1.22\ L.mg^{-1}$ $R^2 = 0.936$	$B = 6.71$ $A = 92.44\ L.mg^{-1}$ $R^2 = 0.886$	$B = 19.66$ $A = 380.13\ L.mg^{-1}$ $R^2 = 0.894$
Dubini Radushkevich	$\ln q_e = \ln Q_s - K\ \varepsilon^2$	$Q_s = 522.72\ mg.g^{-1}NP$ $K \times 10^{-4} = 3.17\ mol^2.KJ^2$ $R^2 = 0.612$	$Q_s = 20.64\ mg.g^{-1}NP$ $K \times 10^{-5} = 4.01\ mol^2.KJ^2$ $R^2 = 0.711$	$Q_s = 110.98\ mg.g^{-1}NP$ $K \times 10^{-8} = 1.37\ mol^2.KJ^2$ $R^2 = 0.916$

Appendix 5. Review of maximum protein adsorption capacity on MSN

Table A4. Amount of proteins absorbed in MSNs with different pore sizes reported in the literature

Ref	Protein	NP diameter (nm)	NP Pore size (nm)	NP Surface area (m^2/g)	Adsortion time	Reported adsorbed protein	Reported units	mg protein /g NP	pH	Method
[18]	Human serum albumin	67	2.2	1255	5 - 80 min	4.3	mg/m^2	5353	7.4	Saturated absorption capacity calculated using a pseudo-second-order kinetic equation
[18]	Human serum albumin	68	3	947	5 - 80 min	4.4	mg/m^2	4209	8.4	
[18]	Human γ-globulin	67	2.2	1255	5 - 80 min	3.2	mg/m^2	4026	9.4	
[18]	Human γ-globulin	68	3	947	5 - 80 min	2.8	mg/m^2	2694	10.4	
[18]	Human fibrinogen	67	2.2	1255	5 - 80 min	0.6	mg/m^2	727	11.4	
[18]	Human fibrinogen	68	3	947	5 - 80 min	0.5	mg/m^2	508	12.4	
[19]	Human serum	120	0	50	1 h	0.8	mg/m^2	38	7.4	The adsorbed protein was determinated by TGA
[19]	Human serum	120	2.7	1016	1 h	0.2	mg/m^2	213	7.4	
[19]	Human serum	120	4.8	680	1 h	0.2	mg/m^2	170	7.4	
[19]	Human serum	120	6.2	421	1 h	0.3	mg/m^2	134	7.4	
[19]	Human serum	120	7.4	360	1 h	0.4	mg/m^2	137	7.4	
[19]	Human serum	120	14	176	1 h	0.8	mg/m^2	146	7.4	

[20]	Fetal bovine serum	85	0	20	1 h	5.3	mg/m^2	106	7.4	The adsorbed protein was determinated by TGA
[20]	Fetal bovine serum	251	0	10	1 h	7.6	mg/m^2	73	7.4	
[20]	Fetal bovine serum	482	0	5	1 h	8.5	mg/m^2	44	7.4	
[20]	Fetal bovine serum	914	0	1.8	1 h	22.9	mg/m^2	41	7.4	
[20]	Fetal bovine serum	73	3	1010	1 h	6.1	mg/m^2	6130	7.4	
[20]	Fetal bovine serum	869	2	1012	1 h	14.5	mg/m^2	14674	7.4	
[21]	Bovine serum albumin	<200	5.41 and 24.5	312	24 h	307	mg/g	307	4.8	The adsorbed protein was determinated by protein quantification in the supernatant
[21]	Bovine serum albumin	<200	4.19 and 44.2	425	24 h	263	mg/g	263	4.8	
[21]	Immunoglobulin G	<200	5.41 and 24.5	312	24 h	262	mg/g	262	7.4	
[21]	Immunoglobulin G	<200	4.19 and 44.2	425	24 h	115	mg/g	115	7.4	
[22]	Lysozyme	200-400	1.8	890	100 h	275	mg/g	275	7.6	The adsorbed amount of protein was obtained by protein quantification in the supernatant
[22]	Lysozyme	200-400	2.2	1001	100 h	125	mg/g	125	7.6	
[22]	Lysozyme	200-400	3.8	1186	100 h	90	mg/g	90	7.6	
[23]	Myoglobin from equine skeletal muscle	74	<5	ND	24	104	mg/g	104	6	The adsorbed protein was determinated by protein quantification in the supernatant
[23]	Myoglobin from equine skeletal muscle	83	5--10	ND	24	71	mg/g	71	6	
[23]	Myoglobin from equine skeletal muscle	94	20-25	ND	24	147	mg/g	147	6	
[23]	Bovine serum albumin	74	<5	ND	24	467	mg/g	467	4	

[23]	Bovine serum albumin	83	5--10	ND	24	427	mg/g	427	4	
[23]	Bovine serum albumin	94	20-25	ND	24	396	mg/g	396	4	
[23]	Factor VIII	74	<5	ND	24	0	mg/g	0	6.5	
[23]	Factor VIII	83	5--10	ND	24	0	mg/g	0	6.5	
[23]	Factor VIII	94	20-25	ND	24	6.8	mg/g	6.8	6.5	
*	Bovine serum albumin	100	20	900	2	640	mg/g		7	The adsorbed protein was determinated by protein quantification in the supernatant
*	mCherry	100	20	900	2	39	mg/g		7	
*	Horseradish peroxidase	100	20	900	2	87	mg/g		7	

- Obtained in this thesis

Appendix 6. Pairwise Structure Alignment of GFP and *m*Cherry

Table A5. Parameter obtained from the pairwise structure alignment of GFP and *m*Cherry

PDB ID	RMSD	TM-score*	Identity	Aligned residues	Sequence length
2vad					225
1qyq	1.71	0.92	25%	208	237

***TM-Score (Template Modeling Score):** This metric is used to measure the structural similarity between two protein structures [24]. The score ranges from 0 to 1, with the following interpretations:

TM-Score between 0 and 0.3: Indicates random or insignificant structural similarity.

TM-Score between 0.5 and 1: Suggests that the two protein structures share approximately the same fold, indicating significant structural similarity.

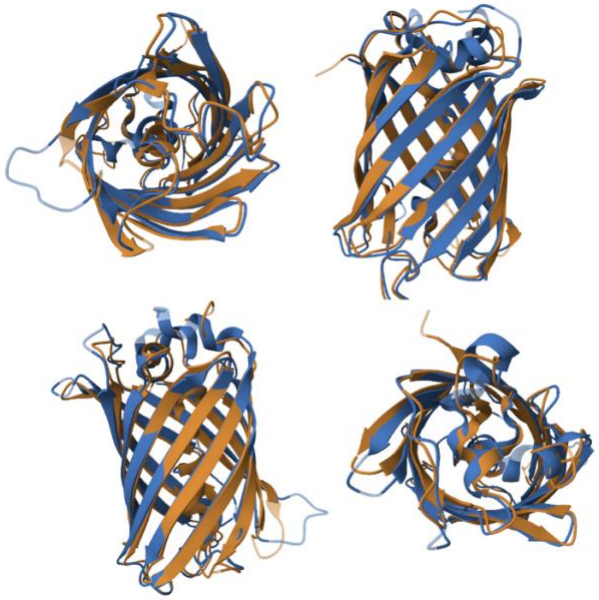

Figure A6. Different views of the structural alignment between *m*Cherry and GFP. The figure showcases the alignment from various angles, highlighting the similarities and differences in the overall protein folds of the two fluorescent proteins.

Appendix 7. Emission and excitation spectra of free *m*Cherry in solution and adsorbed on *lp*-Au@*m*SiO_2 particles

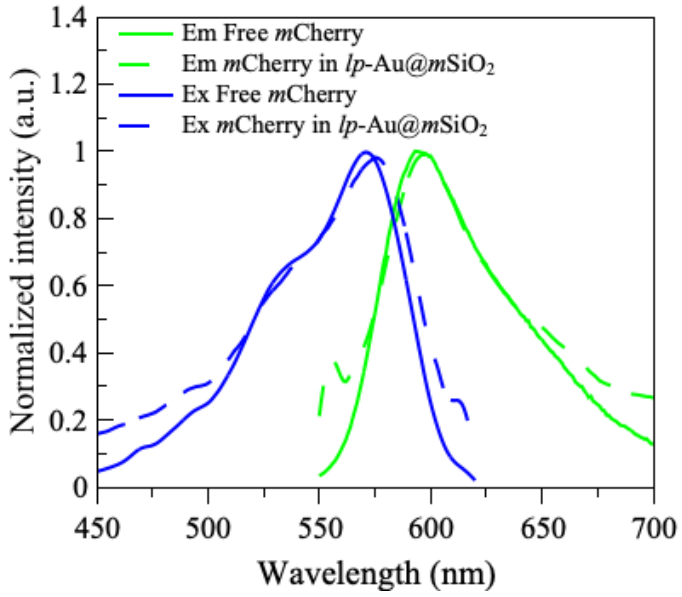

Figure A7. Normalized excitation spectra (emission at 640 nm) and emission spectra (540 nm) for *mCherry* free in solution and adsorbed on *lp*-Au@*m*SiO_2 particles

References

1. Li H, Li Z, Liu L, et al (2015) An efficient gold nanocarrier for combined chemo-photodynamic therapy on tumour cells. RSC Adv 5:34831–34838. https://doi.org/10.1039/C4RA17249C

2. Wu C, Lim Z-Y, Zhou C, et al (2013) A soft-templated method to synthesize sintering-resistant Au–mesoporous-silica core–shell nanocatalysts with sub-5 nm single-cores. Chem Commun 49:3215–3217. https://doi.org/10.1039/C3CC39202C

3. Sanz-Ortiz MN, Sentosun K, Bals S, Liz-Marzán LM (2015) Templated Growth of Surface Enhanced Raman Scattering-Active Branched Gold Nanoparticles within Radial Mesoporous Silica Shells. ACS Nano 9:10489–10497. https://doi.org/10.1021/acsnano.5b04744

4. An J, Yang X-Q, Cheng K, et al (2017) In Vivo Computed Tomography/Photoacoustic Imaging and NIR-Triggered Chemo-Photothermal Combined Therapy Based on a Gold Nanostar-, Mesoporous Silica-, and Thermosensitive Liposome-Composited Nanoprobe. ACS Appl Mater Interfaces 9:41748–41759. https://doi.org/10.1021/acsami.7b15296

5. Santana Vega M, Guerrero Martínez A, Cucinotta F (2019) Facile Strategy for the Synthesis of Gold@Silica Hybrid Nanoparticles with Controlled Porosity and Janus Morphology. Nanomaterials (Basel) 9:348. https://doi.org/10.3390/nano9030348

6. Sekhar ACS, Meera CJ, Ziyad KV, et al (2013) Synthesis and catalytic activity of monodisperse gold–mesoporous silica core–shell nanocatalysts. Catal Sci Technol 3:1190–1193. https://doi.org/10.1039/C3CY20772B

7. Botella P, Corma A, Navarro MT (2007) Single Gold Nanoparticles Encapsulated in Monodispersed Regular Spheres of Mesostructured Silica Produced by Pseudomorphic Transformation. Chem Mater 19:1979–1983. https://doi.org/10.1021/cm0629457

8. Croissant J, Zink JI (2012) Nanovalve-Controlled Cargo Release Activated by Plasmonic Heating. J Am Chem Soc 134:7628–7631. https://doi.org/10.1021/ja301880x

9. Song JT, Zhang XS, Qin MY, Zhao YD (2015) One-pot two-step synthesis of core-shell mesoporous silica-coated gold nanoparticles. Dalton Transactions 44:7752–7756. https://doi.org/10.1039/c5dt00912j

10. Chen J, Zhang R, Han L, et al (2013) One-pot synthesis of thermally stable gold@mesoporous silica core-shell nanospheres with catalytic activity. Nano Research 6:871–879. https://doi.org/10.1007/s12274-013-0363-1

11. Li X, Shao Y, Lv S, et al (2021) Au@mSiO2 core–shell nanoparticles loaded with fluorescent dyes: synthesis and application for imaging performance. Dalton Trans 50:5624–5631. https://doi.org/10.1039/D1DT00253H

12. Veneziano R, Derrien G, Tan S, et al (2012) One step synthesis of gold-loaded radial mesoporous silica nanospheres and supported lipid bilayer functionalization: Towards bio-multifunctional sensors. Small 8:3674–3682. https://doi.org/10.1002/smll.201200758

13. Hammond-Pereira E, Bryant K, Graham TR, et al (2020) Mesoporous silica-encapsulated gold core-shell nanoparticles for active solvent-free benzyl alcohol oxidation. Reaction Chemistry and Engineering 5:1939–1949. https://doi.org/10.1039/d0re00198h

14. Zhang S, Xu X, Zhang G, et al (2019) One-pot one-step synthesis of Au@SiO2 core-shell nanoparticles and their shell-thickness-dependent fluorescent properties. RSC Advances 9:17674–17678. https://doi.org/10.1039/c9ra02543j

15. Zhang G, Dong L, Zhang S, et al (2021) One-pot synthesis of Au@mSiO2 yolk-shell nanoparticles with enhanced catalytic and surface-enhanced Raman scattering (SERS) properties. Journal of Alloys and Compounds 871:. https://doi.org/10.1016/j.jallcom.2021.159631

16. Bian X, Zhang G, Liu B, Yang J (2022) One-pot synthesis of Au/Ag alloy@SiO2 core–shell nanoparticles and their metal-enhanced fluorescence and surface-enhanced Raman scattering spectroscopies. J Nanopart Res 24:20. https://doi.org/10.1007/s11051-022-05412-8

17. Hao J, Liu B, Maenosono S, Yang J (2022) One-pot synthesis of Au-M@SiO2 (M = Rh, Pd, Ir, Pt) core–shell nanoparticles as highly efficient catalysts for the reduction of 4-nitrophenol. Sci Rep 12:7615. https://doi.org/10.1038/s41598-022-11756-x

18. Ma Z, Bai J, Wang Y, Jiang X (2014) Impact of Shape and Pore Size of Mesoporous Silica Nanoparticles on Serum Protein Adsorption and RBCs Hemolysis. ACS Appl Mater Interfaces 6:2431–2438. https://doi.org/10.1021/am404860q

19. Vidaurre-Agut C, Rivero-Buceta E, Romaní-Cubells E, et al (2019) Protein Corona over Mesoporous Silica Nanoparticles: Influence of the Pore Diameter on Competitive Adsorption and Application to Prostate Cancer Diagnostics. ACS Omega 4:8852–8861. https://doi.org/10.1021/acsomega.9b00460

20. Clemments AM, Botella P, Landry CC (2015) Protein Adsorption From Biofluids on Silica Nanoparticles: Corona Analysis as a Function of Particle Diameter and Porosity. ACS Appl Mater Interfaces 7:21682–21689. https://doi.org/10.1021/acsami.5b07631

21. Shin H-S, Hwang Y-K, Huh S (2014) Facile Preparation of Ultra-Large Pore Mesoporous Silica Nanoparticles and Their Application to the Encapsulation of Large Guest Molecules. ACS Appl Mater Interfaces 6:1740–1746. https://doi.org/10.1021/am404709w

22. Katiyar A, Ji L, Smirniotis PG, Pinto NG (2005) Adsorption of Bovine Serum Albumin and lysozyme on siliceous MCM-41. Microporous and Mesoporous Materials 80:311–320. https://doi.org/10.1016/j.micromeso.2004.11.026

23. Zampini G, Matino D, Quaglia G, et al (2019) Experimental evidences on the role of silica nanoparticles surface morphology on the loading, release and activity of three proteins. Microporous and Mesoporous Materials 287:220–227. https://doi.org/10.1016/j.micromeso.2019.06.005

24. Zhang Y, Skolnick J (2005) TM-align: a protein structure alignment algorithm based on the TM-score. Nucleic Acids Res 33:2302–2309. https://doi.org/10.1093/nar/gki524